Han Zhao
N.A. Fleck
Editors

IUTAM Bookseries

IUTAM Symposium on Mechanical Properties of Cellular Materials

Proceedings of the IUTAM Symposium on Mechanical Properties of Cellular Materials, held September 17–20, 2007, LMT-Cachan, Cachan, France

Springer

IUTAM Symposium on Mechanical Properties of Cellular Materials

IUTAM BOOKSERIES

Volume 12

Aims and Scope of the Series

The IUTAM Bookseries publishes the proceedings of IUTAM symposia under the auspices of the IUTAM Board.

For other titles published in this series, go to
www.springer.com/series/7695

Han Zhao • N.A. Fleck
Editors

IUTAM Symposium on Mechanical Properties of Cellular Materials

Proceedings of the IUTAM Symposium
on Mechanical Properties of Cellular Materials,
held September 17 – 20, 2007, LMT - Cachan,
Cachan, France

Springer

Editors
Han Zhao
Université Paris VI
CNRS LMT Cachan
61 avenue du Président
Wilson
94235 Cachan CX
France
zhao@lmt.ens-cachan.fr

Dr. N.A. Fleck
Cambridge University
Dept. Engineering
Trumpington St.
Cambridge
United Kingdom CB2 1PZ

ISBN: 978-1-4020-9403-3 e-ISBN: 978-1-4020-9404-0
DOI: 10.1007/978-1-4020-9404-0

Library of Congress Control Number: 2008942388

Printed on acid-free paper

springer.com

Preface

The IUTAM symposium on “Mechanical properties of cellular materials” was held from 17–20 September 2007 at the Laboratoire de Mécanique et Technologie (LMT-Cachan), Cachan, France. It was aimed to bring together structural, mechanical and material scientists working on different aspects of this new class of materials (microstructure observation, micromechanical and multiscale modeling, phenomenological models, structural impact behaviour and numerical validation, etc.). The symposium was mostly focused on the following topics:

(a) Microstructure control and their influences
(b) Multi-scale and macroscopic modeling and numeric validations
(c) Failure analysis, applicability of fracture mechanics
(d) High strain rate sensitivity

Forty external scholars have attended the technical sessions of the symposium. The delegates were from 14 countries: Austria (2), Canada (1), China (6), France (12), Germany (1), India (1), Japan (2), The Netherlands (1), Norway (2), Poland (1), Slovenia (1), Switzerland (4), United Kingdom (4), USA (2). A number of local researchers and Ph.D students have also attended the sessions and taken part in the discussions. The symposium sparked off an original dialogue between material scientists who make all kind of cellular materials and the mechanical scientists who characterize and model the behavior of these materials.

This volume collects 22 written contributions to the symposium from invited speakers, which provides a survey of the topics discussed in the symposium. Time and effort spent by the authors in preparing their manuscripts for this book as well as time spent by reviewers in their careful manuscript reading is greatly appreciated. Thanks also are due to IUTAM bureau, Ecole Normale Supérieure de Cachan, National Scientific Research Center (CNRS), French Association of Mechanics (AFM), and EADS Innocampus foundation for sponsoring this event.

Finally, the editors would like to thank all the speakers and contributors, international scientific committee members, local organizing committee members, session chairs, symposium secretary Mrs. Catherine Genin, for their valuable contributions to this symposium and make this volume possible.

Cachan, France *Han Zhao*
Cambridge, UK *Norman Fleck*

Contents

Committees

Scientific Committee

H. Zhao (Chair)	ENSCachan/CNRS/University Paris 6, France
N. Fleck (Co-Chair)	University of Cambridge, UK
J. Banhart	HMI, Germany
J. Hutchinson	University of Harvard, USA
M. Langseth	NTNU, Norway
F.G. Rammerstorfer	Wien University of Technology, Austria
G. Ravichandran	Caltech, USA
Z.M. Zheng (IUTAM representative)	Institute of Mechanics/CAS, China

Local Organization Committee

A. Benallal	LMT-Cachan, France
S. Pattofatto	LMT-Cachan, France
H. Zhao	LMT Cachan, France

Final Program

Monday 17 September

	Monday 17
9h00–9h50	Registration-Coffee
9h50–10h00	Opening
10h00–12h00 Chairman: S. Kyriakydes	**Non-linear Uniaxial Deformation of Microcellular Metals: Model Systems and Simplified Analysis** Y. Conde[1], S. Soubielle[2], R. Müller[1*], J.F. Despois[1*], A. Marmottant[2], R. Goodall[1], F. Diologent[1], L. Salvo[2], and **A. Mortensen[1]** [1] *Laboratory for Mechanical Metallurgy,Ecole Polytechnique Fédérale de Lausanne (EPFL), Lausanne, CH-1015, Switzerland (*Now with Novelis Switzerland S.A., Sierre, CH-3960, Switzerland)* [2] *GPM2 Laboratory, Institut National Polytechnique de Grenoble (INPG), Saint-Martin d'Hères, F-38000 Grenoble, France* **Mechanical Properties and Design of Lattice Composite and Structures** **D.-N. Fang**, Y.-H. Zhang, and X.-D. Cui *Department of Engineering Mechanics, Tsinghua University, Beijing, 100084, China* **Nano-Cellular Materials with Unusual Mechanical and Physical Properties** H.L. Duan[1], J. Wang[2], and **B.L. Karihaloo[3]** [1] *Institute of Nanotechnology, Forschungszentrum Karlsruhe, Germany* [2] *Department of Mechanics and Aerospace Engineering, Peking University, China* [3] *School of Engineering, Cardiff University, UK*
12h00–14h00	Lunch
14h00–15h20 Chairman: J. Banhart	**The High Strain Rate Response of Adipose Tissue** **K. Comley** and N.A. Fleck *Cambridge University Engineering Department, Trumpington St., Cambridge, CB2 1PZ, UK*

	Mechanical Properties of Titanium Foams with Different Oxygen Concentrations **L.P. Lefebvre** and E. Baril *National Research Council Canada/Industrial Materials Institute, 75 de Mortagne, Boucherville, J4B 6Y4 Canada*
15h20–15h40	Coffee break
15h40–17h40 Chairman: L.P. Lefebvre	**X Ray Tomography Study of Cellular Materials: Experiments and Modelling** **E. Maire**, O. Caty, and J. Adrien *Labo GEMPPM. Bat St Exupery. INSA de Lyon. 69621 Villeurbanne cedex.France* **Compressive and Fatigue Behaviour of Alporas Foam Studied by X-Ray Tomography** M. Mukherjee[1,2,*], K.R. Murthy[3], F. Garcia-Moreno[1,2], U. Ramamurty[3], and **J. Banhart**[1,2] [1] *Hahn-Meitner-Institute Berlin, Glienicker Strasse 100, 14109, Berlin, Germany* [2] *Technical University Berlin, Hardenbergstrasse 36, 10623 Berlin, Germany* **Mechanical Properties of Lotus-Type Porous Metals** **H. Nakajima** *The Institute of Scientific and Industrial Research, Osaka University, Ibaraki, Osaka 567-0047, Japan*
18h00	Departure for dinner-reception at “Abbaye des vaux de Cernay”

Tuesday 18 September

9h00–10h20 Chairman: K. Sab	**Open Cell Nickel Superalloy Foam for Diesel Particle Filter Applications: From the Cell morphology to the elastoviscoplastic behaviour** A. Burteau[1], J.-D. Bartout[1], **S. Forest**[1], Y. Bienvenu[1], S. Saberi[2] [1] *Centre des Matériaux, Mines Paris, Paristech, CNRS UMR 7633, BP 87, 91003 Evry Cedex, France* [2] *INCO SP 2101 Hadwen road, Sheridan Park, MISSISSAUGA, ON L5K 2L3, Canada* **On the Crushing of Metallic Open Cell Foams** W.-Y. Jang and **S. Kyriakides** *Research Center for Mechanics of Solids, Structures and Materials, 210 E 24th Street The University of Texas at Austin, Austin, TX 78712, USA*
10h20–10h40	Coffee break
10h40–12h00 Chairman: N.A. Fleck	**Anisotropy in Buckling Behavior of Kelvin Open-Cell Foams Subject to Uniaxial Compression** D. Okumura[1], A. Okada[2], and **N. Ohno**[1] [1] *Department of Mechanical Science and Engineering, Nagoya University, Chikusa-ku, Nagoya 464-8603, Japan* [2] *Department of Computational Science and Engineering, Nagoya University, Chikusa-ku, Nagoya 464-8603, Japan*

	Multi-Scale Plasticity Models for Stable Cellular Solids **D. Mohr** *Solid Mechanics Laboratory, CNRS UMR 7649, École Polytechnique, Palaiseau, 91128, France; Department of Mechanical Engineering, Massachusetts Institute of Technology, Cambridge, MA 02139, USA*
12h00–14h00	Lunch
14h00–15h20 Chairman: B. Karihaloo	**Elastic Buckling of Two-Dimensional Random Honeycombs: Does a Representative Volume Element Exist?** F. Jouneid and **K. Sab** *Institut Navier, LAMI (ENPC/LCPC), Ecole Nationale des Ponts et Chaussées, 6 et 8 avenueBlaise Pascal, Cité Descartes, Champs-sur-Marne, 77455 Marne la Vallée cedex* **Macroscopic Response, Microstructure Evolution and Instabilities in Porous Elastomers** **P.P. Castañeda[1]** and O. Lopez-Pamies[1,2] [1]*Department of Mechanical Engineering and Applied Mechanics, University of Pennsylvania, USA* [2]*LMS (CNRS UMR 7649), Département de Mécanique, École Polytechnique, France*
15h20–15h40	Coffee break
15h40–17h40 Chairman: N. Ohno	**Mechanical Properties of Semi-Expanded Hollow Sphere Structures** **T. Daxner** and R.W. Tomas *Institute of Lightweight Design and Structural Biomechanics Vienna University of Technology, A-1040 Vienna, Austria* **Indentation Tests on Al Matrix Syntactic Foams** X.F. Tao, G.K. Schleyer, and **Y.Y. Zhao** *Department of Engineering, University of Liverpool, Liverpool L69 3GH, UK*
18h	Wine-Cheese party, visit of LMT

Wednesday 19 September

9h00–10h20 Chairman: S. Forest	**Fracture of Metal Foams** K.R. Mangipudi and **P.R. Onck** *Department of Applied Physics, Zernike Institute for Advanced Materials, University of Groningen, The Netherlands* **Fracture of Foamed Cementitious Materials: A Combined Experimental and Numerical Study** D. Meyer, H.-K. Man, and **Jan G.M. van Mier** *ETH Zurich, Department of Civil, Environmental and Geomatics Engineering Institute for Building Materials, 8093 Zurich, Switzerland*
10h20–10h40	Coffee break

10h40–12h00 Chairman: Jan G.M. van Mier	**Modeling and Simulation of Highly Porous Open Cell Structures: Elasto-Plasticity and Localization Versus Disorder and Defects** M.H. Luxner and **H.E. Pettermann** *Institute of Lightweight Design and Structural Biomechanics Vienna University of Technology, Vienna, Austria* **Thermomechanical Behaviour Prediction of Crimped Mineral Wool** J.-F. Witz, **F. Hild**, and S. Roux *LMT-Cachan, ENS de Cachan/CNRS-UMR 8535/Université Paris 6*
12h00–14h00	Lunch – Party Pavillon Montsouris
	Free afternoon

Thursday 20 September

9h00–10h20 Chairman: M. Langseth	**Influences of Inertia and Material Property on the Dynamic Behavior of Cellular Metals** **J.L. Yu***, Y.-D. Liu, Z.-J. Zheng, and J.-R. Li *CAS Key Laboratory of Mechanical Behavior and Design of Materials, University of Science and Technology of China, Hefei, Anhui 230026, People's Republic of China* **Analysis of the Shock Front Propagation in a Cellular Material** **S. Pattofatto**, I. Nasri, and H. Zhao *LMT-Cachan, ENS de Cachan/CNRS-UMR 8535/Université Paris 6*
10h20–10h40	
10h40–12h00 Chairman: D.N. Fang	**Close-Range Blast Loading of Aluminium Foam Panels: A Numerical Study** A.G. Hanssen[1,2], T. Børvik[2,3], and **M. Langseth[2]** [1]*IMPETUS Afea AS, Strandgaten 32, 4400 Flekkefjord, Norway* [2]*CRI-SIMLab, Centre for Research-based Innovation, The Faculty of Engineering Science and Technology, NTNU, N-7491 Trondheim, Norway* [3]*Norwegian Defence Estates Agency, Research & Development Section, PB 405, Sentrum, No-0103 Oslo, Norway* **Study of Cellular Materials Under Dynamic Loading for Bird Strike Application** **Y. Girard** *EADS Innovation Works, 12, bis rue Pasteur, 92152 Suresnes Cedex France*
12h00–14h00	Lunch
14h00–15h20 Chairman: F. Hild	**Description of the Behaviour of Cellular Composite with Weak Filling Material** **E. Postek[1]** and T. Sadowski[2] [1]*Institute of Geophysics and Tectonics, School of Earth and Environment, University of Leeds, LS2 9JT, Leeds, United Kingdom* [2]*Faculty of Civil and Sanitary Engineering, Lublin University of Technology, ul. Nadbystrzycka 40, 20-618 Lublin*

	Studies on the Dynamic Behavior of Aluminum Alloy Foams **H.-W. Ma**[1,2], Z.-H. Wang[1], L.-M. Zhao[1], and G.-T. Yang[1] [1] *Institute of Applied Mechanics, Taiyuan University of Technology, Taiyuan, 030024, China* [2] *College of Science & Engineering, Jinan University, Guangzhou 510632, China*
15h20–15h40	Coffee break
15h40–16h20 Chairman: P. Onck	**Computational Modelling of Closed- and Open-Cell Cellular Structures with Fillers** **M. Vesenjak**[1], A. Öchsner[2], and Z. Ren[3] [1] *University of Maribor, faculty of Mechanical Engineering, Smetanova 17, SI-2000 Maribor, Slovenia* [2] *Universiti Teknologi Malaysia, Faculty of Mechanical Engineering,81310 UTM Skudai, Johor, Malaysia* [3] *University of Maribor, faculty of Mechanical Engineering,Smetanova 17, SI-2000 Maribor, Slovenia*
19h00	Visit and Banquet at Orsay Museum

List of Participants

N. Auffray ONERA/DMMP 29, Avenue de la division Leclerc BP 72 92322 Châtillon Cedex, France

J. Banhart Hahn-Meitner-Institut Berlin (HMI) Glienicker Street 100, 14109 Berlin, Germany

A. Benallal LMT-Cachan 61, Avenue du président wilson 94235 Cachan Cedex, France

K. Comley Department of Engineering University of Cambridge Trumpington Street Cambridge, CB2 1PZ, UK

C. Davoine ONERA/DMMP 29, Avenue de la division Leclerc BP 72 92322 Châtillon Cedex, France

T. Daxner Technische Universität Wien Institute of Leightweight Design and Structural Biomechanics Gusshausstrasse 25–29, A-1040 Vie Austria

I. Elnasri LMT-Cachan ENS Cachan/CNRS UMR8535/UPMC/UniverSud Paris 61, Avenue du président wilson 94235 Cachan Cedex, France

D.N. Fang Department of Engineering Mechanics Tsinghua University Beijing, 100084, China

N. Fleck Material and Design Division Department of Engineering University of Cambridge Trumpington Street, Cambridge, CB2 1PZ, UK

S. Forest Ecole Nationale Superieure des Mines de Paris/CNRS Centre des Materiaux UMR 7633 B.P. 87 91003 EVRY Cedex, France

Y. Girard EADS-CCR Surenes, 12 bis rue Pasteur 92152 Suresnes Cedex, France

A. Hanssen NUTU, Trondhelm, Norway SIMLab Department of Structural Engineering, NTNU N-7491 Trondheim, Norway

A. Hess Thales communications 160 Boulevard de Valmy BP82 92704 Colombes Cedex, France

F. Hild LMT-Cachan 61, Avenue du président wilson 94235 Cachan Cedex, France

B. Hou School of Aeronautics Northwest Polytechnic University, China 710072 Xi'an, Shaanxi, P.R. China

B. Karihaloo School of Engineering Cardiff University Queen's Buildings Newport Road Cardiff CF24 3AA, UK

S. Kyriakydes Department of Aerospace Engineering & Engineering Mechanics The University of Texas Austin, TX 78712, USA

M. Langseth SIMLab Department of Structural Engineering, NTNU N-7491 Trondheim, Norway

L.-P. Lefebvre Powder Forming Industrial Materials Institute (IMI) National Research Council Canada (NRC) 75 de Mortagne Boulevard Boucherville, QC, Canada, J4B 6Y4

H.W. Ma The College of Science and Engineering Jinan University Guangzhou, 510632, P.R. China

Y.S. Ma Institute of Mechanics China Academy of Sciences No.15 BEI-SI-HUAN-XI Rd 100080 Beijing, China

E. Maire Labo GEMPPM. Bat St Exupery INSA de Lyon. 69621 Villeurbanne Cedex, France

H.K. Man Institut f. Baustoffe (IfB) Schafmattstr. 6 ETH-Hönggerberg, HIF E 11 CH-8093 Zürich, Switzerland

D. Meyer Institut f. Baustoffe (IfB) Schafmattstr. 6 ETH-Hönggerberg, HIF E 11 CH-8093 Zürich, Switzerland

D. Mohr LMS Ecole Polytechnique 91128 Palaiseau Cedex, France

A. Mortensen EPFL – STI – IMX – LMM MXD 140 (Bâtiment MX), Station 12 CH - 1015 Lausanne, Switzerland

H. Nakajima The Institute of Scientific and Industrial Research Osaka University, Ibaraki, Osaka 567-0047, Japan

N. Ohno Department of mechanical engineering Nagoya University Chikusa-ku, Nagoya 464–8603, Japan

P. Onck University of Groningen Materials Science Centre Micromechanics of Materials Nijenborgh 4, 9747 AG Groningen The Netherlands

S. Pattofatto LMT-Cachan 61, Avenue du président wilson 94235 Cachan Cedex, France

H.E. Pettermann Technische Universität Wien Institute of Leightweight Design and Structural Biomechanics Gusshausstrasse 25–29, A-1040 Vie Austria

E. Postek School of Earth and Environment Institute of Geophysics and Tectonics University of Leeds Woodhouse Lane, Leeds, LS2 9JT, UK

K. Sab Université Paris-Est, Institut Navier, LAMI Ecole Nationale des Ponts et Chaussées, 6 et 8 avenue Blaise Pascal 77455 Marne la Vallée Cedex 2, France

Jan G.M. Van Mier Institut f. Baustoffe (IfB) Schafmattstr. 6 ETH-Hönggerberg, HIF E 11 CH-8093 Zürich, Switzerland

M. Vesenjak University of Maribor Faculty of Mechanical Engineering Smetanova 17 SI-2000 Maribor, Slovenia

J.L. Yu Department of Modern Mechanics University of Science and Technology of China Hefei, Anhui 230027, P.R. China

Z.-M. Zheng Institute of Mechanics China Academy of Sciences No. 15 BEI-SI-HUAN-XI Rd 100080 Beijing, China

H. Zhao LMT-Cachan ENS Cachan/CNRS UMR8535/UPMC/UniverSud Paris 61, Avenue du président wilson 94235 Cachan Cedex, France

Y.Y. Zhao Department of Engineering University of Liverpool Liverpool L69 3GH, UK

Uniaxial Deformation of Microcellular Metals: Model Systems and Simplified Analysis

R. Goodall, Y. Conde, R. Müller*, S. Soubielle, E. Combaz, J.F. Despois*, A. Marmottant, F. Diologent, L. Salvo, and A. Mortensen

Abstract Microcellular aluminium can be produced by a process known as replication; this involves the infiltration of a packed bed of NaCl particles which are subsequently leached after metal solidification. The resulting material features a uniform distribution of equisized pores, the shape and volume fraction of which can be tailored, as can the composition and microstructure of the metal making the resulting metal "sponges". These display a regular uniaxial stress-strain behaviour, at both room and elevated temperature, which is interpreted using standard composite models for Young's modulus coupled with variational predictions for non-linear deformation of two-phase composites by Ponte-Castañeda and Suquet, adapted and simplified for the specific case at hand.

1 Introduction

One of the main difficulties in studying new materials is that they are not easy to produce. As a result, material available for testing comes from only a few sources, most of which are primarily driven, not by academic pursuits, but rather by a (legitimate) desire for engineering impact. Available advanced materials are therefore often ill-suited for the derivation of clear microstructure/property relations: to this end, microstructurally simple materials having suboptimal properties are often preferable. Given this fact, and also because the processing of advanced materials is interesting per se, the approach we have adopted in our research on microcellular metals has been to produce ourselves the materials that we study.

R. Goodall, Y. Conde, R. Müller, E. Combaz, J.F. Despois, F. Diologent, and A. Mortensen (✉)
Laboratory for Mechanical Metallurgy, Ecole Polytechnique Fédérale de Lausanne (EPFL), Lausanne, CH-1015, Switzerland

S. Soubielle, A. Marmottant, and L. Salvo
GPM2 Laboratory, Institut National Polytechnique de Grenoble (INPG), Saint-Martin d'Hères, F-38000 Grenoble, France

* Now with Novelis Switzerland S.A., Sierre, CH-3960, Switzerland

H. Zhao, N.A. Fleck (eds.), *Mechanical Properties of Cellular Materials,*
IUTAM Bookseries 12,

To produce samples of highly porous metals we use a process known as replication, which is well suited for the production of open-pore "foams" (more aptly called "sponges") of aluminium and its alloys [1, 2]. We present briefly in what follows our current research program on this theme, describing first the process and the materials it produces, and then giving a few highlights on their uniaxial mechanical behaviour and on the approach we have adopted towards its interpretation.

2 Replicated Microcellular Aluminium

As we practice it towards the production of microcellular aluminium, replication processing consists of producing a porous preform of internally bonded NaCl powder, which is infiltrated under pressure with an aluminium-based melt that is subsequently solidified. The salt is then removed by dissolution in water, leaving behind an interconnected network of metal containing between roughly 60% and 90% open pore space [1, 2].

What distinguishes the material produced in this way from other microcellular metals are the following features:

- The cell distribution and size are regular and quite controllable (since these are determined by the salt powder, which can be sorted, notably by sieving)—as a consequence, the behaviour of these foams is free of the macroscopically visible inhomogeneities or irregularities found with most commercial foams.
- Small cell sizes are possible: we have produced aluminium foams having an average cell diameter as small as 10 µm. This, in turn, has two advantages, namely: (i) samples featuring only a minority of cells situated along the machined outer surface can be produced and tested [3], and (ii) plasticity size effects are observed in these material.
- The metal making the cells can be of essentially any usual aluminium alloy, including high-strength alloys and also 99.99% pure aluminium.
- And finally, the mesoscopic foam architecture can be controlled via alterations in salt powder, in the salt preform preparation process, and also by varying the infiltration pressure.

Figure 1 gives two examples of structures thus produced, showing how the pore shape can be altered from irregular equiaxed (Fig. 1a) to spherical (Fig. 1b) by melting the NaCl particles ahead of packing the preform [4]. The metal grain size in replicated aluminium foam is generally much larger than the pore size: the vast majority of its struts are thus single-crystalline.

Open-pore foams of 99.99% pure aluminium can be made by replication if attention is paid to avoid contamination in processing. Alternatively, an aluminium alloy can be used, in which case the metal making the foam also has a microstructure of its own (which we call the foam "microstructure", as opposed to the internal foam architecture, or "mesostructure"). Figure 2 gives an example of two microstructures produced in the classical Al-4.5wt%Cu alloy by altering solidification conditions

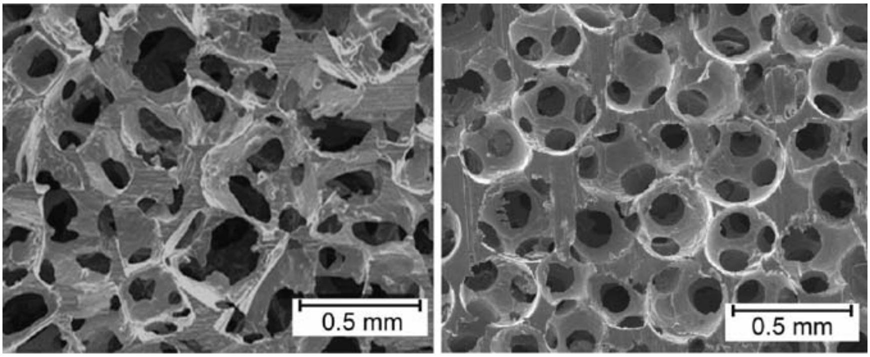

Fig. 1 Replicated pure aluminium foam structures of relative density 15%. *Left*: a foam produced with as-received angular salt particles; *right*: a foam with spherical pores [4]

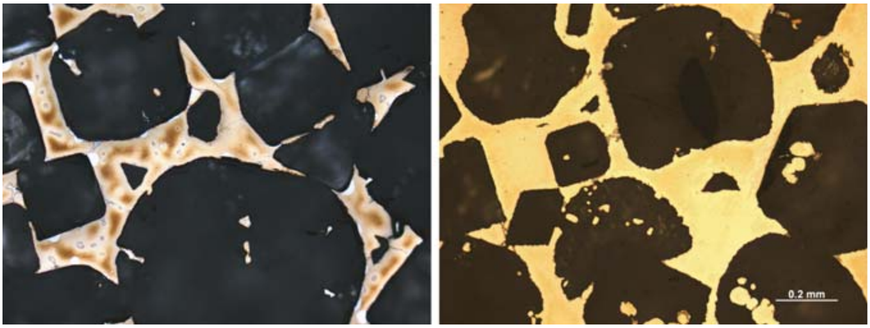

Fig. 2 Optical micrographs of 400 μm cell diameter Al-4.5% Cu foamsolidified at 50 °C/min (*left*) showing dendrite arms with microsegregation and solidified at 0.5 °C/min (*right*), displaying a loss of dendritic character and essentially no microsegregation

during processing. As seen, when solidified slowly, the metal making the foam can be made non-dendritic and nearly free of microsegregation, in conformity with expectations from composite solification theory [5].

3 Monotonic Uniaxial Behaviour

Highly porous metals can be viewed as composites of the metal combined with a zero-stiffness second phase. In this limit, models for the basic linear properties of composite materials can be made sufficiently user-friendly to serve as a convenient framework for the interpretation of uniaxial test data. Expressions for the Young's modulus of the microcellular material can then be obtained using established models. One example is the Tanaka-Mori model, which in the present instance equals the Hashin-Shtrikhman upper bound: for this reason, few microcellular materials will match its predictions. Another is the differential effective medium model [6–8] which turns out to match the Gibson-Ashby model in predicting that the foam modulus E_f is proportional to the square of the relative density V_m. Other models available include estimates made from three-point bounds, as well as expressions derived by interpolation of results of large-cell finite-element simulations of realistic microstructures of microcellular materials. Relevant expressions are listed in [8].

At high levels of porosity typical of microcellular materials, the various composite elasticity models yield predictions for E_f that are widely separated. Therefore, the Young's modulus of a microcellular material provides a discriminating gauge of their load-bearing efficiency. Using then its Young's modulus as a measure of a foam's load-bearing capacity, we analyse the non-linear foam behaviour using recent advances in non-linear composite micromechanics. For simplicity, we focus on uniaxial deformation and assume that the metal making the microcellular material deforms as if it were incompressible (which is not unreasonable given the omnipresence of free surfaces). The Young's modulus of the foam, E_f, is then simply proportional to the Young's modulus, E_o, of the metal from which it is made:

$$E_\mathrm{f} = F \cdot E_\mathrm{o} \tag{1}$$

where F is a function of V_m that, again, gauges the foam's load bearing efficiency. F can be derived from composite theory [8], or can even simply be the ratio of measured foam to metal moduli. If the metal making the foam deforms in uniaxial tension according to the simple Hollomon power law:

$$\sigma = c \cdot (e)^n \tag{2}$$

where σ denotes stress and e strain while c and n are constants, then the foam will exhibit the same power law with the same exponent n [9, 10]. As shown elsewhere [8, 11], variational results given by Ponte-Castañeda and Suquet for the non-linear deformation of composites predict the foam stress-strain law as:

$$\sigma_\mathrm{f} = C \cdot (e_\mathrm{f})^n \text{ with } \frac{C}{c} = F^{\frac{1+n}{2}} V_\mathrm{m}^{\frac{1-n}{2}} \tag{3}$$

This result is easily transposed to steady-state power-law creep [11]. If the metal creep law is:

$$\dot{\varepsilon} = \dot{\varepsilon}_\mathrm{o} \cdot \left(\frac{\sigma}{\sigma_\mathrm{o}}\right)^N \text{ with } \dot{\varepsilon}_\mathrm{o} = K \exp(-Q/RT) \tag{4}$$

then the creep rate of the foam is:

$$\dot{\varepsilon}_\mathrm{f} = \dot{\varepsilon}_\mathrm{of} \cdot \left(\frac{\sigma_\mathrm{f}}{\sigma_\mathrm{of}}\right)^N \text{ with } \sigma_\mathrm{of} = \sigma_\mathrm{o} F^{\left(\frac{1+N}{2N}\right)} V_\mathrm{m}^{\left(\frac{N-1}{2N}\right)} \text{ and } \dot{\varepsilon}_\mathrm{of} = \dot{\varepsilon}_\mathrm{o} \tag{5}$$

Note that one recovers the expressions derived using engineering beam theory by Gibson, Ashby et al. [12] for both the foam yield stress (with $n = 0$) and the foam creep rate if F is proportional to V_m^2.

4 Comparison with Experiment

Replicated aluminium foams behave somewhat differently from current industrial close-cell foams in that their stress-strain curves, in both tension and compression, are relatively smooth and regular. Stress oscillations and the long, somewhat irregular, plateau characteristic of commercial closed-pore foams, are not observed. Figure 3 gives an example of compressive stress-strain curves for a series of microcellular aluminium-based materials of roughly equal density. Salient features of their deformation are as follows.

None of the well-established analytical models for Young's modulus match values measured on replicated aluminium foams: values obtained tend to be lower, and match those for one of the less load-bearing structures simulated by Roberts and Garboczy (the "Gaussian random field" structure). In load-bearing applications, the present replicated aluminium foams are thus clearly not the best available.

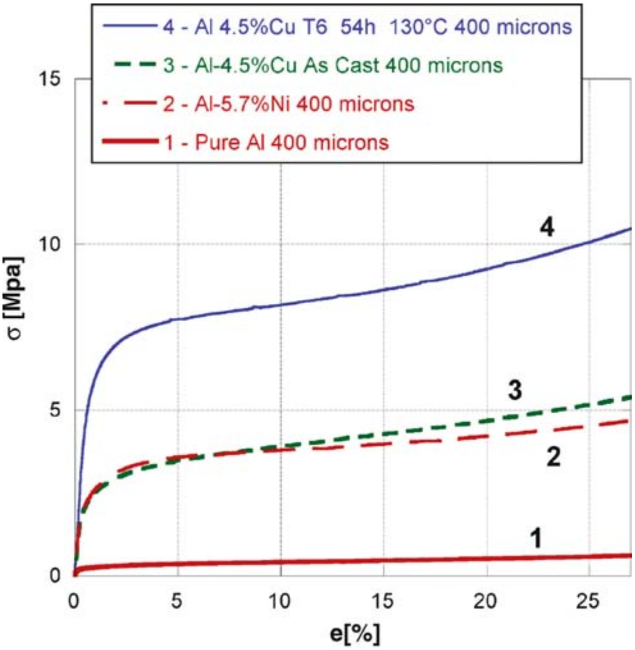

Fig. 3 Effect of the alloy on the uniaxial compression stress–strain curve of microcellular replicated foams with 400 μm cell-size, all with $\rho = 17\%$

Commercial closed-cell foams, and also open-pore Duocel$^{\text{TM}}$ foams made from polyurethane foams, are stiffer at equal relative density. That the Duocel$^{\text{TM}}$ foams would outperform replicated aluminium agrees with intuition: the neat structure of a polyurethane foam, which is reproduced in Duocel$^{\text{TM}}$ foams, features long straight struts and small nodes, making it obviously better at carrying load than the less regular structure of replicated aluminium foams, which have more material distributed at their nodes and short struts that narrow towards their middle. The reason why polyurethane foams have a superior structure is that, in their processing, full minimization of capillary energy can be reached: capillary forces displace what will become the foam solid material away from foam nodes towards the foam struts, the plateau-border shape of which is, furthermore, quite efficient from a structural standpoint. The various solid particle preform preparation techniques we have used so far have apparently been unable to duplicate this effect [4, 13–17], suggesting that there is still room for improvement of the process in terms of the foam mesostructures it produces.

Among replicated aluminium foams, equiaxed salt particles yield stiffer foams than do more irregularly shaped non-equiaxed comminuted salt particles. On the other hand, provided the particles are equiaxed, within the range of structures we have produced so far, we have found surprisingly little difference in the mechanical performance of the foams, even if resulting structures are obviously different [4, 15, 16]. The two structures in Fig. 1, for example, have roughly the same stiffness and uniaxial flow curve at equal relative density.

Replicated microcellular aluminium flow curves can generally be fitted to a simple power-law (Hollomon) relation linking stress and strain. Comparison of measured flow curves with theory shows good agreement overall; however, as has been repeatedly observed [18], the foam flow stress constant C is too small by a “knock-down” factor near three. More detailed experimentation would be useful to ascertain and better quantify the effect, notably because in metal foams what constitutes the intrinsic metal flow stress is often not known with precision (frequently, microindentation hardness is used but this often is an imperfect measure). The question thus remains open, and will perhaps find its explanation in the role played by such processes as microinstabilities or internal damage in the plastic deformation of these materials.

Indeed, a salient feature of the deformation of replicated aluminium foams is the rapid development of internal damage. Many local and generally unstable modes of irreversible deformation exist in these materials, including strut microbuckling, strut neckdown and fracture, as well as the microfracture of brittle intermetallics; in situ tomographic observation of deforming replicated aluminium gives clear evidence of these effects, in both uniaxial compression and tension of replicated microcellular aluminium. These cause a degradation in their flow stress and in the foam stiffness, lower their rate of work hardening and thus limit their tensile ductility (in replicated aluminium foam this is around a few percent, i.e., better than in many aluminium foams but well below the elongation of their base metal).

Although suboptimal from a structural standpoint, alloying the metal from which the foam is made provides an efficient way to raise their performance. Indeed, the replication process makes it possible to cast foam of essentially any aluminium alloy (there are no bubble stability requirements, for example); hence, high-performance aluminium alloys can be used. When heat-treated optimally (which poses interesting processing challenges, in quenching for example), replicated foams can be made to match strength levels obtained with commercial foams, both open and closed pore.

Very fine pores can be produced in replicated aluminium: in the finest structures we have produced to date, foam struts are as small as one micrometre in diameter. At these fine scales, plasticity size effects become apparent: all else constant, pure aluminium foams show a rising flow stress and an increased rate of work hardening as their pore size decreases. This effect, similar to plasticity size effects seen for example in “nanopillars” (these fine-scale microcellular aluminium samples can in fact be viewed as a vast array of many thousand “nanopillars”), is interesting in its complexity, showing notably a dependence of the flow stress on the oxidation state of the foam pore surface.

Under constant load at elevated temperature, replicated aluminium foams yield classical three-stage metallic creep curves. The steady-state creep rate obeys a simple power-law, with the expected activation energy. For pure aluminium, the creep exponent exceeds that of the metal by roughly three—an observation which suggests that replicated microcellular aluminium conform with the stress-invariant substructure model of Sherby [19]. The material furthermore shows a very high dependence of its secondary creep rate on relative density (it varies roughly as ${V_\mathrm{m}}^{-20}$), also in broad agreement with the analysis summarized above (Eq. (5)).

5 Conclusion

The replication process provides a method for the production of microcellular open-pore aluminium (“foam” or “sponge”) with wide latitude for meso- and microstructural control. Resulting materials show a regular and reproducible uniaxial deformation behaviour which can be interpreted on the basis of current composite micromechanical theory. Comparison of data with theory shows broad agreement; however, on selected points micromechanical theory is insufficient to capture fully the behaviour of the material. These include the presence and role of internal damage, as well as the presence of plasticity size effects, which become apparent in the finest foams produced in our laboratory.

We gratefully acknowledge support of this research program by the Swiss National Science Foundation, Project No. 200020-100179/1, by internal funds of the Laboratory for Mechanical Metallurgy at EPFL, and by the Ministère de l’Education Nationale de la Recherche et de la Technologie of France at the INPG.

References

1. Conde, Y., J.F. Despois, R. Goodall, A. Marmottant, L. Salvo, C. San Marchi, and A. Mortensen, *Replication Processing of Highly Porous Materials*. Advanced Engineering Materials, 2006. **8**(9) 795–803.
2. Despois, J.F., A. Marmottant, Y. Conde, R. Goodall, L. Salvo, C.S. San Marchi, and A. Mortensen, *Microstructural Tailoring of Open-Pore Microcellular Aluminium by Replication Processing*. Materials Science Forum, 2006. **512**(April) 281–288.
3. Kocks, U.F., *The Relation Between Polycrystal Deformation and Single-Crystal Deformation*. Metallurgical Transactions, 1970. **1**(5) 1121.
4. Goodall, R., A. Marmottant, L. Salvo, and A. Mortensen, *Spherical Pore Replicated Microcellular Aluminium*. Materials Science and Engineering A, 2007. **465** 124–135.
5. Mortensen, A. and M.C. Flemings, *Solidification of Binary Hypoeutectic Alloy Matrix Composite Castings*. Metallurgical Transactions, 1996. **27A**(3) 595–609.
6. Zimmerman, R.W., *Elastic Moduli of a Solid Containing Spherical Inclusions*. Mechanics of Materials, 1991. **12**(1) 17.
7. Sevostianov, I., J. Kovacik, and F. Simancik, *Elastic and Electric Properties of Closed-Cell Aluminium Foams. Cross Property Connection*. Materials Science and Engineering A, 2006. **420** 87–99.
8. Despois, J.F., R. Mueller, and A. Mortensen, *Uniaxial Deformation of Microcellular Metals*. Acta Materialia, 2006. **54**(16) 4129.
9. Ponte-Castañeda, P. and P. Suquet, *Nonlinear Composites*. Advances in Applied Mechanics, 1998. **34** 171–302.
10. Suquet, P., *Continuum Micromechanics*, ed. S. Kaliszky, M. Sayir, and W. Schneider. 1997: Springer-Verlag Wien, New York. pp. 347.
11. Mueller, R., S. Soubielle, R. Goodall, F. Diologent, and A. Mortensen, *On the Steady-State Creep of Microcellular Metals*. Scripta Materialia, 2007. **57**(1) 33–36.
12. Andrews, E.W., L.J. Gibson, and M.F. Ashby, *The Creep of Cellular Solids*. Acta Materialia, 1999. **47**(10) 2853–2863.
13. San Marchi, C. and A. Mortensen, *Deformation of Open-Cell Aluminum Foam*. Acta Materialia, 2001. **49**(19) 3959.
14. San Marchi, C., J.F. Despois, and A. Mortensen, *Uniaxial Deformation of Open-Cell Aluminum Foam: The Role of Internal Damage*. Acta Materialia, 2004. **52**(10) 2895.
15. Gaillard, C., J.F. Despois, and A. Mortensen, *Processing of NaCl Powders of Controlled Size and Shape for the Microstructural Tailoring of Aluminium Foams*. Materials Science and Engineering A, 2004. **374**(1–2) 250.
16. Goodall, R., J.F. Despois, A. Marmottant, L. Salvo, and A. Mortensen, *The effect of Preform Processing on Replicated Aluminium Foam Structure and Mechanical Properties*. Scripta Materialia, 2006. **54**(12) 2069.
17. Despois, J.F., A. Marmottant, L. Salvo, and A. Mortensen, *Influence of the Infiltration Pressure on the Structure and Properties of Replicated Aluminium Foams*. Materials Science and Engineering: A, 2007. **462** 68–75.
18. Gibson, L.J. and M.F. Ashby, *Cellular Solids - Structure and Properties - Second Ed*. 1997, Cambridge University Press, Cambridge.
19. Sherby, O.D., R.H. Klundt, and A.K. Miller, *Flow Stress, Subgrain Size, and Subgrain Stability at Elevated Temperature*. Metallurgical Transactions A, 1977. **8** 843–850.

Mechanical Properties and Design of Lattice Composites and Structures

Dai-Ning Fang, Xiao-Dong Cui, Yi-Hui Zhang, and Han Zhao

1 Introduction

Recently, lattice materials have been attractive for use as cores in light-weight sandwich panels, for energy-absorption and packaging applications, or as heat transfer devices. Lattice structure is a kind of periodic trusses patterned like moleculelattice. Usually there is no filling in the space between frames of those 2D or 3D constructions, thus sufficient quantity of mass can be reduced.

The mechanical properties of 2D lattice materials have been discussed at length, including the stiffness, yield, buckling, impact behavior, and etc. [1–5]. Since yield and fracture are major structural collapse modes for the lattice structures, a comprehensive understanding of their yielding and fracture behaviors are indispensable for engineering applications. Deshpande et al. [6] analyzed the elastic properties, plastic yielding and elastic buckling surfaces of octet truss structure. Zhang et al. [7] designed two novel statically indeterminate planar lattice structures, the SI-square and N-Kagome lattice structures (see Fig. 1), calculated their initial yield surfaces, and verified their special mechanical properties. Recent work by Fleck et al. [8] predicts the fracture toughness of three 2D lattice materials, and it reveals that the Kagome has an elevated macroscopic toughness by a characteristic elastic zone near the crack tip to release the stress in quasi-static state.

Noting that initial structural imperfection is inevitable in the manufacture of lattice materials, the effects of imperfection should be determined urgently. Besides, the tensile and compressive yield strengths of composite materials are commonly different, thus the collapse behavior of such kind of lattice structures made from composite materials should be different from those made from metals.

In this paper, the analytical yield surfaces of two planar lattice structures are calculated first in Section 2 when the tensile and compressive yield strengths of the

---

D.-N. Fang (✉), X.-D. Cui, and Y.-H. Zhang
Department of Engineering Mechanics, Tsinghua University, Beijing, 100084, China

H. Zhao
LMT-Cachan, ENS de Cachan/CNRS-UMR 8535/Université Paris 6, France

H. Zhao, N.A. Fleck (eds.), *Mechanical Properties of Cellular Materials,*
IUTAM Bookseries 12,

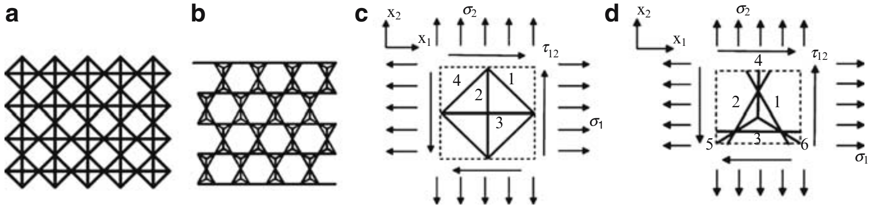

Fig. 1 The configurations of the (**a**) SI-square and (**b**) N-Kagome lattice structures, and (**c–d**) the two unit cells under combined in-plane stress states

solid material are different, and a generalized Deshpande-Fleck yield criterion is put forward. In Section 3, the effects of initial imperfection on the dynamic stretching of 2D lattices are investigated by finite element method for the three topologies: the regular hexagonal honeycomb, the regular triangular honeycomb and the Kagome lattice, as sketched in Fig. 4. A complete evolution of crack induced by the structural imperfection is also discussed.

2 A Generalized Yield Criterion

For lattice structures under different kinds of in-plane loadings, three types of stress may exist inside the cell walls: bending, tension or shear stress. The lattices dominantly subjected to tensile or compressive stress are called *stretching-dominated structures*. The SI-square and N-Kagome lattice structures both belong to this category of lattice structures. In the present analysis of yield surface, the material of cell walls is assumed to be perfectly elastic-plastic. Timoshenko's beam and column theories [9] are adopted, and each cell wall is simplified as a strut only subjected to axial force.

2.1 Analytical Yield Surfaces

Consider a case that the unit cell of the SI-square lattice structure is subjected to the in-plane axial stresses σ_1 and σ_2 in two orthogonal directions, and shear stress, τ_{12}, as shown in Fig. 1c. The calculation indicates that the two struts in the same direction have same internal forces and just yield simultaneously. Therefore, only four pairs of internal forces are considered which can be obtained easily from the equilibrium equations, i.e.

$$\begin{aligned} N_1 &= \frac{2-\sqrt{2}}{2}(\sigma_1+\sigma_2)bl - \tau_{12}bl,\ N_2 = -\left(\sqrt{2}-1\right)\sigma_1 bl + \sigma_2 bl \\ N_3 &= \sigma_1 bl - \left(\sqrt{2}-1\right)\sigma_2 bl,\ N_4 = \frac{2-\sqrt{2}}{2}(\sigma_1+\sigma_2)bl + \tau_{12}bl \end{aligned} \tag{1}$$

where N_i is the internal force of ith strut, $i = 1..4$. l and b are the wall length and out-of-plane dimension of the lattice structure, respectively. The in-plane wall thickness is noted as t.

Without loss of generality, let the tensile and compressive yield strengths be equal to σ_{ys} and $R\sigma_{ys}$, respectively, where R is a scaling factor. In this case, the yield condition for the ith strut can be written as $|N_i| = Q\sigma_{ys}bt,\ i = 1..4$, where $Q = 1$ for $N_i > 0$, and $Q = R$ for $N_i < 0$. The initial yielding of the unit cell occurs when any strut in the unit cell yields. Therefore, the initial yield equation of the SI-square cell under in-plane stress state can be expressed as

$$\max\left[|N_i| \big/ (Qbt\sigma_{ys}) - 1\right] = 0,\ i = 1..4 \tag{2}$$

The full expression of normalized initial yield surface equation is obtained by substituting Eq. (1) into Eq. (2).

The analytical yield surface of the N-Kagome cell (shown in Fig. 1d) can be calculated similarly. Here, the similar deduction is not iterated.

The analytical yield surfaces of the SI-square and N-Kagome cells are demonstrated in Figs. 2 and 3, where r denotes the relative density. The initial yield surfaces are closed, convex and anisotropic. It is clear that with the decrease of the compressive yield strength, some boundaries of the yield surfaces shift inward while the others stay at the original location. The ratio of compressive yield strength to tensile yield strength, R, may influence both the shape and size of the yield surface.

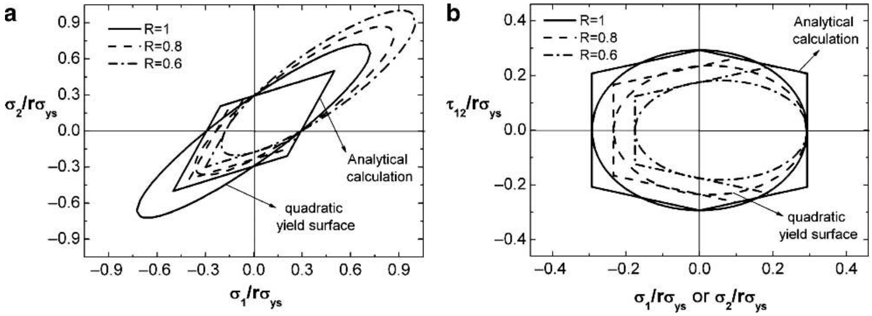

Fig. 2 The initial yield surfaces of the SI-square cell with different ratios of compressive yield strength to tensile yield strength in different stress spaces

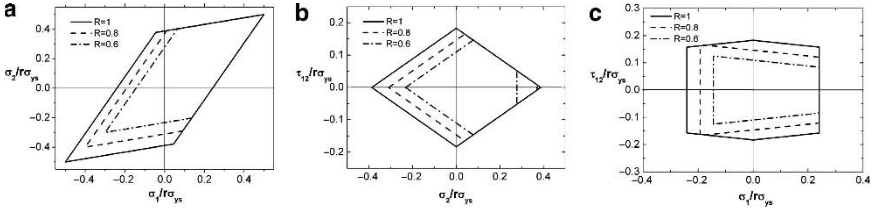

Fig. 3 The initial yield surfaces of the N-Kagome cell with different ratios of compressive yield strength to tensile yield strength in different stress spaces

2.2 Smoothed Yield Surface by a Generalized Deshpande-Fleck Yield Criterion

While the yield surface equations presented in Section 2.1 are useful for displaying the yield stress under specific load paths, a closed-form smooth yield surface would be advantageous in applications. In this section, further discussion is made on the applicable condition of the Deshpande-Fleck yield criterion [6] in the case of plane stress or plane strain state. The original form of Deshpande-Fleck yield criterion is given by

$$\begin{aligned}\Phi \equiv {} & A(\sigma_1-\sigma_2)^2+B(\sigma_2-\sigma_3)^2+C(\sigma_3-\sigma_1)^2\\ & +D\tau_{12}^2+E\tau_{23}^2+F\tau_{13}^2+G\sigma_m^2-1=0\end{aligned} \tag{3}$$

where *A*-*G* are material parameters to be determined, and $\sigma_1,\ \sigma_2,\ \sigma_3,\ \tau_{12},\ \tau_{23}$ and τ_{13} are the six stress components. Under the in-plane stress state, this criterion can be written as

$$\begin{aligned}\Phi \equiv {} & \left(A+C+G/9\right)\sigma_1{}^2+\left(-2A+2G/9\right)\sigma_1\sigma_2{}^2\\ & +\left(A+B+G/9\right)\sigma_2{}^2+D\tau_{12}{}^2-1=0\end{aligned} \tag{4}$$

According to analytical results of the three uniaxial yield strengths, σ^*_{pl1}, σ^*_{pl2} and σ^*_{pl3}, the in-plane shear yield strength τ^*_{12} and the hydrostatic yield strength σ^*_m, those parameters, *A*–*D* and *G* in Eq. (4), can be calculated by the following equations,

$$\begin{aligned}& A+C+G/9=1/\sigma^*_{pl1}{}^2,\ A+B+G/9=1/\sigma^*_{pl2}{}^2,\\ & C+B+G/9=1/\sigma^*_{pl3}{}^2,\ D=1/\tau^*_{12}{}^2,\ G=1/\sigma^{*\,2}_m\end{aligned} \tag{5}$$

Since this yield surface is a quadratic, convex and closed curve, it must be an elliptical curve. Therefore, the coefficients in Eq. (4) should satisfy

$$\left(-2A+2G/9\right)^2-4\left(A+C+G/9\right)\left(A+B+G/9\right)<0 \tag{6}$$

This condition can be simplified by substituting Eq. (5) in, i.e.

$$\begin{aligned}\Delta = {} & \left[\left(1/\sigma^*_{pl1}-1/\sigma^*_{pl2}\right)^2-1/\sigma^{*2}_{pl3}-1/3\sigma^{*2}_m\right]\\ & \left[\left(1/\sigma^*_{pl1}+1/\sigma^*_{pl2}\right)^2-1/\sigma^{*2}_{pl3}-1/3\sigma^{*2}_m\right]<0\end{aligned} \tag{7}$$

where Δ is a coefficient determined by the structural parameters. It is found by further calculation that this condition (Eq. (7)) is valid for the SI-square cell but not satisfied by the N-Kagome cell.

In order to generalize the Deshpande-Fleck plastic yield criterion for the case that the tensile and compressive yield strength of the solid material are different, a generalized Deshpande-Fleck yield criterion is put forward by incorporating six linear terms of stress components, i.e.

$$\Phi = A(\sigma_1-\sigma_2)^2+B(\sigma_2-\sigma_3)^2+C(\sigma_3-\sigma_1)^2+D\tau_{12}{}^2+E\tau_{23}{}^2 \tag{8}$$

$$+F\tau_{13}{}^2+G\sigma_m{}^2+H\sigma_1+I\sigma_2+J\sigma_3+K\tau_{12}+L\tau_{23}+M\tau_{13}-1=0 \tag{9}$$

where *A*-*M* are material parameters, which can be determined by the uniaxial and shear yield strength with respect to the material principal axes and the hydrostatic yield strength.

For the in-plane stress state, this yield criterion can be simplified as

$$\begin{aligned}\Phi = A(\sigma_1-\sigma_2)^2+B\sigma_2{}^2+C\sigma_1{}^2+D\tau_{12}{}^2\\ +G\sigma_m{}^2+H\sigma_1+I\sigma_2+K\tau_{12}-1=0\end{aligned} \tag{10}$$

For the SI-square cell, the in-plane uniaxial yield strength and shear yield strength can be calculated from the in-plane yield surface. The out-of-plane yield strength and hydrostatic yield strength can be obtained from the triaxial yield surface equation [7], i.e. $\sigma^*_{pl3} = r\sigma_{ys}$ for tensile yielding and $\sigma^*_{pl3} = -Rr\sigma_{ys}$ for compressive yielding, $\sigma^*_m = \sqrt{3}r\sigma_{ys}/3$.

The smooth yield surfaces of the SI-square cell given by this generalized Deshpande-Fleck criterion are compared with the analytical surfaces in Fig. 2. It is demonstrated that the generalized yield criterion is capable of capturing the shift of the yield surface for different ratios *R*. Good agreement is found between the predicted yield surface of the generalized yield criterion and analytical results in (σ_1,τ_{12}) space and (σ_2,τ_{12}) space. However, in (σ_1,σ_2) space this generalized yield criterion overestimates the yield stresses under biaxial tension. Since the mechanical properties of the N-Kagome cell do not satisfy the applicable condition of the Deshpande-Fleck yield criterion, the corresponding prediction of the generalized Deshpande-Fleck yield criterion is not carried out.

3 Finite Element Simulation of the Dynamic Stretching

In this section, the deformation progress of the lattice materials with structural imperfection under the dynamic stretching and the effects of structural imperfection on energy-absorption are analyzed by means of the finite element simulation. Each lattices with and without imperfection (sketched in Fig. 4.) are simulated using ABAQUS explicit (version 6.5).

In the finite element simulations, the constitutive relations of the metal material are characterized by JOHNSON COOK plastic model in plastic phase. The uniaxial tensile behavior is characterized by

$$\sigma = \begin{cases} E\varepsilon, \quad \varepsilon \le \varepsilon_Y \\ \left[A+B\left(\bar{\varepsilon}^{pl}\right)^n\right]\left[1+C\ln\left(\dot{\bar{\varepsilon}}^{pl}/\dot{\varepsilon}_0\right)\right],\ \varepsilon > \varepsilon_Y \end{cases} \tag{11}$$

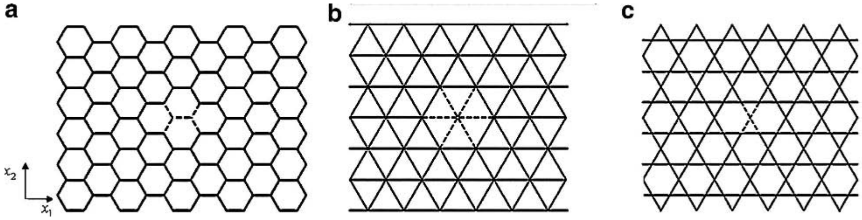

Fig. 4 The 2D lattices investigated in this study: (**a**) hexagonal honeycomb, (**b**) triangular honeycomb, and (**c**) Kagome lattice. The dash line marks the location of imperfection

where $A, B, C, n, \dot{\varepsilon}_0$ are the material parameters, σ the true stress, E the elastic modulus, ε_Y the initial yield strain, $\bar{\varepsilon}^{pl}, \dot{\bar{\varepsilon}}^{pl}$ the equivalent plastic strain and its rate.

In order to avoid the influence of boundary effect, 50 unit cells by 50 unit cells are employed to compose each lattice [8]. Euler–Bernoulli beam elements with linear interpolation functions (element type B21 in ABAQUS notation) is suffice in the finite element analysis and numerical convergence is confirmed by refined meshes and shorter time steps. The dynamic stretching is carried out by imposing a pair of constant velocity $V_0/2$ on the two ends in the vertical direction. To eliminate the influence of wave propagation, an initial velocity $V = (V_0/L_0)x_2$ is imposed on the entire lattice in the vertical direction considering the compressibility of the lattice materials [10, 11], where x_2 and L_0 denote the coordinate as sketch in Fig. 4 and the length of the lattice structure in the x_2 direction, respectively.

3.1 The Deformation Progress of the Lattice Materials Under Dynamic Stretching

The dynamic stretching behaviors of the lattice materials mentioned above are investigated by finite element method, including the perfect and imperfect structures. Bending-dominated hexagonal honeycomb exhibits a different behavior with stretching-dominated lattices, and the influences of this distinction on the dynamic stretching behavior are discussed.

The deformation progress of bending-dominated hexagonal honeycomb is demonstrated first. The characteristic stages during the stretching are captured and displayed in Fig. 5. At the earlier stretching stage, the beams near the imperfection start to bend, and the imperfection turns to be a round hole from the original shape; as the stretching goes on, four cracks develop from the imperfection simultaneously, and then they propagate gradually along the ±30°, ±150° directions with the x_1 axis respectively; the crack propagation directions change when the effect of shrinking achieves a certain extent, and the cracks finally encounter each other, forming a approximate round hole; two apparent shrinking strips are formed at the

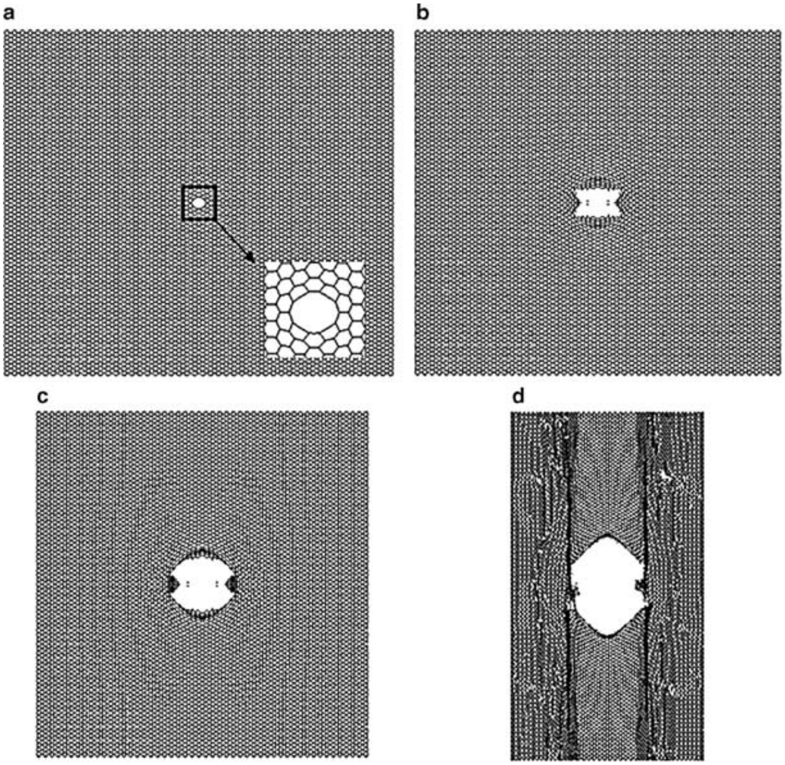

Fig. 5 The deformation of hexagonal honeycomb under dynamic stretching: (**a**) $\bar{t} = 3$, (**b**) $\bar{t} = 12.5$, (**c**) $\bar{t} = 25$, (**d**) $\bar{t} = 70$

two sides of the hole in the vertical direction, and the hole is torn into two symmetric parts till the whole lattice is stretched to fracture. The stress in the bilateral parts of the hole along the stretching direction is obviously under the average level because of the forming of the hole.

Considering the similarity of the deformation behavior of the stretching-dominated Kagome and triangular lattices, only the Kagome lattice is taken for illustration of the deformation progress. As sketched in Fig. 6, the imperfection in Kagome lattice translates to a transverse propagating crack at the beginning; similar to the hexagonal honeycomb, four cracks in the ±60°, ±120° directions with the x_1 axis develop after the transverse crack propagates across several unit cells; compared with the hexagonal honeycomb, the velocity of crack propagate is much higher and the cracks almost penetrate the whole lattice before the fracture of the entire lattice. Therefore, the hexagonal honeycomb exhibits more potential in preventing the crack propagation than the Kagome and triangular lattices.

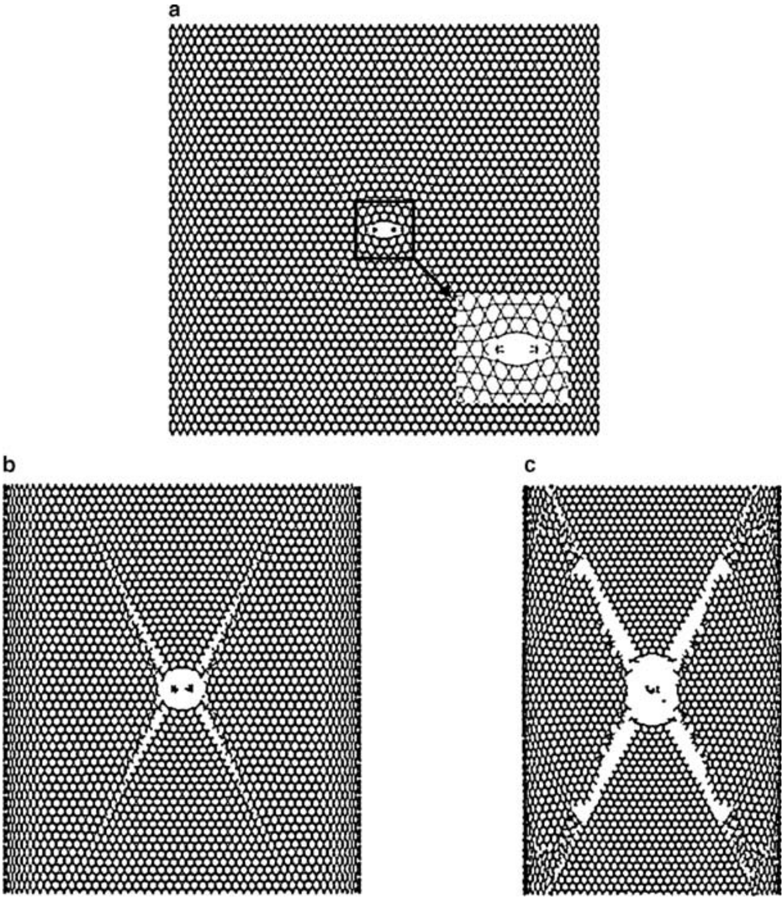

Fig. 6 The deformation of Kagome lattice under dynamic stretching: (**a**) $\bar{t} = 16.5$, (**b**) $\bar{t} = 35$, (**c**) $\bar{t} = 60$

3.2 *The Effect of Structural Imperfection on Energy-Absorption*

Obviously, structural imperfection reduces the energy-absorption ability of the lattice materials. Under dynamic stretching, the plastic dissipation is calculated to analyze the effect of structural imperfection on energy-absorption, and the numerical result is normalized according to

$$\begin{gathered}\bar{t} = t\big/t_d, t_d = \bar{\varepsilon}_f^{pl} L\big/V_0 = 0.026s \\ \bar{U}_p = U_p\big/U_s, U_e = \left(rV\sigma_Y^2\right)\big/(2E) = 2\times 10^5 J\end{gathered} \tag{12}$$

The numerical result in Fig. 7 shows the time histories of the plastic dissipation of the lattices for the three topologies. The effect of structural imperfection on plastic

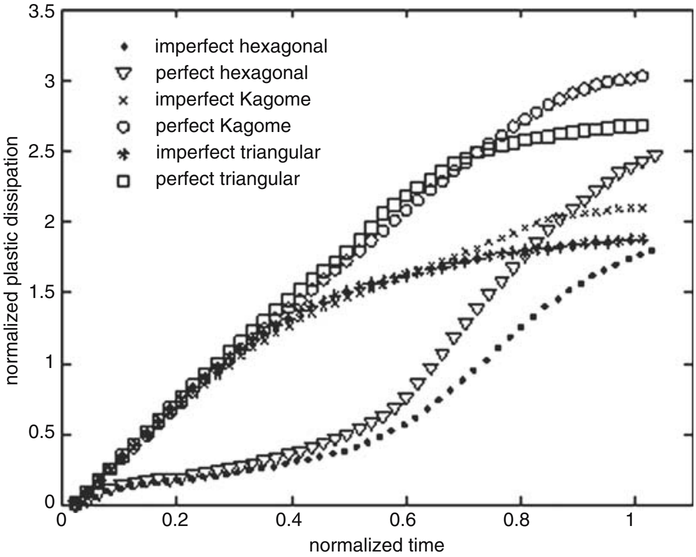

Fig. 7 The time histories of plastic dissipation of the lattices for three topologies

dissipation of the lattice materials can be neglected at the earlier stage of the dynamic stretching since the cracks induced by the structural imperfection do not grow large enough until the transition time, $\bar{t} \approx 30$. The effect of structural imperfection on plastic dissipation can not be neglected any more after that. The three kinds of lattices almost have the same transition time from Fig. 7.

With the same relative density, the stiffness of hexagonal honeycomb is far less than the other two kinds of lattices, so the plastic dissipation is a less value at the beginning. Large deformation occurs as the sketching goes further, the topology of hexagonal honeycomb transfers to an approximate rectangle. Therefore, the rising velocity of its plastic dissipation increases quickly. The Kagome lattice shows slight advantage in plastic dissipation compared with the triangular honeycomb.

4 Conclusions

The distinction between the tensile and compressive yield strengths of the solid material can influence the yield surfaces of the lattice structures in both the shape and size. A generalized Deshpande-Fleck yield criterion can capture this shift of yield surface. It is found that the Deshpande-Fleck yield criterion can not keep the predicted yield surfaces closed for certain types of lattice structures. And a simple applicable condition of the Deshpande-Fleck yield criterion is presented.

The deformation progress of the lattices with structural imperfection under dynamic stretching is also simulated, and the bending-dominated hexagonal honeycomb exhibits a different behavior which grants it potential in preventing crack from propagating. A transition time is found in determining the effects of structural imperfection on energy-absorption.

Acknowledgement The authors are grateful for the support by National Natural Science Foundation of China under grants #90305015 and #10328203. Supported by the Special Funds for the Major State Basic Research Projects of China (#G2003CB615603, #G2006CB601202) is also acknowledged.

References

1. Gibson, L.J., Ashby, M.F., 1997. Cellular Solids: Structure and properties. 2nd edition. Cambridge University Press, Cambridge.
2. Wang, A.J., McDowell, D.L., 2004. In-plane stiffness and yield strength of periodic metal honeycombs. ASME Journal of Engineering Materials and Technology 126, 137–156.
3. Wang, A.J., McDowell, D.L., 2005. Yield surfaces of various periodic metal honeycombs at intermediate relative density. International Journal of Plasticity 21, 285–320.
4. Xue, Z., Hutchinson, J.W., 2003. Preliminary assessment of sandwich plates subject to blast loads. International Journal of Mechanical Sciences 45, 687–705.
5. Xue, Z., Hutchinson, J.W., 2004. A comparative study of impulse-resistant metal sandwich plates. International Journal of Impact Engineering 30, 1283–1305.
6. Deshpande V.S., Fleck N.A., Ashby M.F., 2001. Effective properties of the octet-truss lattice material. Journal of the Mechanics and Physics of Solids 49, 1747–1769.
7. Zhang, Y.H., Qiu, X.M., Fang, D.N., 2007. Mechanical properties of two novel planar lattice structures. International Journal of Solids and Structures (submitted).
8. Fleck, N.A., Qiu, X., 2007. The damage tolerance of elastic–brittle, two-dimensional isotropic lattices. Journal of the Mechanics and Physics of Solid 55, 562–588.
9. Gere, J.M., Timoshenko, S.P., 1984. Mechanics of Materials. 2nd edition. Wadsworth, Belmont, CA.
10. Shenoy, V.B., Freund, L.B., 1999. Necking bifurcations during high strain rate extension. Journal of the. Mechanics and Physics of Solids 47, 2209–2233.
11. Needleman, A., 1991. The effect of material inertia on neck development. In Topics in Plasticity, Yang, W. H. Ed., AM Press, Ann Arbor, MI, pp. 151–160.

Nano-Cellular Materials with Unusual Mechanical and Physical Properties

H.L. Duan, J. Wang, and B.L. Karihaloo

Abstract Surface stress has a profound effect on the mechanical and physical properties of nano-structured materials, especially of nanoporous materials. This paper begins with an overview of the theory of elasticity with surface stress. This is followed by the prediction of the effective elastic constants and coefficients of thermal expansion of nanoporous materials with spherical or cylindrical voids. It is shown that the elastic constants of nanoporous materials can be tailored to desired values through pore surface modification or coating.

Keywords Generalized Young-Laplace equation · Surface stress · Nanoporous materials · Effective elastic constants · Effective coefficient of thermal expansion

1 Introduction

Surface forces have a substantial effect on the physical properties of materials at the nanoscale, as evidenced for example by the dramatic increase in the elastic constants of nanowires, nanobeams, nanoplates, etc. over and above the elastic constants of the parent bulk materials (Gleiter, 2000; Miller and Shenoy, 2000; Cuenot et al., 2004; Zhou and Huang, 2004; Duan et al., 2005a; Wang et al., 2006). This increase is attributed to the surface stress effect. Judicious modifications of the surface can therefore open the possibility for practical realization of nano-materials with novel properties. Nanochannel-array materials with ordered arrays of nanopores possess a large surface area and thus provide an obvious opening for designing functional

---

H.L. Duan
Institute of Nanotechnology, Forschungszentrum Karlsruhe, Germany

J. Wang
Department of Mechanics and Aerospace Engineering, Peking University, China

B.L. Karihaloo (✉)
School of Engineering, Cardiff University, UK

H. Zhao, N.A. Fleck (eds.), *Mechanical Properties of Cellular Materials,*
IUTAM Bookseries 12,

nano-porous/cellular materials with new physical and chemical properties (Masuda and Fukuda, 1995; Martin and Siwy, 2004). Pore surface modification with functional organo-silane has already been achieved with nanochannel-array materials (Shi et al., 2004). Thus pore surface modifications are possible and these can be exploited to create nano-porous materials that are very stiff and light and have very low thermal conductivity. One important and immediate application of these materials may be in the fabrication of sandwich structures, as porous/cellular materials are widely used as cores in sandwich construction in many important industries because they are light and excellent thermal and noise insulators. Sandwich construction is indispensable to aerospace/aircraft and other transport industry and to modern construction industry. The porous/cellular core of a sandwich has to carry the major part of the shear loading (Gibson and Ashby, 1997), but as it lacks shear stiffness it has to be very thick to be dimensionally stable. Nano-porous/cellular materials with stiffness that matches or even exceeds that of the parent materials would enable considerable reduction in the size and weight of structural elements without sacrificing their strength and other important physical properties.

In this paper we will show that by changing the surface properties, the properties of the nanochannel-array materials can be tailored. We suggest two possible routes to the practical realization of the surface modification for the stiffening of the nanochannel-array materials. Stiff nano-cellular materials have high dimensional stability, low weight, low thermal conductivity and high bending stiffness and strength. These critical properties have the potential to make a radical breakthrough in sandwich-type construction which is preferred in aerospace/aircraft and other transport industries.

2 Theory of Elasticity with Surface Stress

The basic equations of surface elasticity consist of the generalized Young-Laplace equation for solids and the constitutive equation of the surface. The former is (Gurtin and Murdoch, 1975)

$$\sigma \cdot \mathbf{n} = -\nabla_S \cdot \tau \tag{1}$$

where $\mathbf{n}$ is the unit normal vector to the surface, and σ denotes the stress tensor in the bulk materials. τ is the surface stress tensor, $\nabla_S \cdot \tau$ denotes the surface divergence of a tensor field τ (Gurtin and Murdoch, 1975). The generalized Young-Laplace equation (Eq. (1)) can be derived in various ways, for example, by the principle of virtual work. For a curved surface Γ with two orthogonal unit base vectors $\mathbf{e}_1$ and $\mathbf{e}_2$ in the tangent plane and a unit vector $\mathbf{n}$ perpendicular to the surface, $\nabla_S \cdot \tau$ can be expressed as follows (Duan et al., 2005b):

$$\begin{aligned}\nabla_s \cdot \tau \ &= -\left(\frac{\tau_{11}}{R_1} + \frac{\tau_{22}}{R_2}\right)\mathbf{n} + \frac{\mathbf{e}_1}{h_1 h_2}\left[\frac{\partial(h_2\tau_{11})}{\partial\alpha_1} + \frac{\partial(h_1\tau_{21})}{\partial\alpha_2} + \frac{\partial h_1}{\partial\alpha_2}\tau_{12} - \frac{\partial h_2}{\partial\alpha_1}\tau_{22}\right]\\ &\quad + \frac{\mathbf{e}_2}{h_1 h_2}\left[\frac{\partial(h_2\tau_{12})}{\partial\alpha_1} + \frac{\partial(h_1\tau_{22})}{\partial\alpha_2} - \frac{\partial h_1}{\partial\alpha_2}\tau_{11} + \frac{\partial h_2}{\partial\alpha_1}\tau_{21}\right]\end{aligned} \tag{2}$$

where α_1 and α_2 denote the two parameters determining the surface such that $\alpha_1 =$ constant and $\alpha_2 =$ constant give two sets of mutually orthogonal curves on Γ, and h_1 and h_2 are the corresponding metric coefficients. R_1 and R_2 are the radii of the principal curvatures, and τ_{11}, τ_{22} and τ_{12} are the components of the surface stress tensor $\boldsymbol{\tau}$. As can be seen from Eq. (2), the first term on the right corresponds to the classical Young-Laplace equation; the remaining terms signify that a non-uniform distribution of the surface stress or a uniform surface stress on a surface with varying curvature needs to be balanced by a bulk shear stress in the bulk materials.

Besides the generalized Young-Laplace Eq. (1), we need a surface constitutive equation to solve boundary-value problems with the surface stress effect. For an elastically isotropic surface, it is (Duan and Karihaloo, 2007)

$$\begin{cases} \boldsymbol{\tau} = \lambda_s(\mathrm{tr}\varepsilon^s)\mathbf{1} + 2\mu_s\varepsilon^s - \Delta\mathrm{T}\alpha_s\kappa_s\mathbf{1} \\ \varepsilon^s = \frac{1}{2}\left(\mathrm{D}\otimes\mathbf{u} + \mathrm{D}\otimes\mathbf{u}^T\right), \mathrm{D}\otimes\mathbf{u} = \mathbf{P}\cdot(\nabla_s\otimes\mathbf{u}) \end{cases} \tag{3}$$

where $\mathbf{P} = \mathbf{I}^{(2)} - \mathbf{n}\otimes\mathbf{n}$, $\mathbf{I}^{(2)}$ is the second-order identity tensor in a three dimensional space, ε^s is the surface strain tensor, λ_s and μ_s are the surface moduli, $\kappa_s = 2(\lambda_s + \mu_s)$, α_s is the coefficient of thermal expansion (CTE) of the surface, $\mathbf{1}$ is the second-order unit tensor in two-dimensional space, and $\Delta\mathrm{T}$ is the temperature difference.

Apart from Eqs. (1) and (3) for the surface, the basic set of equations for solving elastostatic boundary-value problems consist of the conventional equilibrium equation, strain-displacement relation, and constitutive equation for the bulk materials.

3 Effective Elastic Moduli and CTE of Nanoporous Materials

Duan et al. (2005a), and Duan and Karihaloo (2007) gave the micromechanical framework to predict the effective elastic moduli and the effective coefficient of thermal expansion (CTE) of the heterogeneous materials containing nanoinhomogeneities. In the following, we will predict the effective elastic moduli and CTE of nanoporous materials containing spherical or cylindrical voids by using this framework.

3.1 Nanoporous Materials with Spherical Voids

Following the micromechanical framework in the paper of Duan et al. (2005a), it is found that the three homogenization schemes, namely the composite spheres assemblage model (CSA, Hashin, 1962), the Mori-Tanaka method (MTM, Mori and Tanaka, 1973), and the generalized self-consistent method (GSCM, Christensen and Lo, 1979) give the same result for the effective bulk modulus of the nanoporous materials with spherical voids. The resulting expression for the effective bulk modulus is

$$\kappa_e = \frac{2\mu\left[4f\mu\kappa_s^T + 3\kappa(2 - 2f + \kappa_s^T)\right]}{9f\kappa + 6\mu(2 + \kappa_s^T - f\kappa_s^T)} \tag{4}$$

where f is the volume fraction of the nanopores in the material, $\kappa_s^T = 2(\lambda_s^T + \mu_s^T), \lambda_s^T = \lambda_s/(R\mu), \mu_s^T = \mu_s/(R\mu)$, R is the radius of spherical void, μ and κ are the shear and bulk moduli of the matrix.

In order to obtain a simple analytical solution for the effective shear modulus, we use the Mori-Tanaka method to predict the effective shear modulus of the nanoporous materials with the spherical voids; the resulting expression of the effective shear modulus is

$$\mu_e = \frac{\mu[5 + 8f\xi_3(7 - 5\nu)]}{5 - f(5 - 84\xi_1 + 20\xi_2)} \tag{5}$$

in which ν is the Poisson ratio of the matrix, and the constants ξ_1, ξ_2 and ξ_3 are

$$\begin{aligned} &\xi_1 = \tfrac{15(1-\nu)(\kappa_s^T + 2\mu_s^T)}{112H}, \quad \xi_2 = \tfrac{15(1-\nu)(4+3\kappa_s^T + 2\mu_s^T)}{16H} \\ &\xi_3 = \tfrac{5(2+\kappa_s^T)(1-\mu_s^T)}{16H} \\ &H = -7 - 11\mu_s^T - \kappa_s^T(5 + 4\mu_s^T) + \nu[5 + 13\mu_s^T + \kappa_s^T(4 + 5\mu_s^T)] \end{aligned} \tag{6}$$

The effective Young modulus corresponding to κ_e and μ_e given in Eqs. (4) and (5) is $E_e = 9\kappa_e\mu_e/(3\kappa_e + \mu_e)$. Moreover, the effective CTE of the nanoporous materials with spherical voids can be obtained from Levin's formula with surface stress (Duan and Karihaloo, 2007)

$$\frac{\alpha\kappa - \frac{2\alpha_s\kappa_s}{3R}}{\kappa - \frac{2\kappa_s}{3R}} = \frac{\alpha_e\kappa_e - f\alpha\kappa - \frac{2f\alpha_s\kappa_s}{3R}}{\kappa_e - f\kappa - \frac{2f\kappa_s}{3R}} \tag{7}$$

3.2 Nanoporous Materials with Cylindrical Voids

For the nanoporous materials with aligned cylindrical nanopores (called as nanochannel-array materials), for brevity, we assume that the matrix is linearly elastic and isotropic and the surface of the aligned cylindrical nanopores is isotropic. Since the nanochannel-array materials have aligned and approximately hexagonal close-packed array of cylindrical pores, they will exhibit an overall transversely isotropic property. Therefore, we shall predict the five effective elastic constants: the transverse plane-strain bulk modulus k_{Te}, the longitudinal Young modulus E_{Le}, the longitudinal Poisson ratio ν_{Le}, the longitudinal shear modulus μ_{Le}, and the transverse shear modulus μ_{Te}. The subscript "L" denotes a longitudinal property along the axis of the pores, and "T" a transverse property perpendicular to them. We shall use three micromechanical models, namely, the composite cylinder assemblage model (CCA), the generalized self-consistent method (GSCM), and MTM to predict the effective elastic constants of the nanochannel-array materials with aligned cylindrical nanopores. GSCM and CCA give the same predictions for E_{Le}, k_{Te} and ν_{Le}, i.e.,

$$
\begin{aligned}
E_{Le} &= \frac{\mu\{[18\kappa(1-f)+8f\mu\kappa_s^*](2-2f+\mu_s^*+3f\mu_s^*)+3\kappa\kappa_s^*(3-2f-f^2+8f\mu_s^*)\}}{(3\kappa+\mu)(4-4f+\chi^*)+3f\mu\chi^*} \\
k_{Te} &= \frac{\mu\,[3\kappa(4-4f+\chi^*)+\mu(4-4f+\chi^*+3f\chi^*)]}{12f\kappa+\mu\,[4(3+f)+3(1-f)\chi^*]} \\
\nu_{Le} &= \nu-\frac{2f(1-\nu)\,[4\mu_s^*-(1-\nu)\chi^*]}{4(1-f)+(1+f-2f\nu)\chi^*}
\end{aligned}
\tag{8}
$$

where $\chi^* = \kappa_s^* + 2\mu_s^*$, $\lambda_s^* = \lambda_s/(a\mu)$, $\kappa_s^* = 2(\lambda_s^* + \mu_s^*)$, $\mu_s^* = \mu_s/(a\mu)$, and a is the radius of the cylindrical void. In order to obtain a simple analytical solution, MTM is used to predict the effective transverse shear modulus μ_{Te}. The expression of μ_{Te} is

$$
\mu_{Te} = \frac{\mu[4(1-f)+(3-f-2\nu)\chi^*]}{4(1+3f-4f\nu)+[3(1+f)-2(1+2f)\nu]\chi^*} \tag{9}
$$

The corresponding effective transverse Young modulus (E_{Te}) of the nanochannel-array materials is

$$
E_{Te} = \frac{4\mu_{Te}k_{Te}}{k_{Te}+\mu_{Te}+4\nu_{Le}^2\mu_{Te}k_{Te}/E_{Le}} \tag{10}
$$

It is seen that unlike the classical results without surface stress effect, the effective moduli of the nanoporous materials with spherical or cylindrical voids depend on the size of the voids. The effective moduli are functions of the two intrinsic length scales $l_\kappa (= \kappa_s/\mu)$ and $l_\mu = (\mu_s/\mu)$.

4 Tailoring of Stiffness

It is seen from above that the effective elastic moduli and CTE depend on the surface moduli λ_s and μ_s. Therefore, the effective elastic moduli and CTE can be tailored by surface modification. More details can be found in the paper of Duan et al. (2006). An alternative route to achieving the stiffening of a transversely isotropic nano-cellular material is by coating the cylindrical pore surfaces. Following the procedure in the recent work of Wang et al. (2005), it can be proved that the effect of the surface elasticity is equivalent to that of a thin surface layer on the pore surface. In this case, the surface elastic moduli λ_s and μ_s in Eq. (3) can be expressed by elastic constants and thickness of the coating layer

$$
\lambda_s = \frac{2\mu_c\nu_c t}{(1-\nu_c)}, \quad \mu_s = \mu_c t, \quad \alpha_s = \alpha_c \tag{11}
$$

where ν_c, μ_c and α_c are the Poisson ratio, the shear modulus and CTE of the surface coating layer, respectively, and t is its thickness. Therefore, by a proper choice of the properties and thickness of a coating layer, the properties of nanoporous materials can be tailored.

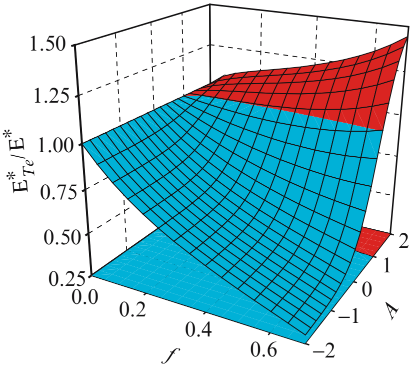

Fig. 1 The ratio of the specific effective Young modulus of a nano-cellular material to that of the non-porous solid (E^*_{Te}/E^*) versus the porosity f and the parameter A $(= \log_{10}(\mu_c/\mu))$. The blue area represents the region where $E^*_{Te}/E^* < 1$ and the red area the region where $E^*_{Te}/E^* > 1$

In practical applications such as in aerospace engineering, the specific stiffness, i.e. stiffness/density ratio, of a material is very important. The ratio of the specific Young modulus of the nanoporous material, denoted by E^*_{Te}, to that of the non-porous solid, denoted by E^*, is

$$\frac{E^*_{Te}}{E^*} = \frac{E_{Te}}{\beta E}, \quad \beta = 1 - f + f\frac{\gamma_c}{\gamma}\left(\frac{2t}{a} + \frac{t^2}{a^2}\right) \tag{12}$$

where γ_c and γ are the densities of the coating and the matrix, respectively. E^*_{Te}/E^* is only dependent on the ratio *t/a* of the coating thickness to the radius of the pores, and not dependent on the absolute size of the pores. Thus this technique is not limited to nanopores. To show the effect of the coating, the variation of E^*_{Te}/E^* versus the porosity f and the parameter A $(= \log_{10}(\mu_c/\mu))$ is plotted in Fig. 1. The parameters used in Fig. 1 are $t/a = 0.1$ and $\gamma_c/\gamma = 1$. It is seen that $E^*_{Te}/E^* > 1$ can be obtained at values of $A > 1$. If the coating material has a smaller density, then the ratio E^*_{Te}/E^* will be larger than that shown in Fig. 1.

5 Conclusions

This paper shows that the surface stress has an important effect on the mechanical and physical properties of materials at the nano-scale. We have also shown that the properties of the nano-cellular materials can be tailored by judicious manipulation of the pore surface elasticity and suggested two possible routes to achieving this. The same surface modification techniques can also be used for nano-porous solids with open cells. The results of the present paper provide an opening for designing nano-cellular materials with novel physical/mechanical properties by means of pore surface manipulation.

References

Christensen RM., Lo KH. Solutions for effective shear properties in three phase sphere and cylinder models, *J. Mech. Phys. Solids*. **27**, 315–330, 1979.

Cuenot S., Frétigny C., Demoustier-Champagne S., Nysten B. Surface tension effect on the mechanical properties of nanomaterials measured by atomic force microscopy, *Phys. Rev*. B. **69**, 165410, 2004.

Duan HL., Karihaloo BL. Thermoelastic properties of heterogeneous materials with imperfect interfaces: generalized Levin's formula and Hill's connections, *J. Mech. Phys. Solids*. **55**, 1036–1052, 2007.

Duan HL., Wang J., Huang ZP., Karihaloo BL. Size-dependent effective elastic constants of solids containing nano-inhomogeneities with interface stress, *J. Mech. Phys. Solids*. **53**, 1574–1596, 2005a.

Duan HL., Wang J., Huang ZP., Karihaloo BL. Eshelby formalism for nano-inhomogeneities, *Proc. R. Soc*. A. **461**, 3335–3353, 2005b.

Duan HL., Wang J., Karihaloo BL., Huang ZP. Nanoporous materials can be made stiffer than non-porous counterparts by surface modification, *Acta Mater*. **54**, 2983–2990, 2006.

Gibson LJ., Ashby MF. Cellular Solids - Structure and Properties, 2nd edition, Cambridge, Cambridge University Press, 1997.

Gleiter H. Nanostructured materials: basic concepts and microstructure, *Acta Mater*. **48**, 1–29, 2000.

Gurtin ME., Murdoch AI. A continuum theory of elastic material surfaces, *Arch. Rat. Mech. Anal*. **57**, 291–323, 1975.

Hashin Z. The elastic moduli of heterogeneous materials, *J. Appl. Mech*. **29**, 143–150, 1962.

Martin CR., Siwy Z. Molecular filters-pores within pores, *Nat. Mater*. **3**, 284–285, 2004.

Masuda H., Fukuda K. Ordered metal nanohole arrays made by a two-step replication of honeycomb structures of anodic alumina, *Science*. **268**, 1466–1468, 1995.

Miller RE., Shenoy VB. Size-dependent elastic properties of nanosized structural elements, *Nanotechnology*. **11**, 139–147, 2000.

Mori T., Tanaka K. Average stress in matrix and average elastic energy of materials with misfitting inclusions, *Acta Metall*. **21**, 571–574, 1973.

Shi JL., Hua ZL., Zhang LX. Nanocomposites from ordered mesoporous materials, *J. Mater. Chem*. **14**, 795–806, 2004.

Wang J., Duan HL., Zhang Z., Huang ZP. An anti-interpenetration model and connections between interface and interphase models in particle-reinforced composites, *Int. J. Mech. Sci*. **47**, 701–718, 2005.

Wang J., Duan HL., Huang ZP., Karihaloo BL. A scaling law for properties of nano-structured materials, *Proc. Roy. Soc*. A. **462**, 1355–1363, 2006.

Zhou LG., Huang HC. Are surfaces elastically softer or stiffer? *Appl. Phys. Lett*. **84**, 1940–1942, 2004.

The High Strain Rate Response of Adipose Tissue

K. Comley and N.A. Fleck

Abstract Microscopy suggests that adipose tissue can be idealised as an oil-filled closed-cell foam. Collagenous viscoelastic basement membrane forms the solid walls of the foam and the cavities of the foam are filled with lipid. The lipid has sufficiently low viscosity that it can be treated as an incompressible inviscid fluid. Measurements of the uniaxial compressive stress versus strain behaviour of the tissue have been made for strain rates from quasi-static to 6,000 s^{-1}. Screw driven tensile test machines were used to collect data at strain rates less than 200 s^{-1}. A split Hopkinson pressure bar constructed from polycarbonate was used for strain rates greater than 1,000 s^{-1}. The measured stress versus strain curves are non-linear with stiffening at increasing strains. The response at low strain appears to be strongly rate sensitive. It is instructive to fit a standard linear solid (or Kelvin model) comprising three elements: a spring (stiffness E_1) and dashpot (viscosity η) in series, which are both in parallel with a second spring (stiffness E_2) to the data. The stiffness modulus E_2 is taken as the average stress at 10% strain and low strain rates and is found to be 1.15 kPa. E_1 is taken to be 0.5 GPa which corresponds to the assumed bulk modulus of the tissue. A least squares regression fit of the experimental data gives a time constant of 97 ns.

1 Introduction

The compressive stress versus strain response of adipose tissue has been measured for strain rates, $\dot{\varepsilon}$, from quasi-static to 6,000 s^{-1}. The high strain rates were achieved using a split Hopkinson pressure bar constructed from Polycarbonate. It is shown that a standard linear solid can be used to model the constitutive properties of the tissue.

K. Comley (✉) and N.A. Fleck
University of Cambridge Centre for Micromechanics, Cambridge, UK

H. Zhao, N.A. Fleck (eds.), *Mechanical Properties of Cellular Materials,*
IUTAM Bookseries 12,

1.1 Microstructure of Adipose Tissue

Adipose tissue (fat) comprises a matrix of lipid filled cells called adipocytes, two collagen based structures: interlobular septa and basement membrane, together with various other structures such as blood vessels. Sixty percent to 80% of the weight of adipose tissue is lipid, 5–30% water and the remaining 2–3% is protein (Greenwood and Johnson, 1983).

Light microscopy of adipocytes shows a thin rim of cytoplasm surrounding the bulk of a single lipid vacuole and a small nucleus, see Fig. 1b. The diameter of each cell is approximately 80 µm. At body temperature lipid is a light viscous oil (Cormack, 1987), see Fig. 1a.

Each adipocyte is entirely surrounded by a two dimensional woven filamentous collagenous structure and forms part of the Basement Membrane (Abrahamson, 1986), see Fig. 1c. It is composed of type IV collagen. Using an Scanning Electron Microscope (SEM) it is observed that the basement membrane of each adipocyte is connected to its neighbour in a foam-like structure, see Fig. 2.

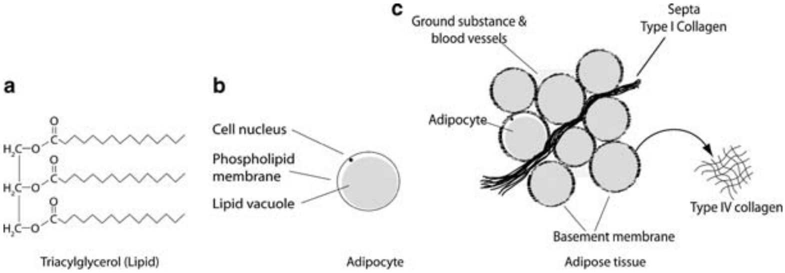

Fig. 1 Diagram of adipose tissue and is constituents

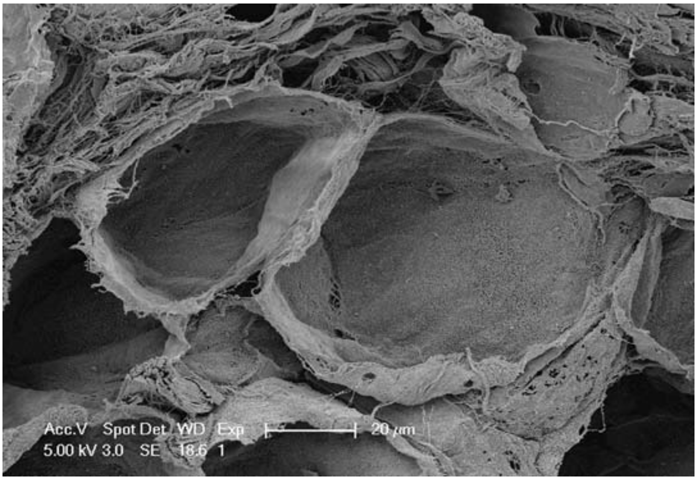

Fig. 2 Scanning Electron Micrograph of the basement membrane

The lobules of adipocytes are threaded by a dilute concentration of Type I collagen bundles known as the interlobular septa (Urmacher, 1997), see Fig. 1b. The spaces between the adipocytes and collagen matrices are filled with ground substance.

It is suggested that adipose tissue can be treated as an oil-filled, closed-cell foam. The solid walls of the foam are formed by viscoleastic basement membrane, and the cavities contain lipid. The viscosity of the lipid is sufficiently low that it behaves as an incompressible inviscid fluid.

2 Experimental Setup

2.1 Specimen Preparation

Fresh Porcine skin tissue from three different pigs was supplied by a local abattoir, Dalehead Foods, Linton. The skin samples, including subcutaneous fat to depths of 20 mm, were removed from the jowl of the pig immediately after slaughter. The samples were stored in Phosphate Buffered Saline (PBS) at room temperature prior to testing, which always commenced within 3 h of slaughter.

Circular cylindrical samples of the adipose tissue were cut to a diameter of 10 mm from the skin using a sharp punch. The samples were of height $h = 3\,\mathrm{mm}$ for the Hopkinson bar tests and $h = 8\,\mathrm{mm}$ for the low strain rate tests.

2.2 Test Methods

2.2.1 Low Strain Rate Testing (Below $2\,\mathrm{s}^{-1}$)

Cylindrical samples were compressed between smooth plastic platens using an Instron screw driven tensile test machine. The samples were compressed to a fixed displacement at a given rate. The force generated in the samples was recorded via a 5 N load cell with an accuracy of 20 mN.

2.2.2 Medium Strain Rate Testing (20–$250\,\mathrm{s}^{-1}$)

Cylindrical samples were compressed to a fixed displacement at a given rate between smooth plastic platens using a Schenk hydraulic tensile test machine and a purpose built cantilever beam transducer (Doebelin, 1966). The beam was made from aluminium and fitted with four strain gauges in a standard Wheatstone bridge arrangement. The measurement accuracy for a static load was 50 mN. The stiffness and sensitivity of the beam (Fleck, 1983) was 20.46 N/mm and $141\,\mu\varepsilon/\mathrm{N}$ respectively.

Displacement of the platens was measured using a Linear Displacement Transducer (LDT) accurate to 0.01 mm under static conditions. The deflection of the beam during loading must be subtracted from the measured deflection. A formula for the deflection of the beam was determined experimentally and validated by comparing it to standard beam theory.

2.2.3 High Strain Rate Testing (Above $1{,}000\,\mathrm{s}^{-1}$)

High strain rate compression tests were conducted using a split Hopkinson pressure bar (Follansbee, 1985). The sensitivity of the pressure bars was increased by the use of polycarbonate instead of steel. Wave dispersion effects were found to be negligible, in agreement with the attenuation measurements of Wang et al. (1992).

3 Results

The measured uniaxial compression response of adipose tissue is shown in Figs. 3–5 for the three strain rate regimes. In broad terms the stress versus strain curves are non-linear with stiffening at increasing strain.

All the tests were carried out at room temperature in dry conditions (i.e. the specimens were not submerged in a saline bath). Low strain rate validation tests with the tissue fully saturated in saline at 37 °C, were carried out to more closely mimic *in-vivo* conditions. No significant differences in the response were observed.

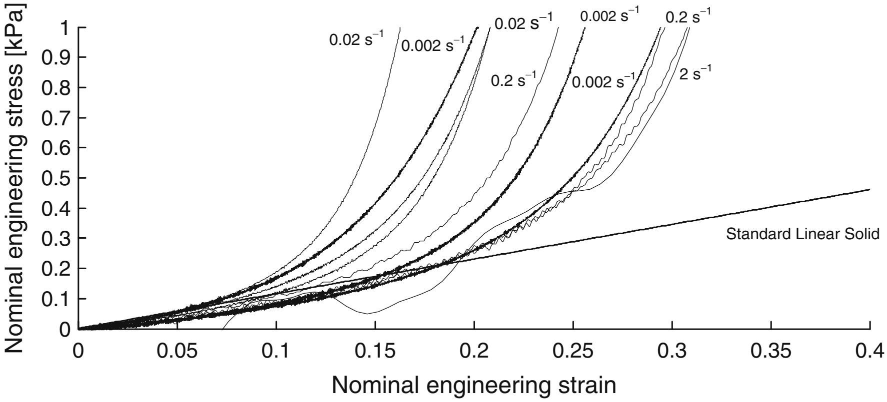

Fig. 3 Unconfined uniaxial compression of adipose tissue at strain rates between 0.002 and $2\,\mathrm{s}^{-1}$. A standard linear solid is used to model the data

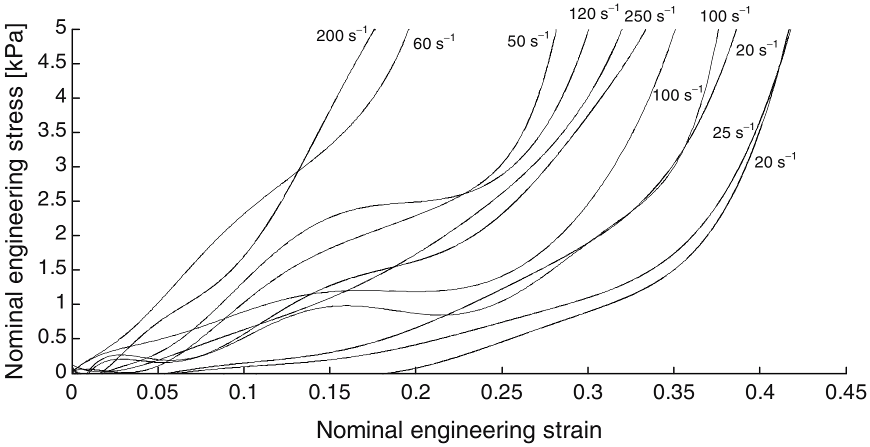

Fig. 4 Unconfined uniaxial compression of adipose tissue at strain rates from 20 to $250\,\mathrm{s}^{-1}$

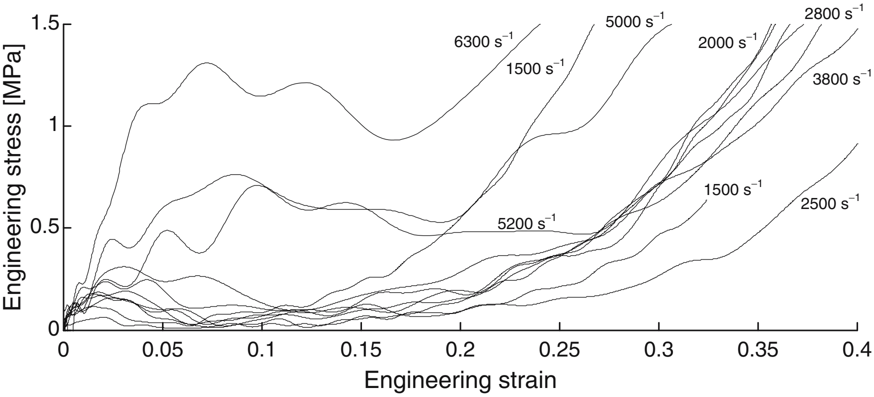

Fig. 5 Unconfined uniaxial compression of adipose tissue using a split Hopkinson pressure bar at strain rates between 1,500 and $6,300\,\mathrm{s}^{-1}$

4 Discussion

The sensitivity of the response to strain rate is explored by plotting the measured stress at a fixed level of 10% strain against strain rate, see Fig. 6. This level of strain was chosen as the response is approximately linear. We conclude from Fig. 6 that the stress level is insensitive to strain rate for $\dot{\varepsilon} < 10\,\mathrm{s}^{-1}$, but increases sharply with strain rate for $\dot{\varepsilon} > 10\,\mathrm{s}^{-1}$. We note that the stress increases from about 1,000 Pa to about 1 MPa as $\dot{\varepsilon}$ is increased from 10^2 to $10^4\,\mathrm{s}^{-1}$.

It is instructive to attempt a curve-fit of the Standard Linear Solid (Lakes, 1998) to the data. The Standard Linear Solid is represented by three elements: a spring (stiffness E_1) and dashpot (viscosity η) in series, which are both in parallel with a second spring (stiffness E_2).

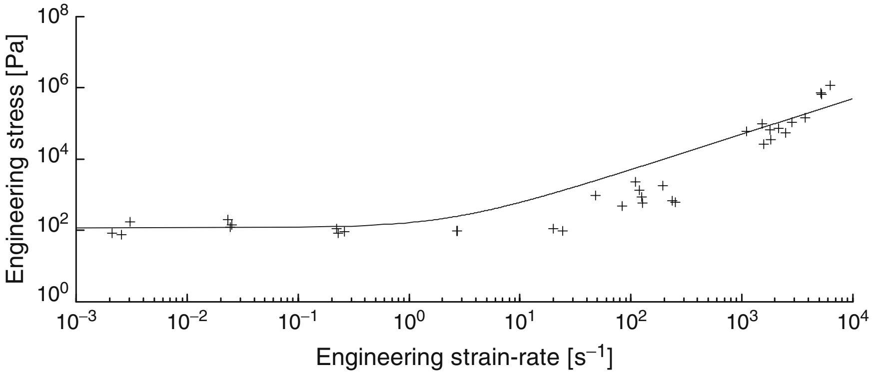

Fig. 6 Uniaxial compression of adipose tissue at 10% strain (+). A standard linear solid model has been fitted to the data (−)

The input conditions are

$$\begin{aligned} \varepsilon(t) &= 0, \quad t \leq 0 \\ \varepsilon(t) &= \dot{\varepsilon}t, \quad t > 0 \end{aligned} \tag{1}$$

The relaxation time for the solid is defined as

$$\tau \equiv \frac{\eta}{E_1} \tag{2}$$

The differential equation for the Standard Linear Solid is given by

$$\frac{d\sigma}{dt} + \frac{\sigma}{\tau} = \frac{d\varepsilon}{dt}(E_1 + E_2) + \frac{\varepsilon E_2}{\tau} \tag{3}$$

From which a viscoelastic modulus, E(t), can be derived

$$E(t) = E_2 + E_1 e^{-t/\tau} \tag{4}$$

The Boltzmann Superposition Integral for stress as a function of strain is

$$\sigma = \int_0^t E(t-u)\frac{d\varepsilon(u)}{du}du \tag{5}$$

and substitution of Eqs. (1) and (4) into Eq. (5) gives

$$\sigma(t) = E_2\dot{\varepsilon}t + E_1\dot{\varepsilon}\tau[1 - \exp(-t/\tau)] \tag{6}$$

It remains to match Eq. (6) to the observed response in order to obtain values for (E_1, E_2 and η). The value of the stiffness modulus E_2 is taken as the average stress at 10% strain at low strain rates and was found to be 1.15 kPa. This is consistent with the values of elastic moduli reported in Samani et al. (2003) and Nightingale et al. (2003).

The standard linear solid predicts an instantaneous modulus of $(E_1 + E_2)$. The tests reported here do not investigate a sufficiently high strain rate for the unrelaxed modulus to be measured: here we take E_1 to be 0.5 GPa, corresponding to the bulk modulus of tissue reported by Saraf et al. (2007).

A least squares regression gives a time constant of 97 ns. Hence the dynamic viscosity, $\eta = \tau E_1$, of the basement membrane is estimated to be 48 Pa s. Conclusions

Microscopy suggests that adipose tissue resembles a fluid-filled closed-cell foam. A test method has been developed to measure the compressive response of animal fat over a wide range of strain rate. The measured response is strongly rate sensitive and the standard linear solid gives a reasonable fit to the observations.

Acknowledgement The authors gratefully acknowledge Torben Strom Hansen and Peter Juhlin at Novo Nordisk A/S for providing funding and their continued support.

References

Abrahamson DR (1986) Recent studies on the structure and pathology of basement membranes. J Pathol 149:257–278
Cormack DH (1987) Ham's histology. JB Lippincott Company, Philadelphia, PA
Doebelin EO (1966) Measurement systems: Application and design. McGraw-Hill, New York
Fleck NA (1983) Some aspects of clip gauge design. Strain 19:17–22
Follansbee PS (1985) The Hopkinson bar. In: Kuhn H, Medlin D (eds) ASM Handbook: Vol 8 mechanical testing and evaluation ASM International, Materials Park, Ohio. pp 198
Greenwood MRC, Johnson PR (1983) The adipose tissue. In: Weiss L (ed) Histology, cell and tissue biology. MacMillan, New York. pp 178–199
Lakes RS (1998) Viscoelastic solids. CRC, Boca Raton, FL
Nightingale K et al. (2003) Shear-wave generation using acoustic radiation force: In vivo and ex vivo results. Ultrasound Med Biol 29:1715–1723
Samani A et al. (2003) Measuring the elastic modulus of ex vivo small tissue samples. Phys Med Biol 48:2183–2198
Saraf H et al. (2007) Mechanical properties of soft human tissues under dynamic loading. J Biomech 40:1960–1967
Urmacher CD (1997) Normal skin. In: Sternberg SS (ed) Histology for pathologists. Lippincott-Raven, Philadelphia, PA. pp 25–45
Wang L et al. (1992) Generalization of split Hopkinson bar technique to use viscolelastic bars. I J Impact Eng 15:669–686

X Ray Tomography Study of Cellular Materials: Experiments and Modelling

E. Maire, O. Caty, A. King, and J. Adrien

Abstract This paper summarizes different results obtained by the authors applying X-ray tomography to the study of cellular materials (metals, ceramics and polymers). From the 3D images, three different kinds of analysis are carried out. The first is image processing to retrieve the morphological characteristics (density, size, tortuosity) of the studied materials. The second is the analysis of the deformation modes using in situ or ex situ mechanical tests (tension, compression, fatigue). The third is devoted to FE calculations in which models are produced to represent as exactly as possible the architecture of these materials as seen in tomography. These different points are successively presented and exemplified in the present paper.

1 Introduction

For a good understanding of the physico-mechanical properties of a cellular material, the cellular microstructure i.e. the morphology of the arrangement of the solid and gaseous phases in the cellular material has to be characterized. Ideally, these measurements should be performed on a three-dimensional (3D) image of the sample. Cellular materials are not easy to observe by means of standard microscopy techniques. This is due to the highly porous nature of the structure which precludes easy polishing. SEM is often used but it only allows to see the outer surface of the solid phase in the cells located close to the surface of the sample to study. It is very well known however that edge effects are strong in these materials so what we see at the surface is likely to be different than what happens in the bulk.

X-ray tomography has appeared recently to be a very powerful tool allowing to characterize the microstructure of cellular materials [1–9]. Compared to confocal microscopy, it allows to visualize the complete structure and not only the first layer of cells close to the surface. Being non destructive, it is also probably easier to

---

E. Maire (✉), O. Caty, A. King, and J. Adrien
Université de Lyon, INSA-Lyon, MATEIS CNRS UMR5510, 7 avenue Jean Capelle, F-69621 Villeurbanne, France

H. Zhao, N.A. Fleck (eds.), *Mechanical Properties of Cellular Materials,*
IUTAM Bookseries 12,

implement than serial sectioning that requires filling of the holes. Thus it appears to be one of the more versatile techniques capable of providing non destructive 3D images of a complete sample of cellular material.

Based on different experiments and examples obtained by the authors in recent years, it will be emphasized in the present paper that X-ray tomography is well adapted to the characterization of different aspects of the microstructure of various cellular solids. It will also be shown that the technique can be used to study the deformation modes by means of in situ loading in compression, tension, and fatigue. Different methods for using tomography results as inputs for models, especially Finite Element meshes, will finally be discussed.

2 X-Ray Tomography

The general principle of the tomography technique has been described in many papers [10, 11]. Its experimental implementation requires an X-ray source, a rotation stage and a radioscopic detector. Two kinds of set-ups can be used for studying a cellular micro structure:

- Standard tomography can be performed using a laboratory X-ray source. Prototypes have been designed in industrial or academic laboratories [12]. Several experimental set-ups of this kind are also now commercially available and give good quality images with a resolution down to about 2 µm.
- A synchrotron source is required to perform high resolution x-ray tomography. This experiment can be performed on several beam lines at the ESRF in Grenoble or at several other synchrotron sources in the world (SPRING 8 in Japan, SLS in Switzerland, etc.).

To understand better the deformation modes of a material, it can be very useful to observe a same zone at different strain levels. However it is not trivial to apply an in situ deformation during a tomographic experiment because the testing device has to rotate without obstructing the irradiation of the sample by the x-ray source. In the present study, we use a special loading device developed to allow such a rotation [10]. The forces between the top and the bottom grip are transmitted through a polymer tube surrounding the sample which is transparent to X-rays.

3 Image Analysis of the Initial Microstructure

The important parameters to characterize the cellular microstructure of a cellular material are: the global density and its fluctuation in the sample, the cell size distribution and the wall thickness distribution. Some of these parameters can be obtained using conventional techniques (weighing, 2D image analysis) but for some of them it is necessary to use 3D data to get a complete characterization. Density can trivially be measured after segmentation of a 3D data set. Tomography gives

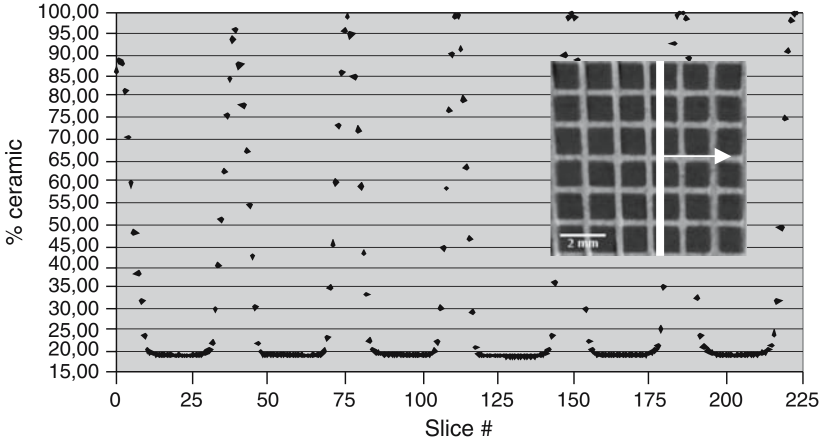

Fig. 1 Relative density (measured in slices such as the white thick line) along one direction for the honeycomb cellular ceramic shown in the inset

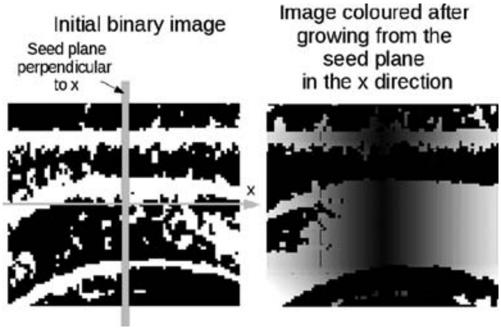

Fig. 2 Measurement of the tortuosity. The white phase in the figure on the left is coloured by growing starting from a sedd plane. The lighter the grey lavel in the coloured image, the longer the path through the phase

a superior information as it allows density to be mapped in 3D. Density profiles such as this shown in Fig. 1 for a honeycomb Al_2O_3 cellular material (relative density: 20%) can be calculated. This can be used to measure the homogeneity of the distribution of the solid phase inside a material.

The tortuosity T of the pathways through a porous network is a key parameter for modeling different transport properties (acoustic or thermal waves for example), or for fluid dynamics through the pores. In the present study, T is calculated by the following procedure (see also Fig. 2, summarizing the procedure in 2D): firstly, all of the pore voxels located in the central plane (the seed plane) of a representative volume of material are labeled with number 1. All adjacent pore voxels (according to a neighbouring criterion) are then labeled 2, and so on through the pore network, effectively creating a distance map of the distance through the phase of interest from the original seed plane. A graph can then be plotted of the average label value in each plane parallel to the seed plane as a function of the linear distance normal to the seed plane. Because the path through the network is tortuous, the gradient of this plot is greater than unity and the gradient of a line is fitted to the plot gives a measure of T.

This procedure can be repeated for different directions through the microstructure to reveal any anisotropic effects. In our case the measurement is performed in the three orthogonal principal directions of the images. A segmented 3D data set is an ideal object on which to measure this kind of property of the material with no bias due to sampling effects as it would be the case for a 2D data set. The voxel nature of the data can induce a bias in the measurement of an oblique distance. Depending on the neighbouring criterion (NC) used, the distance map calculated can then vary significantly. If the criterion 'only face touching' (six possible neighbours for a voxel) is selected, the distance measured is very large and tortuosity is overestimated. If the criterion 'face + edge + vertex touching' (27 possible neighbours for a voxel) is selected, the distance is conversely very small and tortuosity is underestimated. The better criterion is 'face + edge touching' (12 neighbours for a voxel) because in most of the cases, it allows to calculate a distance close to the actual Euclidean distance. T can vary from 1.1 when using 27 neighbours to 1.7 (using six neighbours) in a same data-set.

It is of course also most useful to obtain a measure of the characteristic size of each of the two phases. Measuring a typical size in an interconnecting network of two phases is not a trivial procedure. A typical size can be calculated using a computational processing procedure composed of a sequence of standard mathematical morphology operations applied to the binarized 3D images. This sequence of operation allows to measure the granulometry (i.e. the density distribution of the thickness) of the studied phase in the material [13–15]. Again, because of the voxel nature of the data-set, the NC used to perform the erosion/dilation steps has a direct impact on the value of the size measured. The measurement can also be anisotropic if the SE is chosen anisotropic (no erosion in one direction for example) Fig. 3 shows the comparison of such a granulometry measurement performed using three isotropic NCs (6 or 26 neighbours and also a criterion based on the Euclidean distance) on a same data-set of porous plaster material (relative density: 50%).

4 Deformation Studies

Several authors have used in situ or ex situ deformation experiments for analyzing the mechanical properties of cellular materials [1–6, 16]. We have for instance published [17] an in-situ tomographic study of the deformation of some of the most standard commercially available aluminum closed cell foams. Most of these studies concerned materials loaded in a monotonous mode. In [18], we have also studied a more isotropic loading mode by constraining the compression of syntatic polymer foams inside bulk polymer cylinders.

The example in the present paper is more recent. It shows the evolution of the structure of a sintered hollow Ni spheres structure (relative density: 11%) during compression/compression fatigue. The Fig. 3 shows a tomographic slice extracted from the bulk of the material at different number of cycles during the fatigue life. One can see from this set of images that like it is the case in many examples of

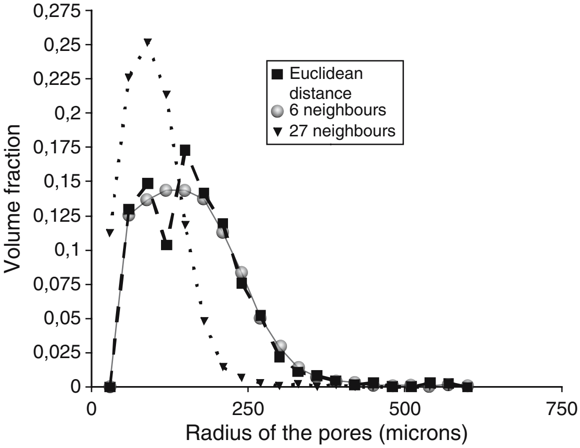

Fig. 3 Comparison of the size distribution measured using different neighbouring conditions on a same 3D data set. Using six neighbours gives a smaller size

these cellular materials, the global deformation of the sample is due to very local damage events. Different damage modes can be distinguished: preexisting defects, buckling, bending of cell walls... Note also that as the number of cycles increases, a large number of fracture events can be observed. The same material when loaded in compression monotonously shows much less fracture. Another contribution in the field of fatigue is the article of Banhart et al. in the present book.

Using digital image correlation, it is possible to measure the displacement at the scale of the microstucture provided that two images of a same region at two different deformation states are available. These images are very easy to obtain at least in 2D using standard in situ experiments in SEM or Optical Microscopy. These methods have thus been extensively developed using 2D images as inputs. Algorithms based on 3D images are now available to process tomographic datasets in the same way [4, 19] and have been used in [20] to analyse the deformation of cellular materials. A good example of this kind of study can also be found in the article of Hild et al. in the present book.

5 Simulating Physical and Mechanical Properties

The architecture has a crucial effect on the global behavior of metal foams. It has quickly become apparent that when developing models to describe these materials it is necessary to consider the cellular structure. The following different approaches can be used:

- Meshes generated from a Voronoi description of the microstructure
- Voxel/element meshes
- Meshes of the actual shape of the cellular architecture

Implementing the methods of the first family requires the extraction, from the tomographic image, of the coordinates of the cell vertices and then to construct beam or plate elements defined by these points [16]. This provides a direct representation of the actual cellular structure of the foam. Alternately, using image analysis methods such as these presented in the preceding section, one can get information such as the cell size distribution. It is then possible to create a numerical structure (for example, from sphere packing) having the same distribution.

The second family is based on a straightforward transcription of the voxel structure of a tomographic image into a mesh of cubic elements (the lateral dimension of each element is equal to the resolution in the tomographic image. The mesh has the same dimensions (number of elements in each direction) as the image. The mechanical properties of each element are tailored by the gray level of the corresponding voxel. This method is rather time consuming because, to be representative, the image and hence the mesh must be large enough, leading to long calculation times.

The third family is the one we chose in [21]. The actual shape of the beams and struts of the architecture are exactly reproduced thanks to their description by tetrahedral elements. Ulrich et al. [22] have compared the voxel/element and the tetrahedral mesh of the actual shape in the case of a classical cellular material: trabecular bone. The tetrahedral mesh was found to be more accurate for the same resolution. This method is more difficult to implement because an appropriate meshing technique and the definition of the volumes to mesh are required but commercial softwares are now available for this purpose. An example of such a mesh, produced for the foams presented in Fig. 3 is shown in Fig. 4. The FE model obtained reproduces the actual structure of the cellular material. It can be loaded numerically, allowing the determination of local regions where stresses concentrate. The output

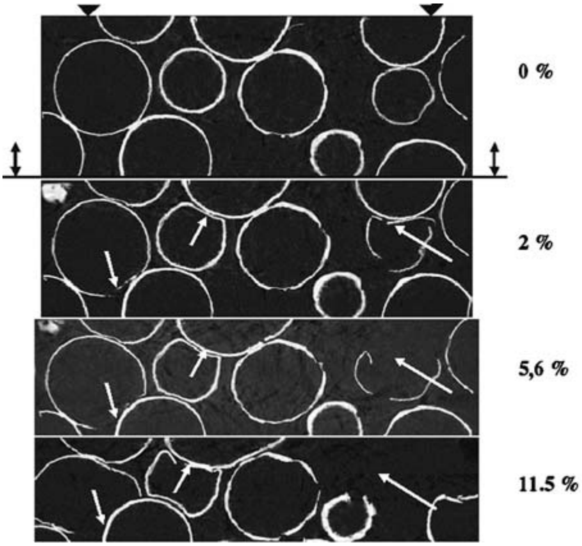

Fig. 4 Tomographic slices of a random assemblage of hollow nickel spheres at different deformation stages during a fatigue compression/compression experiment

of the calculation can then be post processed using a fatigue initiation criterion. The method is currently being improved for the case of cellular materials with large cells and very thin walls. In this case, the solution is to replace the tetrahedral elements currently used with shell elements and to give to the shell the exact thickness measured using the 3D images.

6 Conclusion

The paper has shown that X-ray tomography can be used to characterize different cellular materials. Examples of results have been given for three kinds of analysis. Firstly, the 3D data sets can be used to determine the morphology of the structure in terms of density distribution mapping, tortuosity and size measurement. In these last two cases, the voxel nature of the image induces bias in the measurement which must be accounted for. Secondly, X-ray tomography has been used to analyze the deformation modes during different kinds of in situ testing (compression, tension, and fatigue). Thirdly, different methods for using tomography results as inputs for models, especially Finite Element meshes, have been discussed. The one chosen by the authors with the aim of reproducing most accurately the actual shape has been described in more detail (Fig. 5).

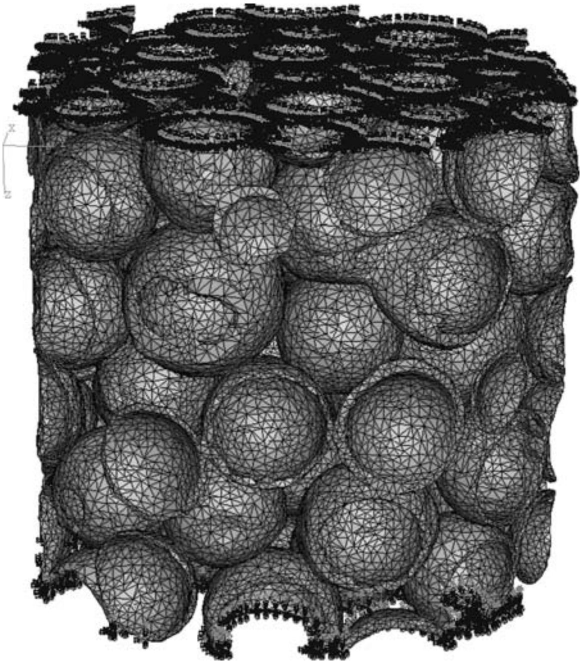

Fig. 5 FE mesh and boundary conditions for the random assemblage of hollow nickel spheres shown in Fig. 4

References

1. H. Bart-Smith, A.F. Bastawros, D.R. Mumm, A.G. Evans, D.J. Sypeck, H.N.G. Wadley. *Acta mater*. **46** (10), p. 3582 (1998).
2. E. Jasiuniene, J. Goebbels, B. Illerhaus, P. Lowe, A. Kottar. In *Cellular Metals and Metal Foaming Technology*, Eds. J. Banhart, M.F. Ashby, N.A. Fleck, Verlag MIT Publishing, Bremen, Germany, p. 251 (2001).
3. G. Gioux, T.M. McCormack, L.J. Gibson. *Int. J. Mech. Sci*. **42**, p. 1097–1117 (2000).
4. B.K. Bay, T.S. Smith, D.P. Fyhrie, M. Saad. *Exp. Mech*. **39**, p. 218 (1999).
5. H.P. Degisher, A. Kottar, F. Foroughi. In *X-Ray Tomography in Material Science*, Eds. Baruchel, Buffière, Maire, Merle, Peix, Phs. Hermes, Paris, p. 165 (2000).
6. A.H. Benouali, L. Froyen, In *Cellular Metals and Metal Foaming Technology*, Eds. J. Banhart, M. Ashby, N. Fleck, MIT-Verlag, Bremen, Germany, p. 269 (2001).
7. A. Elmoutaouakkail, L. Salvo, E. Maire, G. Peix. Adv. Eng. Mater. **4** p. 803–807 (2002).
8. L. Helfen, T. Baumbach, H. Stanzick, J. Banhart, A. Elmoutaouakkil, P. Cloetens, K. Schladitz. *Adv. Eng. Mater*. **4** p. 808–813 (2002).
9. O.B. Olurin, M. Arnold, C. Körner, R.F. Singer. *Mat. Sci. Eng*. ***A*** **328** p. 334 (2002).
10. J.Y. Buffière, E. Maire, P. Cloetens, G. Lormand, R. Fougères. *Acta Mater*. **47** p. 1613 (1999).
11. E. Maire, J.Y. Buffière, L. Salvo, J.J. Blandin, W. Ludwig, J.M. Létang. *Adv. Eng. Mater*. **3** p. 539 (2001).
12. E. Cendre et al. *Proceedings of the First World Congress on Industrial Process Tomography*, Umist University (UK) p. 362 (1999).
13. E. Maire, P. Colombo, J. Adrien, L. Babout, L. Biasetto. *J. Eur. Ceram. Soc*. **27** pp. 1973–1981 (2007).
14. Vogel. *Eur. J. Soil Sci*. **48** pp. 365–377 (1997).
15. Vogel, Roth. *Adv. Water Resour*. **24** pp. 233–242 (2001).
16. J.A. Elliott, A.H. Windle, J.R. Hobdel, G. Eeckhaut, R.J. Oldman, W. Ludwig, E. Boller, P. Cloetens, J. Baruchel. *J. Mater. Sci*. **37** p. 1547 (2002).
17. E. Maire, A. Elmoutaouakkil, A. Fazekas, L. Salvo. *MRS Bull*. **28** p. 284 (2003).
18. J. Adrien, E. Maire, N. Gimenez, V. Sauvant-Moynot. *Acta Mater*. **55** pp. 1667–1679 (2007).
19. M. Bornert, J.M. Chaix, P. Doumalin, J.C. Dupré, T. Fournel, D. Jeulin, E. Maire, M. Moreaud et H. Moulinec. *Instrumentation, Mesure, Métrologie* 2004/4 pp. 43 a 88.
20. L. Salvo, P. Belestin, E. Maire, M. Jacquesson, C. vecchionacci, E. Boller, M. Bornert et P. Doumalin. *Adv. Eng. Mater*. **6** pp. 411–415 (2004).
21. S. Youssef, E. Maire, R. *Acta Mater*. **53** pp. 719–730 (2005).
22. D. Ulrich, B. Van Rietbergen, H. Weinans, P. Ruegsegger. *J. Biomech*. **31** p. 1187 (1998).

Anisotropic Mechanical Properties of Lotus-Type Porous Metals

H. Nakajima, M. Tane, S.K. Hyun, and H. Seki

Abstract The mechanical properties of lotus metals were experimentally investigated and the effect of the anisotropic pores on the mechanical properties was clarified. The mechanical strength in the direction parallel to the pore direction linearly decreases with increasing porosity, while that perpendicular to the pore direction drastically decreases. This is caused by the anisotropy of stress concentration. The porosity dependence of the mechanical strength obeys a power-law formula.

1 Introduction

Porous metals including foamed metals possess unique features such as low density, high surface area, sound absorption, etc. [1, 2]. Therefore, the porous metals are expected to be used in various fields. However, conventional porous metals possess a shortcoming of low strength. This is because their pore shape is irregular and the distribution of pores is random. Hence, the conventional porous metals with low strength cannot be used as structural materials although they show unique features. Lotus-type porous metals (lotus metals) with cylindrical pores oriented in one direction, shown in Fig. 1, can be fabricated by unidirectional solidification of metals in pressurized gas atmospheres (pressurized gas method) or casting into a mold in which gaseous compounds are placed (thermal decomposition method) [3–5]. Owing to the cylindrical pores oriented in one direction, stress hardly concentrates around the pores for loadings in the longitudinal direction of the pores (pore direction). Furthermore, the porosity of lotus metals is small compared with that of conventional porous metals. Therefore, the mechanical properties of lotus

---

H. Nakajima (✉), M. Tane, S.K. Hyun, and H. Seki
The Institute of Scientific and Industrial Research, Osaka University, 8-1 Mihogaoka, Ibaraki, Osaka 567-0047, Japan

H. Zhao, N.A. Fleck (eds.), *Mechanical Properties of Cellular Materials,*
IUTAM Bookseries 12,

Fig. 1 Pore structure of lotus-type porous metals fabricated by continuous casting method [4]

metals are superior to those of the conventional porous metals [6]. Thus, lotus metals are expected to be used as light-weight structural materials. When lotus metals are used as structural materials, the anisotropic mechanical properties originating from anisotropic porous structure should be clarified. It should be noted that the mechanical properties of conventional porous metals except for some metallic foams [7, 8] are almost isotropic.

In the present paper, anisotropic mechanical properties (elastic constants, ultimate tensile strength, compressive yield stress, and fatigue strength) of lotus metals are summarized and the effect of the anisotropic pores on the mechanical properties is discussed.

2 Elastic Constants

Lotus metals macroscopically exhibit hexagonal (transverse-isotropy) elastic symmetry with c-axis parallel to the pore direction [9–11]. In this case, there are five independent elastic constants, c_{11}, c_{33}, c_{13}, c_{44} and $c_{66} = (c_{11}–c_{12})/2$. To determine all of them, we used the resonant ultrasound spectroscopy (RUS) [12] and mode-selective electromagnetic acoustic resonance (EMAR) [13] techniques. By using RUS, we measured the resonant spectrum consisting of eight vibration groups: flexure $(\mathrm{B}_{1u}, \mathrm{B}_{2u}, \mathrm{B}_{3u})$, torsion (A_u), shear $(\mathrm{B}_{1g}, \mathrm{B}_{2g}, \mathrm{B}_{3g})$, breathing (A_g), where the group notation follows [14]. Subsequently, the mode identification regarding the shear and breathing groups was carried out with EMAR. The elastic constants were determined through iterative calculations from the resonant spectrum obtained by this RUS-EMAR combination technique.

Figure 2 shows the porosity dependence of Young's moduli $E_\perp$ and $E_{//}$ of (a) lotus iron [9], (b) lotus magnesium [10], and (c) lotus copper [11], where $E_{//}$ and $E_\perp$ indicate Young's moduli in the directions parallel and perpendicular to the pore direction, respectively. For all the lotus metals, $E_{//}$ decreases linearly with

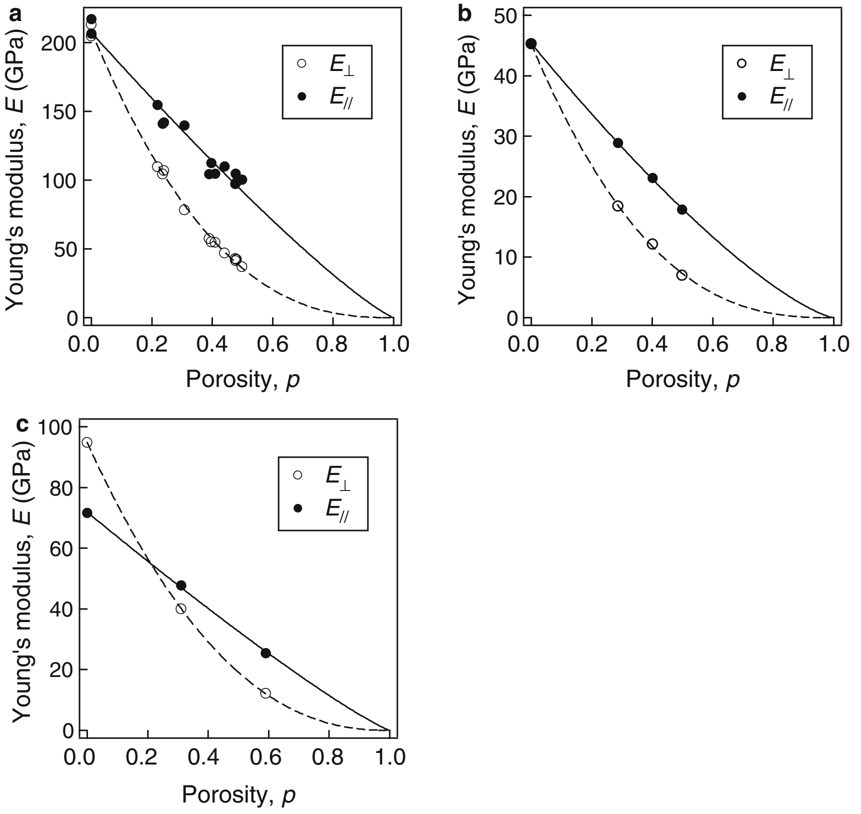

Fig. 2 Porosity dependence of two Young's moduli, $E_{//}$ in the direction parallel to the pore direction and $E_{\perp}$ in the direction perpendicular to the pore direction. Each line is obtained by fitting Eq. (1) to the measurements. (**a**) Lotus iron, (**b**) lotus magnesium, and (**c**) lotus copper

increasing porosity, while $E_{\perp}$ decreases drastically with increasing porosity. This is because stress hardly concentrates around pores for a loading in the pore direction direction, while large stress concentration occurs for a loading in the direction perpendicular to the pore direction.

Since lotus metals are fabricated though the unidirectional solidification method, the preferential orientation in the crystal growth usually appears. This is the case for lotus copper and lotus magnesium; their preferential growth directions are $\langle 100 \rangle$ for lotus copper and $\langle 0002 \rangle$ and $\left\langle 11\bar{2}0 \right\rangle$ for lotus magnesium. Since $\langle 100 \rangle$ of copper is soft direction in terms of elastic stiffness, the nonporous copper $(p = 0)$ shows an elastic anisotropy, $E_{\perp} > E_{//}$, as seen in Fig. 2c. In contrast to lotus copper, nonporous magnesium virtually exhibits an elastic isotropy because the elastic property of single-crystal magnesium is nearly isotropic [15]. Since lotus iron has no texture, two directional Young's moduli of nonporous iron are substantially equal to each

Table 1 Values of *m* for Young's modulus, ultimate tensile strength and fatigue strength in the direction parallel and perpendicular to the pore direction

Young's modulus					
Lotus Cu		Lotus Fe		Lotus Mg	
//	⊥	//	⊥	//	⊥
1.1	2.3	1.2	2.6	1.3	2.6
Ultimate tensile strength				Fatigue strength	
Lotus Cu		Lotus Fe		Lotus Cu	
//	⊥	//	⊥	//	⊥
1.1	3.0	1.2	3.6	0.9	2.7

other despite the fact that the single crystal iron shows a relatively strong elastic anisotropy. Thus, it is noted that the texture effects on the matrix metal are observed case by case.

By extensive researches on the effective physical properties, e.g. the electrical conductivity, the yield stress, and the elastic modulus of the porous materials, their porosity dependencies are experimentally found to follow the power-law formula [16–18];

$$M = M_0(1-p)^m, \tag{1}$$

where M and M_0 are the physical properties of porous and nonporous material, respectively, and m is the coefficient determined empirically. The solid and broken lines in Fig. 2 indicate Eq. (1) fitted to the measurement data. Thus, one finds that the measurements almost lie on them, which indicates that Eq. (1) approximately holds for the elastic constants of the anisotropic porous metals. The m values for each lotus metal are shown in Table 1.

3 Tensile Strength

Tensile tests were performed on lotus copper and lotus iron fabricated with hydrogen or nitrogen atmosphere using the Instron Universal Testing Machine (Model 4482, Instron Corp., Canton, MA, USA) at room temperature. Figure 3a shows the porosity dependence of the ultimate tensile strengths, where $\sigma_{t//}$ and $\sigma_{t\perp}$ represent the ultimate tensile strength along the directions parallel and perpendicular to the pore directions, respectively [6]. The ultimate tensile strength of lotus copper exhibits anisotropy, which is also caused by the anisotropy of stress concentration. Furthermore, the tensile strength is also found to exhibit a power law behavior (the m values are shown in Table 1). Figure 3b shows the porosity dependence of the ultimate tensile strength of lotus iron fabricated in hydrogen (Fe-H) or nitrogen (Fe-N) atmosphere [19]. The ultimate tensile strength of lotus iron fabricated in nitrogen atmosphere is larger than that in hydrogen atmosphere, and for a loading in the pore

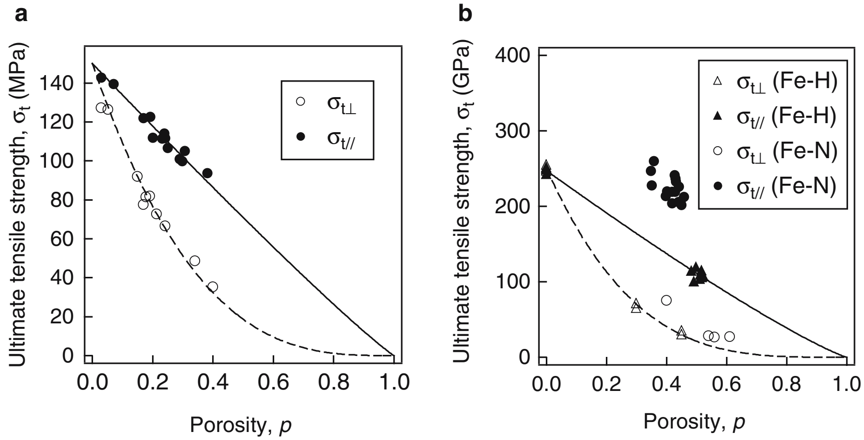

Fig. 3 Porosity dependence of the ultimate tensile strength of (**a**) lotus copper and (**b**) lotus iron fabricated in hydrogen (Fe–H) or nitrogen (Fe–H) atmosphere, where $\sigma_{t//}$ and $\sigma_{t\perp}$ represent the ultimate tensile strength along the directions parallel and perpendicular to the pore directions, respectively. Each line is obtained by fitting Eq. (1) to the measurements

direction the tensile strength of lotus iron fabricated in nitrogen atmosphere is almost consistent with the tensile strength of nonporous iron, which are caused by the solid solution hardening of solute nitrogen.

4 Fatigue Strength

Constant stress amplitude fatigue tests were carried out on lotus copper with a servo-valve-controlled electro-hydraulic testing machine (V-1912, Saginomiya Corp.) in air at room temperature. Cyclic tension-compression stress of $R = -1$ was applied to nonporous and lotus copper specimens, where R is the ratio of the minimum stress to the maximum stress. The frequency of cyclic stress was 5 Hz.

Figure 4 shows the log plots of σ_a against the number of cycles to failure N_f for nonporous and lotus copper, where cyclic stress was applied in the direction (a) parallel and (b) perpendicular to the pore direction [20]. The lines denote fittings of the following function to the experimental data:

$$\log \sigma_a = C \log N_f + D \tag{2}$$

where C and D are fitting coefficients. For both the directions, the numbers of cycles to failure of lotus copper and nonporous copper decrease with increasing stress amplitude. The fatigue strength at finite life decreases in both the directions with increasing porosity. Nonporous copper does not show anisotropy in the fatigue strength at finite life. On the other hand, the fatigue strength at finite life of lotus

Fig. 4 Log plots of stress amplitude σ_a against the number of cycles to failure N_f for lotus copper, where cyclic stress was applied in the direction (**a**) parallel and (**b**) perpendicular to the pore direction

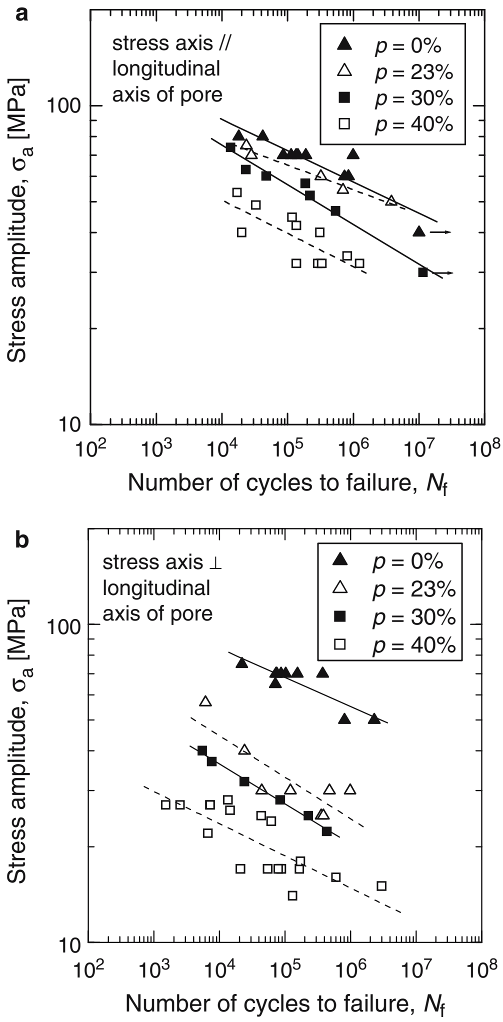

copper shows significant anisotropy; the fatigue strength in the perpendicular direction is lower than that in the parallel direction.

Figure 5 shows the fatigue strength at $N_f = 10^5$ of nonporous and lotus copper as a function of porosity. The lines denote the fittings of Eq. (1) to the experimental data. The porosity dependence of the fatigue strength is similar to those of the elastic constants and ultimate tensile strength, and it obeys the power-law equation of Eq. (1) (the m values are shown in Table 1).

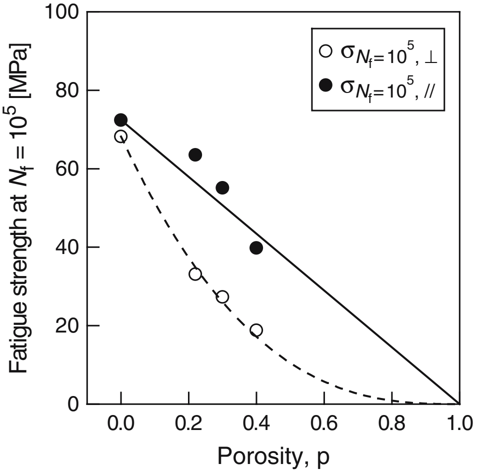

Fig. 5 Fatigue strength at $N_f = 10^5$ of nonporous and lotus copper as a function of porosity p, where stress was applied in the directions parallel and perpendicular to the pore direction; $\sigma_{N_f=10^5,//}$ and $\sigma_{N_f=10^5,\perp}$ are the fatigue strength in the directions parallel and perpendicular to the pore direction, respectively. The lines denote the fittings of Eq. (1) to the experimental data

5 Conclusion

The mechanical properties (elastic constants, ultimate tensile strength, compressive yield stress, and fatigue strength) of lotus metals were studied and the effect of the anisotropic pores on the mechanical properties was clarified. The mechanical strength in the direction parallel to the pore direction linearly decreases with increasing porosity, while that in the perpendicular to the pore direction drastically decreases, which is caused by the anisotropy of stress concentration. The porosity dependence of the mechanical strength obeys a power-law formula. Thus, the power-law formula is useful to predict the mechanical strength of lotus metals.

References

1. J. Gibson and M.F. Ashby, Cellular Solids (2nd ed.), Cambridge University Press, Cambridge (1997).
2. J. Banhart, *Prog Mater Sci* **46** (2001), 559.
3. H. Nakajima, S.K. Hyun, K. Ohashi, K. Ota and K. Murakami, *Colloid Surf A* **179** (2001), 20.
4. H. Nakajima, *Prog Mater Sci* **52** (2007), 1091.
5. H. Nakajima and T. Ide, *Metall Mater Trans* **39A** (2008), 390.
6. S.K. Hyun, K. Murakami and H. Nakajima, *Mater Sci Eng A* **299** (2001), 24. x
7. X. Badiche, S. Forest, T. Guibert, Y. Bienvenu, J.-D. Bartout, P. Ienny, M. Croset and H. Bernet, *Mater Sci Eng* **A289** (2000), 276
8. T. Imwinkelried, *J Biomed Mater Res* **81A** (2007), 964.
9. M. Tane, T. Ichitsubo, H. Nakajima, S.K. Hyun and M. Hirao, *Acta Mater* **52** (2004), 5195.
10. T. Ichitsubo, M. Tane, H. Ogi, M. Hirao, T. Ikeda and H. Nakajima, *Acta Mater* **50** (2002), 4105.
11. M. Tane, T. Ichitsubo, M. Hirao, T. Ikeda and H. Nakajima, *J Appl Phys* **96** (2004), 3696.
12. I. Ohno, *J Phys Earth* **24** (1976), 355.

13. H. Ogi, H. Ledbetter, S. Kim and M. Hirao, *J Acoust Soc Am* **106** (1996), 660.
14. E. Mochizuki, *J Phys Earth* **35** (1987), 159.
15. G. Simmons and H. Wang, Single Crystal Elastic Constants and Calculated Aggregate Properties: A Handbook (2nd ed.), MIT Press, Cambridge (1971).
16. K.K. Phani, *Am Ceram Soc Bull* **65** (1986), 158.
17. J. Kovácik, *Acta Mater* 46 (1998), 5413.
18. J. Kovácik and F. Simancik, *Scr Mater* **39** (1998), 239.
19. S.K. Hyun and H. Nakajima, *Mater Trans* **43** (2002), 526.
20. H. Seki, M. Tane, M. Otsuka and H. Nakajima, *J Mater Res* **22**, (2007), 1331.

Mechanical Behavior of Nickel Base Foams for Diesel Particle Filter Applications

M. Duchamp, J.D. Bartout, S. Forest, Y. Bienvenu, G. Walther, S. Saberi, and A. Boehm

Abstract An original processing route by powder metallurgy was developped to alloy pure Ni foams so, that the foam becomes refractory for high temperature applications. The modelling of such a foam at high temperature starts from the behavior of the basic constitutive material, then we use micromechanical models to predict the mechanical properties under tension and in compression creep. A 3D finite element analysis of a volume analysed by X-ray tomography is performed to study the foam deformation mechanisms in both conditions.

1 Introduction

Open-cell Ni foams are mainly used as battery electrodes. The very large specific surface of the INCOFOAM® pure Ni foams also leads to outstanding filtration properties [1, 2]. A Diesel Particulate Filter (DPF) application requires the alloying of the INCOFOAM® material to improve the oxidation resistance and to provide thermal stability. For that purpose, a foam alloying route using powder metallurgy was developed by INCO and IFAM (patent number: DE 103 01 175.7). The alloyed foams designed for the DPF application are named INCOFOAM®HighTemp. The typical alloy composition of the foams studied in this work is that of Inconel 625. A short

---

M. Duchamp, J.D. Bartout, S. Forest (✉), and Y. Bienvenu
Centre des Matériaux, Mines Paris, Paristech, CNRS UMR 7633, BP 87, 91003 Evry Cedex, France
samuel.forest@ensmp.fr

G. Walther
Fraunhofer-Institut, IFAM, Dresden, Germany

S. Saberi
Inco SP, Mississauga, Canada

A. Boehm
Inco GmbH, Munich, Germany

H. Zhao, N.A. Fleck (eds.), *Mechanical Properties of Cellular Materials,*
IUTAM Bookseries 12,

review of the alloying techniques is given in [13, 14]. Inconel 625 foams were recently synthesized by powder metallurgy in [10, 11] and by vapor deposition in [9].

The objective of the work is to provide tools for the design of DPF considering critical aspects of the life-time of a real filter, from its manufacturing to the in service conditions. The manufacturing of complex filter shapes can induce damage in the foam that could affect the durability of the filter component. Creep in the filter is likely to start during high temperature regeneration regime.

A predictive model for tensile properties for both Ni and alloyed foams is presented. It assumes that the bending of the struts is the main deformation mechanism in the foam [7]. A simplified morphology is deduced from 3D reconstruction of microtomography of Ni foams [3], 2D image analysis and electrical resistivity measurements. Creep of alloyed foams is also investigated in this work. Two creep mechanisms are evidenced from the experimental point of view and we confronted an existing model [14] to a large experimental data set of alloyed foams creep measurements. The proposed model describes better high temperature (above 800°C) creep than low temperature creep. A 3D investigation of microtomographic foam images with the Finite Elements Method is finally used in order to assess the assumptions of the models presented before.

2 Materials and Experimental Techniques

2.1 Materials

The Ni base alloyed foams are obtained by a powder metallurgy alloying route using pure Ni foams INCOFOAM® as a template. The materials considered in this work are given in Table 1. The INCOFOAM® are produced as foam plates and we distinguish a coiling direction RD, a transverse direction TD and the normal direction ND. The process is divided into three steps: binding, coating and finally sintering. The amount and the composition of the powder sintered on the foam is set to reach the theoretical composition of Inconel 625. SEM pictures of both a pure Ni foam INCOFOAM® and an alloyed foam INCOFOAM®HighTemp having the same initial morphology are presented in Fig. 1. The porous Ni foam structure is not affected by alloying. In both cases, the hollow struts can be seen. We define the volume fraction Φ of a foam as the ratio between the solid volume and the total volume of the foam. We also define the mechanical volume fraction of a foam Φ_{mech} which is the volume fraction of the foam that really contributes to the mechanical properties of the foam. For pure Ni foams, we consider that $\Phi_{mech} = \Phi_{Ni}$ whereas for alloyed foams, we can see on Fig. 1 that a reduced part of the sintered particles mass really contributes to the mechanical properties of the foam. For the alloyed foams, we deduce $\Phi_{Ni} \leq \Phi_{mech} \leq \Phi_{Alloyed}$. This point will be discussed further in this work.

We also applied the alloying procedure by powder metallurgy to 10 μm thick pure Ni foils to study the influence of the alloying process on the constitutive material of the foam. A cross section SEM picture of the alloyed foil is given in Fig. 2.

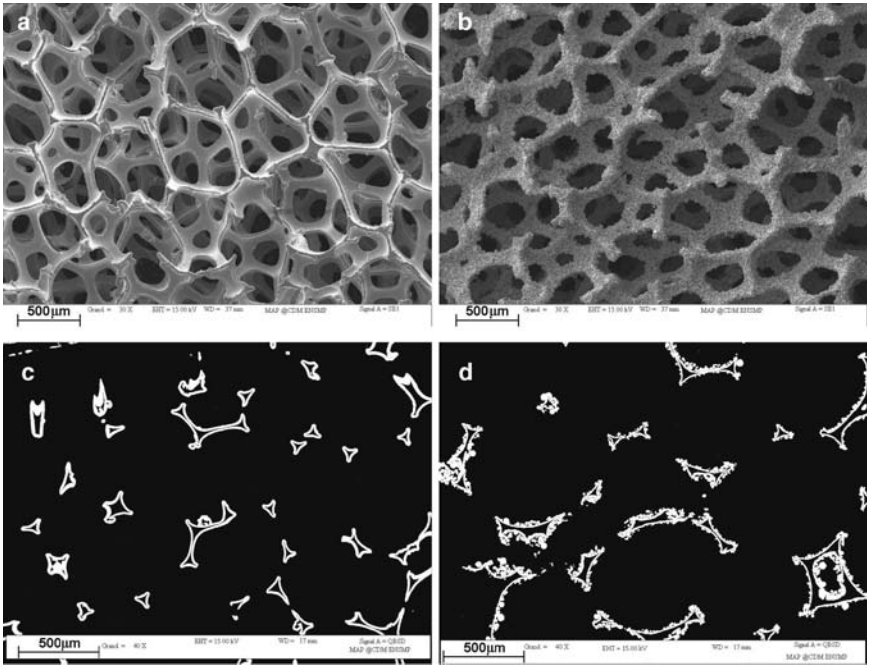

Fig. 1 SEM pictures of (**a**) initial Ni foam (**b**) alloyed foam (**c**) initial Ni foam cross section (**d**) alloyed foam cross section

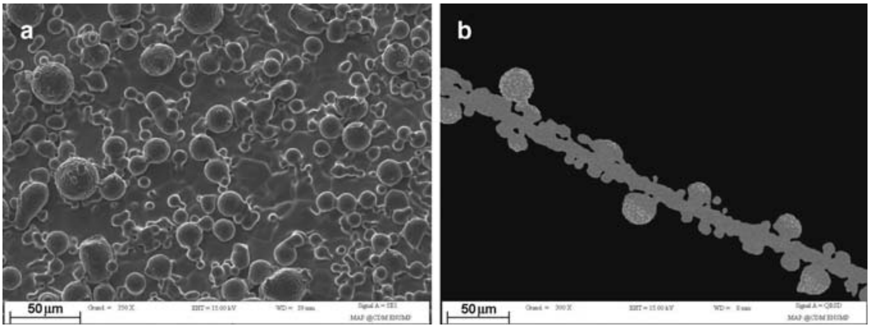

Fig. 2 Alloyed Ni foil with powder metallurgy. SEM picture of (**a**) the foil surface (**b**) the foil cross section

Microtomography analyses [3, 4] on Ni foams have shown that the cell volume distribution is monomodal and centered on 0.025 mm^3. The corresponding cell diameter is equal to 390 µm. The cells are not spherical but elongated ellipsoids. Their main axes called $a < b < c$ have also a monomodal distribution centered on $a = 316\,\mu\text{m}$, $b = 399\,\mu\text{m}$ and $c = 479\,\mu\text{m}$. The ratios of the equivalent axes $R = b/a$ and $Q = c/a$ represent the morphological anisotropy of the foam. We have: R=1.27 and $Q = 1.52$. These axes have a preferential orientation in the space linked to the manufacturing process: a-axes are mainly oriented in the TD direction, b and *c*-axes are tilted in the ND-RD plane (see Fig. 6). The strut length distribution is monomodal centered on 149 µm.

2.2 Experimental Techniques

Tensile tests were carried out on all foam types presented in Table 1. Dogbone tensile samples were cut out of the foam strips. They were tested in a conventional tensile testing machine at room temperature. Load was measured with a 500 N load cell and elongation was measured with a light resistive extensometer (gauge length 100 mm). Tensile tests were carried out on the foils presented in Table 1.

Table 1 Materials used for this study. CVD is used for Chemical Vapor Deposition and EP for ElectroPlating

Ni foams INCOFOAM®

Label Φ (%)	Electrical anisotropy	Measured cell diameter a (µm)	Cell size (µm)	Thickness (mm)	Manufact. process
C450 3.2	1.66	288	450	1.5	CVD
C450 2.6	1.27	N/C	450	1.6	CVD
C450 13	1.64	316	450	1.5	CVD
D580 2.5	1.36	382	580	1.9	EP
D580 2.1	1.44	N/C	580	1.9	EP
D800 2.1	1.39	466	800	2.5	EP
D800 1.6	1.46	N/C	800	2.5	EP
D1200 1.9	1.36	788	1,200	3.0	EP
D1200 1.3	1.18	N/C	1,200	3.0	EP

Alloyed foams INCOFOAM®hightemp

Label Φ (%)	Electrical anisotropy	a (µm)	Thickness (mm)	Ni base foam
A763 8.4	1.65	285	1.5	C450 3.2
A808 7.6	1.08	295	1.6	C450 2.6
A782 6.8	1.34	422	2.0	D580 2.5
A809 5.5	1.25	353	2.0	D580 2.1
A790 4.9	1.34	650	2.5	D800 2.1
A810 3.8	1.54	522	2.5	D800 1.6
A793 4.7	1.28	803	3.1	D1200 1.9
A811 2.8	1.34	724	3.1	D1200 1.3

Foils

Label	Constitutive material	Foil thickness (µm)
FCommercial	Commercial Inconel 625	25
FAlloyed	IN625	10

Monotonic compression and creep compression tests were also carried out on the alloyed foams. Discs (diameter 20 mm) were cut out of the foam strip with a turning lathe and tested at high temperature in a radiative furnace. The applied creep stress levels are set close to the plateau stress of the compressive stress–strain curves of the foams.

Resistivity measurements were performed on foam samples (20 × 3 cm) cut in RD and TD with a modified four wire technique. The electrical anisotropy is the ratio of resistivity in the TD and the RD directions. It was applied on both Ni foams and alloyed foams. This measure gives a good approximation of foam anisotropy [6]. The ratio of measured resistivity along directions TD, Ω_{TD} and RD, Ω_{RD} give the anisotropy ratio assuming the model of Fig. 6. This ratio is called electrical anisotropy in Table 1.

$$\frac{\Omega_{TD}}{\Omega_{RD}} = \frac{c}{a} = Q \tag{1}$$

The measured electrical anisotropy values lye between 1.18 and 1.66.

3 Experimental Results

3.1 Tensile Tests

Tensile tests were performed at room temperature on pure Ni foams and alloyed foams. Some tensile curves are given in Figs. 3 and 4. As already observed in [6], foams have a strongly anisotropic behavior. The stress levels along RD are about twice the stress level along TD. Another effect is the stiffening of the foam due to the alloying process. The stress level is about five times higher for the alloyed foam. We observe a certain embrittlement due to the alloying process. The ductility of the foams is divided by a factor two.

Tensile tests were also performed on the foils presented in Table 1. The commercial foil FCommercial exhibits a stress peak typical for superalloy tensile curves whereas the alloyed foil FAlloyed exhibits a smoother behavior. This can be due to the wrinkling of the foil surface caused by capillarity forces during the high temperature sintering process. The foil FAlloyed, obtained by powder metallurgy technique, is less ductile. The ultimate strain at fracture is five times lower than that of the commercial foil FCommercial. We identified an elastoplastic constitutive model with the von Mises criterion f and a linear hardening coefficient H described by the Eqs. (2, 3). The calibrated parameters can be found in 2 as well as the parameters for 10 µm thick pure Ni foils found in [5].

$$\varepsilon = \varepsilon^e + \varepsilon^p, \quad f(\sigma) = \sqrt{\frac{3}{2}\sigma^{dev} : \sigma^{dev}} - \sigma_y \tag{2}$$

$$\sigma_y = \sigma_0 + Hp, \quad \dot{\varepsilon^p} = \dot{p}\frac{\partial f}{\partial \sigma} \tag{3}$$

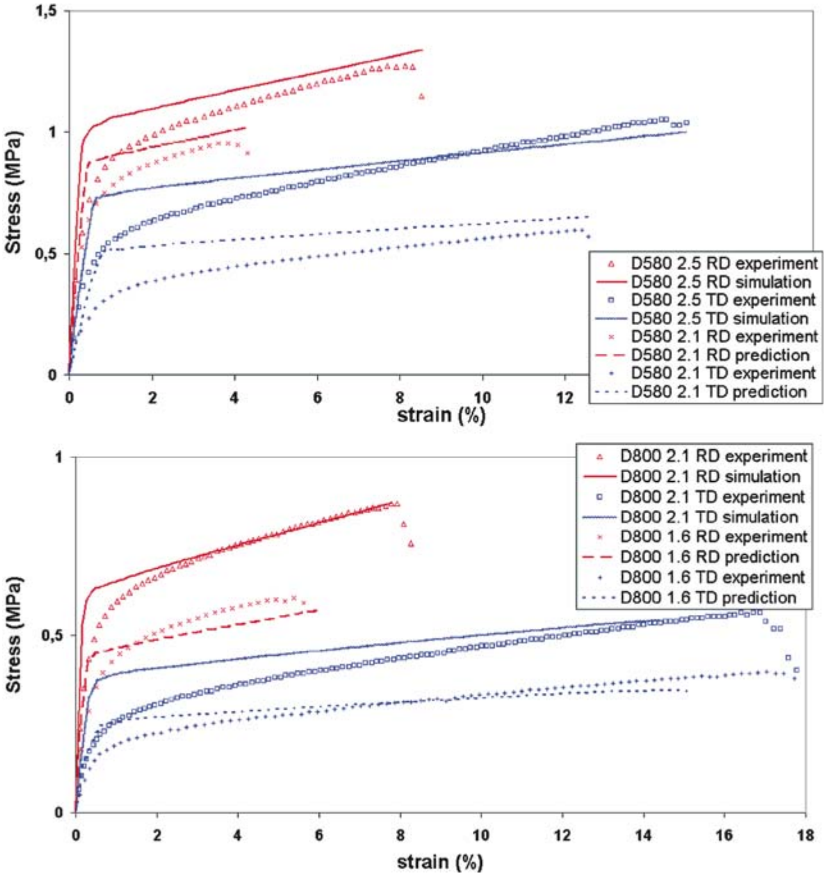

Fig. 3 Experimental, simulated and predicted tensile tests of foam strips cut in the RD and the TD of *(top)* D580 2.5 and D580 2.1 *(bottom)* D800 2.1 and D800 1.6

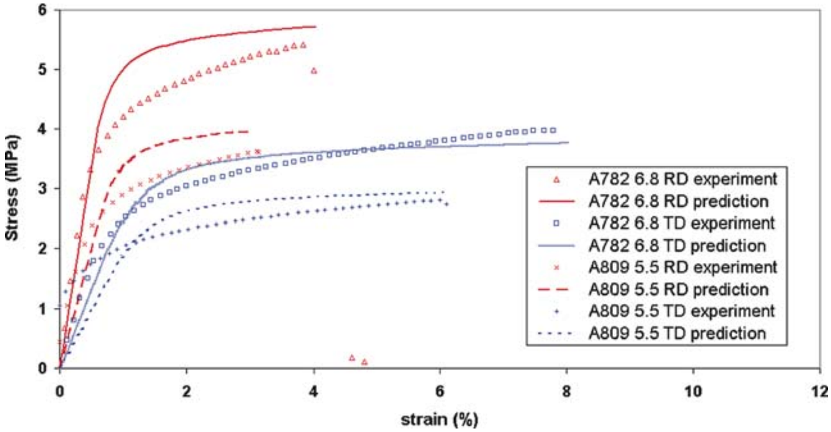

Fig. 4 Experimental and predicted tensile tests of foam strips cut in the RD and the TD of A782 6.8 and A809 5.5

where σ^{dev} is the deviatoric part of the stress tensor and p the equivalent plastic deformation.

3.2 Creep Tests

Creep tests were performed on alloyed foam disks. When a constant stress is applied, a steady-state strain rate occurs after a short transient. The steady-state strain rate of cellular materials can be related to the uniaxial stress by the power law:

$$\dot{\varepsilon}^* = A^* \sigma^{*n^*} \tag{4}$$

where the constant A^* depends on the temperature. This equation is the analogous to the power law equation for bulk materials (with the macroscopic constants A^* and n^*) like in equation 9. We tested the alloyed foams at 500°C, 600°C, 700°C, and 800°C and we plotted the stress and the strain rate values in Fig. 5. A transition in

Table 2 Identified material data of the linear hardening law (Eqs. 2, 3) for foils FCommercial, FAlloyed and a 10 µm pure Ni foil [5]

	Young's modulus E (GPa)	Yield stress σ_0 (MPa)	Hardening modulus H (MPa)
FCommercial	200	478	5,800
FAlloyed	200	373	2,080
Pure Ni foil [5]	204	70	1,800

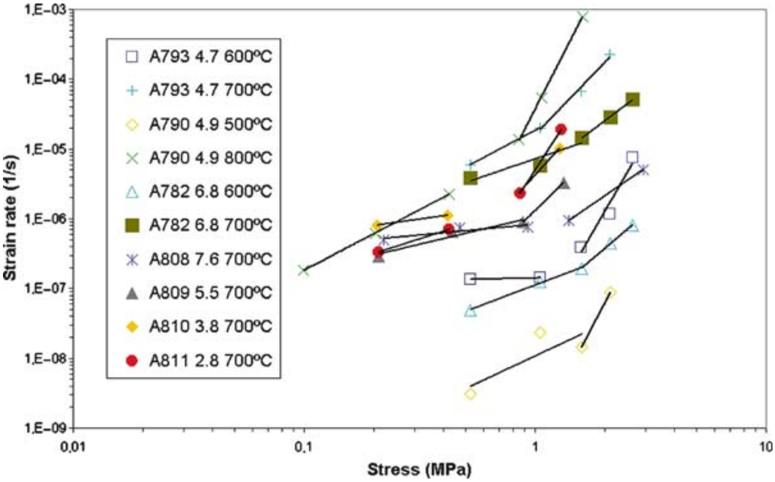

Fig. 5 Log–log diagram for different INCOFOAM®HighTemp types tested at different temperatures

Table 3 Power-law equation parameters for different kinds of INCOFOAM®HighTemp

		Low stress		High stress	
Alloyed foams	Temperature (°C)	n^* (–)	A^* (MPa$^{-n^*}$ s^{-1})	n^* (–)	A^* (MPa$^{-n^*}$ s^{-1})
A793 4.7	600	7.6×10^{-2}	1.4×10^{-7}	5.7	2.3×10^{-8}
	700	1.7	1.9×10^{-5}	3.4	1.6×10^{-5}
A790 4.9	500	1.5	1.1×10^{-8}	6.6	7.6×10^{-10}
	800	1.7	9.8×10^{-6}	6.4	3.7×10^{-5}
A782 6.8	600	1.2	1.1×10^{-7}	2.8	5.3×10^{-8}
	700	1.1	7.2×10^{-6}	2.5	4.5×10^{-6}
A808 7.6	700	3.1×10^{-1}	8.3×10^{-7}	2.3	4.4×10^{-7}
A809 5.5	700	7.8×10^{-1}	1.1×10^{-6}	3.3	1.3×10^{-6}
A810 3.8	700	4.6×10^{-1}	1.7×10^{-6}	3.6	4.2×10^{-6}
A811 2.8	700	1.0	1.7×10^{-6}	5.1	5.0×10^{-6}

the n^* creep stress exponent is observed for stress values in the order of 0.5 MPa at temperatures above 700°C and stress values in the order of 1 MPa at temperature below 700°C . We identified the constants A^* and n^* (see Table 3) for low stresses and high stresses. The low stress regime n mean value is equal to 1.0, high stress regime n mean value is equal to 4.2.

4 Modeling of the Foam Behavior

4.1 Tensile Elastoplastic Behavior of Foams

A simple mechanical model for pure Ni and of alloyed foams in tension at room temperature is presented. It incorporates the previous morphological parameters (parameters Φ, Q, R and the measured cell equivalent axis a).

The model is based on the assumption that the bending of the struts is the main deformation mechanism of the foam [7]. The idealized cell geometry of Fig. 6 is used to link the morphological parameters to the foam volume fraction Φ:

$$\Phi = \frac{4t^2\,(a+b+c)}{abc} = \frac{4t^2}{a^2}\,\frac{Q+R+1}{RQ} \tag{5}$$

where t the beams thickness. Subsequently, the anisotropy ratio R is taken equal to 1 for simplicity.

When the cell is deformed in the direction parallel to the RD, the beams parallel to TD and ND are bent. The bending of the nonlinear beams is computed with the Finite Element Method using 2D simulation under plane stress conditions. Prescribing the bending of a strut in the plane by applying an angle θ to the right edge, we

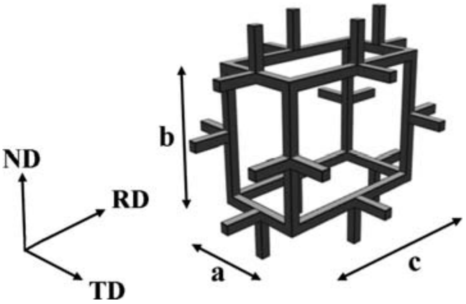

Fig. 6 Simplified foam cell elongated in the coiling direction

compute the deflection δ of the beam and we post-process the bending moment M in the beam at each step of the computation. When the foam is tested in the RD direction, then the beams of length a and b and of thickness t are bent. We impose that $\delta_a = \delta_b = \delta_{RD}$ and we compute both the bending moments in the a beam M_a and in the b beam M_b. When the foam is tested in the TD direction, we apply the same procedure to b and c beams.

Then, scale transition rules are introduced to link the deflection to the overall deformation of the foam, on the one hand, and between the bending moment moment on a single beam and the foam stress, on the other hand. Scale transition parameters B and C are introduced in Eqs. (6 and 7). They depend on the foam morphology. They are identified from the macroscopic stress-strain curves for a given morphology of Ni foams: $B = 0.4 \pm 0.1$ and $C = 95 \pm 25$. These values are valid for a wide range of Ni foams morphologies (450, 580, 800 and 1,200 µm cell size). The influence of the choice of the cross section of the beam can also be shown to affect the parameter B and C. For simplicity, a rectangular section is chosen. Subsequently, the constants B and C identified for a pure Ni foam morphology are kept unchanged to predict the behavior of lighter pure Ni foams and to predict the behavior of the corresponding alloyed foams.

$$\sigma^*_{RD} = \frac{C}{ab}\left(\frac{M_a}{a^2} + \frac{M_b}{b^2}\right), \quad \varepsilon^*_{RD} = B\frac{\delta_{RD}}{c} \tag{6}$$

$$\sigma^*_{TD} = \frac{C}{bc}\left(\frac{M_b}{b^2} + \frac{M_c}{c^2}\right), \quad \varepsilon^*_{TD} = B\frac{\delta_{TD}}{a} \tag{7}$$

In Fig. 3, the calibrated tensile curves are plotted with the experimental tensile curves for two different Ni foam morphologies D580 2.5 (b) D800 2.1 (solid lines), and for the lighter foams inherited from the same foam morphology (a) D580 2.1 (b) D800 1.6 (dash lines). The anisotropy changes slightly, the thickness t of the beams decreased and the parameter a was taken constant equal to 382 µm . We observe a good agreement between the model and the experiment for the stress levels. However, yield stresses are over-estimated. This is a consequence of the idealized elongated cell orientation along RD. If the cells had a distributed orientation in the RD-TD plane, the elastic–plastic transition domain would be smoother.

The alloying process of foams has two effects on the foams mechanical properties: the foam constitutive material strengthening and the increasing of the mechanical volume fraction. Our assumption is that the first phenomenon is the most important: $\Phi_{mech} = \Phi_{Ni}$. The behavior law of the FAlloyed (Section 3.1) representing the constitutive material is implemented in the model to predict the stress-strain curves of the alloyed foams A782 6.8 (based on the D580 2.5) and A809 5.5 (based on the D580 2.1). Parameter Q is set to the measured value but we kept unchanged the other morphological parameters. In particular, the scale transition parameters B and C are the parameters calibrated on the D580 2.5 Ni foam. In Fig. 4, the predicted and the experimental tensile curves are plotted. We observe a good agreement between experimental and predicted curves. The yield stress of foams is overestimated for the predictions in the RD and the elastic modulus is underestimated for tensile tests in the TD.

4.2 Creep of Alloyed Foams

The metallic foams placed in the exhaust line are mainly exposed to gas flow that creates forces on foam struts. The foams are loaded in compression and we expect them to deform especially at high temperature by creep deformation. The alloying of the pure Ni foams increases the creep resistance of the foams by solid solution strengthening mainly. The creep model given in [14] is used in this section. The alloyed foams were tested at temperatures in the $500-800°\mathrm{C}$ range for stresses in the $0.1-3\,\mathrm{MPa}$ range. Moreover, the volume fraction range is relatively large (if we consider $\Phi_{mech} = \Phi_{Ni}$: 1.3−3.2% or $\Phi_{mech} = \Phi_{Alloyed}$: 2.8−8.4%). Our large experimental data set enable an accurate validation of the creep model.

Two different approaches of foam creep modeling were developed in the literature. The approach in [14] accounts for a creep mechanism transition. The stress in the foam struts for a macroscopic stress σ^* is estimated as follows:

$$\sigma_{strut} \approx \frac{\sigma^*}{\Phi_{mech}} \tag{8}$$

In this section, we do not make assumptions on the value of Φ_{mech}. In Table 4, the range of the volume fraction and the range of applied stress in the struts during creep tests are computed for each alloyed foam.

In Fig. 7, the tested temperature-stress domain and the DPF application domain are localized to identify the creep deformation mechanism that occurs during the creep tests. At high stresses and high temperature, power-law creep occurs in the struts and at low stresses and low temperature, diffusional creep occurs in the struts. The creep tests were carried out in the transition between power-law creep domain and diffusional creep domain. This explains the slope transition in the log–log diagram 5. The total foam creep rate is assumed to be the sum of two contributions. The power-law creep rate equation for bulk material is given by:

$$\dot{\varepsilon} = K\sigma^n \exp\left(\frac{-Q}{RT}\right) \tag{9}$$

Table 4 Ranges of estimated applied stress in the struts during creep tests and in service conditions of alloyed foams

Alloyed foam label	Φ_{mech} range	Creep tests σ_{strut} (MPa)	Creep tests σ_{strut} (MPa)	DPF application σ_{strut} (MPa)
		$\sigma^* = 2.5$ MPa	$\sigma^* = 0.1$ MPa	$\sigma^* = 0.01$ MPa
A763 8.4	$3.2-8.4$	$30-78$	$1-3$	$0.1-0.3$
A782 6.8	$2.5-6.8$	$37-100$	$1-4$	$0.1-0.4$
A790 4.9	$2.1-4.9$	$51-119$	$2-5$	$0.2-0.5$
A793 4.7	$1.9-4.7$	$53-131$	$2-5$	$0.2-0.5$
A808 7.6	$2.6-7.6$	$33-96$	$1-4$	$0.1-0.4$
A809 5.5	$2.1-5.5$	$45-113$	$2-5$	$0.2-0.5$
A810 3.8	$1.6-3.8$	$66-156$	$3-6$	$0.3-0.6$
A811 2.8	$1.3-2.8$	$89-192$	$4-8$	$0.4-0.8$

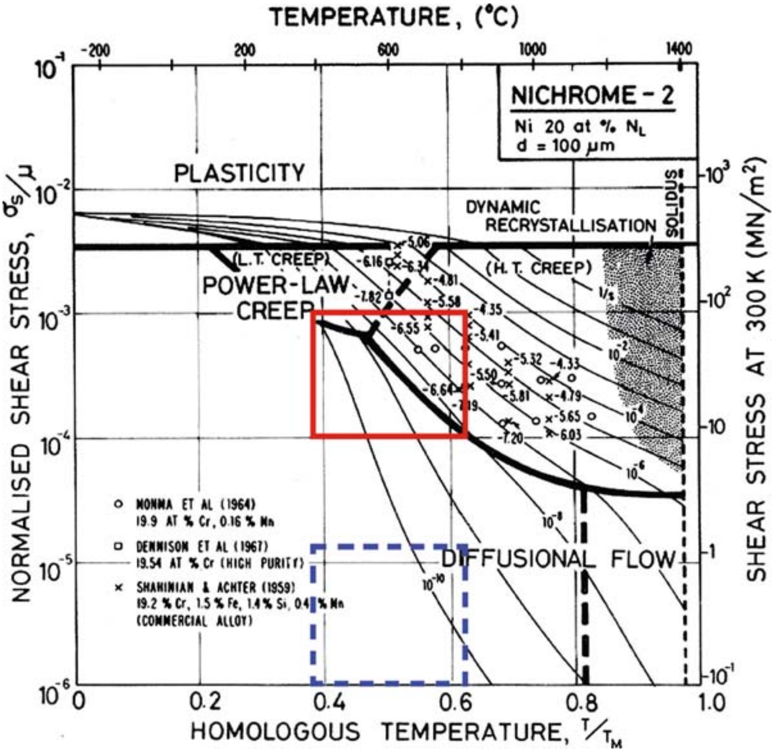

Fig. 7 Tested domain (black square) and DPF application domain (dashed square) in the deformation mechanism map of a typical Ni-20%Cr alloy [8]

where K is the Dorn constant, n is the stress exponent, Q is the activation energy, R is the gas constant and T is the temperature in Kelvin. The diffusional creep rate equation for bulk material is:

$$\dot{\varepsilon} = \frac{14\sigma\Omega}{\kappa T d^2} D_{eff}, \quad \text{with} \quad D_{eff} = D_V \left[1 + \frac{\pi}{d}\frac{\delta D_b}{D_V}\right] \tag{10}$$

where Ω is the atomic volume, κ the Boltzmann constant, d the grain size, and D_{eff} is the effective diffusion coefficient. D_V is the diffusion coefficient for lattice diffusion of Ni, and δD_b the diffusion constant for boundary diffusion. The values of all the parameters are given in [8] for the typical Ni-20%Cr alloy and are used for models computation of creep of the alloyed foams. Considering the "bamboo structure" of the Ni foams exhibited in [5], we take the grain size d equal to 10 µm that is to say the typical thickness of the walls of the struts.

In the first model, the deformation mechanism of the foam is assumed to be the bending of the struts [7]. We directly use the equations introduced in [14]. Thus, the total foam creep model equation can be written:

$$\dot{\varepsilon}^{b*} = K\frac{0.6}{(n+2)}\left(\frac{1.7(2n+1)}{n}\right)^n \Phi_{mech}^{-(3n+1)/2} \sigma^{*n} \exp\left(\frac{-Q}{RT}\right) + \frac{14.3\Omega}{\kappa T d^2}\sigma^* \Phi_{mech}^{-2} D_{eff} \tag{11}$$

The second model was developed in [12] and assumes that the foam deformation mechanism is the pure strut compression of beams oriented in the same direction as the loading direction. The total foam creep is in this model:

$$\dot{\varepsilon}^{c*} = K\left(\frac{\Phi_{mech}}{3}\right)^{-n} \sigma^{*n} \exp\left(\frac{-Q}{RT}\right) + \frac{14\Omega}{\kappa T d^2}\sigma^* \left(\frac{\Phi_{mech}}{3}\right)^{-1} D_{eff} \tag{12}$$

Experimental creep data measured at 500°C, 600°C, 700°C, and 800°C are compared with both bending and compression model in Figs. 8 and 9. The values that we used are proposed in [8]: $n = 4.6$, $Q = 285$ kJ/mol, and $K = 3.8$ MPa$^{-4.6}$ s^{-1}. The effect of "mechanical" volume fraction was also plotted, solid lines representing the real volume fraction model, the dash lines representing the initial Ni foam volume fraction. As observed in [16–18], the compression model is in better agreement with the experimental data than the bending model that overpredicts by about two orders of magnitude the experimental data. We reach a good agreement at high temperature considering that $\Phi_{mech} = \Phi_{Ni}$. This model overpredicts the experimental data at temperature below 600°C by about two orders of magnitude. These results remain true for the other data that are not presented here.

4.3 Finite Element Modelling of Real Foam Microstructures

The increasing computing capacity enables us to perform more realistic simulations taking the actual shape of the cells into account. We used the finite element method

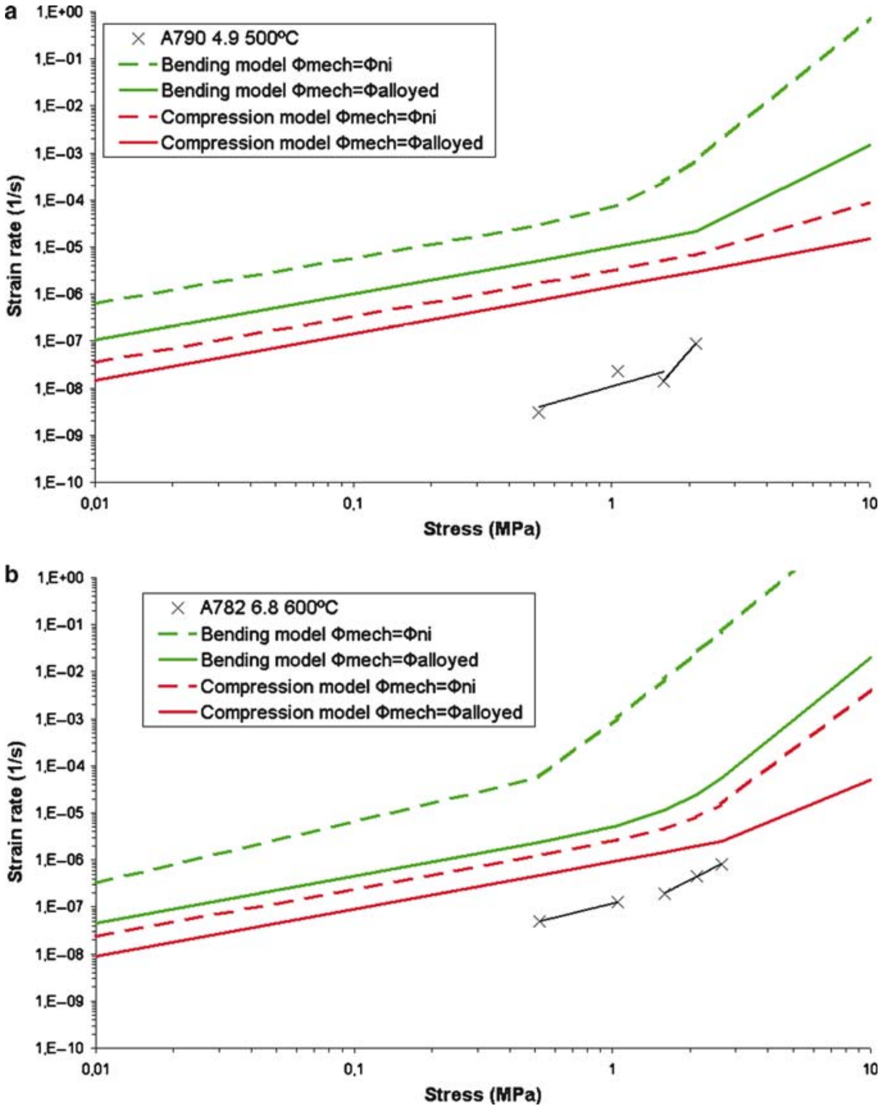

Fig. 8 Comparison between experimental creep data and both the bending model and the compression model based on power-law creep (high stresses) and diffusional creep (low stresses) of the struts of the (**a**) A790 4.9 at 500°C (**b**) A782 6.8 at 600°C. The influence of mechanical volume fraction is plotted: solid lines represent the maximal volume fraction $\Phi_{mech} = \Phi_{Alloyed}$ (all the added mass on the foam during the sintering process contributes to mechanical properties) and dash lines represent the minimal volume fraction $\Phi_{mech} = \Phi_{Ni}$ (the alloying of the foam only modifies the initial strut material)

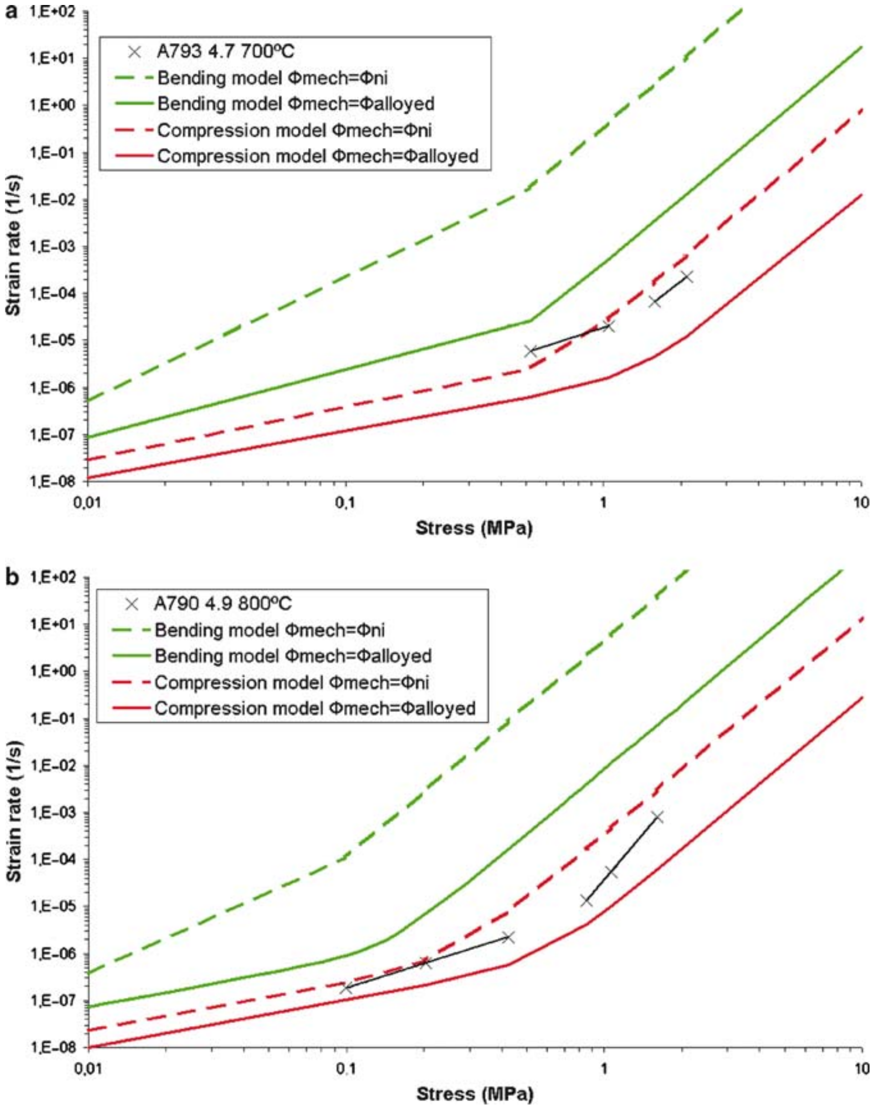

Fig. 9 Comparison between experimental creep data and both the bending model and the compression model based on power-law creep (high stresses) and diffusional creep (low stresses) of the struts of the (**a**) A793 4.7 at 700°C (**b**) A790 4.9 at 800°C . The influence of mechanical volume fraction is plotted: solid lines represent the maximal volume fraction $\Phi_{mech} = \Phi_{Alloyed}$ (all the added mass on the foam during the sintering process contributes to mechanical properties) and dash lines represent the minimal volume fraction $\Phi_{mech} = \Phi_{Ni}$ (the alloying of the foam only modifies the initial strut material)

on the microtomographic volume analyzed in [3] (a $200 \times 200 \times 99$ voxel) to identify the deformation mechanisms of the foam during monotonic tensile tests.

The Amira$^{\text{TM}}$ software is used to generate a mesh from the raw binary figures cropped to a $800 \times 800 \times 800\,\mu\text{m}^3$ volume. The considered volume contains about four cells. The foam surface is first triangulated with the help of the marching cube algorithm and the number of triangles is set to a reasonable number. Then, a volume mesher generates a tetrahedral mesh using the advancing front method. The obtained mesh has 77,000 elements. The measured volume fraction was 19% whereas the real volumic fraction is only 13%. This procedure provides meshes with a very good quality that can be directly implemented in the ZeBuLon$^{\text{TM}}$ finite element code. We used second order tetrahedral elements [15]. The behavior law of Ni is the elastic–plastic law with linear hardening identified in Section 4.1. Node sets are created on the opposite faces of the cube volume element in direction TD. One of the node set displacement is prescribed to zero and the other is set to ten pixel in the TD.

The computation was performed with a single PC (2 GHz CPU frequency and 4 Gb memory) within 13 h. In Fig. 10, the plastic deformation map is presented. Plastic deformation initiate mainly at the nodes. The local plastic deformation is much higher than the overall foam deformation. At higher deformation levels, the

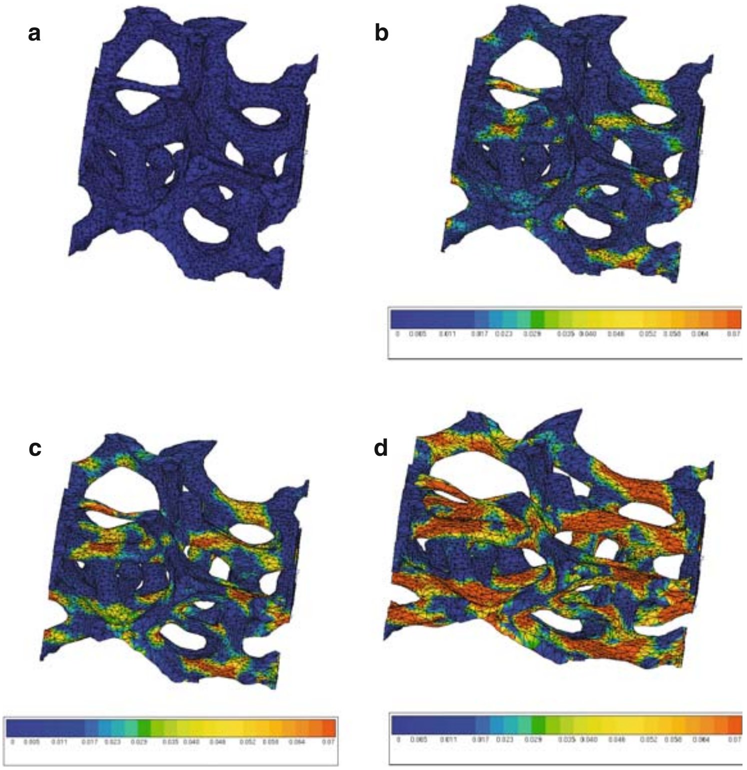

Fig. 10 Plastic deformation during a simulated tensile test of a foam cube with dimensions $800^3\,\mu\text{m}^3$. Deformation is magnified by a factor 20

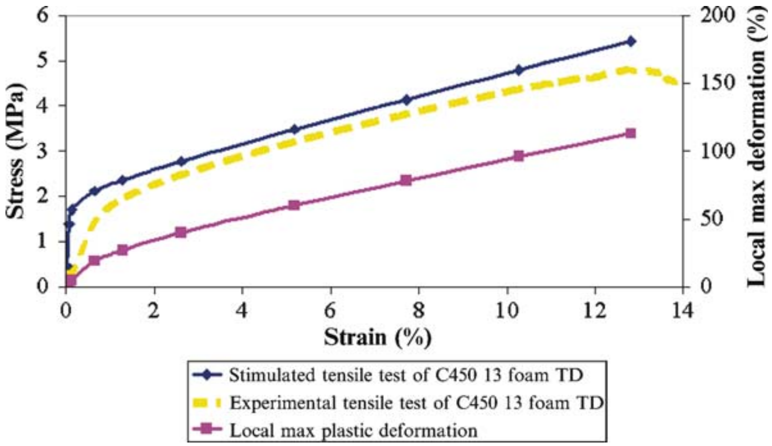

Fig. 11 Experimental and FEM simulated tensile tests of the C450 13 Ni foam at room temperature

plastic deformation is located in the struts the direction of which is parallel to the loading direction. These struts are loaded in tension. The other struts undergo very low deformation. We post-processed the computation to get a macroscopic stress–strain. In Fig. 11, we plot the maximum local plastic deformation and the average stress in direction RD vs. the macroscopic strain. The simulated elastic modulus is too high in comparison to the experiment, but the plastic slopes are in very good agreement. We report a factor 10 between the local maximum plastic deformation and the global foam deformation. This means that there is practically no pure elastic regime in a foam tensile test.

One possible reason for the discrepancy between the computed and experimental elastic stiffness may be the size of the volume element considered which is probably far from the representative volume element size of the material, at least for elastic properties. The elastic bending of some particular struts is found to be the first mechanism that occurs in the foam, assumed in the simple model of Section 4.1.

References

1. V. Paserin, S. Marcuson, J. Shu, D.S. Wilkinson: *CVD Technique for Inco Nickel Foam Production*, Advanced Engineering Materials 6 No. 6 (2004).
2. J. Banhart: *Manufacture, characterisation and application of cellular metals and metal foams*, Progress in Materials Science 46 (2001) 559–632.
3. T. Dillard, F.N'Guyen, E. Maire, L. Salvo, S. Forest, Y. Bienvenu, J.D Bartout, M. Croset, R. Dendievel, P. Cloetens: *3D quantitative image analysis of open-cell nickel foams under tension and compression loading using X-ray microtomography*, Philosophical Magazine 85 No. 19 (July 2005), 2147–2175.
4. A. Benouali, L. Froyen, T. Dillard, S. Forest, F. NGuyen: *Investigation on the influence of cell shape anisotropy on the mechanical performance of closed cell aluminium foams using micro–computed tomography*, Journal of Materials Science 40 (2005) 5801–5811.

5. V. Goussery, Y. Bienvenu, S. Forest, A.F. Gourgues, C. Colin, J.D. Bartout: *Grain Size Effects on the Mechanical Behavior of Open-cell Nickel Foams*, Advanced Engineering Materials 6 No. 6 (2004).
6. X. Badiche, S. Forest, T. Guibert, Y. Bienvenu, J.D. Bartout, P. Ienny, M. Croset, H. Bernet: *Mechanical properties and non-homogeneous deformation of open-cell nickel foams: application of the mechanics of cellular solids and of porous materials*, Materials Science and Engineering A 289 (2000) 276–288.
7. L.J. Gibson, M.F. Ashby: *Cellular solids. Structure and properties - Second edition*, Cambridge University Press, Cambridge (1997).
8. H.J. Frost, M.F Ashby: *Deformation-Mechanism Maps: the Plasticity and Creep of Metals and Ceramics*, Pergamon Press, New York (1982).
9. D.T. Queheillalt, D.D. Hass, D.J. Sypeck, H.N.G Wadley: *Synthesis of open-cell metal foams by templated directed vapor deposition*, Journal of Materials Research, 16 No. 4 (2001).
10. P. Quadbeck, J. Kaschta, R.F. Singer: *Superalloy IN625 with Cellular Microstructure - Fabrication Route and Mechanical Properties*, Advanced Engineering Materials 6 No. 8 (2004).
11. D.T. Queheillalt, Y. Katsumura, H.N.G Wadley: *Synthesis of stochastic open cell Ni-based foams*, Scripta Materialia, 50 (2004) 313–317.
12. A. Hodge, D. Dunand: *Measurement and Modelling of Creep in Open-Cell NiAl Foams*, Metallurgical and Materials Transactions 34A (2003) 2353–2362.
13. H. Choe, D. Dunand: *Synthesis, structure, and mechanical properties of Ni-Al and Ni-Cr-Al superalloy foams*, Acta Materialia 52 (2004) 1283–1295.
14. H. Choe, D. Dunand: *Mechanical properties of oxidation-resistant Ni-Cr foams*, Materials Science and Engineering A 384 (2004) 184–193.
15. S. Youssef, E. Maire, R. Gaertner: *Finite element modelling of the actual structure of cellular materials determined by X-ray tomography*, Acta Materialia 53 (2005) 719–730.

Anisotropy in Buckling Behavior of Kelvin Open-Cell Foams Subject to Uniaxial Compression

D. Okumura, A. Okada, and N. Ohno

Abstract This paper describes buckling modes and stresses of elastic Kelvin open-cell foams subjected to [001], [011] and [111] uniaxial compressions. Cubic unit cells and cell aggregates in model foams are analyzed using a homogenization theory of the updated Lagrangian type. The analysis is performed on the assumption that the struts in foams have a non-uniform distribution of cross-sectional areas as observed experimentally. The relative density is changed to range from 0.005 to 0.05. It is thus found that long wavelength buckling and macroscopic instability primarily occur under [001] and [011] compressions, with only short wavelength buckling under [111] compression. The primary buckling stresses under the three compressions are fairly close to one another and almost satisfy the Gibson-Ashby relation established to fit experiments. By also performing the analysis based on the uniformity of strut cross-sectional areas, it is shown that the non-uniformity of cross-sectional areas is an important factor for the buckling behavior of open-cell foams.

1 Introduction

Gibson and Ashby (1982) estimated the buckling collapse strength Σ_c of elastic foams under compression by applying the Euler buckling theory to a cell model consisting of orthogonal struts. They thus analytically derived

$$\Sigma_c = CE_s(\rho_0/\rho_s)^2, \tag{1}$$

D. Okumura and N. Ohno (✉)
Department of Mechanical Science and Engineering, Nagoya University, Furo-cho, Chikusa-ku, Nagoya 464-8603, Japan

A. Okada
Defense Aircraft Engineering Department, Mitsubishi Heavy Industries, Ltd., 10, Oye-cho, Minato-ku, Nagoya 455-8515, Japan

H. Zhao, N.A. Fleck (eds.), *Mechanical Properties of Cellular Materials,*
IUTAM Bookseries 12,

where C is a coefficient, E_s denotes Young's modulus of the base solid, and ρ_0/ρ_s indicates the relative density. They showed that Eq. (1) fits experimental results considerably well if $C \approx 0.05$, i.e.,

$$\Sigma_c \approx 0.05E_s(\rho_0/\rho_s)^2. \tag{2}$$

The above equation is therefore regarded as an experimentally verified semi-empirical relation.

The cell model of Gibson and Ashby mentioned above has a simple cell morphology that is based on orthogonal struts with identical cross-sectional areas. The cell morphology can be rendered fairly realistic by use of Kelvin's tetrakaidecahedral cells, which are arranged in a body-centered cubic lattice to fill the space. The buckling behavior of elastic Kelvin open-cell foams under compression has been analyzed using finite element methods by Laroussi et al. (2002), Gong and Kyriakides (2005), Gong et al. (2005b), and Demiray et al. (2006). One of the findings in these studies is that long wavelength buckling occurs in such open-cell foams subjected to uniaxial compression in the [001] direction, yet the buckling behaviors in other loading directions have not been analyzed. The analysis performed by Gong and Kyriakides (2005) and Gong et al. (2005b) is regarded as an accurate one, because they took into account the non-uniformity of strut cross-sectional areas observed experimentally (Gong et al., 2005a). It is then of interest to discuss the Gibson-Ashby relation (2) in light of the buckling stresses of Kelvin open-cell foams furnished with non-uniform and uniform distributions of strut cross-sectional areas. It is also of interest to analyze the buckling behaviors in other typical directions such as [011] and [111], which have not been investigated yet.

In this study, buckling modes and stresses of elastic Kelvin open-cell foams subjected to [001], [011] and [111] uniaxial compressions are analyzed using the updated Lagrangian type two-scale theory developed by Ohno et al. (2002) and Okumura et al. (2004). By supposing cubic unit cells and cell aggregates in model foams, the analysis is performed on the assumption that the struts in foams have a non-uniform distribution of cross-sectional areas as observed by Gong et al. (2005a). The analysis is also performed by ignoring the non-uniformity of strut cross-sectional areas. The relative density is changed to range from 0.005 to 0.05. The buckling stresses and modes obtained are then discussed to investigate the dependence on uniaxial compression directions and the influence of strut cross-sectional area distributions. It is thus shown that the primary buckling stresses determined for the three compression directions are fairly close to one another and justify the Gibson-Ashby relation (2) unless the non-uniformity of strut cross-sectional areas is ignored.

2 Open-Cell Model Foams and Cubic Unit Cells

Figure 1 illustrates the open-cell model foams analyzed, in which Kelvin's tetrakaidecahedral cells are periodically arranged in a body-centered cubic lattice. The model foams are supposed infinitely large and subjected to uniaxial

Fig. 1 Kelvin open-cell foam and directions of uniaxial compression

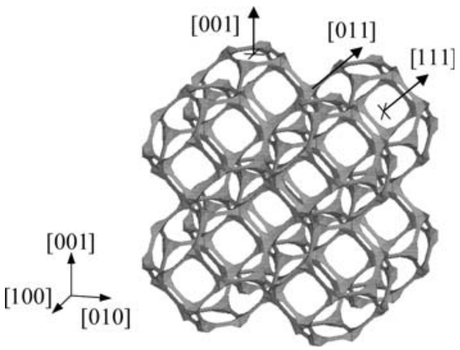

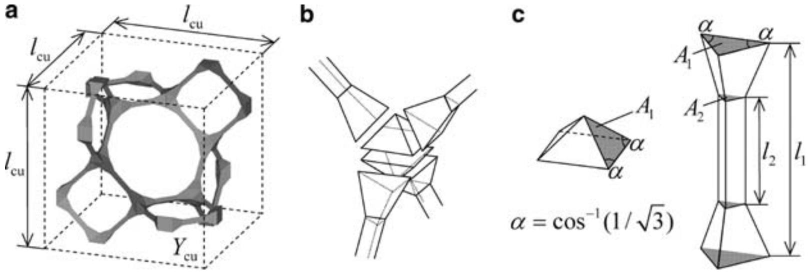

Fig. 2 (**a**) Cubic unit cell Y_{cu}, (**b**) strut-junction connection, and (**c**) shape of struts and junctions

compression in a direction fixed in the space. Figure 1 shows three typical compression directions, [001], [011] and [111], considered in this study.

The model foams mentioned above have a cubic unit cell Y_{cu}, shown in Fig. 2a, owing to the periodicities along [100], [010] and [001] (Gong and Kyriakides, 2005; Gong et al., 2005a, b). As seen in Fig. 2a, a junction is formed by four connecting struts, which have a non-uniform distribution of triangular cross-sectional areas. This kind of junction has been observed experimentally (Gong et al., 2005a; Mills, 2007). Figure 2b and c illustrate the strut-junction connection and their shapes assumed in this study; each strut is expressed using two truncated tetrahedrons and one triangular bar, and each junction is comprised of two regular square pyramids. Then, since one Y_{cu} contains 24 struts and 24 pyramids, it is shown that the relative density ρ_0/ρ_s is represented as

$$\rho_0/\rho_s = 8l_{cu}^{-3}\left[2^{5/4}A_1^{3/2} + (l_1 - l_2)(A_1 + A_1^{1/2}A_2^{1/2} + A_2) + 3A_2 l_2\right] \tag{3}$$

where l_{cu} denotes the size of Y_{cu}, and A_1, A_2, l_1 and l_2 are the areas and lengths characterizing the struts (Fig. 2c). From now on, the foams with non-uniform and uniform distributions of strut cross-sectional areas will be referred to as non-uniform and uniform (cross-section) models, respectively.

The values of ρ_0/ρ_s are taken to be 0.005, 0.010, 0.020, and 0.050 for the non-uniform and uniform models in this study. It is assumed that the non-uniform model has $l_2/l_1 = 0.5$ and $A_2/A_1 = 0.15$ based on the experimental measurements of Gong et al. (2005a), while the uniform model has $A_2/A_1 = 1$. In the analysis, Young's modulus E_s of a base solid was employed to non-dimensionalize stresses, and Poisson ratio ν_s was taken to be 0.3.

3 Macroscopic Instability Analysis

Macroscopic instability was first analyzed to investigate the possibility of long wavelength buckling using the two-scale theory developed by Ohno et al. (2002) and Okumura et al. (2004).

Figure 3 shows the macroscopic instability points found in the macroscopic instability analysis performed for the two models of $\rho_0/\rho_s = 0.01$. As seen from the figure, the two models gave quite different results. When the non-uniform model was employed, the macroscopic instability condition was satisfied under [001] and [011] compressions. The uniform model, on the other hand, allowed the condition to be fulfilled only under [011] compression. Macroscopic instability under [011] compression was thus common to the two models. However, the macroscopic instability condition was satisfied much earlier in the non-unified model than in the unified model under [011] compression. We therefore can say that the non-uniformity of strut cross sectional areas is an important factor for the stability of open-cell foams.

Let us remember that macroscopic instability of periodic solids is identified with microscopic bifurcation with an infinitely long wavelength (Geymonat et al., 1993). The results above then suggest that long wavelength buckling can occur in the non-uniform model under [001] and [011] compressions and also in the uniform model under [011] compression.

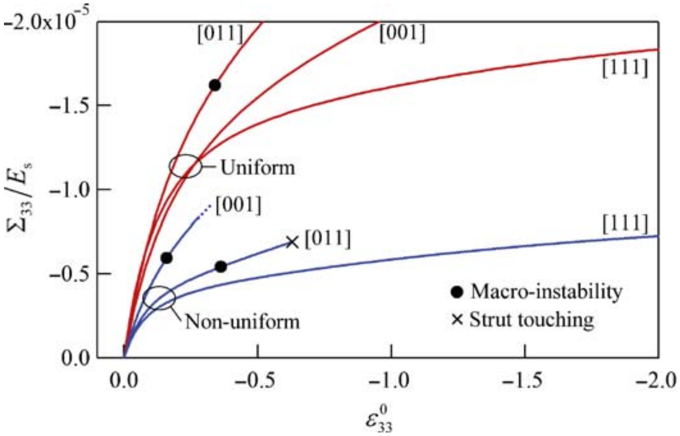

Fig. 3 Macroscopic instability points by non-uniform and uniform models of $\rho_0/\rho_s = 0.01$ under [001], [011], and [111] compressions

4 Microscopic Bifurcation Analysis

Microscopic bifurcation analysis of the model foams was performed subsequently to the macroscopic instability analysis discussed in the preceding section. Cell aggregates were introduced as periodic units for that bifurcation analysis, because long wavelength buckling was suggested by the macroscopic instability analysis.

The following three types of cell aggregates were employed as periodic units in the microscopic bifurcation analysis: $Y_N^{(3\mathrm{D})}$, $Y_N^{[001]}$ and $Y_N^{[011]}$, which are aggregates of Y_{cu} as illustrated in Fig. 4a–c. The periodic unit $Y_N^{(3\mathrm{D})}$ contains N^3 Y_{cu}s. This periodic unit allows us to find microscopic bifurcation that has the $k_{[100]}Y_{\mathrm{cu}}$-, $k_{[010]}Y_{\mathrm{cu}}$- and $k_{[001]}Y_{\mathrm{cu}}$-periodicities along [100], [010] and [001]. On the other hand, $Y_N^{[001]}$ and $Y_N^{[011]}$ are effective for finding microscopic bifurcations that have long wavelengths along [001] and [011], respectively.

The microscopic bifurcation points obtained for the non-uniform model are indicated in Figs. 5 and 6. Under [001] and [011] compressions, the microscopic bifurcation condition was satisfied at lower stresses with increasing number of cells in $Y_N^{(3\mathrm{D})}$, $Y_N^{[001]}$ and $Y_N^{[011]}$ (Figs. 5 and 6). The bifurcation stresses provided by $Y_{16}^{[001]}$ and $Y_{16}^{[011]}$ were almost equal to the macroscopic instability stresses under [001] and [011] compressions, respectively (Fig. 6). It follows from these results that long wavelength buckling occurred in the non-uniform model under [001] and [011] compressions.

An identical bifurcation point was found under [111] compression using the non-uniform model, though the number of cubic unit cells in $Y_N^{(3\mathrm{D})}$ was increased from $N^3 = 1$ to 6^3 (Fig. 5). Here it should be recalled that [111] compression led to no macroscopic instability point, suggesting no long wavelength bifurcation (Section 2). It is then clear that the microscopic bifurcation in the non-uniform model under [111] compression had a short wavelength. The buckling behavior of the non-uniform model under [111] compression was thus completely different from

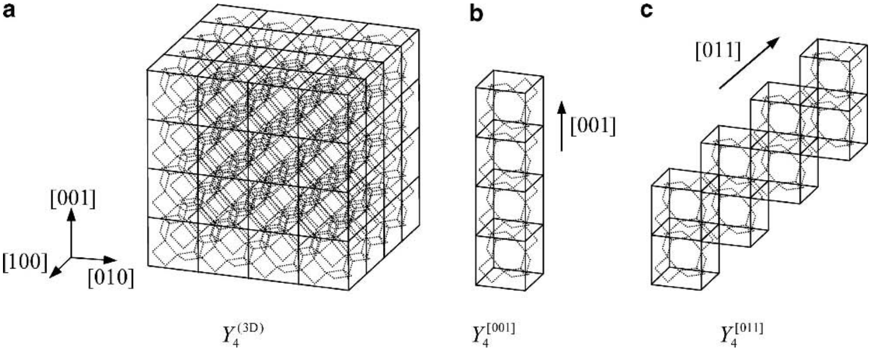

Fig. 4 Illustration of cell aggregates $Y_N^{(3\mathrm{D})}$, $Y_N^{[001]}$, and $Y_N^{[011]}$ with $N = 4$

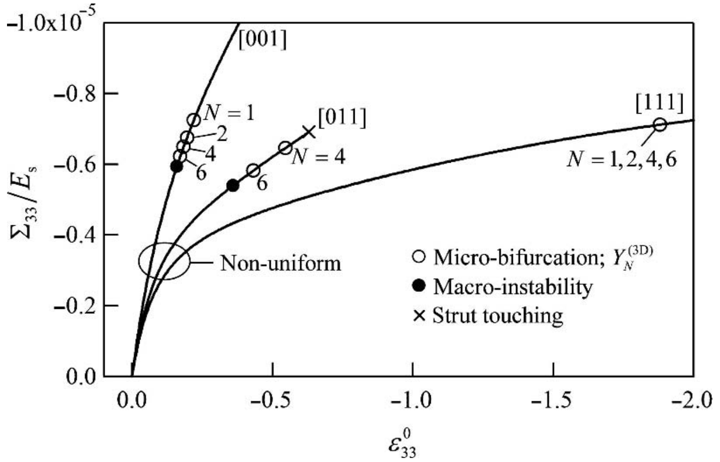

Fig. 5 Microscopic bifurcation points determined by use of $Y_N^{(3D)}$ for non-uniform model of $\rho_0/\rho_s = 0.01$

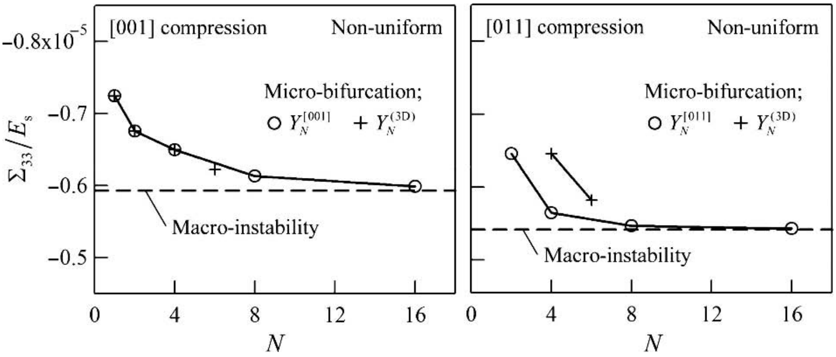

Fig. 6 Dependence of microscopic bifurcation stress on the size number *N* of periodic units under [001] and [011] compressions; non-uniform model, $\rho_0/\rho_s = 0.01$

those under [001] and [011] compressions. It must be, however, pointed out that the short wavelength buckling stress determined for the non-uniform model under [111] compression was fairly close to the macroscopic instability stresses of that model under [001] and [011] compressions (Fig. 5).

Figure 7 shows the microscopic buckling points determined for the uniform model by use of $Y_N^{(3D)}$. As seen from the figure, long wavelength buckling occurred under [011] compression, in accordance with the result of macroscopic instability analysis (Fig. 3).

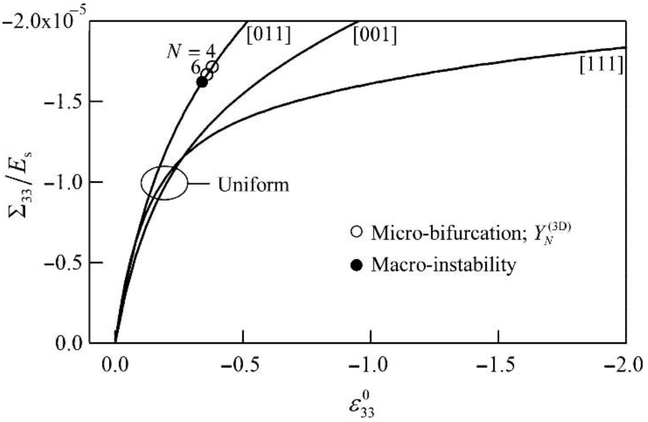

Fig. 7 Microscopic bifurcation points determined by use of $Y_N^{(3D)}$ for uniform model of $\rho_0/\rho_s = 0.01$

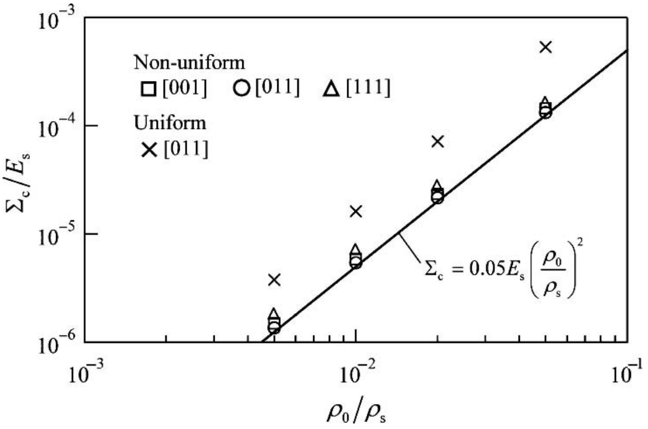

Fig. 8 Relation between buckling stress Σ_c and relative density ρ_0/ρ_s

5 Comparison to Gibson-Ashby Relation

As was shown in Sections 3 and 4, macroscopic instability or infinitely long wavelength buckling primarily occurred in the non-uniform model under [001] and [011] compressions and in the uniform model under [011] compression, and only short wavelength buckling happened in the non-uniform model under [111] compression. The buckling stresses determined for these primary buckling modes are plotted against ρ_0/ρ_s and compared to the Gibson-Ashby relation (2) in Fig. 8. As seen from the figure, the buckling stresses attained in the present analysis provide compressive strength Σ_c with the proportionality to $E_s\,(\rho_0/\rho_s)^2$ as expressed in Eq. (1). This implies that the bending of struts is effective for the buckling modes of elastic Kelvin open-cell foams. However, since a simple cell model was employed to derive Eq. (1), the coefficient in this equation was determined by fitting several experiments, as was remarked in Section 1. The resulting equation, Eq. (2), is thus regarded as an experimentally verified semi-empirical relation. As demonstrated in Fig. 8, the primary buckling stresses by the non-uniform model almost satisfy Eq. (2), whereas the uniform model gives a considerable deviation from Eq. (2). We therefore can say that the compressive strength of open-cell foams has been successfully evaluated by analyzing macroscopic instability and short wavelength buckling of the non-uniform model.

References

Geymonat, G., Müller, S., Triantafyllidis, N., 1993. Arch. Ration. Mech. Anal. 122, 231–290.

Gibson, L.J., Ashby, M.F., 1982. Cellular Solids: Structure and Properties, Cambridge University Press, Cambridge.

Gong, L., Kyriakides, S., 2005. Int. J. Solids Struct. 42, 1381–1399.

Gong, L., Kyriakides, S., Jang, W.-Y., 2005a. Int. J. Solids Struct. 42, 1355–1379.

Gong, L., Kyriakides, S., Triantafyllidis, N., 2005b. J. Mech. Phys. Solids 53, 771–794.

Laroussi, M., Sab, K., Alaoui, A., 2002. Int. J. Solids Struct. 39, 3599–3623.

Mills, N.J., 2007. Int. J. Solids Struct. 44, 51–65.

Ohno, N., Okumura, D., Noguchi, H., 2002. J. Mech. Phys. Solids 50, 1125–1153.

Okumura, D., Ohno, N., Noguchi, H., 2004. J. Mech. Phys. Solids 52, 641–666.

Elastic Buckling of 2-D Random Honeycombs: Does a Representative Volume Element Exists?

F. Jouneid and K. Sab

Abstract Several studies have focused on the linear and non linear behavior of elastic random honeycombs. In this paper, some numerical tests are presented to explore the existence of a Representative Volume Element (RVE) for elastic buckling of these microstructures. The Voronoi tessellation technique and the finite element method are used to estimate the load plateau of two-dimensional cellular solids having irregular shapes. Elastic buckling and finite deformation calculations are conducted and compared. For a given size of specimen and a given precision, the Monte-Carlo method is used to determine the number of simulated specimens. The existence of a RVE for elastic buckling is numerically established when the microstructure is not "too" irregular and all the cells are hexagonal. In this case, it is found that the elastic buckling analysis gives a good estimation for the beginning of the load plateau regime.

1 Introduction

In this paper, two-dimensional low density cellular solids (honeycombs) are considered. There are three phases in the behavior of elastic cellular material: An elastic-linear regime followed by a plateau regime, corresponding to the buckling of the cells, which ends with the thickening regime.

Many studies concerning the elastic-linear regime were performed analytically and numerically (see [3]). Moreover, it is well-known that the elastic buckling of regular hexagonal honeycombs leads to the plateau regime: Zhang and Ashby [11] studied honeycombs' buckling under in-plane biaxial stresses. Ohno et al. [6] established the buckling condition for a given mode. Saiki et al. [8] determined the

---

F. Jouneid and K. Sab (✉)
Université Paris-Est, Institut Navier, LAMI, Ecole Nationale des Ponts et Chaussées, 6 et 8 avenue Blaise Pascal, 77455 Marne la Vallée Cedex 2, France
sab@lami.enpc.fr

H. Zhao, N.A. Fleck (eds.), *Mechanical Properties of Cellular Materials,*
IUTAM Bookseries 12,

size of the representative volume element. Chuang and Huang [1] studied the effect of solid distribution of cell walls on the elastic buckling of honeycombs under uniaxial compression using a semi-analytical method. Yang and Huang [10] completed this study by adopting a biaxial compression mode. Okumura et al. [7] studied the post-buckling of elastic honeycombs under biaxial compression. Random two-dimensional cellular solids have been studied by Silva and Gibson [9] who analyzed the effect of non-uniform cell shape on the elastic properties of cellular solids. Zhu et al. [13] studied the relationship between the perturbation degree of cell shape and the elastic properties. The two studies used Voronoï diagram for the generation of the microstructure. Fazekas et al. [2] completed the previous works using another method for the microstructure generation. Li et al. [5] added the effect of random cell wall thickness to the random microstructure. Finally Zhu et al. [12] studied the effects of random microstructure on the non linear regime.

The aim of this work is to numerically explore the existence of a RVE for the elastic buckling of random two-dimensional cellular solids having irregular shapes. The Voronoï tessellation technique and the finite element method are used to estimate the load plateau of these microstructures. Both elastic buckling and finite deformation calculations are conducted and compared.

2 Numerical Microstructures

We use the Voronoï tessellation technique to generate our random microstructures. When a set of seeds, placed in 2-D space simultaneously, grow in all directions with a uniform speed, a 2-D Voronoï diagram is formed. The Voronoï tessellation structure is fully determined by the initial locations of the seeds. We have two layouts of seeds: regular layout and perturbed layout. In the first case we lay out the centers of such kind that the polygons of Voronoï are hexagons, this is possible if the centers are placed such as they are presented in the Fig. 1

In the second case (perturbed layout), the locations of the seeds used to construct Voronoi diagrams with irregular cell shapes are perturbed from a regular lattice of

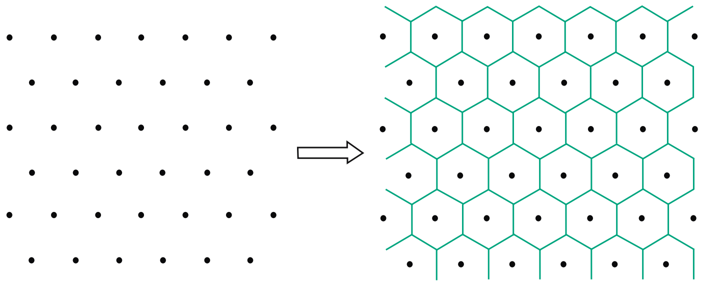

Fig. 1 Vornoi diagram of regular layout seeds

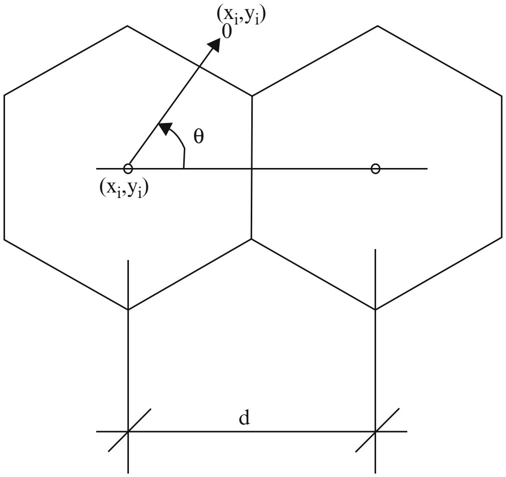

Fig. 2 Coordinate perturbations of the *j*th seed (x_j, y_j)

seeds. Figure 2 shows the coordinate perturbations of a regularly packed seed. The perturbed coordinates of seed *j*, (x_j, y_j) may be represented by (1):

$$\begin{aligned} x_j &= x_i + \alpha(d\cos\theta_i)\varphi_i \\ y_j &= y_i + \alpha(d\sin\theta_i)\varphi_i \end{aligned} \tag{1}$$

where (x_i, y_i) are the two coordinates of the same seed in the regular lattice, d is the distance between two regularly packed (unperturbed) seeds, θi ($\in [0, 2\pi]$) is a random angle (with a uniform distribution) between the horizontal-axis and the line connecting the unperturbed and perturbed seeds, $\varphi_i(\in [0,1])$ is a random variable with a uniform distribution, and $\alpha(\in [0,1])$ is the amplitude used to quantify the degrees of cell shape irregularity. The smaller α is, the more regular the Voronoi diagram is. Regular hexagonal honeycombs are obtained when $\alpha = 0$, and completely irregular honeycombs are defined when $\alpha = 1$.

Once the centers are placed, we generate the Voronoï diagram thanks to a specific data-processing program, to obtain periodic samples. In first step, the seeds are generated and translated in the 8 directions as shown in Fig. 3. Then, we generate the corresponding Voronoi diagram and we extract the periodic sample. Using Matlab software, the above described procedure (Fig. 4) allows us to generate samples of various sizes with different levels of perturbation.

3 Finite Element Analysis

Three types of finite element analysis have been performed: linear regime, elastic buckling and finite deformation. The above described 2D structures are viewed as assemblies of Timoshenko elastic beams, which include bending, axial and shear

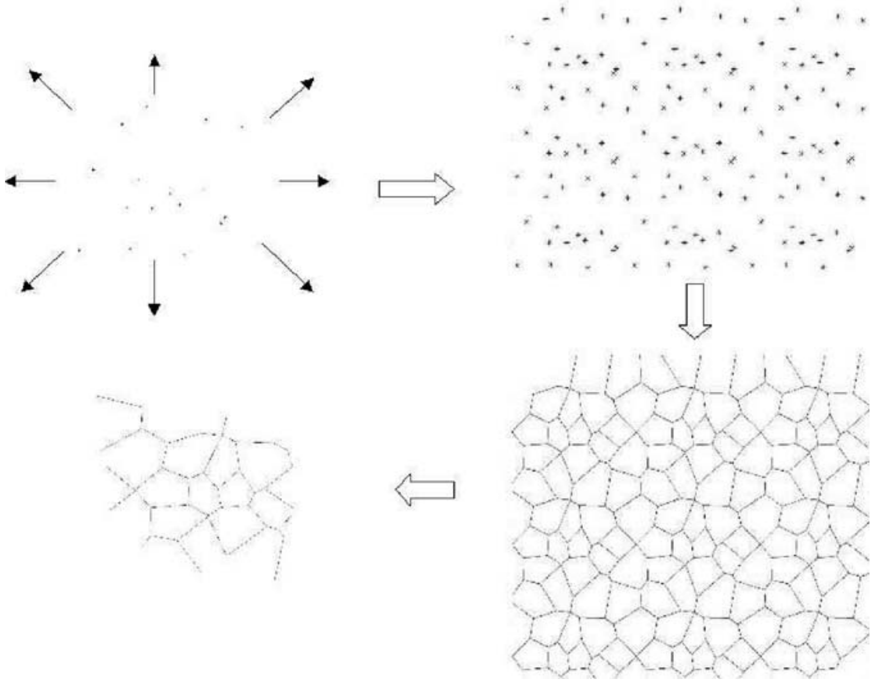

Fig. 3 Construction of the periodic sample

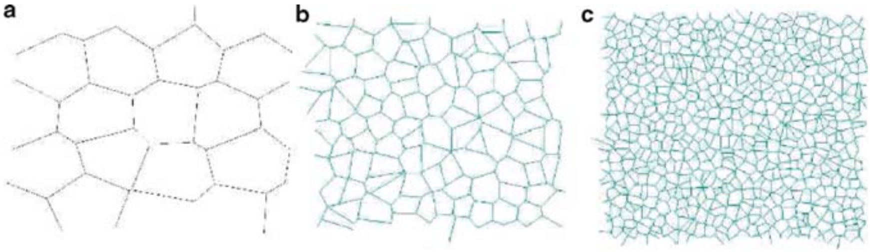

Fig. 4 Various perturbed samples : (**a**) 4 × 4 cells at $\alpha = 30\%$, (**b**) 10 × 10 cells at $\alpha = 80\%$, (**c**) 24 × 24 cells at $\alpha = 80\%$

deformations. Finite deformation analysis has been performed using ABAQUS 6.4 software, while the other two types of analysis have been performed using Matlab software. The relative density d_r is equal to 1% for all samples. The solid Young's modulus and Poisson's ratio are $E_s = 70{,}000$ Mpa and $\nu_s = 0.3$. Uniaxial compression in the Y-direction is simulated. The normalization rule for the stresses is $\Sigma^* = \frac{1}{E_s d_r^2}\Sigma$. All the generated random samples being periodic, periodic boundary conditions [4] have been used. The homogenized Young modulus, the critical overall strain and the critical overall stress corresponding to *the first buckling mode of the* *specimen* have been computed for a wide range of volume size and a large number of realizations of the random microstructure. The number of simulated samples N is determined using Monte-Carlo method. The average ensemble $E(Z)$ of random variable Z can be computed as follows: let $(Z_1, ..., Z_N)$ be N independent realizations of Z and:

$$\overline{Z}_N = \frac{1}{N}(Z_1 + ... + Z_N) \tag{2}$$

$$\sigma_N^2 = \frac{1}{N-1}\sum_{i=1}^{N}(Z_i - \overline{Z}_N)^2 \tag{3}$$

$$\varepsilon_N = 1.96\frac{\sigma_N}{\overline{Z}_N\sqrt{N}} \tag{4}$$

Then, the probability of finding $E(Z) \in [\overline{Z}_N - \varepsilon_N\overline{Z}_N, \overline{Z}_N + \varepsilon_N\overline{Z}_N]$ is asymptotically equal to 0.95. For all our simulations, the number of simulated samples N is such that $\varepsilon_N \leq 2\%$.

4 Results and Discussion

4.1 *Regular Honeycomb* $(\alpha = 0)$

Figure 5 shows the results for 4 × 4 cells. The effective Young modulus E_{hom} is 0.105 Mpa, the effective Poisson ratio ν_{hom} is 0.9997, the critical overall strain E_{22}^{cr} is 9.14% and the normalized critical overall stress Σ_{22}^{*cr} is 0.1371. The same results are obtained for 2 × 2, 4 × 4, 14 × 14, 18 × 18 and 32 × 32 cells. Note that the intersection of the two straight lines which approximate the stress-strain curve coincides with the point $(\Sigma_{22}^{*cr}, E_{22}^{cr})$ corresponding to the first elastic buckling mode (Fig. 6). This is explained by the fact that this buckling mode is a global mode which initiates the finite deformation of the specimen.

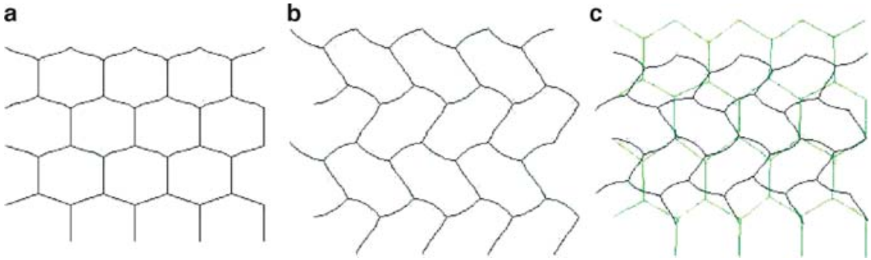

Fig. 5 (**a**) linear regime; (**b**) first buckling mode (**c**) finite deformation

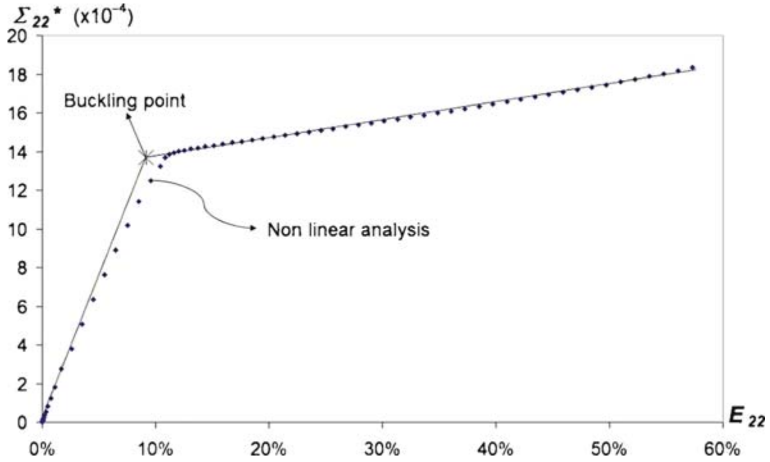

Fig. 6 Behavior of 4 × 4 determinist cells

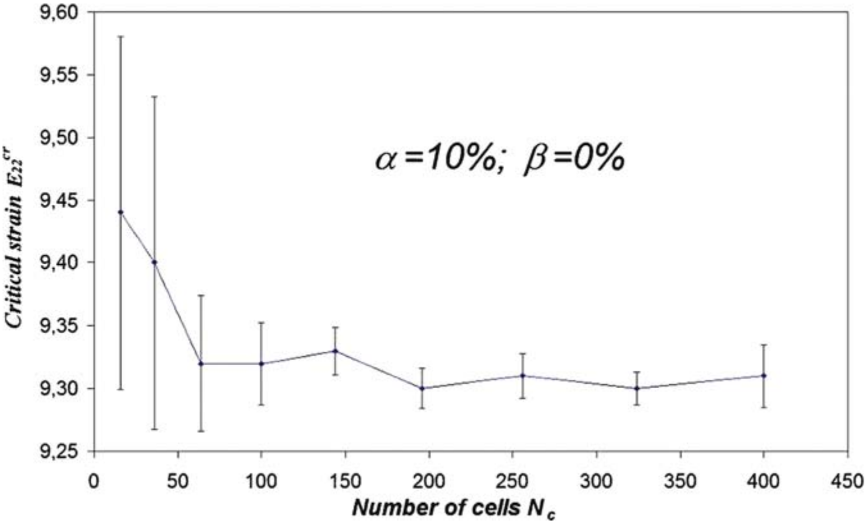

Fig. 7 Critical strain E_{22}^{cr} at $\alpha = 0.1$

4.2 Random Honeycomb $(\alpha \neq 0)$

The Monte-Carlo method is used to explore the existence of RVE for elastic buckling of random honeycombs $(\alpha \neq 0)$. Ten values for α have been considered: $\alpha = 10\%$, $\alpha = 20\%$,..., $\alpha = 90\%$ and $\alpha = 100\%$. In Fig. 7, the average critical overall strain is plotted versus the number of cells in the specimen, N_c, for $\alpha = 10\%$.

This figure shows that the RVE exists for $N_c \geq 64$. A finite deformation analysis of some specimens (less than five) has been also conducted for $N_c = 64$ and

$\alpha = 10\%$. The stress-strain curves obtained are almost the same. Figure 8 shows the behavior of one specimen and the buckling point $(\Sigma_{22}^{*cr}, E_{22}^{cr})$. As for the deterministic case, the buckling point coincides with the beginning of the load plateau regime. The same conclusion is valid for $\alpha = 0.2$.

Indeed, Fig. 9 shows the existence of the RVE in this case. The buckling point $(\Sigma_{22}^{*cr}, E_{22}^{cr})$ and the non linear stress–strain curves for three samples containing $N_c = 64$ cells are plotted in Fig. 10.

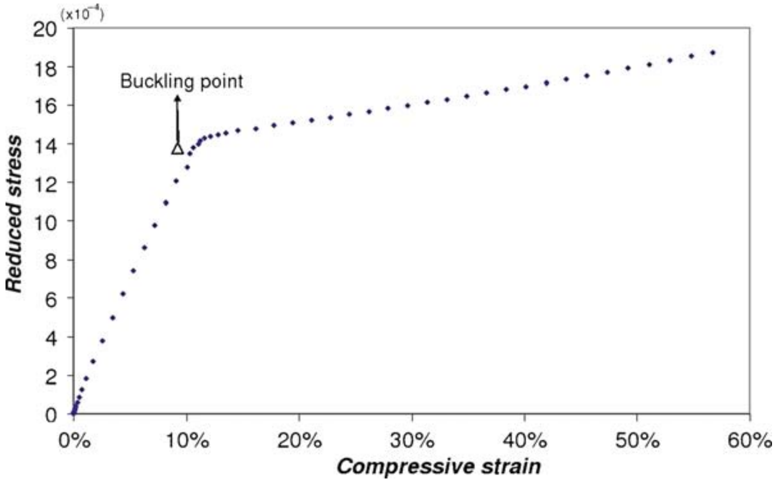

Fig. 8 Stress–strain curve of a random specimen. $N_c = 64$, $\alpha = 10\%$

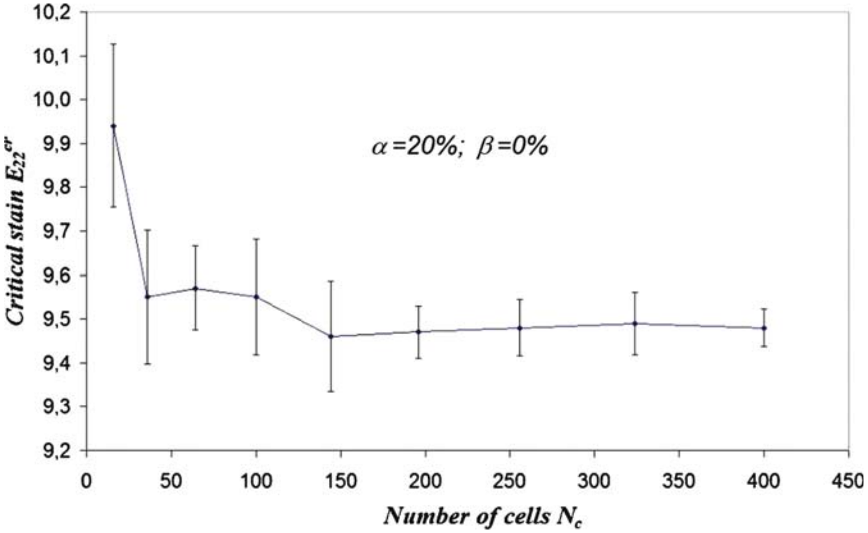

Fig. 9 Critical strain E_{22}^{cr} at $\alpha = 0.2$

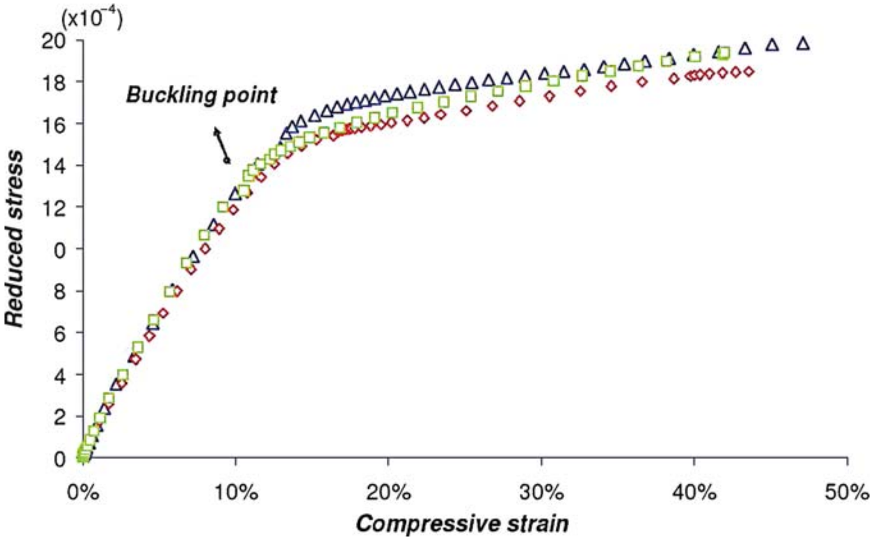

Fig. 10 Stress–strain curve of three specimens. $N_c = 64$, $\alpha = 20\%$

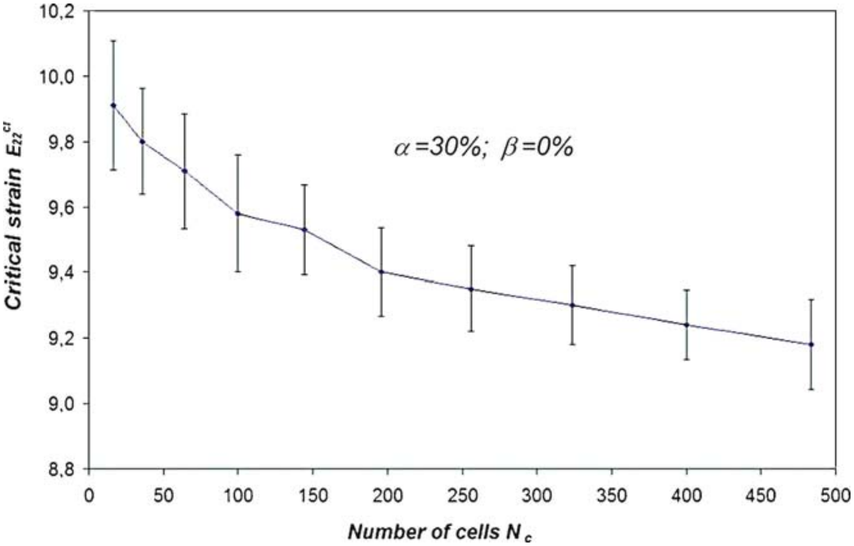

Fig. 11 Critical strain E_{22}^{cr} at $\alpha = 0.3$

The existence of RVE for elastic buckling is lost for $\alpha = 30\%$,..., $\alpha = 90\%$ and $\alpha = 100\%$. See Figs. 11 and 12 for $\alpha = 30\%$ and $\alpha = 80\%$ .The stress–strain curves for four samples of 64 cells and $\alpha = 80\%$ are shown in Fig. 13. Three buckling points taken from Fig. 12 for the sizes 64, 256 and 576 cells are also plotted. As the size of the sample increases, the critical overall strain corresponding to the *first*

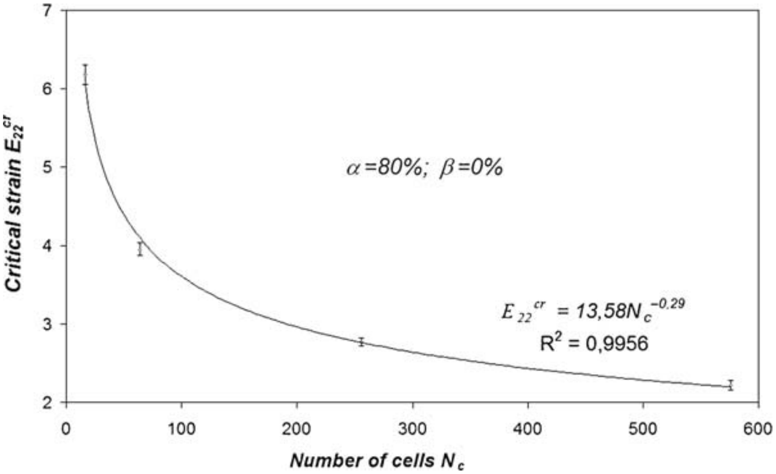

Fig. 12 Critical strain E_{22}^{cr} at $\alpha = 0.8$

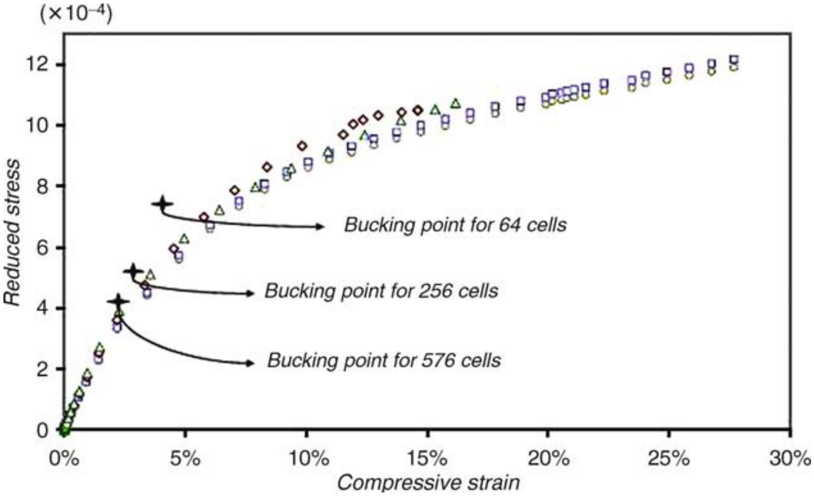

Fig. 13 Stress–strain curve of 3 specimens. $N_c = 64$, $\alpha = 80\%$

buckling mode decreases to zero. This is due to very localized buckling modes which are not representative for the global deformation of the samples. Hence, the elastic buckling analysis is not relevant for the prediction of the load plateau regime.

We propose the following explanation for the loss of the RVE for elastic buckling. The cells of the regular microstructure ($\alpha = 0$) are hexagonal (six sides) and every peak is connected to three peaks. When α increases, other cell shapes appear like pentagons, squares and triangles. Numerical simulations show that this happens for $\alpha \geq 0.24$. So, for $\alpha \leq 0.23$, all the cells are hexagonal and the first buckling mode is a global one. We can set a link between the loss of RVE and the loss of the hexagonality of cells.

As a conclusion, the existence of a RVE for elastic buckling is numerically established when the microstructure is not “too” irregular and all the cells are hexagonal. In this case, it is found that the elastic buckling analysis gives a good estimation for the beginning of the load plateau regime.

References

1. Chuang CH, Huang JS (2002) Effects of solid distribution on the elastic buckling of honeycombs. International Journal of Mechanical Sciences, 44:1429–1443.
2. Fazekas A, Dendievel R, Salvo L, Bréchet Y (2002) Effect of microstructural topology upon the stiffness and strength of 2d cellular structures. International Journal of Mechanical Sciences, 44:2047–2066.
3. Gibson LJ, Ashby MF (1997) Cellular Solids: Stucture and properties. Second ed. Cambridge University Press, Cambridge, UK.
4. Laroussi M, Sab K, Alaoui A (2002) Foam mechanics: nonlinear response of an elastic 3d-periodic microstructure. International Journal of Solids and Structures, 39:3599–3623.
5. Li K, Gao XL, Subhash G (2005) Effects of cell shape and cell wall thickness variations on the elastic properties of two-dimensional cellular solids. International Journal of Solids and Structures, 42:1777–1795.
6. Ohno N, Okumura D, Noguchi H (2002) Microscopic symmetric bifurcation condition of cellular solids based on a homogenization theory of finite deformation. Journal of the Mechanics and Physics of Solids, 50:1125–1153.
7. Okumura D, Ohno N, Noguchi H (2002) Post-buckling analysis of elastic honeycombs subject to in-plane biaxial compression. International Journal of Solids and Structures, 39:3487–3503.
8. Saiki I, Terada K, Ikeda K, Hori M (2002) Appropriate number of unit cells in a representative volume element for micro-structural bifurcation encountered in a multi-scale modeling. Computer Methods in Applied Mechanics and Engineering, 191:2561–2585.
9. Silva MJ, Gibson LJ (1997) The effects of non-periodic microstructure and defects on the compressive strength of two-dimensional cellular solids. International Journal of Mechanical Sciences, 39:549–563.
10. Yang MY, Huang JS (2005) Elastic buckling of regular hexagonal honeycombs with plateau borders under biaxial compression. Composite Structures, 71:229–237.
11. Zhang J, Ashby MF (1992) Buckling of honeycombs under in-plane biaxial stresses. International Journal of Mechanical Sciences, 34:491–509.
12. Zhu H, Thorpe S, Windle A (2006) The effect of cell irregularity on the high strain compression of 2d voronoi honeycombs. International Journal of Solids and Structures, 43:1061–1078.
13. Zhu HX, Hobdell JR, Windle AH (2001) Effects of cell irregularity on the elastic properties of 2d voronoi honeycombs. Journal of the Mechanics and Physics of Solids, 49:857–870.

Mechanical Properties of Semi-expanded Hollow Sphere Structures

T. Daxner and R.W. Tomas

Abstract Recently, technologies for the production of cellular materials have been proposed that allow for a seamless change of the geometries of such materials from being similar to sintered hollow sphere structures to resembling comparatively regular polyhedra. In order to investigate, how the linear elastic properties of such materials are effected by this change in geometry, analyses of the expansion process are carried out by the finite element method for obtaining cell wall thickness distributions. These material distributions are then transferred to finite element unit cell models that are suitable for predicting the effective, macroscopic elastic properties. It is found that Young's modulus, as well as the shear modulus increase monotonically with increasing degree of expansion. Furthermore, negative Poisson's ratios are predicted for configurations that are comparable to sintered hollow sphere structures, while positive Poisson's ratios are observed for highly expanded configurations.

1 Introduction

By coating polymer spheres with a metal powder slurry, confined expansion of the spheres, and subsequent sintering it is possible to produce a wide range of different cellular structures: hollow metal sphere aggregates are the end product if no significant expansion of the polymer spheres takes place, and sintered polyhedra are the result if the coated polymer spheres are subjected to a high degree of confined expansion prior to sintering [1, 2]. With suitable process parameters, tailored intermediate configurations can be produced. The question arises, which degree of expansion is best with regard to achieving advantageous effective mechanical properties such as high effective stiffness.

T. Daxner (✉) and R.W. Tomas
Institute of Lightweight Design and Structural Biomechanics, Vienna University of Technology, Gusshausstr. 27-29(E317), A-1040 Vienna, Austria
daxner@ilsb.tuwien.ac.at

H. Zhao, N.A. Fleck (eds.), *Mechanical Properties of Cellular Materials,*
IUTAM Bookseries 12,

Therefore, the focus of this study is on intermediate stages of expansion and their corresponding geometrical and elastic properties.

2 Method

Finite element unit cell models are employed as idealized mechanical models for the real micro-structures. These models are generated from densely packed hollow sphere arrangements by a simulation of the actual expansion process of the polymer spheres and their coating. This way, realistic geometries and wall thickness distributions are obtained for the subsequent study of the sintered end products. Figure 1 shows the face-centered cubic arrangement of hollow spheres which is the assumed base geometry for the idealized model.

Starting from this regular arrangement of spheres, the first task is to simulate the expansion process of the polymer spheres and their coating in order to obtain realistic geometries and wall thickness distributions for the subsequent study of the semi-expanded end product.

Corresponding simulations are performed on a very small sub-cell of the face-centered cubic arrangement, making full use of the many symmetries that can be found in this example of a structure possessing cubic symmetry. Figure 2 shows the basic setup of the finite element models that are employed for predicting the expansion process. The expansion model corresponds to 1/48 of a full sphere owing to the exploitation of all symmetries.

In reality, the driving force behind the expansion process is the release of gas by the foaming agent. In the simulations, a uniform pressure load on the interior of the spherical shell is assumed to be an appropriate representation of this process. For the expansion analysis, an elastic–plastic cell wall material is chosen, with weak linear hardening being prescribed for achieving a stable expansion process and representing the ‘green’ state of the cell wall. 20-node, isoparametric brick elements with quadratic shape functions are used both in the nonlinear expansion analysis and in the subsequent linear elastic analysis. Appropriate boundary conditions on the expansion model in Fig. 2 take into account the models’ symmetries.

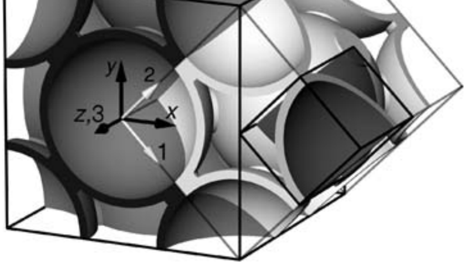

Fig. 1 Rendering of a face-centered cubic arrangement of hollow spheres. The small dark-grey sub-cell at the right side of the image was used for the determination of the shear properties

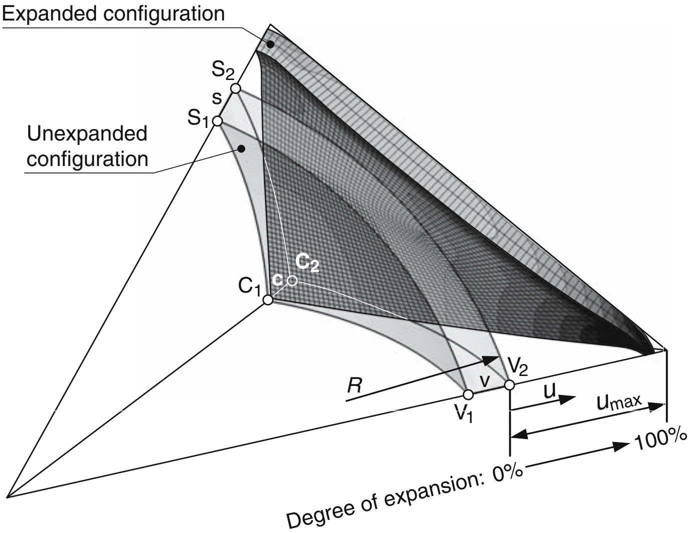

Fig. 2 Sketch showing the expansion model which contains 1/48 of a single sphere (relative density $\rho_{\mathrm{rel}} = 20\%$, degree of expansion $\xi = 88\%$)

From selected stages of the expansion analysis, deformed meshes are extracted and used for composing a symmetric unit cell model corresponding to the small framed cube at the right hand side of Fig. 1. The orientation of this symmetric sub-cell is chosen such that shear stress states in the x-y plane correspond to biaxial compression/tension stress states in the rotated 1–2–3 coordinate system (see Fig. 1). For the cell walls in the sintered state a Poisson's ratio of $\nu_{\mathrm{S}} = 0.4$ is assumed.

The symmetric sub-cell is subjected to uniaxial tension in the three-direction for predicting the effective Young's modulus and the effective Poisson's ratio as well as to biaxial tension/compression for obtaining the effective shear modulus.

3 Results and Discussion

By simulating the expansion of the sphere coating, cell wall thickness distributions for different stages of expansion are predicted. Referring to Fig. 2, the degree of expansion ξ is defined as the radial displacement u of the point V_2 divided by the maximum distance $u_{\max}$ this node has to travel for realizing a (fictitious) fully expanded structure.

The minimal and the maximal wall thicknesses are given by the length of the edges 'v' and 'c' in Fig. 2, respectively. Figure 3 shows cross-sections through the coating shell along the points C_1, C_2, V_2, and V_1 for different stages of expansion.

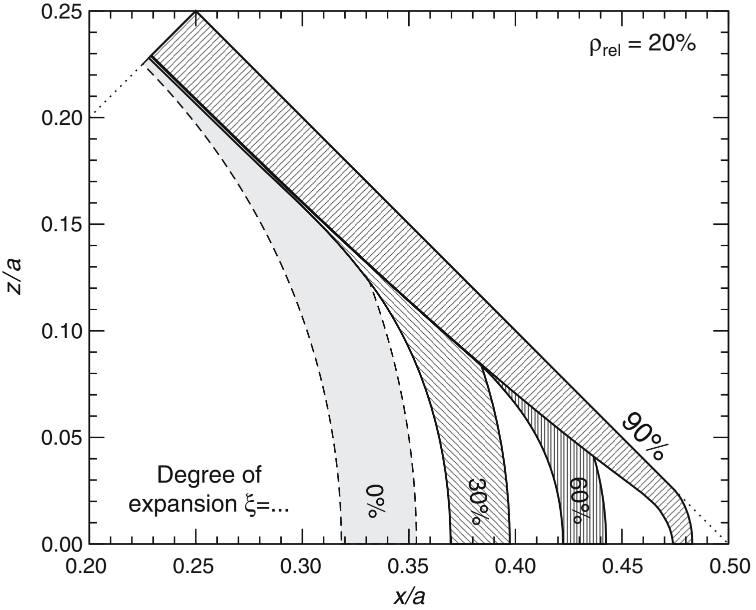

Fig. 3 Cross-sections of an expanding hollow sphere with a relative density of $\rho_{\text{rel}} = 20\%$ along a plane containing an initial contact point (*top left*) and a vertex (*bottom right*) of the circumscribed rhombic dodecahedron ($a = 4R/\sqrt{2}$)

The gradual reduction of the cell wall thickness during the expansion process is shown in Fig. 3. The thinning of the shell is most pronounced along edge 'v' while the region around edge 'c' shows the highest instantaneous wall thickness at all times.

Focusing the attention on the lowest and the highest instantaneous wall thickness as described above leads to Fig. 4. Both measures are normalized by the initial wall thickness in this figure and plotted against the degree of expansion. Remarkably, the curves for the normalized predicted wall thickness values nearly coincide for different relative densities. The rate of cell wall reduction is highest at the edge 'v', which experiences the largest displacement of all points on the shell. In contrast to this, the edge 'c' at the contact point of the shell and its neighbor is not displaced at all at its outer end, and, consequently, shows only very limited straining in the in-plane and normal directions.

The strong decrease of the local wall thickness at edge 'v' and the corresponding high plastic membrane strains can lead to porosity or rupture of the cell wall in this region.

Simulating the expansion process leads to wall thickness distributions for different degrees of expansion and different relative densities. Additionally, the deformed finite element meshes of the semi-expanded shell can be used directly for building up symmetric unit cell models suitable for predicting the effective elastic constants Young's modulus E^*, shear modulus G^*, and Poisson's ratio ν^*, respectively. Being

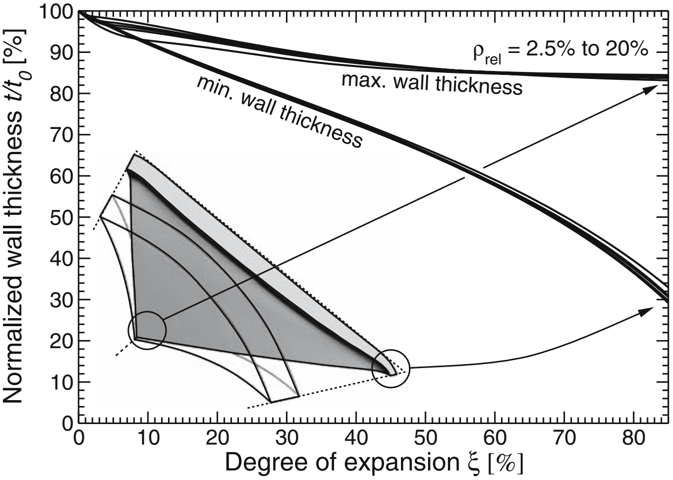

Fig. 4 Development of the relative wall thickness at the thinnest and the thickest part of the expanding sphere, for different relative densities

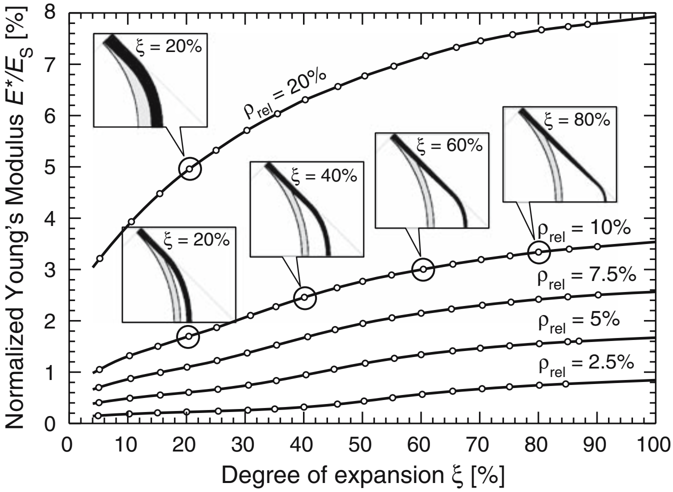

Fig. 5 Predicted, macroscopic Young's modulus E^*, normalized by the modulus of the bulk material E_S for different relative densities and degrees of expansion

based on the proposed idealized face-centered cubic arrangement of cells, the predicted values can serve as estimates for the elastic properties of the real material and for detecting trends in their dependence on the degree of expansion and the relative density.

Corresponding data can be found with respect to the effective Young's modulus in Fig. 5 for a wide range of relative densities and degrees of expansion. The major conclusion, which can be drawn from the results presented in Fig. 5, is, that the elastic stiffness increases monotonically with the degree of expansion.

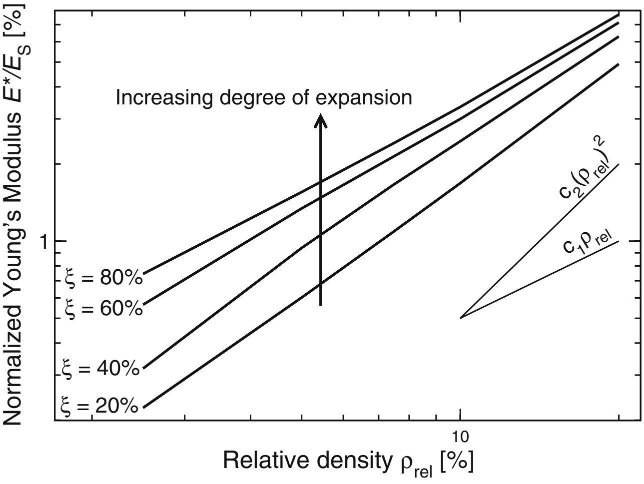

Fig. 6 Predicted, macroscopic Young's modulus E^*, normalized by the modulus of the bulk material E_S for different relative densities and degrees of expansion

A reason for this trend can be indicated by plotting the effective Young's modulus as a function of the relative density in a double-logarithmic diagram for different degrees of expansion. Figure 6 shows a corresponding diagram. In this kind of diagram the inclination of the individual curves allows conclusions about the dominant deformation mechanism, because the elastic stiffness of cellular structures scales linearly with the relative density for structures dominated by cell wall stretching and, respectively, with the square of the relative density for bending dominated structures. Interpreting Fig. 6 in this way indicates the dominance of bending deformation modes for structures that do not differ much from the case of unexpanded hollow sphere arrangements, i.e., for low degrees of expansion. For highly expanded hollow spheres, the inclination of the top-most line in Fig. 6 suggests a deformation mode that corresponds to cell-wall stretching. Since stretching is mechanically more efficient than bending, the increased relative stiffness of the expanded structures can be explained.

The next linear elastic property under consideration is the effective Poisson's ratio ν^*. Again, the dependence on relative density and degree of expansion was examined. Figure 7 shows the effective Poisson's ratios that were predicted by the finite element analyses. It can be seen, that Poisson's ratios are negative for low degrees of expansion, i.e., configurations that do not differ too much from the classical sintered sphere geometry. For these structures uniaxial compression leads to contraction in the direction normal to the loading direction. The mechanical reason for this behavior can be found in the deformation mode depicted in the lower insert picture in Fig. 7; this deformation mode looks very similar to the one found for snap-through buckling of spherical shells.

As the degree of expansion increases, the effective Poisson's ratio also increases; for very high degrees of expansion, ν^* converges to values between 0.3 and 0.35

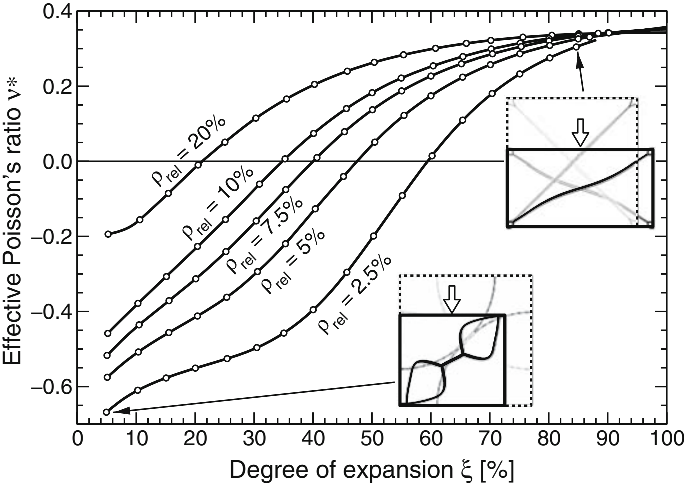

Fig. 7 Predicted, effective, macroscopic Poisson's ratio ν^* for different relative densities and different degrees of expansion

depending on the relative density. Since the Poisson's ratio changes sign from negative to positive as the degree of expansion is increased, it is theoretically possible to find intermediate configurations with zero effective Poisson's ratio for all relative densities. With respect to relative density, Poisson's ratio is found to increase with increasing density.

The third effective property, that is necessary for fully describing the linear elastic behavior of materials with cubic symmetry, is the effective shear modulus G^*. Consequently, the relevant predicted relationships between the shear modulus, the relative density, and the degree of expansion are depicted in Fig. 8. The shear modulus is found to vary less with the degree of expansion than the effective Young's modulus. For low degrees of expansion ($\xi < 15$) the effective shear modulus is markedly lower than for higher degrees of expansion. This phenomenon, which is more pronounced for higher relative densities, can be attributed to shear deformation of the sinter bridges that connect the hollow spheres in the case of little expansion. For higher degrees of expansion, the deformation is distributed more uniformly throughout the structure, leading to a higher shear stiffness.

With the given set of elastic parameters, the effective Young's modulus E^*, the effective Poisson's ratio ν^*, and the effective shear modulus G^*, the effective tensor of elasticity of a material with cubic symmetry can be fully described. One important additional result with respect to elastic anisotropy is the effective Young's modulus $E^*_{[111]}$ that is relevant for uniaxial loading along the space diagonals of the cubic unit cell. It can be calculated as:

$$E^*_{[111]} = \frac{3E^*G^*}{E^* + G^*[1-2\nu^*]} \tag{1}$$

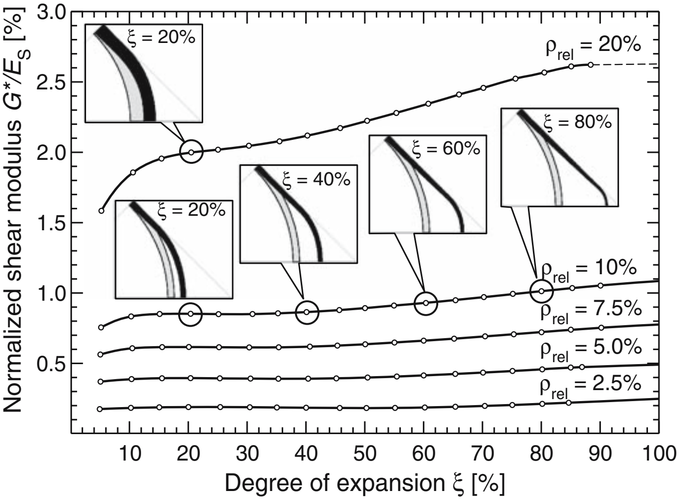

Fig. 8 Predicted macroscopic shear modulus G^*, normalized by the modulus of the bulk material E_S for different relative densities and degrees of expansion

For the considered structures, this modulus is in the range of 75–95% of the effective Young's modulus E^* predicted for the directions of the axes of cubic symmetry.

4 Summary

The expansion process and the linear elastic behavior of semi-expanded sintered hollow sphere structures have been investigated.

With regard to the cell wall thickness distribution resulting from the expansion process it was found that the local reduction of the wall thickness in relation to the original wall thickness is more or less independent of the relative density.

The elastic stiffness along the axes of cubic symmetry was found to increase monotonically with increasing degrees of expansion owing to a change of the linear elastic deformation mechanisms from predominantly cell wall bending for the unexpanded case to cell wall stretching for the expanded case. Poisson's ratio was also shown to depend on the degree of expansion, with negative Poisson's ratios being predicted for low degrees of expansions and positive Poisson's ratios being the result for high degrees of expansion. For each relative density an intermediate stage of expansion with zero lateral deformation ($\nu^* = 0$) under uniaxial loading was found.

References

1. Reinfried M, Waag U, Stephani G, Kieback, B (2006) Three Dimensional Metallic Honeycomb Structure. In: Nakajima H, Kanetake N (eds) Porous Metals and Metal Foaming Technology. The Japan Institute of Metals, Sendai, pp 161–164.
2. Friedl O, Motz C, Färber J, Stoibner M, Pippan, R (2006) Experimental Characterisation of the Deformation in Hollow Sphere Structures. In: Nakajima H, Kanetake N (eds) Porous Metals and Metal Foaming Technology. The Japan Institute of Metals, Sendai, pp 479–482.

Indentation Tests on Al Matrix Syntactic Foams

X.F. Tao, G.K. Schleyer, and Y.Y. Zhao

Abstract This paper investigates mechanical response of Al matrix syntactic foams manufactured by pressure infiltration casting under indentation test. Syntactic foams with ceramic microspheres of three different particle sizes and inner structures were manufactured and tested. Because the hollow microspheres are stronger than the porous ones, the syntactic foam with hollow microspheres has a higher compressive strength than that of the foam with porous microspheres. As a result, the former has a higher indentation load than the latter at any fixed displacement. However, the latter is more ductile than the former. The indentation load is increased significantly when a disc spreader is used. A combination of weak foam and a thick disc may give rise to an optimum indentation resistance.

1 Introduction

Syntactic foam is a particular type of solid foam, which consists of hollow spheres embedded in a continuous matrix. Such foams are originally made with polymeric matrices and ceramic spheres. However, metallic syntactic foams containing hollow ceramic spheres can also be fabricated by traditional casting or infiltration techniques used for metal matrix composites. Compared to other metal foams which have low densities, high specific stiffness, high energy absorbing capabilities and good mechanical and acoustic damping capacities, the metallic syntactic foams have much better ability of energy absorption although with a little higher density than that of normal metal foams. They have the potential to serve as lightweight structures against impact.

In the applications of syntactic foams, failures due to indentation and penetration are very common. Early work has indicated that the indentation behaviour of foam is

---

X.F. Tao, G.K. Schleyer, and Y.Y. Zhao (✉)
Department of Engineering, University of Liverpool, Liverpool L69 3GH, UK

H. Zhao, N.A. Fleck (eds.), *Mechanical Properties of Cellular Materials,*
IUTAM Bookseries 12,

largely determined by its compressive strength [1, 2]. Stupak and Donovan investigated the effects of indenter and absorber geometries on the deformation mechanism and energy absorption of polymer foams [3]. Indentation tests on a closed-cell aluminium foam were also conducted to study its response, including the effects of the size and geometry of the indenter and the cell size of the tested foam [4, 5].

The objective of this work is to characterize the indentation resistance of Al matrix syntactic foams fabricated by pressure infiltration casting with ceramic microspheres of different microstructures and sizes. The indentation behaviour of the syntactic foams with a mild steel load spreader of different thicknesses is also studied, as they are most likely to be used with steel skins in impact applications.

2 Experimental

The raw materials used in the fabrication of the syntactic foam samples are Al alloy 6082 and ceramic microspheres supplied by Envirospheres Pty Ltd. The ceramic microspheres have a composition of 60 wt% SiO_2 and 40 wt% Al_2O_3 and a particle size range of 75–500 μm. The inner structure of the individual microspheres is either hollow or porous, designated in this paper as hollow ceramic microspheres (HCM) and porous ceramic microspheres (PCM), as shown in Fig. 1. The ceramic microspheres were divided into three different types according to their particle size. The inner structure of the microspheres in each type is either PCM, or HCM or a combination of the two, as shown in Table 1.

Three types of Al matrix syntactic foams, corresponding to Type A, B and C ceramic microspheres and designated as Foams I, II, III, respectively, were fabricated by pressure infiltration casting. The details of the fabrication process were described in [6] and are briefly introduced here. A block of Al 6082 was placed at the top of ceramic microspheres contained in a steel tube and was heated in an electric furnace

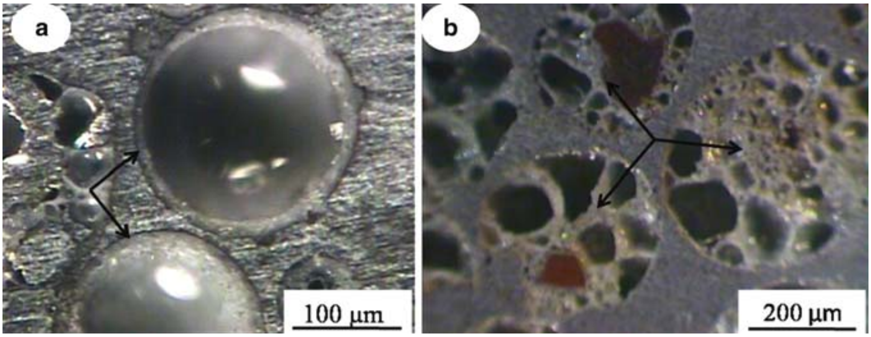

Fig. 1 Optical micrographs of the polished cross sections of two syntactic foam samples showing the two different inner structures of (**a**) hollow ceramic microspheres (HCM) and (**b**) porous ceramic microspheres (PCM), as indicated by the arrows

Table 1 Classification of three types of microspheres

Type	A	B	C
Size range (μm)	250–500	125–250	75–125
Inner structure	PCM	65%PCM, 35% HCM	HCM
Average compressive strength (MPa)	38	67	135

at 700°C for 30 min. The assembly was removed from the furnace and the molten Al alloy was pressed into the ceramic spheres. After full solidification, the sample was removed from the tube and machined into a cylinder with a diameter of 20 mm and a depth of 10 mm. Standard T6 heat treatment was performed on these samples before indention tests.

Axisymmetric indentation tests were performed on the samples using a cylindrical punch with a semi-sphere head. The punch had a diameter of 5 mm, thus the indentation was at a distance of more than two indenter diameters from the sample edge such that the edge effect was negligible. All the three types of syntactic foams were tested in five different conditions: either being indented directly without a spreader or with a spreader, which is a circular mild steel disc with a diameter of 20 mm and a thickness of 0.5, 1, 1.5 or 2 mm. The mild steel used for making the spreader is BS 970 070M20, which has a yield strength of approximately 215 MPa and a tensile strength of approximately 430 MPa. For each test condition, two samples were tested to ensure good reproducibility. The tests were performed on an Instron 4,045 machine with a crosshead speed of 1 mm/min and a displacement of about 9 mm for samples without a spreader and about 10 mm for samples with a spreader.

3 Results and Discussion

3.1 Indentation Response Without a Spreader

Figure 2 shows the vertical cross section of a Foam I sample after the indentation test. It illustrates the different deformation zones, which are present in all the samples tested. A hole was created in the top part of the sample where the indenter penetrated through. Directly below the hole, a crush zone was formed due to compaction. Inside the indentation hole, traces of tearing were observed at the perimeter.

Figure 3 shows the indentation load-displacement curves of the three types of syntactic foams, Foams I, II and III. For each curve, the load initially increases nearly linearly with displacement. At a certain displacement, the load starts either to drop abruptly or to increase with a lower gradient. With increasing displacement further, the load increases steadily as the foam directly under the indenter densifies. For Foam I, the curve is nearly linear up to a displacement of roughly 2 mm

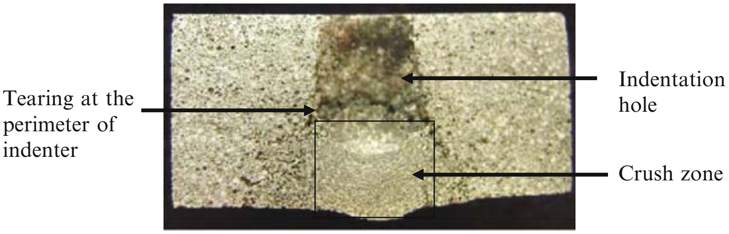

Fig. 2 Cross section of a syntactic foam sample after indentation

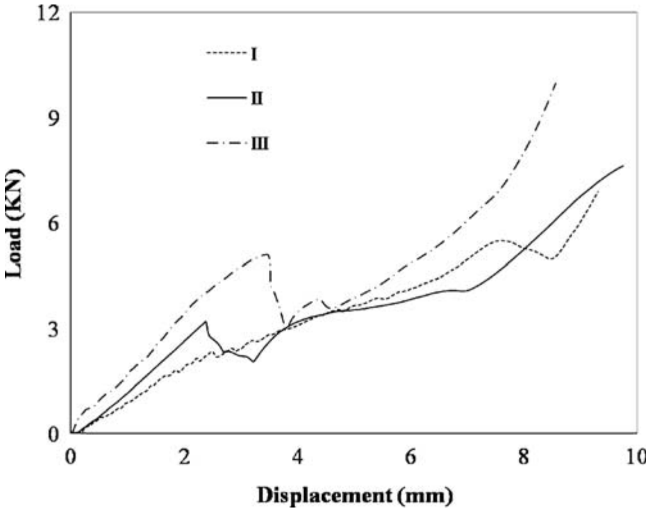

Fig. 3 Indentation load-displacement curves of three different types of syntactic foams without a spreader

but has small oscillations. The load increases steadily with displacement up to a displacement of about 8 mm, at which a drop in load appears. For Foams II and III, the load increases nearly linearly with displacement until a sudden drop at a displacement of about 2.5 and 3.5 mm, respectively. The load then increases again with displacement. The curves of Foams II and III are much smoother than that of Foam I with no discernible oscillations. The load at which the curve deviates from linearity corresponds to the start of a significant collapse of the foam and is designated as indentation collapse load, which is equivalent to the indentation yield load in some cases. The indentation collapse loads of Foams I, II and III are 2.2, 3.2 and 4.9 KN, respectively.

The indentation collapse load of a foam is determined to a large extent by its compressive strength [1, 2]. The indentation load at any displacement is the sum of the force required to crush the foam beneath the indenter and that required to tear the foam at the perimeter of the indenter [5]. Because Foams I, II and III have a similar volume percentage of Al, they are expected to have a similar shear strength [6]. The collapse load therefore largely depends on the maximum force required to crush the foam and accordingly is a function of the compressive plateau strength of the foam. Although the three types of ceramic microspheres have the same chemical composition, HCM has a higher compressive strength than that of PCM, due to different inner structures. The compressive strengths of Type A, B and C are 38, 67 and 135 MPa, respectively, as shown in Table 1. As a consequence, the resultant syntactic foams, Foams I, II and III, have increasing compressive strengths, leading to increasing indentation collapse loads.

Figure 4 shows the macro- and micrographs of the three types of syntactic foams after indentation tests. In Foam I, no macroscopic damage is visible except within the indentation area, and the damage at the perimeter of the indentation hole is not significant. This explains the steady load-displacement curve of Foam I in Fig. 3. The small oscillations in the curve are a result of the repeating cycles of yield, collapse and densification of the ceramic microspheres [5]. In Foams II and III, cracks spanning from the indentation hole to the outer edge of the samples are observed. Considerable deformation is also observed in the region at the perimeter of the indentation hole, indicating significant tearing damage. The initiation of the cracks is believed to result in the abrupt drop in the load-displacement curves for Foams II and III in Fig. 3.

The different behaviour between Foam I and Foams II and III is largely because of the different compressive strengths of the foams. The region of the foam outside the indentation hole is subject to an internal pressure when the sample is subjected

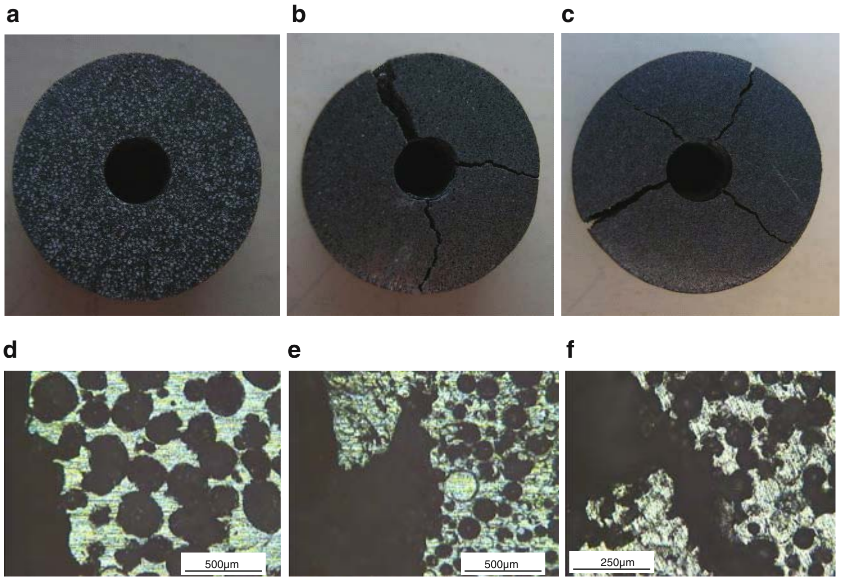

Fig. 4 Macrographs of the three types of syntactic foams: (**a**) I, (**b**) II and (**c**) III; and micrographs of the regions near the indentation holes of the three types of syntactic foams: (**d**) I, (**e**) II and (**f**) III

to indentation. Foam I has a relatively low compressive plateau strength. The stress in the region outside the indentation hole may generate a compressive stress higher than the compressive strength of the foam while the shear stress is still below the shear strength of the foam. This region will undergo plastic deformation without brittle fracture. Foams II and III, however, have relatively high compressive strength. The stress in the region outside the indentation hole may generate a shear stress high enough to cause brittle fracture but a compressive stress still below the compressive strength of the foam. As a consequence, cracks are formed. The different sizes of ceramic micropheres may also affect the ductility, as in the case of particulate reinforced metal matrix composites, where the coarser the reinforcement, the more brittle the composite becomes [7].

It is worth noting that the Al matrix syntactic foams have a much higher indentation resistance than that of Al foams, although the density of the former is normally much higher than that of the latter. For example, an Alporas closed-cell Al foam with a density of $0.22\,\mathrm{g/cm^3}$ has an indentation yield load of 0.1 kN when tested using an indenter with the same shape and size as the one used in this study [5]. In comparison, the syntactic Foams I, II and III have a density of about $1.45\,\mathrm{g/cm^3}$ and indentation collapse loads of 2.2, 3.2 and 4.9 kN, respectively.

3.2 Indentation Response with a Spreader

Figure 5 shows the load-displacement curves of the three types of syntactic foams under indentation with a mild steel disc of 0.5, 1, 1.5 or 2 mm thick. The load-displacement curves obtained without a spreader is also included for comparison purposes. For Foam I, the load-displacement curve is very sensitive to the thickness of the disc. For Foams II and III, however, increasing disc thickness from 0.5 to 1 mm or from 1.5 to 2 mm has no significant effect on the load-displacement curve. The sharp drops in the indentation load-displacement curves are associated with the perforation of the discs, whereas the small drops are associated with cracking of the samples.

Figure 6 shows the top surfaces of the samples of Foam I after indentation with discs of different thicknesses, before the discs were penetrated. In the indentation test with a disc on the top of the syntactic foam sample, the disc acts as a load spreader. The indentation load is distributed to a larger area than the cross section of the punch before the disc is perforated. When the thickness of the disc increases, as shown in Fig. 6, the disc transfers the indentation load to a larger area on the foam. At any fixed displacement, the indentation load increases with increasing disc thickness, as shown in Fig. 5a. Due to the good ductility of Foam I, no shear cracks are observed in the samples for the four test conditions.

Figure 7 shows the top surfaces of the samples of Foams II and III after indentation with discs of different thicknesses, before the discs were penetrated. The effect of load spreading of a 0.5 mm disc is similar to that of a 1 mm disc, and the effect of a 1.5 mm disc is similar to that of a 2 mm disc. This phenomenon is also evidenced

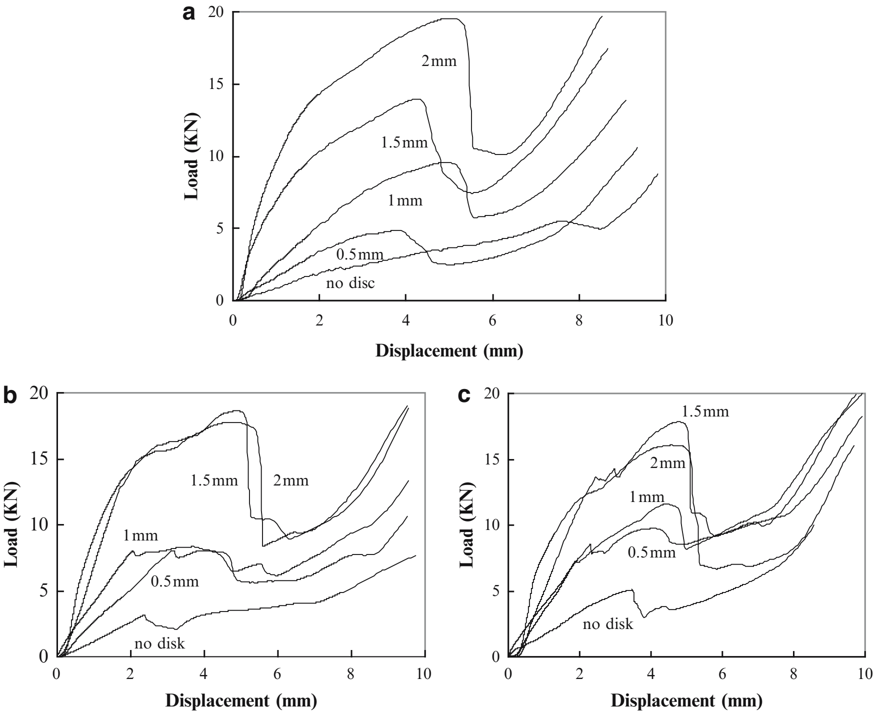

Fig. 5 Indentation load-displacement curves for the three types of syntactic foams with or without discs (**a**) Foam I, (**b**) Foam II and (c) Foam III


0.5 mm 1 mm 1.5 mm 2 mm

Fig. 6 Top surfaces of Foam I samples after indentation with discs of different thicknesses, before the discs were penetrated. The plastic deformation areas are indicated by circles

in the load-displacement curves in Fig. 5b and c. This is likely due to the higher compressive strengths of Foams II and III than that of Foam I, which makes the load spreading less sensitive to disc thickness. When the disc thickness is increased from 0.5–1 to 1.5–2 mm, however, there is a significant difference in the response of the foam to indentation. With a thick disc, the indentation load is spread to a greater area, resulting in fewer and shorter cracks in the region outside the indentation hole, as shown in Fig. 7. The indentation load at any fixed displacement is also increased as shown in Fig. 5b and c.

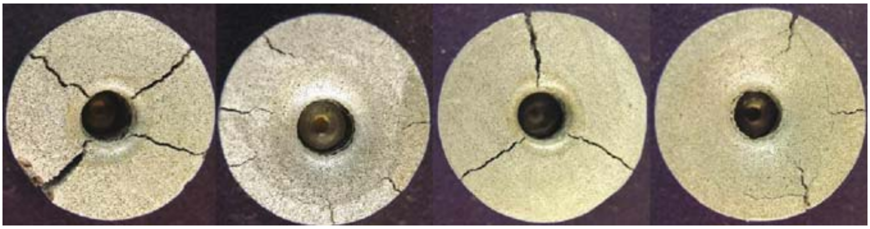

II, 0.5 mm II, 2 mm III, 0.5 mm III, 2 mm

Fig. 7 Top surfaces of Foam II and III samples after indentation with discs of different thicknesses, before the discs were penetrated

Foam I has a slightly higher maximum indentation load than Foams II and III when tested with a 2 mm disc spreader. It seems lower compressive plateau strength of the foam facilitates better load spreading. Taken into account of the strength of the disc, a combination of weak foam and a thick disc may lead to better indentation resistance.

4 Conclusions

The three types of Al matrix syntactic foams, Foams I, II and III, have indentation collapse loads of 2.2, 3.2 and 4.9 kN, respectively. The indentation collapse load is largely determined by the compressive plateau strength of the syntactic foam, which in turn depends on the compressive strength of the reinforcing ceramic microspheres. Foam I has better ductility than Foams II and III, because PCM is weaker than HCM. When a disc is used in the indentation test, the indentation load is distributed to a larger area than the cross section of the punch. The indentation collapse load is increased significantly. The thicker the disc, the higher the indentation load. In some cases, a combination of weak foam and a thick disc may lead to better indentation resistance.

References

1. Wilsea M., Johnson K.L. and Ashby M.F., Int. J. Mech. Sci. 17:457 (1975).
2. Shaw M.C. and Sata T., Int. J. Mech. Sci. 8:469 (1966).
3. Stupak P.R. and Donovan J.A., Polym. Eng. Sci. 34:857 (1994).
4. Andrews E.W., Gioux G., Onck P. and Gibson L.J., Int. J. Mech. Sci. 43:701 (2001).
5. Olurin O.B., Fleck N.A. and Ashby M.F., Scripta Mater. 43:983 (2000).
6. Zhang L.P. and Zhao Y.Y., J. Comp. Mater. 41:2105 (2007).
7. Smith C.A., Reinforcement Roles, in: Composite, Discontinuous Reinforcement for Metal-Matrix Composites, ASM Handbook, Vol. 21, ASM International, Materials Park, Ohio (2001).

Fracture of Metal Foams: A Discrete Modelling Approach

K.R. Mangipudi and P.R. Onck

Abstract A discrete model based on two-dimensional Voronoi tessellation has been used to study damage and fracture in open-cell metal foams. The present study focuses on elastic-fracture behaviour of the foam. A competition mechanism among various damaging struts leading to damage localization and formation of a fracture band has been observed. The effect of relative density is presented in terms of scaling relationships for the peak stress and peak strain are presented here. Finally the detrimental effect of the effect of the presence of the precipitates will be studied as well, showing a severe knock-down in the strength and ductility.

1 Introduction

Metal foams possess attractive mechanical properties like high stiffness to weight ratio. When used to build light-weight structures they require a good combination of strength and ductility. They are ductile under compression but rather brittle in tension with a few percent of overall strain to fracture. In closed-cell metal foams the primary embrittling phases are inclusions and second-phase particles that form during solidification [1]. The composition of these precipitates can be traced back to the viscosity enhancing ingredients and foaming agents added during the foaming process. In open-cell foams made by investment casting fractography revealed plate-like precipitates on the grain boundaries which appeared to be mostly perpendicular to the strut length [2].

When loaded in tension, struts in Duocel open-cell foam fail either by ductile necking or by brittle failure due to cleavage of the grain boundary precipitates. These brittle struts account for up to 20–30% of the total number of failed struts [2].

K.R. Mangipudi and P.R. Onck (✉)
Zernike Institute for Advanced Materials, Department of Applied Physics, University of Groningen, The Netherlands
p.r.onck@rug.nl

H. Zhao, N.A. Fleck (eds.), *Mechanical Properties of Cellular Materials,*
IUTAM Bookseries 12,

During recent tensile experiments on open-cell foams using acoustic measurements [3], brittle failure of the struts was identified with high amplitude recordings. In annealed foam samples no significant high amplitude events were recorded, while substantial acoustic emissions were recorded with samples in the T6-tempered condition wherein the stress levels within the matrix can raise high enough to cause cleavage of precipitates. The differences in the acoustic emission can be explained by the presence of brittle precipitates clearly showing that a large acoustic activity is connected to a small fracture strain. A heat treatment will change the microstructure and the associated yield stress and hardening behaviour of the strut-material. How this will affect the overall behaviour depends sensitively on the foam's cellular architecture, the precipitate distribution and its relative density. The goal of this work is to study these dependencies using a multi-scale modelling framework that takes all these ingredients into account.

2 Multi-scale Model

Random Voronoi structures in two dimensions are used to describe the structure of open-cell metal foams (Fig. 1). The mechanical behaviour of each material point in the strut is characterized by a uniaxial tensile curve featuring linear elasticity, power law hardening and softening due to damage. Individual struts are discretized with Euler-Bernoulli beam elements. An updated Lagrange formulation is adopted. Within a linear Finite Element (FE) setup plasticity of the beam elements is incorporated using viscoplastic framework. In the following section, we summarize

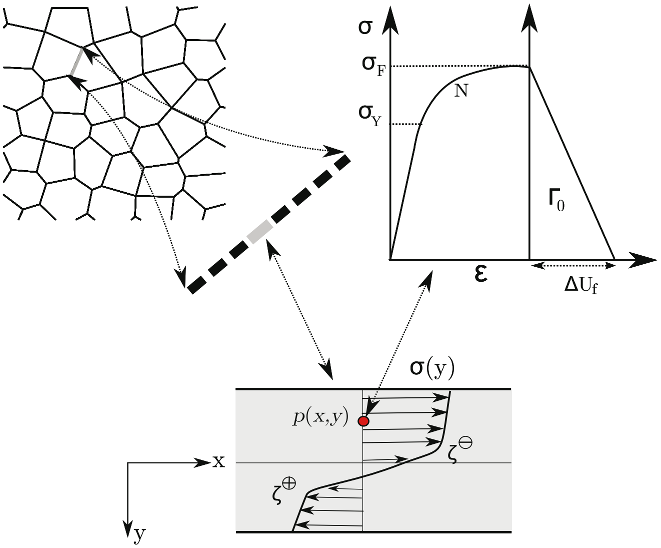

Fig. 1 Information flow between different length scales

the FE equations and discuss the application of the viscoplastic method to model time-independent plasticity and fracture. It should be emphasized here that the viscoplastic framework is used only for numerical reasons; we are not dealing with physical time-dependent processes.

2.1 Finite Element Equations

We make use of the additive decomposition of elastic and viscoplastic strain rates ($\dot{\varepsilon}^e$ and $\dot{\varepsilon}^{\upsilon p}$ respectively) and the elastic constitutive relation, *viz.*,

$$\dot{\varepsilon} = \dot{\varepsilon}^e + \dot{\varepsilon}^{\upsilon p}, \tag{1}$$

$$\dot{\sigma} = E\dot{\varepsilon}^e. \tag{2}$$

Note that we make use of symbolic notation only; no reference is made to the tensorial nature of the symbols. The virtual work principle in its rate form can be written as

$$\int_v \Big\{(\delta\varepsilon)\,\dot{\sigma} + (\dot{\delta\varepsilon})\sigma\Big\}\,dV = \int_A \delta u \dot{f}_{ext}\; dA. \tag{3}$$

With the help of Eqs. (1 and 2) and rearranging the terms, we have

$$\int_v \Big\{(\delta\varepsilon)E\dot{\varepsilon} + (\dot{\delta\varepsilon})\sigma\Big\}\,dV = \int_A \delta u \dot{f}_{ext} dA + \int_V (d\varepsilon)\dot{\sigma}^* dV. \tag{4}$$

where $\dot{\sigma}^* = E\dot{\varepsilon}^{\upsilon p}$ Using the standard beam interpolation functions for the displacements as a function of the nodal displacements and rotations, the following updated Lagrangian finite element equations are obtained:

$$(\mathbf{K}_M + \mathbf{K}_G)\dot{\mathbf{U}} = \dot{\mathbf{F}}_{ext} + \dot{\mathbf{F}}^*, \tag{5}$$

where $\mathbf{K}_M$ and $\mathbf{K}_G$ are the material and geometric stiffness matrices respectively, $\dot{\mathbf{U}}$ is the rate of unknown nodal displacements and rotations and $\dot{\mathbf{F}}^*$ is the rate of viscoplastic forces. Equation (5) is non-linear in time as the viscoplastic force rate and geometric stiffness matrix are a function of the current stress state.

2.2 Plasticity and Fracture

2.2.1 Plasticity as a Limit of Viscoplasticity

The viscoplastic strain rate of a beam under uniaxial tension can be written as a power-law dependence on the force P according to

$$\dot{\varepsilon}^{vp} = \dot{\varepsilon}_0 \left(\frac{P}{P_0} \right)^n, \tag{6}$$

where $\dot{\varepsilon}_0$ and n are material parameters for creep, $P_0 = \sigma_0 t,\ \sigma_0$ is the reference stress and t is the beam thickness. By adopting this power-law creep relation (Eq. (6)) and setting the exponent $n \to \infty$, rate-independent plasticity is recovered with σ_0 as the yield stress. In this limit, the material parameters ($\dot{\varepsilon}_0$ and n) loose their physical significance and become parameters of the numerical algorithm.

In the classical Euler-Bernoulli (EB) elastic beam theory, the generalized strain measures are the axial strain ε and curvature κ. For perfect plasticity, the viscoplastic curvature rate can be expressed in a similar form as (Eq. 6):

$$\dot{\kappa}^{vp} = \dot{\kappa}_0 \left(\frac{M}{M_0} \right)^n, \tag{7}$$

where M is the bending moment, $M_0 = (1/4)bt^2\sigma_0$ is the plastic yield moment and σ_0 is the yield stress [4]. At the beginning of each time step, the vector of the rate of the nodal viscoplastic forces $\dot{\mathbf{F}}^*$ is computed using Eqs. (6 and 7) based on the generalized stress state in the previous increment (e.g. P and M). Taking Eqs. (6 and 7) with a large n ensures that the normal force P and moment M in the beam follow the reference force $(\sigma_0 t)$ and reference moment (M_0) when the material is plastically loading. To incorporate strain hardening, the form of these two equations is preserved and the reference quantities σ_0 and M_0 are taken to be dependent on the accumulated plastic strain and curvature.

2.2.2 Plastic Hardening

The following hardening behaviour is considered for a material point in the beam cross section:

$$\sigma = \frac{\varepsilon}{|\varepsilon|}\sigma_Y \left(1 + \frac{E}{\sigma_Y}|\varepsilon^p| \right)^N \qquad \forall\, |\varepsilon| > \frac{\sigma_Y}{E}, \tag{8}$$

where E is the Young's Modulus, N is the strain hardening exponent and σ_Y is the yield stress and ε^p is the accumulated plastic strain.

Let a section along the strut length at location x (see Fig. 1) be subjected to an axial strain $\bar{\varepsilon}$ and a bending strain κ. Then the axial strain at the material point $p(x,y)$ is,

$$\varepsilon_{xx}(y) = \bar{\varepsilon} - y\kappa. \tag{9}$$

The quantities $\zeta^{\oplus}$ and $\zeta^{\ominus}$ in Fig. 1 represent the position of the boundaries between elastic and plastic portions of the beam and are given by

$$\zeta^{\oplus} = -\frac{1}{\kappa}\left(\frac{\varepsilon_{xx}\left(\frac{t}{2}\right)}{|\varepsilon_{xx}\left(\frac{t}{2}\right)|}\frac{\sigma_Y}{E} - \bar{\varepsilon} \right) \text{ and } \zeta^{\ominus} = -\frac{1}{\kappa}\left(\frac{\varepsilon_{xx}\left(\frac{-t}{2}\right)}{|\varepsilon_{xx}\left(\frac{-t}{2}\right)|}\frac{\sigma_Y}{E} - \bar{\varepsilon} \right). \tag{10}$$

Plastic flow in the beam is initiated as soon as the first fiber (i.e. either the top or the bottom fiber) has yielded. The non-linear stress state across the beam thickness $\sigma(y)$ is integrated to obtain closed form expressions for the normal force $P_0 = \int \sigma dy$ and the moment $M_0 = \int \sigma y dy$ as functions of axial strain $\bar{\varepsilon}$ and curvature κ. This integration is straightforward, but the final expressions are complex and are not presented here. These stress resultants will be used as the reference quantities in the Eqs. (6 and 7):

$$P_0 = P_0(\bar{\varepsilon}, \kappa) \quad \text{and} \quad M_0 = M_0(\bar{\varepsilon}, \kappa). \tag{11}$$

2.2.3 Fracture

When the stress at either of the extreme fibers reaches the critical fracture stress (σ_F) of the material, damage is initiated which reduces the forces and momment to zero with the help of a damage parameter $D \in [0, 1]$. In order to achieve mesh independency, the damage parameter is formulated in terms of displacements instead of strains. The fracture displacement in an infinitesimally thin fiber of initial length l_0 located at y is computed from

$$\Delta u_f(y) = l_0(\exp(\bar{\varepsilon} - y\kappa) - \exp(\varepsilon_\mathrm{F})), \tag{12}$$

where ε_F is the strain at σ_F. The damage parameter D is defined in such a way that always a certain amount of specific fracture energy per unit area of the cross section (Γ_0) is dissipated,

$$D = \frac{1}{t\Delta U_f} \int_{-\frac{t}{2}}^{\frac{t}{2}} \Delta u_f(y) dy, \tag{13}$$

where $\Delta U_f = 2\Gamma_0/\sigma_\mathrm{F}$. At the initiation of fracture, the normal force (P_{init}) and the moment (M_{init}) in the beam element are recorded. We assume linear softening for normal force and moment according to

$$\begin{pmatrix} P_0 \\ M_0 \end{pmatrix} = (1 - D) \begin{pmatrix} P_{init} \\ M_{init} \end{pmatrix}. \tag{14}$$

During the fracture of an element, Eq. (14) provides the reference quantities for the viscoplastic framework to be used in Eqs. (6 and 7).

3 Results

Simulations are performed on Voronois of 7 × 7 cells with a narrow cell size distribution. Each strut is divided into 100 equal-sized elements. When required, precipitates are placed at random locations within the structure. In the simulations presented here we neglect plasticity and limit ourselves to elasticity and fracture.

Young's modulus E is taken to be 70 GPa, $\sigma_F = 105$ MPa and $\Gamma_0 = 60 \times 10^3$ N/m. Figure 2a shows a typical stress-strain curve for a 7×7 Voronoi for these material parameters. Three distinctive regions can be observed: (a) a linear regime, (b) a nonlinear regime (roughly from point p until c) and (c) an unloading regime (after point c). The first regime is due to homogenous elastic deformation. During this period the forces and moments in the struts monotonically increase with very little gross deformation. The second regime (having a nonlinear stress-strain response) is a very important phase of deformation and is associated with many mechanisms important in determining the foam strength. In the early part of the second regime, it can be seen from the strain maps that the strain is homogeneous throughout the sample (e.g. Fig. 3a). Initiation of damage in the struts (at point p) takes place well before the peak stress is attained (at point c, see Fig. 2a). Due to this early damage, local unloading occurs and stresses get redistributed resulting in the non-linear stress strain response. The overall tangent stiffness $(d\sigma^*/d\varepsilon^*)$ now becomes a linear combination of elastically loading struts and linearly unloading struts. When the number of failing struts equals a critical value, overall unloading sets in (point c in Fig. 2a). This situation appears when the random failure events localize to form a fracture path defining a future crack (see strain maps c and d in Fig. 3). After point d, the number of damaging struts does not increase further and all further strain accumulates in the fracture path (see Figs. 2a and 3). The damage accumulation in a few failing struts is shown in Fig. 2b. It can be observed that an increase in damage evolution rate in a few struts corresponds with a decrease in others (which are away from the fracture path). These highly active elements are located in the fracture plane as observed in Fig. 3. Figure 2b nicely shows the competition between damaging struts in the strain range between 0.5% and 1.5%, until the fracture path has been formed. Beyond a critical strain of 1.5% unloading of the structure decreases the overall stress linearly to zero, finally to attain complete separation of the sample.

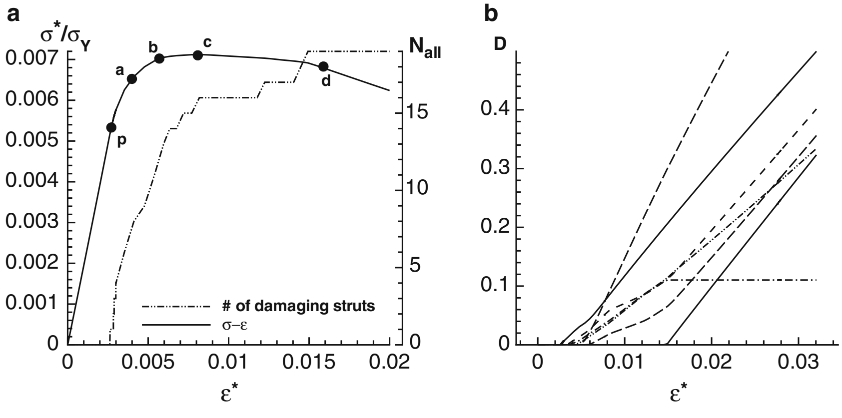

Fig. 2 Elasto-fracture behaviour of a two-dimensional Voronoi structure. Point p corresponds to the first damage event. The numbers *a–d* correspond to the strain maps shown in Fig 3. Fig. 2b shows the damage parameter in individual failing struts for the sample in Fig. 2a

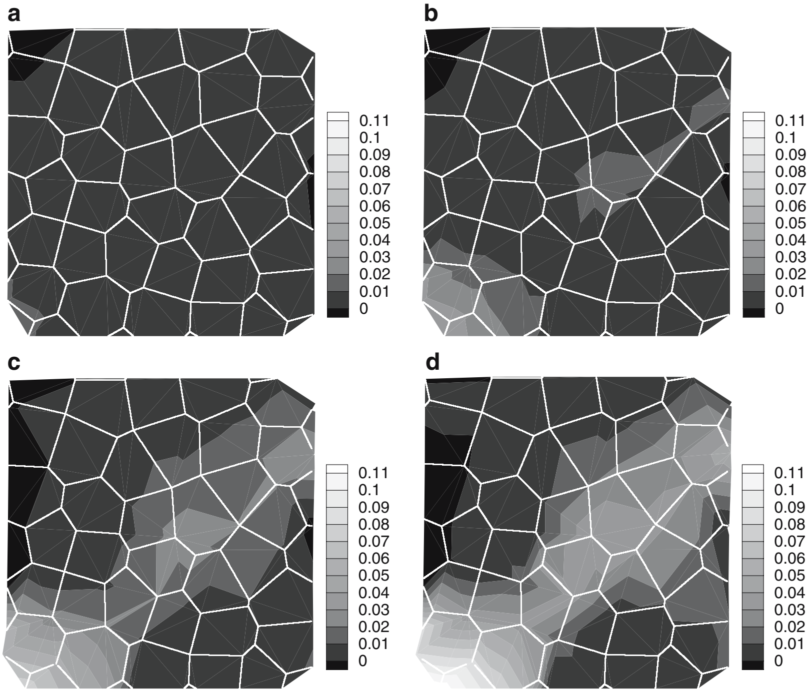

Fig. 3 Strain maps of Voronoi structure. The figures correspond to points *a–d* labeled in Fig. 2a

3.1 Precipitate Volume Fraction and Ductility

Precipitates were placed randomly within the structure of Fig. 2a by declaring random elements to contain a precipitate. The fracture energy of brittle failure (due to the presence of a precipitate) is taken to be four times less than the ductile energy and the precipitate fracture stress to be 90 MPa. The effect of the precipitates on the overall stress–strain response of the Voronoi foam is shown in Fig. 4a for various volume fractions of precipitates. The peak stress and peak strain are considerably knocked down by the introduction of less than 1% of precipitates. The higher the amount of precipitates, the higher is the softening rate (the unloading slope of the curves in Fig. 4a). In Fig. 4b, the peak stress and the peak strain are plotted as a function of the amount of precipitates. By the presence of only 5% precipitates, the peak stress drops by 50%, identifying the precipitates to be highly detrimental for the ductility of metal foams.

3.2 Effect of Relative Density

A strong dependence of the peak stress on relative density is observed (Fig. 5a). The peak stress scales with relative density with an exponent of 2.19. This can be

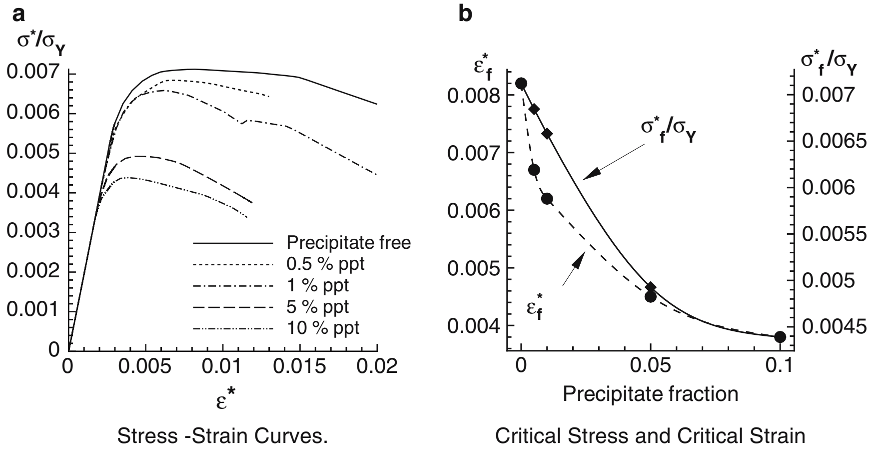

Fig. 4 Effect of precipitates on the ductility of a Voronoi $(\rho^*/\rho_s = 10\%)$

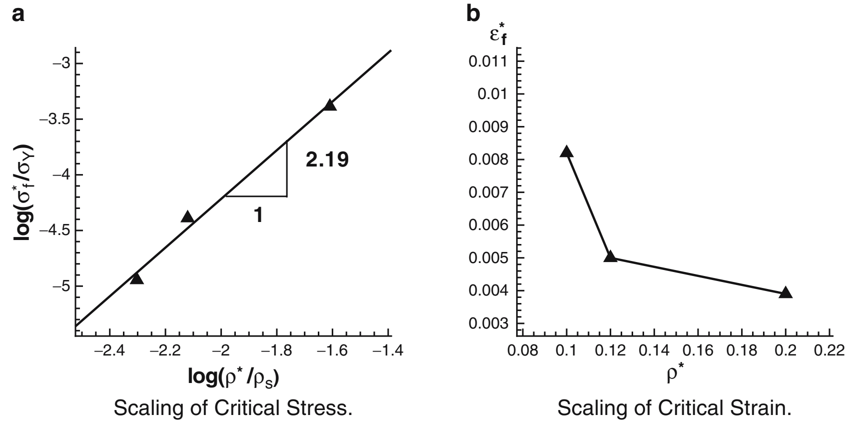

Fig. 5 Effect of density on the critical stress and critical strain

compared with the scaling of the plastic collapse stress which has an exponent of 2.0 for two-dimensional structures. The peak strain decreases with increasing relative density.

4 Conclusions

Using a multi-scale model, we have studied the effect of precipitates and relative density on damage evolution and fracture in two-dimensional Voronoi structures. The peak stress and critical strain were found to decrease with increasing volume fraction of precipitates. The critical strain decreases with relative density, but the peak stress increases, showing a power-law dependence on the relative density with a power around 2.

References

1. Amsterdam E, De Hosson JThM, Onck PR (2006) Acta Mater, 54:17:4465–4472
2. Amsterdam E, Onck PR, De Hosson JThM (2005) J Mat Sci, 40:5813–5819
3. Amsterdam E, De Vries JHB, De Hosson JThM, Onck PR, Acta Mater, Accepted
4. Mangipudi KR, Onck PR (2006) Local Approach to Fracture, 9th European Mechanics of Materials Conference

Fracture of Foamed Cementitious Materials: A Combined Experimental and Numerical Study

D. Meyer, H.-K. Man, and Jan G.M. van Mier

Abstract Foamed cements have the advantage of low density and good thermal isolation properties. In an effort to improve their low mechanical properties, a detailed study of the failure mechanism of foamed cement is undertaken. By means of in-situ micro compression tests inside an X-ray scanner, deformation and fracture of small specimen can be observed in detail.

Using a simple beam lattice model, the material is modelled and fracture is simulated, taking into account as much as possible detail of the material structure. Direct 3D comparison with the outcome of the experiments is possible which is further assisted by using directly the material structures measured on the small samples that are subsequently tested in the X-ray scanner. Some preliminary test results and simulations are presented in this paper.

1 Introduction

Foamed cementitious materials are highly porous materials with favourable properties as low weight, high thermal insulation or high vapour diffusion. Due to its porosity the strength is rather low and up to now it is not common as a load bearing material. The overall goal of the work on foamed cement-based materials is to develop a load bearing material for structural use while keeping its other favourable properties.

The compressive strength of the material decreases with an increase of the foam volume (see Meyer and van Mier, 2006), the tensile strength also, but addition of plastic fibres increases tensile strength significantly (see Meyer and van Mier, 2007) The goal in this part of the work on foamed cementitious materials is the detailed

---

D. Meyer, H.-K. Man, and J.G.M. van Mier (✉)
ETH Zurich, Department of Civil, Environmental and Geomatic Engineering, Institute for Building Materials, 8093 Zürich, Switzerland

H. Zhao, N.A. Fleck (eds.), *Mechanical Properties of Cellular Materials,*
IUTAM Bookseries 12,

observation of the material fracture mechanisms in compression to find a way to improve the material behaviour. Therefore X-ray tomography was used to detect the material structure and the fracture process.

These tests were combined with numerical simulations, based on a 3D beam lattice model. The material structure is directly projected onto the lattice structure. As a consequence, direct 3D comparisons between simulations and mechanical testing are possible.

2 Loading Stage and Tomography Device

X-ray tomography is a common technique to visualise the material structure and cracks. Because of the limited space in common desktop scanners loading stages were used outside the scanner, implying numerous manipulations that might impair the specimen and test accuracy. With a micro loading stage, which allows testing samples inside a desktop scanner, it is possible to avoid sample manipulations between loading and scanning but also, to observe and record the load and deformations during scanning. In Fig. 1a the scheme of the electro-mechanical loading stage is given. Due to the limited space inside the scanner the loading device dimension decreased. An additional important constraint for using the device inside the scanner was that no metal parts or wires should be in the range of the beam. This was possible by building parts of the load frame out of carbon fibre composites. The deformation was measured with the motor controller, as well as with an LVDT fixed on the cross beam, which also contain the load cell.

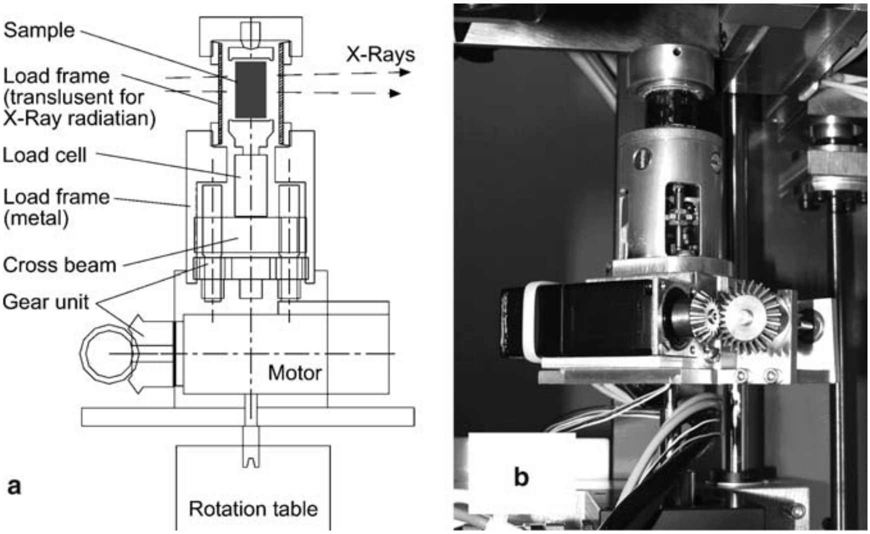

Fig. 1 Loading stage for a X-ray tabletop scanner: (**a**) scheme; (**b**) photo of installed loading device

The capacity of the developed loading-stage is 750 N; the controller allows us to run tests in force- and deformation-control as well as in mixed modes without unloading the sample. The loading stage can be seen in Fig. 1b. The loading stage was also used outside the scanner, and to observe the specimens with an optical camera a second loading frame out of glass was used. The used tomography device is a µCT 40 from SCANCO MEDICAL AG (Bassersdorf, Switzerland). The scanner has a maximum resolution of 6 microns; due to the geometry of our loading stage 10 microns were attainable. The beam energy was 70 kVp and 114 µA with an integration time of 150 ms. For each rotation 4,000 projections were made. Limited by the beam geometry, only 2.1 mm in height could be scanned during one rotation, so called stacks. We limited the sample height to 6.3 mm (three stacks) to reduce the scan time to 1 h per load step.

3 Sample Preparation and Mechanical Testing

The tested samples are foamed cement paste cylinders. The samples have a diameter of 6.7 mm and a height in between 5.8 and 6.3 mm. The foamed cement paste samples were produced ca. 10 months before scanning and testing to reduce the influence of shrinkage, hydration and carbonatisation. The samples were cored from blocks and cut into pieces before grinding them to their final shape. The drill was cooled with compressed air, which also blew away the dust during coring. All samples were grounded by hand using a special sample holder which allowed us to achieve planar and parallel surfaces. Before testing the samples in an X-ray scan, several tests were done outside the scanner to set the main test parameters, such as preload and loading speed. These preliminary tests were also used to define the load-steps for the scanned samples. To eliminate friction between specimen and loading plates special Teflon-Grease-Teflon sandwiches were placed in between the samples and the loading plates at bottom and top, following the method proposed by RILEM TC 148; see Fig. 2a. This setup is very effective, which results in nearly vertical cracks parallel to the loading direction, reaching the top and bottom layer of the samples.

In the Fig. 2b the load-deformation diagram of the test presented in this paper is shown. The scans where done at several load steps. During the scan the deformation was kept constant to keep the cracks opened. In the force-deformation diagram respectable relaxation rates can be observed. The big relaxation is not only based on the sample behaviour; but is also influenced by the carbon load frame and the glued joints.

The first scan was made on the unloaded sample. A second scan was planned at 50% of the maximum load, one at 80%, a fourth at 90–95% and a final scan after reaching peak load. As can be seen in Table 1, these values could be achieved very well for the presented sample. Generally it has to be admitted, that, the scatter of the fracture properties could be remarkable, depending on the density of a sample. This means that it is generally difficult to reach the planned percentage of the

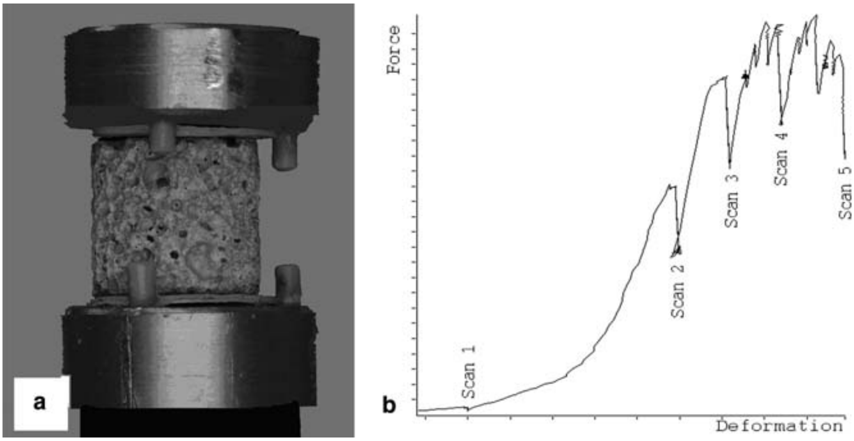

Fig. 2 (**a**) Sample with Teflon-grease-Teflon sandwiches at loading plates. (**b**) Load-deformation curve of a test with five scans

Table 1 Load steps, forces and cracking

Load step	Force	F_{max} (%)	Crack observed
LS 1	5 N	Unloaded	No
LS 2	150 N	55–60	Yes
LS 3	220 N	85–90	Yes
LS 4	255 N	95–100	Yes
LS 5	Post peak	<100	Yes

maximum load. The load steps one to three were done deformation controlled to a defined load. The final loadings were done in deformation-control in single load steps of several microns each, which is the reason for the irregular shape of the load-deformation curve.

4 Results and Analysis from X-Ray Tomography

From the tomography data several kinds of information can be obtained. One of the easiest is to compare the stacks of images of each load step with the others to see if cracks have occurred (see Fig. 3).

Due to the movement and deformation of the sample from one load step to the next, traditional image processing techniques, such as image subtraction could not be used for isolating cracks. One approach to do so, however, is the observation of the change in void quantities from scan to scan (Table 2). An alternative way to observe the crack growth could be the analysis of the total bubble surface in a sample. The bubble surface of different load steps can be compared, as presented in Fig. 4. Interesting is the observation, that the internal surface of the sample is decreasing in the first load steps. The same trend is observed when the total sample volume is plotted against the specimen deformation (see Fig. 4).

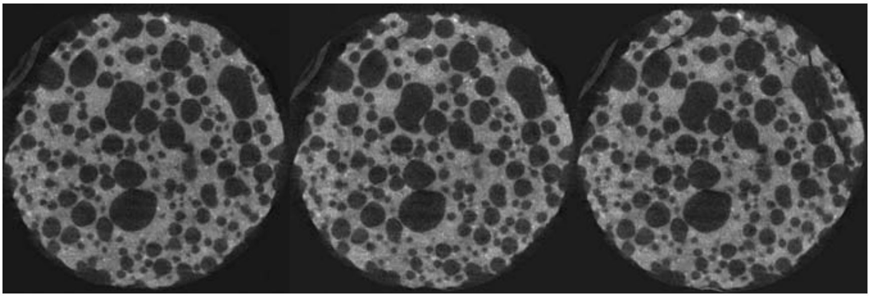

Fig. 3 Formation of cracks observed on the same slice of the sample from unloaded to the collapsed sample (xy-cylices)

Table 2 Pore size distribution for different load steps (only pores larger than 125 voxels = 50 × 50 × 50 microns where considered)

LS	Total $\mathbf{V_{pores}}$ [voxels]	Connected V_{pore} [voxels]	Connected V_{pore} [%]	Number of voids [-]
LS 1	92,079,186	90,982,107	98.809	619
LS 2	93,334,630	92,341,281	98.936	616
LS 3	93,178,803	92,160,323	98.907	618
LS 4	93,326,435	92,306,307	98.907	587
LS 5	94,806,307	93,983,770	99.132	534

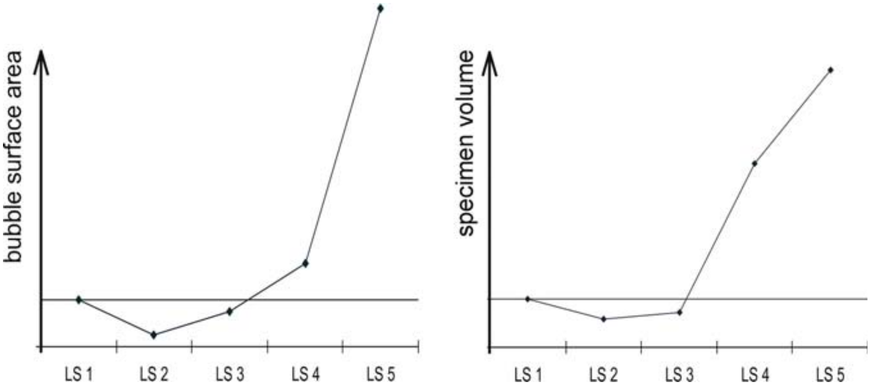

Fig. 4 *Left*: Development of internal bubble surface for the different load steps. *Right*: Development of the total sample volume depending the load step

5 Reality Modelling and Numerical Simulation

Over the years it has been shown that beam-lattice analyses are a suitable tool for simulating fracture in concrete, see Schlangen and van Mier (1992). Mostly these kinds of simulations were done under tension, but not under compression where it was not possible to achieve consecutively correct load-displacement response, including the ratio of tensile over compressive strength with the same parameter scaling, or to achieve correct fracture mechanism, see for example Margoldova and van Mier (1997). Due to limitations in computing capacity, simulations were done in two dimensions only. However, due to the increasing computing power and the use of parallel computing, fracture simulations can now routinely be carried out in 3D, see Lilliu and van Mier (2003).

In the lattice model, concrete is represented by a network of Bernoulli beams. Fracture is simulated by a subsequential removal of one beam in each step. As fracture law, a combination of normal force and bending moment is applied:

$$\frac{\sigma}{f_t} = \frac{1}{f_t}\left(\frac{N}{A} + \alpha\frac{\max\left(M_i, M_j\right)}{W}\right), \tag{1}$$

where a is the cross section area of the beam element and W the section modulus. Mi and Mj are the effective bending moments of the nodes i and j, which is given by: $M_i = \sqrt{M_x^2 + M_y^2}$. The parameter α denotes the role of bending in the fracture law.

In the past and present lattice simulations have been done on concrete, which are modeled as a three-phase material (cement matrix, aggregates and the interface zone). In the case of foamed cement paste, the numerical model can be reduced into a "one"-phase material, consisting of a cement matrix containing large voids (causing a heterogeneous stress field). The foamed concrete model is considered as a simplified material system for studying compressive fracture in brittle disordered materials. The matrix is rather homogeneous; the aggregates are replaced by voids which imply that no ITZ has to be taken into account.

To compare experimental results with those from the simulations it is essential to model the material heterogeneity as good as possible. In the present case we decided to use the sample images (see Fig. 6) from the X-ray tomography as a basis for including the voids (heterogeneity) in the (virtual) specimens. A method was devised to transfer the tomography data directly into the numerical model.

The generation of the microstructure is done as follows (Fig. 5). At first a 3D triangular regular lattice is generated (Fig. 5 left). In the following step the

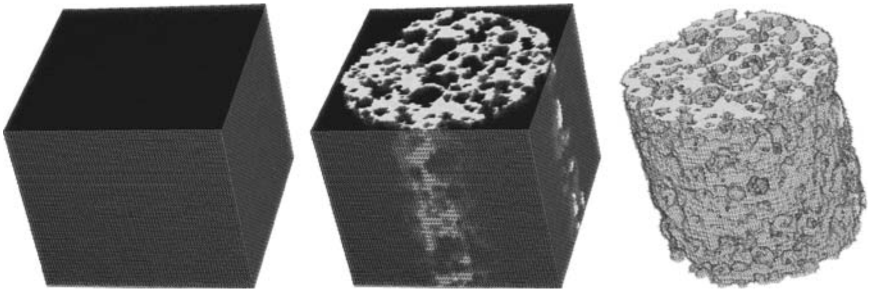

Fig. 5 Mapping the material structure into the lattice. *Left*: Generation of the 3D lattice mesh before overlay of the microstructure (2,403,373 lattice elements). *Centre*: Overlay of the segmented 3D scans on top of the lattice. *Right*: after removal of the unnecessary beam elements (remaining total of 683,490 elements)

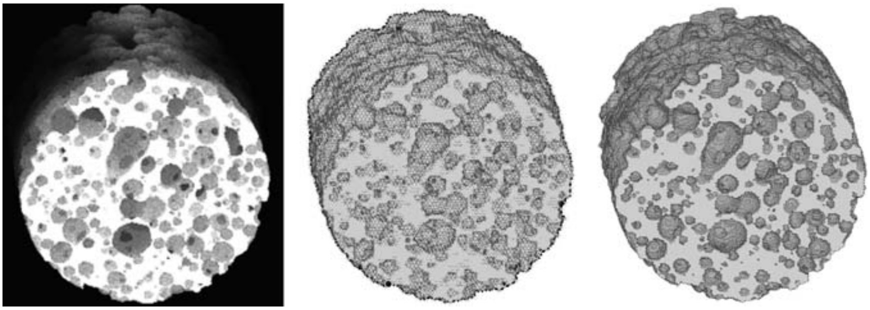

Fig. 6 Comparison of the scanned sample (*left*) with the lattice meshes, centre: lattice mesh with a beam length of 0.1 mm (683,490 elements); *right*: lattice mesh with a beam length of 0.05 mm (6,311,581 elements)

(segmented) 3D microstructure from the CT will be put as overlay onto the lattice; the pixels serve as nodes (Fig. 5 centre).

The assignment of the element properties is determined as follows: if both nodes of an element have the properties of the cement matrix, the resulting beam element will be assigned matrix properties, in all other cases the beam element will be removed immediately and results in void space (Fig. 5 right). With this rather straightforward approach, 3D lattices, which correspond to the real samples, can be constructed rather easily. The lattice mesh will be more accurate in comparison to the real samples the smaller the beam elements are selected (see Fig. 6).

Simulations were done with regular lattices with a beam length of 0.1 mm (683,490 beam elements) under uniaxial compression with $\alpha = 1$. The stiffness of the cement matrix is set to $E = 25\,GPa$; and the tensile strength of the matrix lattice elements was assumed to be 5 MPa. The illustrations of Fig. 7 show crack patterns at different loading stages. A vertical slice is made to depict the crack development inside the specimen. Up to the maximum force, crack initiation starts from the top and the bottom of the holes (under compression the stress intensity has the highest value there). These few small cracks grow vertical and parallel to the loading direction. After reaching the peak, macrocracks start to grow from “hole to hole” (possibly because of the stress intensity along the edges); these large localized cracks are not growing parallel to the loading direction.

It has to be mentioned that in this model a frictional mechanism has yet to be included. Moreover the used fracture law is still debatable.

6 Summary and Outlook

A loading stage was built and designed for the use inside a desktop tomograph. Testing samples in combination to X-ray scanning gives the possibility to reconstruct the 3D structure of specimens under various loadings to describe the material

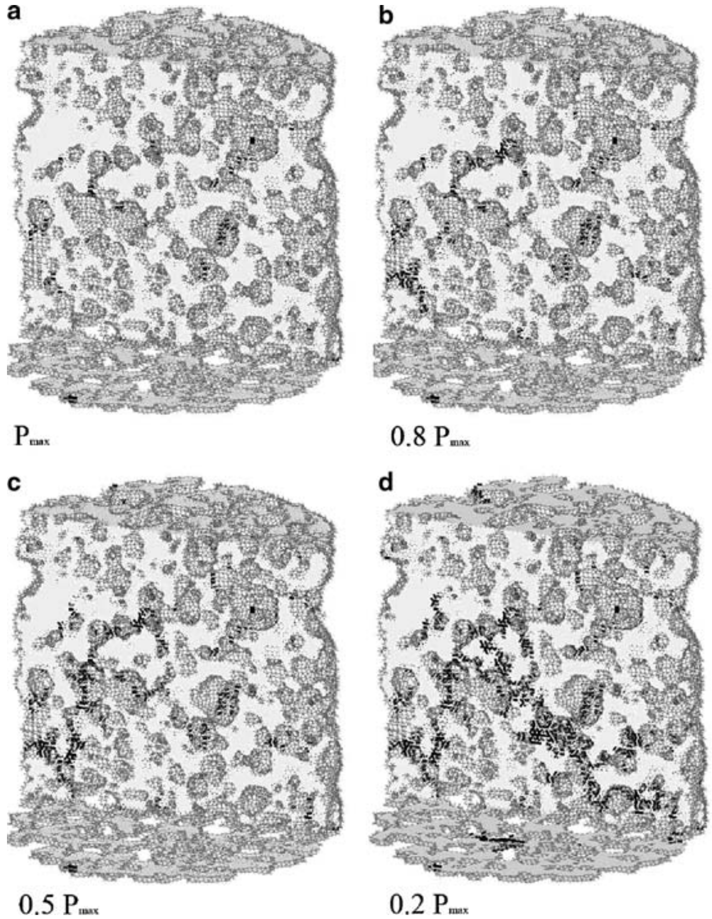

Fig. 7 Fracture simulation of a foamed cement paste specimen with a 3D lattice at different loading stages (*top left*: maximum load; next three stages: post peak)

behaviour and the failure mechanism under compression. The transfer of the 3D material structure from the tomography into a 3D lattice model for numerical simulations additionally allows the possibility of improving the failure criteria of the simulations as well as to improve the understanding of fracture of foamed cementitious materials under compression.

In the future, further investigations are planed on more samples with varying porosity to evaluate the effect of porosity on the material behaviour in detail. These tests will be done for both as physical and numerical experiment, thereby hopefully reaching the final goal of an improved lightweight material with favourable properties as low weight and good thermal conductivity. In addition the development of a failure criterion for compressive failure in numerical simulations using a 3D lattice beam model is one of the expected outcomes.

Acknowledgements This work was supported by SCANCO MEDICAL AG Bassersdorf, Switzerland, specifically the use of the table-top X-ray scanner. We would like to thank Ernst Bleiker from the Institute of Geotechnical Engineering for building the controls for the loading stage. Support by the Swiss National Supercomputing Centre CSCS in Manno (TI), where the numerical analysis was carried out, is gratefully acknowledged.

References

Lilliu G, van Mier JGM (2003) 3D lattice type fracture model for concrete. Engineering Fracture Mechanics 70:927–941

Margoldova J, van Mier JGM (1994) Simulation of compressive fracture in concrete. In: K.H. Schwalbe and C. Berger (eds) Proceedigs of the 10th European Conference on Fracture ECF 10, 1399–1409

Meyer D, van Mier JGM (2006) The influence of the foam behaviour on the properties of foamed cement paste. In Vogel et al. (eds) 6th International Ph.D. Symposium in Civil Engineering, ETH Zürich, Switzerland; Abstract p 96, Paper on CD

Meyer D, van Mier JGM (2007) Influence of different PVA fibres to the crack behaviour of foamed cement paste. In Carpinteri et al. (eds) 6th International Conference on Fracture Mechanics of Concrete and Concrete Structures, Catania, Italy, Taylor & Francis, London, pp 1359–1365

RILEM TC 148:SCC (2000) Test methods for measurement of the strain-softening behaviour of concrete under uniaxial compression. Materials and Structures 33:347–351

Schlangen E, van Mier JGM (1992) Experimental and numerical analysis of micromechanism of fracture of cement based composites. Cement Concrete Composites 14:105–118

Modeling and Simulation of Highly Porous Open Cell Structures: Elasto-Plasticity and Localization *Versus* Disorder and Defects

M.H. Luxner and H.E. Pettermann

Abstract The mechanical properties of open cell structures are investigated by Finite Element simulations. Various three-dimensional generic structures built from an elastic-plastic bulk material are treated both with regular architectures and disordered derivations thereof. Their elastic and elastic-plastic behavior as well as their susceptibility to deformation localization and their defect sensitivity are analyzed. The direction dependent responses are predicted and the governing deformation mechanisms at cell level are identified.

1 Introduction

Highly porous, cellular solids form the basis of many biological and engineering structures. The better understanding of the former and the application of the latter requires knowledge on the relationship between their architecture and their overall mechanical response.

Several analytical and numerical approaches have been developed for describing the mechanical behavior of cellular materials. Analytical models based on beam theory are derived in e.g. [1]. Numerical approaches for closed cell structures are treated e.g. in [2], open cell ones e.g. in [3].

In the present study the effect of structural disorder on the linear and nonlinear mechanical behavior is evaluated by the Finite Element Method (FEM) under consideration of elastic-plastic bulk material properties, large strain theory, and deformation localization.

First, the linear elastic properties are investigated by a periodic microfield approach. Based on three-dimensional periodic unit cell models the entire elastic

---

M.H. Luxner and H.E. Pettermann (✉)
Institute of Lightweight Design and Structural Biomechanics,
Vienna University of Technology, Vienna, Austria
pettermann@ilsb.tuwien.ac.at

H. Zhao, N.A. Fleck (eds.), *Mechanical Properties of Cellular Materials,*
IUTAM Bookseries 12,

tensors are predicted for six different generic structures with regular geometries. The anisotropic stiffness and the directional sensitivities are presented. Out of these six structures the two with the highest and the lowest degree of anisotropy are selected for further studies. On large periodic unit cells geometrical disorder of varying level is introduced to the structures and their effect on the linear elastic behavior is studied.

Second, the nonlinear mechanical behavior is investigated in detail for the two selected structures. Since this, in general, cannot be accomplished by means of periodic unit cell models, large finite sample models are employed which are loaded by uniaxial compression. Different orientations of the structural lattice with respect to the loading direction are realized. As for the linear cases, regular structures are considered first and then a systematic study on the influences of structural disorder is performed. Finally, the above investigations are extended to study the effect of various defects on the overall mechanical behavior in simple cubic architectures.

In a related project corresponding structures are built by rapid prototyping and tested experimentally [4].

2 Modeling Approaches

Six generic three-dimensional structures are selected in an effort to choose topologies with a variety of mechanisms governing their behavior. At first, all of them show regular geometries which are repeated periodically in all principal directions. Six different base cells to be investigated are shown in Fig. 1. They comprise Simple Cubic (SC), Kelvin (KV), Weaire Phelan (WP), Gibson Ashby (GA), Body Centered

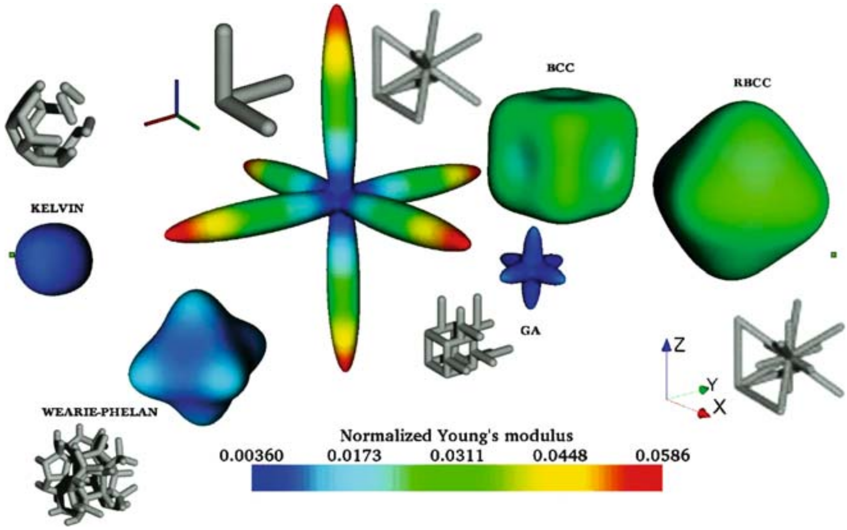

Fig. 1 Base cells of various generic structures and the predicted direction dependent Young's moduli

Cubic (BCC), and Reinforced Body Centered Cubic (RBCC) structures [5, 6]. Each structure consists of struts with circular cross sections of constant diameter. The dimensions of all base cells are $4 \times 4 \times 4$ mm. All base cells possess cubic material symmetry. Note that only struts belonging to a single base cell are shown. All investigations pertain to a relative density of 12.5%, except for the study of the density dependence which rely on range from 10% to 20%.

For periodic structures the consideration of a base cell is sufficient in most cases. However, when introducing structural disorder larger models are required. Disordered structures are generated for SC and KV topologies by modifying arrangements of $8 \times 8 \times 8$ base cells. The vertices of the regular geometries are shifted to random positions by a fixed distance. For the shifting direction a spatially random distribution is adopted. The shifting distance, δ, is expressed in fractions of the strut length, l, of a regular reference structure. Disorder magnitudes of $\delta/l = 1/16, 1/8, 1/4$, and $3/8$ are realized, see Fig. 2. Such disorder in the structures, however, increases the strut lengths and, consequently, affects the density. Thus, for representing the desired density the strut diameter is adapted accordingly.

Depending on the behavior to be predicted an appropriate modeling approach has to be selected. Two different approaches for representing the structures as infinite and finite media, respectively, are employed. The first approach is the unit cell (periodic microfield) method, e.g. [2], which is used for the linear elastic investigations.

The periodic unit cell approach shows severe shortcomings with respect to its ability of representing deformation localization since deformations cannot localize in arbitrary planes. To overcome these limits and to investigate aspects of the behavior of finite sized cellular solids, finite structures are modeled in the second approach. The uniaxial compressive response of cuboidal and cylindrical samples

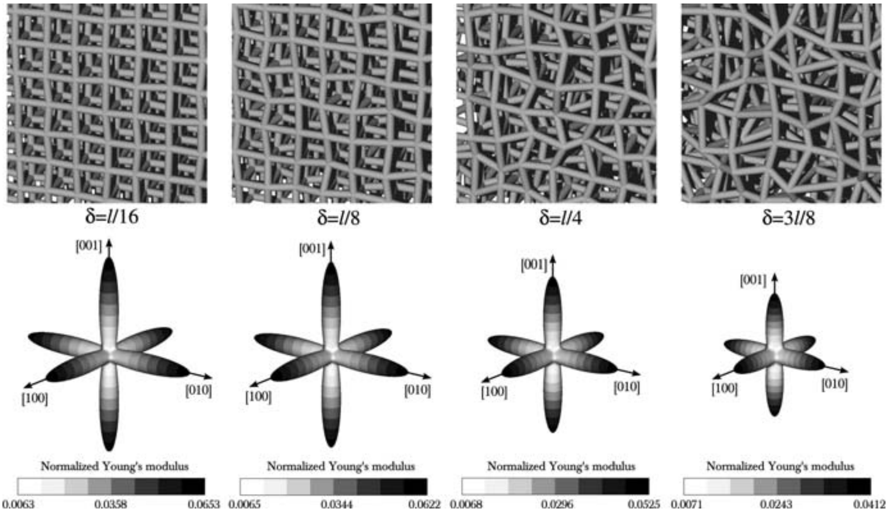

Fig. 2 Simple Cubic structures with various degrees of disorder and the predicted direction dependent Young's moduli [5]

which show lattice orientations of [001], [021], [011], and [111] is investigated. The top boundary conditions are assumed to represent a rigid plate, which remains parallel to the (001) plane, but can move freely otherwise and can rotate around the [001] axis. Furthermore, all degrees of freedom of the bottom face nodes are locked, representing a rigid plate which is fixed. The finite sample analyses account for large deformations.

Beam element based models are computationally cheap, however, straightforward modeling of a vertex suffers from two approximations. First, it does not account for multiple volumes at overlapping domains. Second, such models do not account for possible constraints in the vicinity of the vertices, caused by the material aggregation in these domains. Thus, the distribution of the material in the intersections of the struts should be considered in terms of stiffness and density [3]. To find the strut radius matching the desired relative density of the model the material distribution in a vertex is approximated by a sphere with a radius equal to the strut radius. The connected cylindrical struts end at the sphere's surface, which leaves gaps and may create overlaps. This approximation is used throughout this study for vertices connecting more than two struts. An adaptation of the stiffness in the vicinity of the vertices is introduced by using (quasi) rigid elements inside the spherical domain defined above. This adaptation is considered preferable for vertices connecting four or more struts.

All numerical investigations are carried out by means of the FEM package ABAQUS/Standard (*Version 6.5.3, ABAQUS Inc., Providence, RI*). Beam element based models are utilized throughout this study (except for the evaluation of the density dependence where continuum element models are used). At least four elements are used for the discretization of the compliant part of a strut. For the beam cross sections the number of Gauss points is chosen to be 24 (eight in circumferential direction times three in radial direction). No contact or self contact is considered. A verification of the beam modeling approach has been performed in [3].

When bifurcation buckling can become an issue, care has to be taken not to proceed along the trivial equilibrium path. For the regular SC structure loaded in the principal direction a small transverse force is applied to induce buckling affine deformations. For all other cases, localization (if existing) is triggered by imperfections inherent the FEM models or by structural disorder.

The strut material is isotropic, elastic-plastic, and strain rate independent. The Young's modulus of the bulk material is 1,700 MPa, the Poisson's ratio is 0.3, and the yield stress is 18 MPa. Ludwik type hardening is assumed with a smooth transition to ideally plastic behavior at 42 MPa true stress and 5% logarithmic strain.

3 Elastic Results

Following [1] the Young's modulus, E, is proportional to,

$$E(\underline{\phi}) \propto {\rho_{\mathrm{rel}}}^{\beta(\underline{\phi})}, \tag{1}$$

Table 1 Density exponent for various structures at different directions in the range of relative density from 10% to 20% [3]

Structure	[001]	[011]	[111]
SC	1.00	1.83	1.85
GA	1.98	1.74	1.76
BCC	1.03	1.02	1.01
RBCC	1.01	1.02	1.02

where ρ_{rel} is the relative density, β is the density exponent, and $\underline{\phi}$ reflects the orientation dependence. For selected regular structures and directions these predicted exponents are listed in Table 1 [3]. The exponent indicates the deformation mechanism, as being close to one for normal or shear loading modes and being close to two for bending modes.

Next, the elastic anisotropy for a relative density of 12.5% is studied [3, 5]. Periodic unit cell models of single base cells are employed and the required number of independent load cases is solved for each structure. From these responses the entire elastic tensors are assembled. Three-dimensional visualizations of the normalized Young's moduli of these structures are given in Fig. 1. The SC structure shows the most pronounced anisotropy and directional sensitivity with respect to the Young's modulus. It exhibits very stiff behavior in the principal directions and a strong decrease of the stiffness apart the principal directions. In contrast, the KV structure is the most isotropic one and exhibits nearly equal values for the normalized Young's modulus in all directions. Because of the significant difference in their anisotropy the SC and the KV structure are chosen for subsequent investigations on the influence of structural disorder. Unit cell models are employed but now consist of some $8 \times 8 \times 8$ base cells. Inside the cells structural disorder is introduced as described in Section 2. Four different degrees of disorder are analyzed. For each of them five different models (having the same statistical descriptors but different discrete realizations) are generated and the elastic tensors are predicted [5].

In the case of the SC structure, Fig. 2, it can be seen that with increasing disorder the normalized Young's moduli in the principal directions decrease, whereas for the other directions the normalized Young's moduli increase. A pronounced anisotropy remains even for the most disordered case.

The KV structure shows a very mild decrease of the normalized Young's moduli for all directions (not shown). For the most disordered case the Young's moduli are nearly uniform with respect to the direction, i.e. isotropy is approached closely.

4 Nonlinear Behavior and Localization

Inspired by nature (e.g. cancellous bone), the influence of structural disorder on the nonlinear mechanical behavior is investigated on finite samples which are loaded by uniaxial compression.

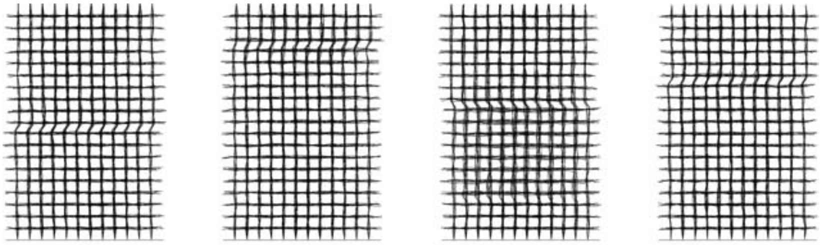

lattice orientation [001]

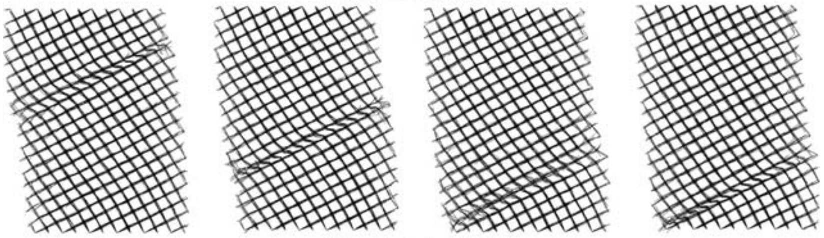

lattice orientation [021]

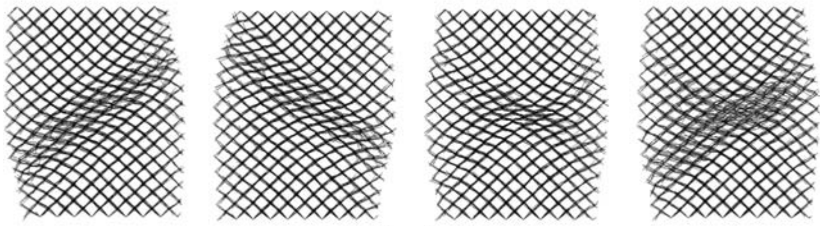

lattice orientation [011]

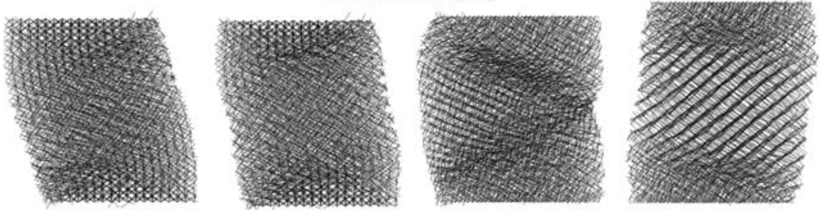

lattice orientation [111]

Fig. 3 Predicted deformation patterns of cylindrical samples under uniaxial compression with disorder $\delta/l = 1/8$ for various lattice orientations [7]

In Fig. 3 the predicted deformation patterns of cylindrical samples with disorder under uniaxial compression are presented [7]. For both the [001] and the [021] orientations localization takes place in principal structural planes extending one and two layers, respectively. Localization starts at different positions, but the localization pattern is always the same. Two different localization patterns can be seen for lattice orientation [011]. The first one can be described as a band of three to four adjacent layers of collapsing cells leaving two non-localizing domains. The second observed localization pattern shows a concentration of deformation in the center of the sample surrounded by collapsing cells in the shape of an “X”.

From the deformed KV structures (not shown) no localization is obvious. For all cases the distributions of the deformations are rather homogeneous over the height of the samples. Also any influence of disorder on the behavior can hardly be seen.

Details can be found in [5–7] where SC and KV structures are studied in detail. Deformation plots and overall stress strain curves are given. Also given are diagrams showing the distribution and evolution of the mesoscopic strain rates and energy densities, and histograms showing the energy distribution in the models.

5 Influence of Defects

Three different classes of defects are introduced by removing a constant number of struts from the structures [6], i.e. for all types of defects the same amount of bulk material is removed from the samples and, therefore, their relative density is decreased from 12.5% to 12.25%.

For the first class of defects 108 non-connected single struts are randomly removed, see Fig. 4 (left). As a second approach 18 vertices are removed from the structures, Fig. 4 (middle). The third class of defects is generated by removing three clusters of struts consisting of 36 struts each, Fig. 4 (right). For each class of defects and each lattice orientation five sets of defects are generated.

The differences in the nonlinear responses of the various structures are discussed in terms of the peak stresses and the strains at which they occur, in the following denoted as “peak strains”. The average peak stresses, the corresponding average peak strains, and the standard deviations (indicated by the error bars) are printed in stress–strain diagrams [6].

First, the structures with lattice orientation (001) are discussed, Fig. 5. Irrespective of the level of the structural disorder, the structures without defects sustain the

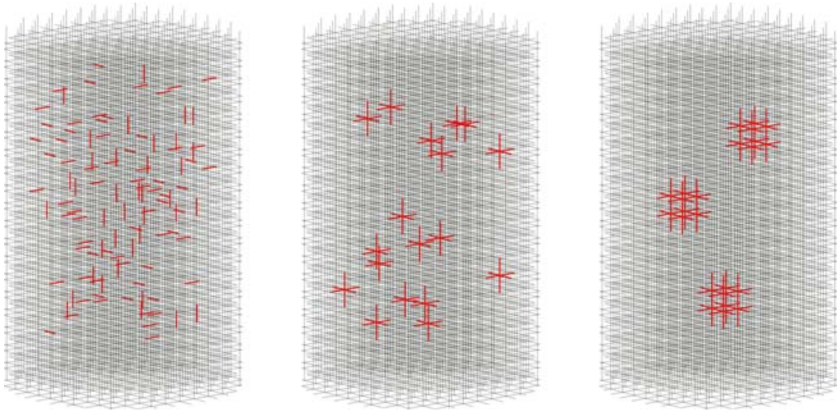

Fig. 4 Three different classes of defects in a simple cubic structure; each class of defects consists of 108 removed struts [6]

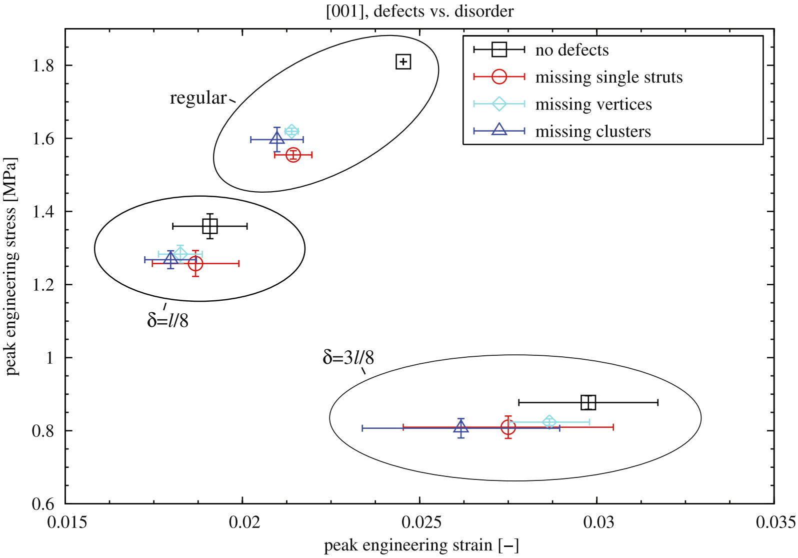

Fig. 5 Averages of the peak stresses and the peak strains of regular and disordered cylindrical Simple Cubic structures with and without defects for lattice orientation [001]; the error bars indicate the standard deviations [6]

highest stresses and strains, followed by structures with missing vertices, missing clusters, and missing single struts. Due to the defects the peak stresses of the regular structures are decreased by about 11–14%, whereas for the disordered structures a decrease of about 6–7% and 6–8% is observed, i.e. for disordered structures with lattice orientation (001) defects result in a smaller decrease of the peak stress than for a corresponding regular structure. With respect to the stiffness the missing single strut defects always result in the strongest decrease [6].

Figure 6 shows the predicted responses for the structures with lattice orientation [021]. Similarly to the structures with lattice orientation [001], the structures without defects sustain the highest stresses and strains, followed by the structures with missing vertices. For the other defects no consistent trend regarding the order of the level of the peak stresses is observed. The missing clusters result in the lowest peak stresses for regular and slightly disordered structures, whereas the missing single struts exhibit the lowest peak stresses for the highly disordered structures. The variations of the peak stresses and strains tend to increase with increasing level of structural disorder. Other lattice orientations are discussed in [6].

As a general trend it is observed that for all investigated lattice orientations the peaks of the stress–strain curves of the defective structures with high disorder move closer to each other. This shows that in terms of the peak stresses and its corresponding strains the type of the defect has less influence within a strongly disordered structure, but that the amount of the removed material becomes the governing aspect.

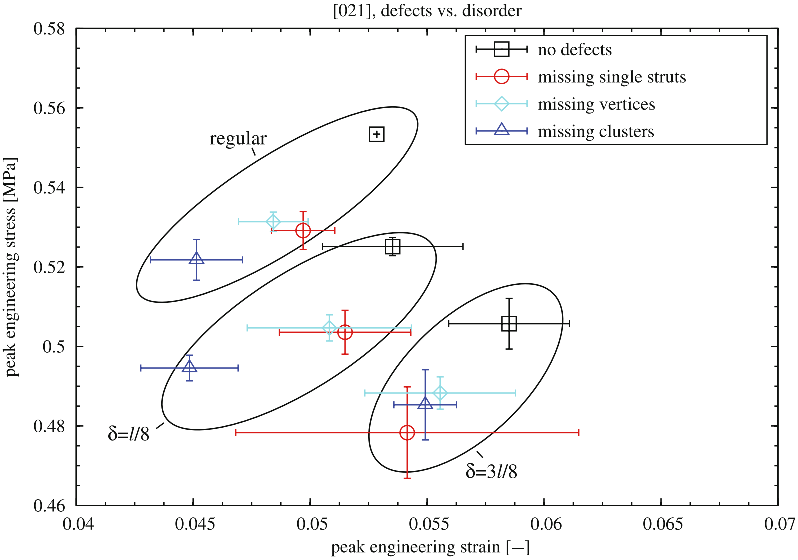

Fig. 6 Averages of the peak stresses and the peak strains of regular and disordered cylindrical Simple Cubic structures with and without defects for lattice orientation (021); the error bars indicate the standard deviations [6]

6 Conclusions

In the present work numerical simulations regarding the mechanical behavior of regular and disordered open cell structures are carried out. Linear elastic as well as nonlinear behavior including deformation localization and defect sensitivity are studied. Three-dimensional Finite Element models based on beam elements with specific consideration of the vertex regions are used, taking into account elastic-plastic bulk material behavior, and large strain theory.

Elastic constitutive characterization of various generic structures is performed in terms of density and directional dependence, and the governing deformation mechanisms are identified. The Simple Cubic and the Kelvin type structures are studied further. Various degrees of structural disorder are introduced and the effects on the linear elastic and nonlinear behavior are predicted. For the Simple Cubic structure the disorder leads to a decrease of anisotropy. Next, the effect of structural disorder on the localization of the deformation is studied under uniaxial compression. For the Simple Cubic structures localization is found for the regular and slightly disordered structures. At the highest level of disorder investigated localization is no longer occurring in Simple Cubic structures. The Kelvin structures do not exhibit a marked direction dependence in the nonlinear regime and no localization is found.

Finally, the effect of three different types of defects on the mechanical behavior of regular and disordered open cell structures is investigated. It is shown that structural disorder reduces the defect sensitivity.

Acknowledgements This work was financially supported by the AUSTRIAN SCIENCE FUND under contract P15852.

References

1. Gibson LJ, Ashby MF 1997 (1997) Cellular Solids: Structure and properties, second ed. Cambridge University Press, Cambridge, UK
2. Daxner T, Böhm HJ, Seitzberger M, and Rammerstorfer FG (2002) Modeling of Cellular Metals. In: Degischer HP, Kriszt B (eds) Handbook of Cellular Metals, 245–280, Wiley-VCH, Weinheim, Germany
3. Luxner MH, Stampfl J, Pettermann HE (2005) J Mater Sci 40:5859–5866
4. Stampfl J, Seyr MM, Luxner MH, Pettermann HE, Woesz A, Fratzl P (2004) Regular, Low Density Cellular Structures - Rapid Prototyping, Numerical Simulation, Mechanical Testing. In: Landis WJ, Orme C, Wang R (eds) Biological and Bioinspired Materials and Devices - MRS Spring Meeting 2004, Proceedings of Materials Research Society Symposium 823, W8.8, San Francisco, CA, USA
5. Luxner MH, Stampfl J, Pettermann HE (2007) Int J Sol Struct 44:2990–3003
6. Luxner MH (2006) Modeling and simulation of highly porous open cell structures — elasto-plasticity and localization versus disorder and defects. Ph.D. thesis, Vienna University of Technology, Vienna, Austria
7. Luxner MH, Stampfl J, Woesz A, Fratzl P, Pettermann HE (2006) Influence of Structural Disorder on the Performance of 3D Open Cell Structures. In: Mota Soares CA et al. (eds) Proceedings of the III European Conference on Computational Mechanics (ECCM-2006), Lisbon, Portugal

Mechanical Properties of Crimped Mineral Wools: Identification from Digital Image Correlation

J.-F. Witz, F. Hild, S. Roux, and J.-B. Rieunier

Abstract Mineral wool is usually used for thermal and acoustic insulation with no need for mechanical performances. However there are some applications where this material must have a significant stiffness and strength to sustain mechanical loads. Crimping is performed to enhance the mechanical properties of mineral wool. As this process is governed by a lot of parameters one looks for ways to characterize the mechanical properties one-line. The aim of the present paper is to present an identification technique for the elastic properties of such a medium, based on texture analysis, digital image correlation, and a Finite Element based identification. Local anisotropic elastic behavior is identified through a combination of different tools based on image processing. First the local orientation map is determined from a reference image. Second, a series of images captured at different loading stages is analyzed with a digital image correlation code to estimate the local displacement field. Last, an inverse problem procedure is applied to evaluate the four elastic moduli of the material. The first experimental step is to perform mechanical tests on this type of material, and then the measurement and identification steps. A hexapod is used to perform a biaxial experiment (compression and shear).

Keywords Image correlation · Identification · Anisotropic media · Mineral wool · Inverse problem

1 Introduction

Mineral wool is naturally textured product used for its thermal and acoustic properties. The natural layering of this material leads to a low thermal conductivity,

---

J.-F. Witz, F. Hild (✉), and S. Roux
LMT-Cachan, ENS Cachan/CNRS-UMR 8535/Université Paris 6,
61 avenue du Président Wilson, F-94235 Cachan Cedex, France,

J.-F. Witz and J.-B. Rieunier
CRIR, Isover-Saint-Gobain, 19 rue Emile Zola,F-6290 Rantigny, France
witz@lmt.ens-cachan.fr

H. Zhao, N.A. Fleck (eds.), *Mechanical Properties of Cellular Materials,*
IUTAM Bookseries 12,

and a very compliant material. When mechanical properties are required, an on-line process called *crimping*, which aims at modifying the local orientation of fibers, and therefore enhancing their mechanical performances. Both crimped and non-crimped products display a local anisotropic structure, and for the crimped products the preferential orientation varies spatially very significantly. The crimping process depends on several parameters that lead to different structures with different mechanical properties.

The complexity of the microstructure coupled with the local and unknown mechanical properties make an *a priori* prediction of overall properties based on their specific texture extremely desirable, this goal is being difficult to achieve because of the complexity of the microstructure. It is proposed in the present study to tackle this problem by exploiting different image processing techniques. The first one [1], based on a single picture of the material, consists in analyzing the "texture", or the map of preferential orientation, as well as the degree of anisotropy. The second one relies on the use of Digital Image Correlation (DIC), a photomechanics technique [2], developed to estimate displacement fields from various pictures of a specimen subjected to a mechanical loading. Last, an anisotropic elastic modeling is proposed, using the anisotropy analysis. The latter is used in order to identify the unknown anisotropic elastic moduli of elementary volumes by using measured displacement fields as references. A scheme of the different steps is presented in Fig. 1.

Section 2 introduces the material under study and the various textures which can be produced through crimping. Section 3 presents briefly the local texture analysis and its results on the crimped specimen under consideration. Section 4 gives the basics of the DIC procedure that allows one to obtain displacement fields decomposed over a continuous bilinear interpolation basis. A finite-element modeling of the anisotropic elastic solid modeling adopted herein is introduced in Section 5.

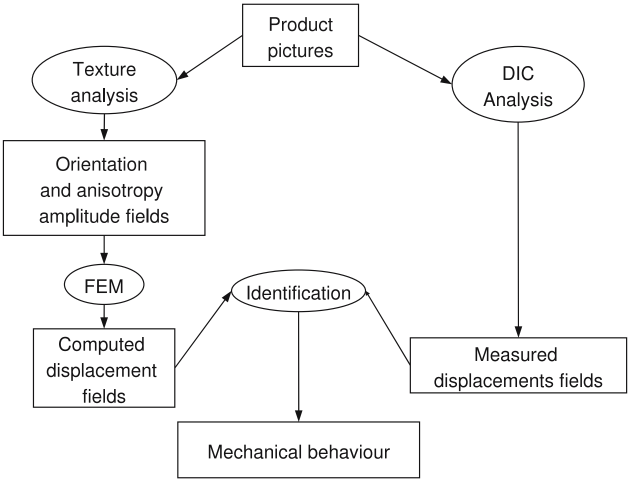

Fig. 1 Identification process from digital images to elastic parameters of mineral wool

The key procedure of identification of the local anisotropic elastic properties is presented in Section 6. Section 7 presents the experimental biaxial set-up. The results of the identification process are shown in Section 8. Finally, Section 9 presents the results of the computed displacement fields and their comparison with results of a experimental compression/shear test.

2 Crimped Glass Wool

Glass wool is a cellular solid made of glass fibres with micrometric diameter and millimetric to centimetric length sprayed with a binder, and cured in an oven for freezing the arrangement of the fibres and hence providing some elasticity. However, as such, the material is extremely compliant, a property used to reduce its volume for transport and storage, while preserving its ability to recover its nominal density for thermal insulation use. When mechanical performance are demanded (typically medium density products), the fiber mat is processed before the curing stage to produce a structure endowing the material with a higher mechanical strength. This step is called crimping and it produces a better mechanical behavior due to a more favorable fiber orientation. However, the increase of stiffness goes together with an enhanced thermal conductivity. This duality can be balanced depending on applications. The crimping process shown schematically in Fig. 2 (top) performs a compression of the fibre mat both across its thickness and along the line direction

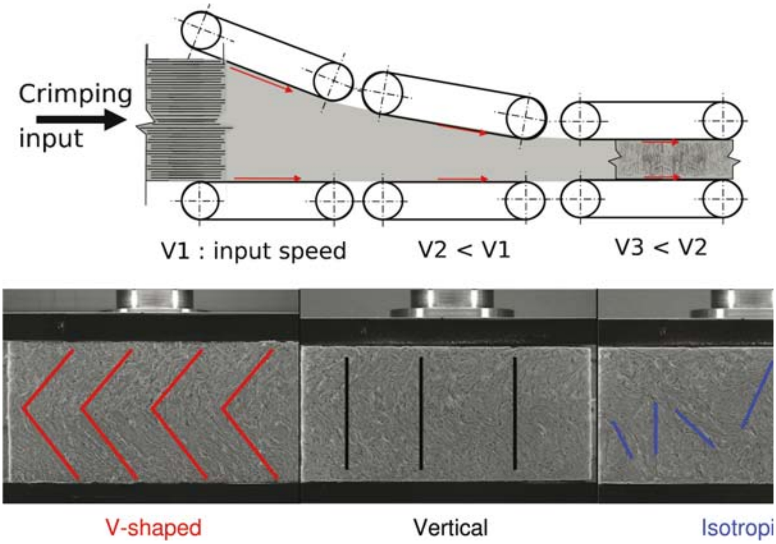

Fig. 2 Schematic view of the crimping process (*top*) and examples of different textures produced through crimping (*bottom*), with characteristic features such as “V-shaped” crimping (*left*), fine-scale vertical texture (*center*), and coarse isotropic texture (*right*)

because of the progressive reduction of velocity of the conveyor belts in which the mat is fed. A horizontal compression is taking place at each belt transition which produces a "buckling" or "folding" of the layers of higher fiber density. This process modifies significantly the fibre orientation as shown in some examples in Fig. 2 (bottom). The elastic response of the finished product and its loading abilities are very sensitive to the different parameters of this crimping process. The aim of this study is to able to predict the mechanical performances from a simple examination of its texture.

3 Anisotropy Analysis

The detection of local anisotropy is performed from black and white images of a section of the material. The direction of longer persistence of the grey level is defined as the principal axis of anisotropy. A lot of methods use the gradient of pictures to capture changes in orientation assuming the image to be sufficiently smooth [3, 4]. The method used here does not require this smoothness assumption and allows to capture the anisotropy encoded by the fine texture (*i.e.,* high frequency modes) [1]. The analysis is based on the regularized correlation texture tensor of small sub-images, i.e. zones of interest (ZOI) extracted from a digital picture of the product face. Let $f(x)$ be the gray-scale value of each pixel of the subimage. The following tensor is computed from the discrete Fourier transform $\tilde{f}(\mathbf{k})$.

$$\mathbf{T} = \iint |\tilde{f}(\mathbf{k})|^2 \frac{\mathbf{k} \otimes \mathbf{k}}{|\mathbf{k}|^{2\alpha}} \mathrm{d}\mathbf{k} \tag{1}$$

For $\alpha = 0$, the above tensor is interpreted as the curvature tensor of the autocorrelation function at the origin. Its two orthogonal eigen-vectors provide the directions of highest and least persistence of the gray-levels and hence the anisotropy axis of the texture of the sub-image. In case of non-smooth images, the curvature tensor of the auto-correlation does not exist, and hence a power-law filtering (factor $|\mathbf{k}|^{2\alpha}$) is introduced to smoothen the autocorrelation and render the estimation less prone to pixel-scale noise. The parameter α is evaluated a priori from the regularity of the analyzed image. The deviatoric part of the tensor Eq. (2)

$$A = \frac{\mathbf{T} - 0.5tr(\mathbf{T})\mathbf{I}}{tr(\mathbf{T})} \tag{2}$$

gives an estimate of the amplitude of the anisotropy, in addition to the dominant orientation. Figure 3 shows an example of the extraction of the principal orientation map on a crimped structure (specimen 90) with sub-image size equal to 32 × 32 pixels. The dominant orientation and anisotropy amplitude are defined locally, there is no continuity between the different ZOIs.

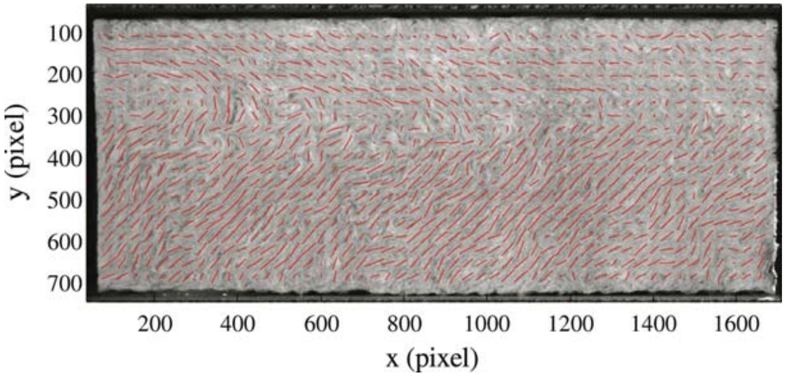

Fig. 3 Anisotropy field of the studied specimen superimposed on the original image

4 Displacements Field Measurement

The texture of the mat after crimping is strongly heterogeneous, so it is impossible to use strain gauges or any method that needs contact. For this purpose, a full field analysis of the displacement under different loadings is useful. A digital image correlation (DIC) technique [5] is applied to a series of pictures taken at different stages of loading, from a side view. The specificity of the latter is that it provides a continuous displacement field based on finite element shape functions (quadratic elements, polynomials of order 1 in both space directions). The latter techniques allows one to obtain both a good resolution (32×32 pixels per element) and good accuracy (5×10^{-3} pixel on the pictures used) in the measurement. The scale is 0.125 mm by pixel. Let $f(\boldsymbol{x})$ and $g(\boldsymbol{x})$ be a gray-scale representation of the images of a reference and deformed image respectively. One notes that contrary to conventional materials that look uniform and need a paint speckle sprayed on them to obtain a random texture on the picture, mineral wools are sufficiently heterogeneous to be photographed without any surface preparation. The digital image correlation technique is based on the assumption of the passive advection of the microstructure, so that the displacement field $\mathbf{u}(\boldsymbol{x})$ obeys the following *optical flow conservation* property

$$g(\boldsymbol{x}) = f[\boldsymbol{x} + \boldsymbol{u}(\boldsymbol{x})] \tag{3}$$

The ill-posed problem of determining the displacement field is first regularized by prescribing a restricted subspace for $\mathbf{u}$, here chosen to be finite-element shape functions, $N_n(\boldsymbol{x})$, quadratic elements, polynomials of order 1 in both space directions

$$u_\alpha(\boldsymbol{x}) = \sum_{\alpha,n} a_{\alpha n} N_n(\boldsymbol{x}) \tag{4}$$

where α gives the direction x or y of the component of the displacement, and n labels the different shape functions. This basis will reveal convenient for the subsequent identification step, as the same mesh will be used. Since the optical flow conservation cannot hold strictly pixel-wise, a weaker formulation is substituted (least squares minimization)

$$\boldsymbol{a} = \text{argmin} \left\{ \iint \left(g(\boldsymbol{x}) - f[\boldsymbol{x} + \sum_n \boldsymbol{a}_n N_n(\boldsymbol{x})] \right)^2 \mathrm{d}\boldsymbol{x} \right\} \tag{5}$$

As Eq. (5) is non linear, a multiscale approach using a Newton linearization scheme on a series of low-pass filtered images down to the original (unfiltered) ones is used. Thus the solution is obtained iteratively from solution of linear problems and deformed image corrections, until the best match between the deformed and the reference image. Each linear problem consists in solving

$$\boldsymbol{Ma} = \boldsymbol{b} \tag{6}$$

where

$$M_{\alpha n \beta m} = \iint [N_m(\boldsymbol{x}) N_n(\boldsymbol{x}) \partial_\alpha f(\boldsymbol{x}) \partial_\beta f(\boldsymbol{x})] \mathrm{d}\boldsymbol{x} \tag{7}$$

and

$$b_{\alpha n} = \iint [g(\boldsymbol{x}) - f(\boldsymbol{x})] N_n(\boldsymbol{x}) \partial_\alpha f(\boldsymbol{x}) \mathrm{d}\boldsymbol{x} \tag{8}$$

The matrix $\boldsymbol{M}$ is symmetric, positive (when the system is invertible) and sparse. These properties are exploited to solve the linear system efficiently.

5 Material Modeling

To obtain the computed displacement fields, a Finite Element code was written. It takes into account the local anisotropy of the material. The material is modeled as a locally orthotropic medium. The local orientation and anisotropy amplitude are included in the model from the direct texture analysis of the studied sample. Locally, the material is assumed to be characterized by an anisotropic elasticity tensor characterized by four elasticity values, S_{nn}, S_{nt}, S_{tt} and S_{uu}. If the anisotropy amplitude $A = 1$, the material is locally non-crimped, and thus, the original elasticity tensor is simply rotated to align to the determined direction of anisotropy from the texture analysis. Otherwise (i.e., $A < 1$), it is assumed that the crimping takes place at a smaller length scale than the element size, and an equivalent elasticity tensor is assumed to result from a homogenization procedure. In the present case, a Reuss' approximation (all directions are "equally loaded") is made

$$\langle \boldsymbol{K} \rangle^{-1} = \int_{-\infty}^{\infty} \boldsymbol{K}^{-1}(\theta) p(\theta) \mathrm{d}\theta \tag{9}$$

where $\boldsymbol{K}(\theta)$ denotes the intrinsic elasticity tensor rotated by an angle θ , and $p(\theta)$ is a Gaussian distribution adjusted so that its mean and width match the determined local orientation and anisotropy amplitude. The effect of the anisotropy amplitude is thus such that in its principal axis, the elasticity tensor has the following form.

$$
\begin{aligned}
\langle \boldsymbol{S}_{11} \rangle^{-1} &= \frac{3 \cdot \langle \boldsymbol{S}_{nn} \rangle^{-1} + 3 \cdot \langle \boldsymbol{S}_{tt} \rangle^{-1} + 2 \cdot \langle \boldsymbol{S}_{nt} \rangle^{-1} + \langle \boldsymbol{S}_{uu} \rangle^{-1}}{8} \cdots \\
&\cdots + \frac{\langle \boldsymbol{S}_{nn} \rangle^{-1} - \langle \boldsymbol{S}_{tt} \rangle^{-1}}{2} \cdot A + \frac{\langle \boldsymbol{S}_{nn} \rangle^{-1} + \langle \boldsymbol{S}_{tt} \rangle^{-1} - 2 \cdot \langle \boldsymbol{S}_{nt} \rangle^{-1} - \langle \boldsymbol{S}_{uu} \rangle^{-1}}{8} \cdot A^4 \\
\langle \boldsymbol{S}_{12} \rangle^{-1} &= \frac{\langle \boldsymbol{S}_{nn} \rangle^{-1} + \langle \boldsymbol{S}_{tt} \rangle^{-1} + 6 \cdot \langle \boldsymbol{S}_{nt} \rangle^{-1} - \langle \boldsymbol{S}_{uu} \rangle^{-1}}{8} \cdots \\
\cdots &+ \frac{- \langle \boldsymbol{S}_{nn} \rangle^{-1} - \langle \boldsymbol{S}_{tt} \rangle^{-1} + 2 \cdot \langle \boldsymbol{S}_{nt} \rangle^{-1} + \langle \boldsymbol{S}_{uu} \rangle^{-1}}{8} \cdot A^4 \\
\langle \boldsymbol{S}_{22} \rangle^{-1} &= \frac{3 \cdot \langle \boldsymbol{S}_{nn} \rangle^{-1} + 3 \cdot \langle \boldsymbol{S}_{tt} \rangle^{-1} + 2 \cdot \langle \boldsymbol{S}_{nt} \rangle^{-1} + \langle \boldsymbol{S}_{uu} \rangle^{-1}}{8} \cdots \\
\cdots &+ \frac{\langle \boldsymbol{S}_{tt} \rangle^{-1} - \langle \boldsymbol{S}_{nn} \rangle^{-1}}{2} \cdot A + \frac{\langle \boldsymbol{S}_{nn} \rangle^{-1} + \langle \boldsymbol{S}_{tt} \rangle^{-1} - 2 \cdot \langle \boldsymbol{S}_{nt} \rangle^{-1} - \langle \boldsymbol{S}_{uu} \rangle^{-1}}{8} \cdot A^4 \\
\langle \boldsymbol{S}_{66} \rangle^{-1} &= \frac{\langle \boldsymbol{S}_{nn} \rangle^{-1} + \langle \boldsymbol{S}_{tt} \rangle^{-1} - 2 \cdot \langle \boldsymbol{S}_{nt} \rangle^{-1} + \langle \boldsymbol{S}_{uu} \rangle^{-1}}{8} \cdots \\
&\cdots \frac{- \langle \boldsymbol{S}_{nn} \rangle^{-1} - \langle \boldsymbol{S}_{tt} \rangle^{-1} + 2 \cdot \langle \boldsymbol{S}_{nt} \rangle^{-1} + \langle \boldsymbol{S}_{uu} \rangle^{-1}}{8} \cdot A^4
\end{aligned} \tag{10}
$$

As a consequence, the entire elasticity map is obtained from the texture analysis of the real material, and is parameterized by the four elasticities of an ideal uncrimped material. Using experimentally measured boundary conditions (displacement from DIC), a standard finite element computation is performed to compute the entire displacement fields.

6 Identification Technique

Different techniques exist to identify elastic properties. A first class called virtual fields method uses special fields (i.e., virtual strain fields) to extract unknown elastic parameters. A linear system is obtained and solved to get the unknowns [6, 7]. A second class of technique uses the constitutive law gap to identify isotropic and anisotropic elastic properties [8]. Another route, the Equilibrium gap method [9, 10], exploits the equilibrium conditions written at the nodes of a FE model where the displacement is known. In the present case, the local properties will depend on the dominant orientation. Consequently the finite element model updating [11] (FEMU) is preferred. Another reason is that the measured displacement field is directly compatible with finite element simulations.

6.1 Model Updating Procedure

The Model Updating procedure determines the elastic constants so that the computed displacement field matches as well as possible the measured displacement field. The computed displacement field is obtained by solving

$$\boldsymbol{K}_{\text{FEM}}(\{S_i\}).\mathbf{U}_0 = 0 \tag{11}$$

for all internal nodes, and U_0 imposed from the measured values at the boundary. In this expression, $\boldsymbol{K}$ is the stiffness matrix that depends non-linearly on the four elastic constants S_i.

Once a first estimate of the displacement field is computed, four additional "influence" fields, U_i, $i = 1, \ldots, 4$ are computed that correspond to incremental variations of the displacement field for a corresponding change in each of the elastic constant

$$\mathbf{K}_{\text{FEM}}(\{S_i\}).\mathbf{U}_i = -\frac{\partial \mathbf{K}_{\text{FEM}}}{\partial S_i}.\mathbf{U}_0 \tag{12}$$

The difference between the measured $\mathbf{U}_m$ and computed $\mathbf{U}_0$ displacement fields is then projected onto the four influence fields through the minimization of the following objective function

$$J = \iint \left(\mathbf{U}_m - \mathbf{U}_0 - \sum_i \gamma_i \mathbf{U}_i \right)^2 \mathrm{d}\boldsymbol{x} \tag{13}$$

The components γ_i allow one to correct the elastic constants to new values S'_i such that

$$S'_i = S_i \exp(\gamma_i / S_i) \tag{14}$$

The procedure is carried over iteratively down to convergence. The residual error field defined in Eq. (15), where σ^2 is the variance of the measured displacement field is used to quantify the discrepancy density after identification. This identification process only gives the elastic parameters up to a multiplicative constant. There is no way to evaluate the absolute value as no Neumann boundary conditions are used.

$$e(\boldsymbol{x}) = (1/\sigma^2)(\mathbf{U}_m(\boldsymbol{x}) - \mathbf{U}_0(\boldsymbol{x}))^2 \tag{15}$$

7 Experimental Set-up and Identification

In order to validate the model a non-classical loading path has been imagined. The displacement fields are obtained using only one camera, so the loading path must be in the image plan of the camera.

The loading path is a combination of horizontal and vertical displacements as shown in Fig. 4

Biaxial tests have been performed on a hexapod (Fig. 5) to induce compressive and shear loadings. This device offers the possibility to follow complex strain path and opens the way to characterize the mat under loadings close to service conditions. Although the present analysis is limited to the elastic regime, extensions to non-linearities are also accessed experimentally with this set-up.

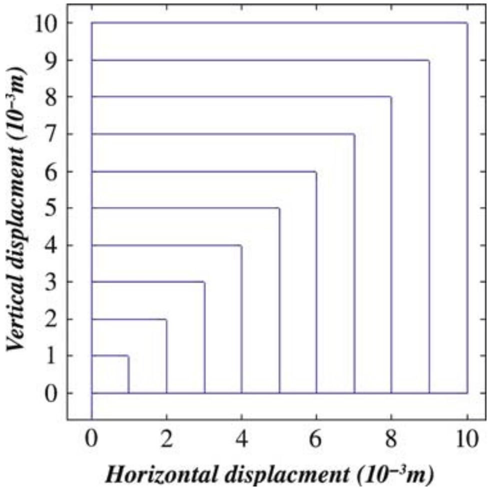

Fig. 4 Load history along horizontal/vertical directions

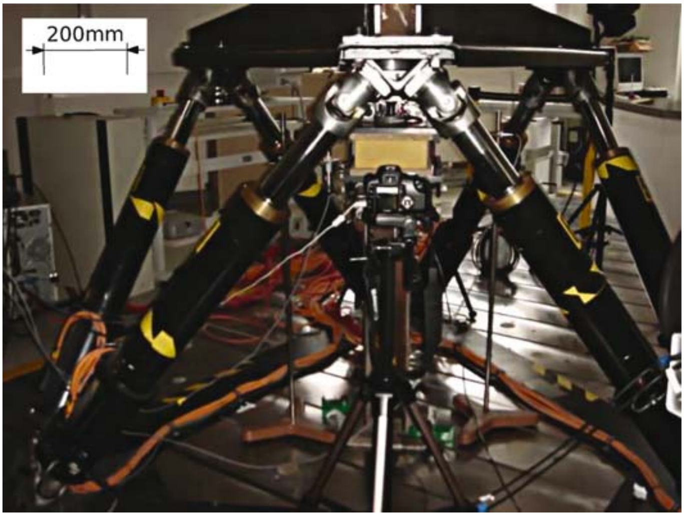

Fig. 5 Hexapod instrumented with camera for DIC measurement of a mechanical test on glass wool

8 Identification Results

Experimental data were obtained from digital image correlations. The identification has been tested on both uniaxial compression and combined compression/shear tests (Table 1).

Fig. 6 shows that a good agreement is observed between measured and predicted displacement fields.

Table 1 Identified local elastic properties (kPa) of specimen

	S_{nn}	S_{nt}	S_{tt}	S_{uu}
Identified value	100.22	0	6.90	95.60

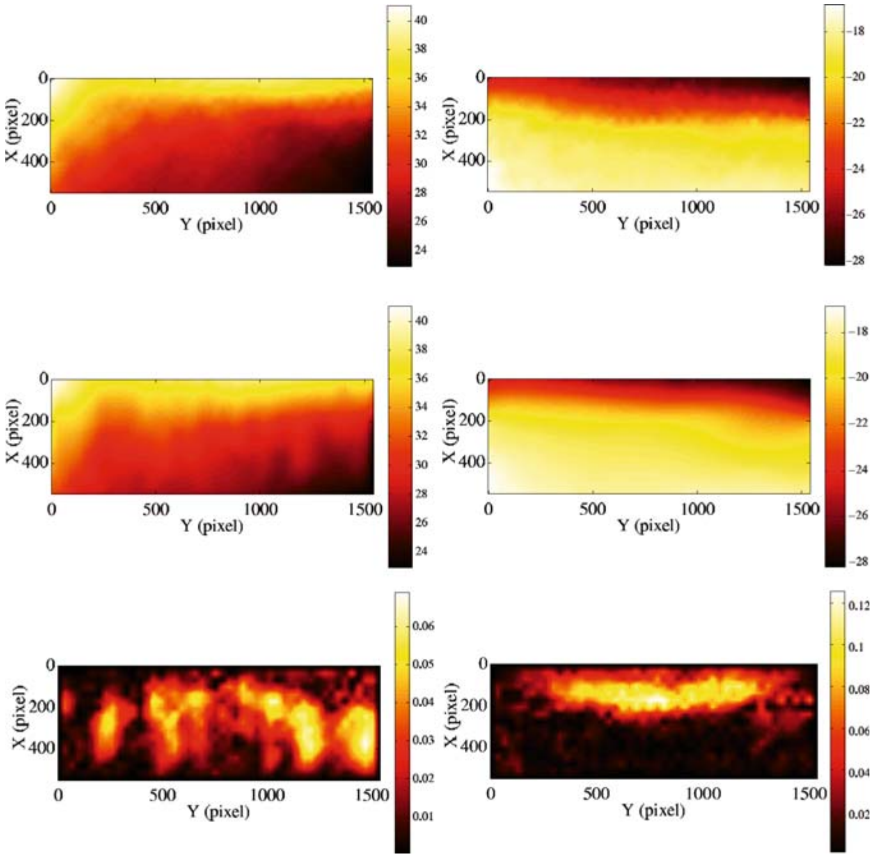

Fig. 6 Comparison between vertical (*left*) and horizontal (*right*) fields, measured displacement on the top, computed ones on the middle, and error on the bottom, for given compressive/shear loading on the identified specimen

The global error defined as the mean of Eq. (15) is less than 3.1%. The agreement between measured and predicted fields is considered as quite good considering the simplifying assumptions.

9 Validation

In order to test the predictive power of the previous approach, the displacement field of a series loading stage on the same specimen has been computed based on the previously determined elastic constants. Figure 7 show a direct comparison between measurements and computation of both components of the displacement field. Two cases are shown in the sequel which have the best and worst global error.

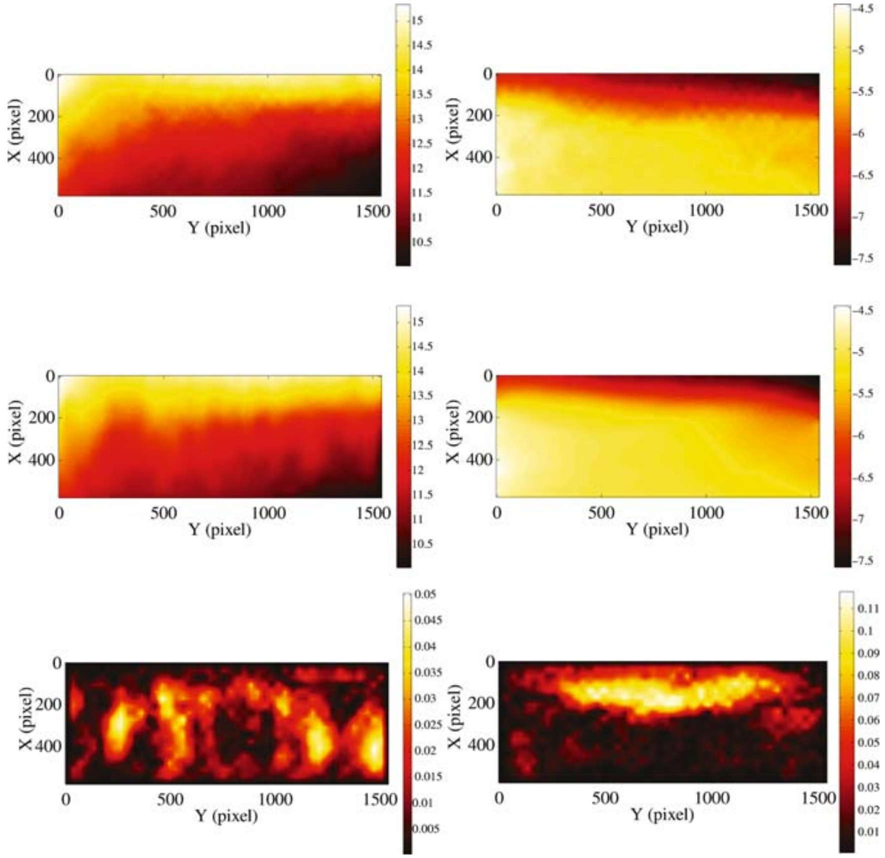

Fig. 7 Comparison between vertical (*left*) and horizontal (*right*) fields, measured displacement on the top, computed ones on the middle, and error on the bottom, on a measured field with the previously determined elastic parameters for a given load level.

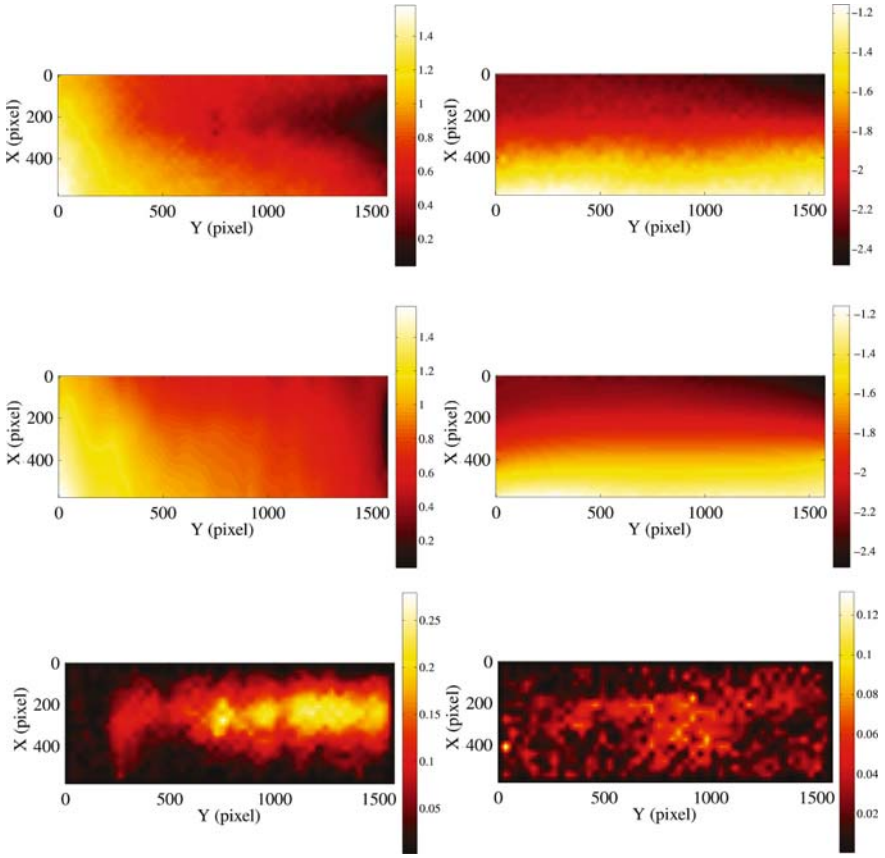

Fig. 8 Comparison between vertical (*left*) and horizontal (*right*) fields, measured displacement on the top, computed ones on the middle, and error on the bottom, on a measured field with the previously determined elastic parameters at another load level

On the example shown in Fig. 7 (best case) the global error (2.3%) reaches a value even lower than the one obtained on the stage used for identification.

The field prediction shown in Fig. 8 (worst case) displays a higher level of disagreement with the measured field (7.3%), The reason for this is not understood, but may be due to a breakdown of the hypothesis of linear elasticity. However, the quality of the prediction is still quite acceptable, and being the worst case, those tests globally validate the approach and obtained results.

10 Conclusion and Perspectives

This study presents a global multiaxial identification procedure for mechanical properties based on different quantitative image analyses. From the observed texture of a heterogeneous material, one has access to the local intrinsic elastic properties. As it is difficult to get a full benefit from a rich amount of data, the method that couples full field measurements and finite element updating allows one to automatically find the best set of parameters for a given model, herein assumed linear orthotropic. The complete procedure (mechanical test with image acquisition, DIC analysis of the displacement field, texture analysis and identification), has been followed up to the identification of elastic constants. The potential of this procedure to match complex loads histories has been highlighted by invoking displacement fields in different testing condition, using the same elastic constants. Those displacement fields and stiffness estimates compare quite well with *ex post* experimentally determined values.

References

1. S. Bergonnier, F. Hild, S. Roux, Local anisotropy analysis for non-smooth images, Patt. Recogn. 40 (2007) 544–556.
2. P.K. Rastogi, eds., *Photomechanics*, Springer, Berlin (Germany) (2000).
3. A.R. Rao, A taxonomy for texture description and identification, Springer New York (1990).
4. C. Germain, J.P. Da Costa, O. Lavialle, P. Baylou, Multiscale estimation of vector field anisotropy. Application to texture characterization, Signal Process., Vol 83 (juillet 2003), 1487–1503.
5. G. Besnard, F. Hild, S. Roux, “Finite-element” displacement fields analysis from digital images: Application to Portevin-Le Châtelier bands, Exp. Mech. 46 (2006) 789–803.
6. M. Grédiac, Principe des travaux virtuels et identification, C. R. Acad. Sci. Paris 309 (1989) 1–5.
7. M. Grédiac, The use of full-field measurement methods in composite material characterization: interest and limitations, Compos.: Part A 35 (2004) 751–761.
8. G. Geymonat, F. Hild, S. Pagano, Identification of elastic parameters by displacement field measurement, C. R. Mec. 330 (2002) 403–408.
9. D. Claire, F. Hild, S. Roux, Identification of damage fields using kinematic measurements, C. R. Mec. 330 (2002) 729–734.
10. D. Claire, F. Hild, S. Roux, A finite element formulation to identify damage fields: The equilibrium gap method, Int. J. Num. Meth. Eng. 61 (2004) 189–208.
11. K.T. Kavanagh, Clough R.W., Finite element applications in the characterization of elastic solids, Int. J. Sol. Struct. 7 (1971) 11–23.

Influences of Inertia and Material Property on the Dynamic Behavior of Cellular Metals

J.L. Yu*, Y.-D. Liu, Z.-J. Zheng, J.-R. Li, and T.X. Yu

Abstract Cellular metals are widely used in light-weight structures and energy absorption devices. Although many experimental studies on the dynamic behavior and rate sensitivity of cellular metals have been reported in the literature, there are some conflicting conclusions on the rate effect of metallic foams. In this paper, some numerical tests are presented to explore the effects of inertia, strain hardening and strain-rate hardening of the cell wall material on the behavior of Voronoi honeycomb samples under dynamic compression. Three deformation modes are found and corresponding nominal stress-strain curves and the plateau stress of the "specimens" are obtained. The results reveal that inertia plays an important role in Shock Mode and Transitional Mode but it does not affect the compressive stress-strain curve of the honeycomb. The strain-rate sensitivity of the honeycombs is less significant than that of the cell-wall material and becomes negligible under high impact velocities. The strain-hardening effect of the cell-wall material is of less importance.

1 Introduction

As a new-class of multifunctional materials, cellular metals, have attracted considerable research interest due to its excellent physical, chemical and mechanical properties. Potential applications of cellular metals include light weight cores for sandwich structures to increase the impact resistance, and improve the energy absorbing capacity. Much effort, including both experimental investigation and numerical analysis, has been made on the dynamic behavior of metallic foams, but

---

J.L. Yu (✉), Y.-D. Liu, Z.-J. Zheng, and J.-R. Li
CAS Key Laboratory of Mechanical Behavior and Design of Materials, University of Science and Technology of China, Hefei, Anhui 230026, People's Republic of China

T.X. Yu
Department of Mechanical Engineering, Hong Kong University of Science and Technology, Clear Water Bay, Kowlong, Hong Kong, People's Republic of China

*Corresponding author: Fax: +86 551 360 6459; e-mail: jlyu@ustc.edu.cn

H. Zhao, N.A. Fleck (eds.), *Mechanical Properties of Cellular Materials,*
IUTAM Bookseries 12,

there are some conflicting conclusions in the rate effect on the deformation behavior of metallic foams in the literature.

Considerable amount of experimental studies has been carried out on the strain rate sensitivity of metallic foams. Mukai et al. (1999) and Dannemann and Lankford (2000) observed a strain rate effect for the closed-cell aluminum foam Alporas (Al-Ca-Ti). In contrast, another closed-cell foam Alulight (Al-Mg-Si) formed by powder processing technique does not exhibit a strain rate effect (Deshpande and Fleck, 2000). Hall et al. (2000) also derived that the strain rate effect is not significant for a closed-cell 6,101 aluminum foam. Analogous confusions exist in open-cell aluminum foams. Duocel (Al 6101-T6) is regarded as a strain-rate insensitive foam (Danneman and Lankford, 2000; Deshpande and Fleck, 2000; Lee et al., 2006). On the other hand, Kanahashi et al. (2000) reported a strong strain rate sensitivity of an open-cell aluminum foam (SG91A). Nevertheless, Wang et al. (2006) found that the yield strength of another open-cell aluminum foam with similar chemical compositions of SG91A (Al-Mg-Si-Fe) are almost insensitive to the strain rate.

In order to clarify the inconsistencies in the literature mentioned above, Tan et al. (2005a) carried out an extensive experimental study on the crushing behavior of closed-cell Hydro/Cymat aluminum foam (Al-Si-Mg). They found that the plastic collapse stress increases with the impact velocity, which is attributed to micro-inertial effects. When the impact velocity exceeds a critical value the deformation of the foam is of 'shock-type' due to inertia effects. Below the critical velocity, the dynamic plateau stresses are insensitive to the impact velocity. Meanwhile, a one-dimensional "steady-shock" model based on a rate-independent, rigid, perfectly-plastic, locking (r-p-p-l) idealization of the quasi-static stress-strain curves for aluminum foams was proposed (Tan et al., 2005b) to provide a first-order understanding of the dynamic compaction process.

Regular honeycombs (Ruan et al., 2003) and 2D Voronoi honeycombs (Zheng et al., 2005) were used to investigate the mechanism of dynamic crushing of cellular metals numerically. The influences of cell wall thickness and the irregularity of honeycombs, as well as the impact velocity, on the deformation mode and the plateau stress were investigated. However, the influence of the material properties of cell wall on the dynamic response of foams has not been studied.

In this paper, we employ 2D Voronoi honeycomb in our numerical simulations. The density and plastic hardening properties of the cell wall material are factitiously changed to investigate the effects of inertia, strain hardening and strain-rate hardening on the crushing behavior of Voronoi honeycombs.

2 Finite Element Models

The Voronoi technique is employed to generate 2D Voronoi honeycombs. The irregularity of a Voronoi honeycomb with N cells in a square area A_0 is defined as (Zheng et al., 2005)

$$k = 1 - \delta / \sqrt{2A_0/\sqrt{3}N}, \tag{1}$$

where δ is the minimum distance between any two nuclei. The relative density of a Voronoi honeycomb is specified by

$$\bar{\rho} = \rho^* / \rho_s = \frac{1}{A_0} \sum h_i l_i, \tag{2}$$

where ρ^* is the density of honeycomb, ρ_s the density of its cell wall material, l_i the ith cell wall length and h_i the corresponding thickness.

In the present study, five random sample patterns are constructed in an area of $100 \times 100\,\mathrm{mm}^2$ with 200 nuclei. The irregularity of the samples is taken to be 0.45. The cell wall thickness is identical for one sample and three values of thickness, i.e. 0.26, 0.36 and 0.48 mm corresponding to the relative densities of 0.073, 0.1 and 0.135, are investigated.

ABAQUS/EXPLICIT is employed to analyze the uniaxial compression behavior of Voronoi honeycombs under different impact velocities. In the finite element models, each edge of the cell wall is divided into a few shell elements of type S4R with five integration points. Three kinds of cell wall materials are considered. The first one is elastic-perfectly plastic with the Young's modulus, yield stress and Possion's ratio being 66 GPa, 175 MPa and 0.3, respectively. The second one is elastic-plastic material with linear strain-hardening. The third one is elastic-perfectly plastic material with strain-rate hardening. The stress-strain relation in the plastic stage for the last two materials are defined as

$$\sigma = \sigma_y + B\varepsilon_p \tag{3}$$

and

$$\sigma = \sigma_y \left[1 + C \ln\left(\dot{\varepsilon}_p / \dot{\varepsilon}_0\right)\right], \tag{4}$$

respectively, where ε_p is the equivalent plastic strain, σ_y the yield strength of the cell wall material, $\dot{\varepsilon}_p / \dot{\varepsilon}_0$ the relative equivalent strain rate, and B and C are material parameters. In this study we take $B = 175\,\mathrm{MPa}$, $C = 0.05$ and $\dot{\varepsilon}_0 = 0.1$.

For quantitative comparison and analysis, the plateau stress is specified by

$$\sigma_p = \frac{1}{\varepsilon_D - \varepsilon_y} \int_{\varepsilon_y}^{\varepsilon_D} \sigma d\varepsilon, \tag{5}$$

where the densification strain ε_D is defined as (Tan et al., 2005a)

$$\frac{d}{d\varepsilon} \left(\frac{1}{\sigma} \int_0^{\varepsilon} \sigma d\varepsilon \right) \bigg|_{\varepsilon = \varepsilon_D} = 0, \tag{6}$$

and ε_y is the yield strain, which is taken as 0.02 in this study.

3 Results and Discussions

3.1 Inertia Effect

The influence of inertia on the crushing behavior of honeycombs is analyzed by changing the density of cell wall material. Elastic-perfectly plastic material property is assigned and four values of the density of cell wall material, i.e. 2.7×10^3, 0.9×10^3, 0.3×10^3 and $0.1 \times 10^3\,\mathrm{kg/m^3}$ are chosen artificially. Zheng et al. (2005) have found that the deformation of Voronoi honeycombs is complicated but it can be catalogued into three modes. A Quasi-static Homogeneous Mode occurs under low impact velocities, in which the crash bands are randomly located and the deformation is macroscopically homogeneous. If the impact velocity is very high, a Shock Mode occurs and cells crush sequentially in a planar manner from the impact end. A Transitional Mode occurs in between, in which the crash bends are more concentrated near the impact end. In the present study, it is found that when the cell wall material density is $2.7 \times 10^3\,\mathrm{kg/m^3}$, the critical velocities between the corresponding modes are about 40 and 90 m/s, respectively, regardless of the cell wall thickness (or the relative density of honeycomb).

Under the Homogeneous Mode, the calculated stress-strain curves under different impact velocities for Voronoi honeycombs with the same sample pattern and relative density (i.e., the cell wall thickness is fixed) almost remain identical, regardless of different densities of cell wall material, as shown in Fig. 1. It is evident that the inertia effect is negligible when the deformations of the honeycombs are macroscopically homogeneous.

The plateau stresses on the impact surface and the support surface under different velocities for the cell wall material density of $2.7 \times 10^3\,\mathrm{kg/m^3}$ are shown in Figs. 2 and 3, where Regions I, II and III correspond to the Homogeneous, Transitional and Shock Modes, respectively. It is found that under the Homogeneous

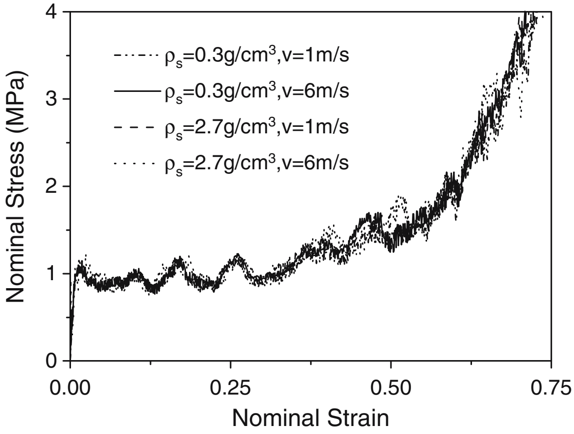

Fig. 1 Stress–strain curves under Homogeneous Mode

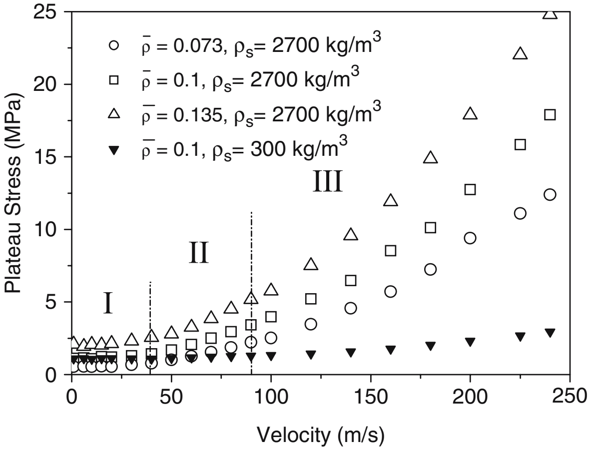

Fig. 2 The plateau stress on the impact surface under different impact velocities

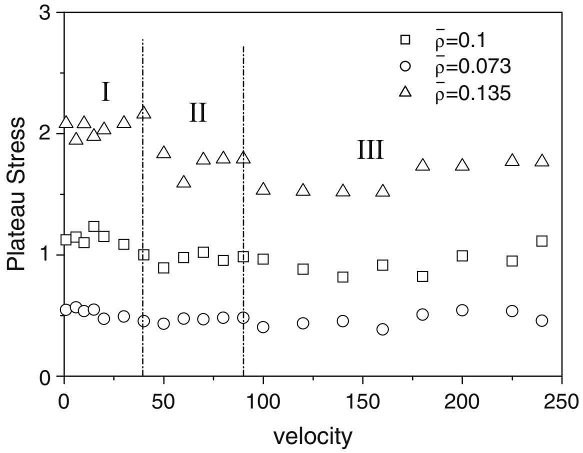

Fig. 3 The plateau stress on the support surface under different impact velocities

Mode, the plateau stresses on the impact surface and the support surface are almost the same, indicating an early achievement of internal force equilibrium. Also, the plateau stress increases remarkably with the increase of the relative densities. Thus, the plateau stress mainly depends on the relative density (the cell wall thickness), in agreement with experimental results reported in the literature.

On the other hand, under the Transitional Mode and Shock Mode, the plateau stress on the impact surface increases rapidly with the increase of impact velocity but the plateau stress on the support surface exhibits little velocity dependence. This is in accordance with the inhomogeneous deformation of the sample. The enhancement of the plateau stress on the impact surface can be explained as follows. The macroscopic strain along the impact direction is not uniform. The layer near the impact surface has the maximum macroscopic strain whilst the stress and strain there are located in the densification portion of the nominal stress–strain curve. The difference in macroscopic strain distribution between the two modes is that under the Shock Mode it is shock-like while under the Transitional Mode it changes gradually.

The plateau stresses on the impact surface under different velocities for the cell wall material density of $0.3 \times 10^3\,\mathrm{kg/m^3}$ is also shown in Fig. 2 for comparison. It seems that with the reduction of inertia, the force equilibrium and uniform deformation become much easier and the critical velocities for modes transition increase dramatically.

3.2 Influence of the Cell-Wall Material Properties

To investigate the effect of the cell-wall material properties on the crushing behavior, we select the linear strain-hardening and strain-rate hardening elastic-plastic materials to study the responses of the Voronoi honeycombs under various velocities. The density of cell wall material is $2.7 \times 10^3\,\mathrm{kg/m^3}$ and the relative density is $\bar{\rho} = 0.1$.

In comparison with the elastic-perfectly plastic material, the relative increase in the plateau stress caused by the linear strain-hardening effect can be specified by

$$\lambda_1 = (\sigma_1 - \sigma_0)/\sigma_0, \tag{7}$$

where σ_0 and σ_1 are the plateau stresses of the elastic-perfectly plastic material and the strain-hardening material, respectively. Note that the relative increase in the flow stress of the solid material is proportional to the plastic strain.

Similarly, the relative increase in the plateau stress caused by the strain-rate hardening effect, compared to elastic-perfectly plastic material, can be defined as

$$\eta_1 = (\sigma_2 - \sigma_0)/\sigma_0, \tag{8}$$

where σ_2 is the plateau stress of the strain-rate hardening material. According to Eq. (4), the relative increase in the flow stress of the solid material is described by

$$\eta_2 = (\sigma - \sigma_y)/\sigma_y = C\ln(\dot{\varepsilon}_\mathrm{p}/\dot{\varepsilon}_0). \tag{9}$$

The variation of the averaged relative increase in the plateau stress on the impact surface of five random samples and their mean square deviations with the impact velocity for honeycombs made of strain-hardening material is shown in Fig. 4. It is found that λ_1 takes a small value over the whole range of the impact velocities studied, so the strain-hardening of cell wall material has minor influence on the plateau stress under both quasi-static and dynamic cases. The effect might be well submerged into experimental scatter for irregular cellular metals.

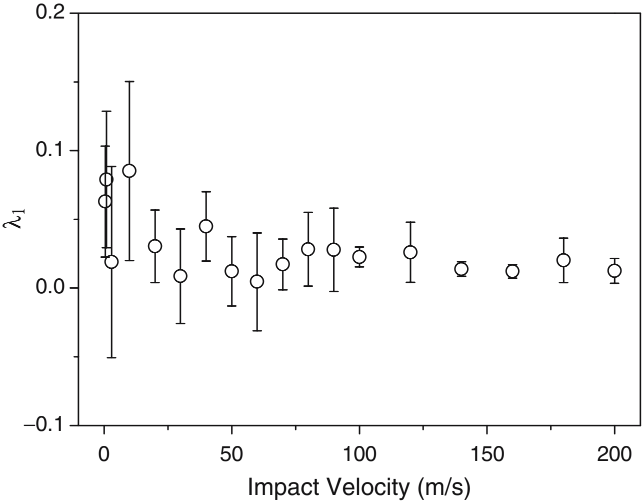

Fig. 4 The relative increase in the plateau stress of honeycombs made of strain-hardening material under different impact velocities

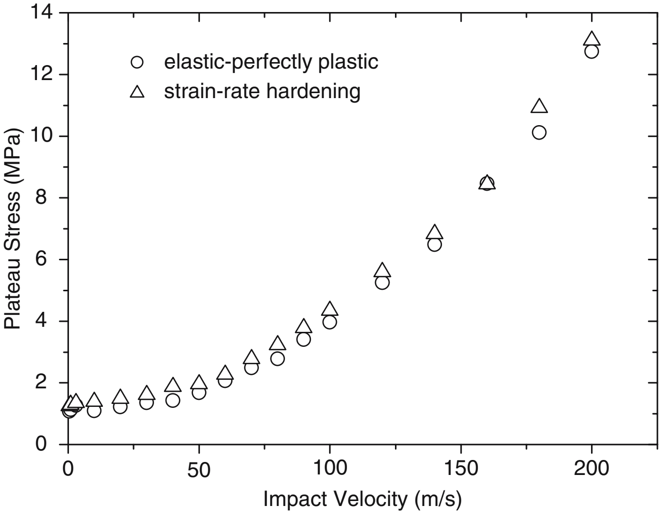

Fig. 5 The plateau stresses on the impact surface under different impact velocities

A comparison of plateau stress on the impact surface of a honeycomb sample made of elastic-perfectly plastic and strain-rate hardening materials is shown in Fig. 5. The variation of the relative increase in the plateau stress with the nominal strain rates for honeycombs made of strain-hardening material is shown in Fig. 6.

It is found from Fig. 5 that the increase in the plateau stress due to the strain-rate sensitivity of cell wall material is small and almost independent of the impact

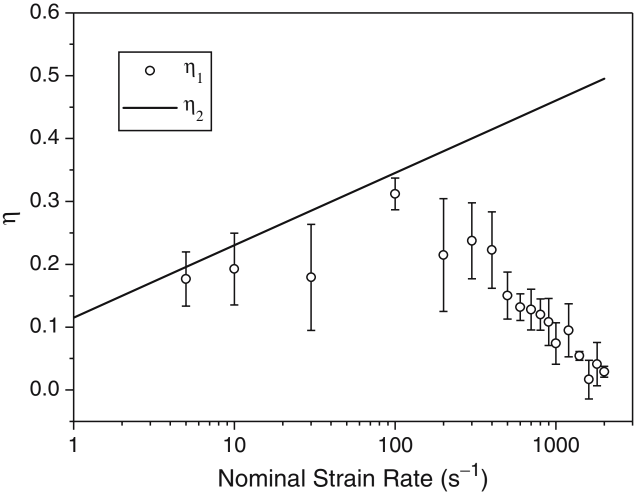

Fig. 6 The relative increase in the plateau stress of honeycombs made of strain-rate hardening material under different nominal strain-rates

velocity. The relative increase in the plateau stress is always less than the relative increase in the flow stress of the corresponding solid material. About 20% increase in the plateau stress is found under the Quasi-static Homogeneous Mode when the strain rate is smaller than $400\,s^{-1}$ for the parameters used in this paper, as shown in Fig. 6. It is interesting to note that under the Transitional Mode and Shock Mode, the strain-rate effect seemingly decreases fast with the impact velocity. This can be attributed to the enhancement of the plateau stress due to the inertia effect.

From the numerical results we also found that the critical velocities of deformation modes are almost independent of the strain hardening and strain-rate hardening of the cell-wall material. The possible explanation is that the plastic strain in most parts of the honeycomb is small except along the plastic hinge lines.

4 Concluding Remarks

The present numerical results indicate that inertia is a dominant factor which affects the dynamic response of cellular metals. The strain-rate sensitivity of cell-wall material leads to an increase in plateau stress but it can not explain the strong rate dependence observed in some metallic foams. More elaborative experiments and punctilious analysis are required to solve the existing puzzle.

Some possible mechanisms responsible to the rate sensitivity of metallic foams need to be further explored, e.g., cell morphology, cell wall material distribution, ductile-brittle transition of the cell wall material, strain-rate sensitivity of its failure strain, and micro-structural characters associated with their manufacture.

Acknowledgement This work reported herein is supported by the National Natural Science Foundation of China (Projects No. 10532020, No. 10672156 and No. 90205003).

References

Dannemann KA, Lankford J (2000) High strain rate compression of closed-cell aluminium foams. Mater Sci Eng A293:157–164

Deshpande VS, Fleck NA (2000) High strain rate compressive behaviour of aluminium alloy foams. Int J Impact Eng 24:277–298

Hall IW, Guden M, Yu CJ (2000) Crushing of aluminum closed cell foams: density and strain rate effects. Scripta Mater 43:515–521

Kanahashi H, Mukai T, Yamada Y, Shimojima K, Mabuchi M, Nieh TG, Higashi K (2000) Dynamic compression of an ultra-low density aluminium foam. Mater Sci Eng A280:349–353

Lee S, Barthelat F, Moldovan N, Espinosa HD, Wadley HNG (2006) Deformation rate effects on failure modes of open-cell Al foams and textile cellular materials. Int J Solids Struct 43:53–73

Mukai T, Kanahashi H, Miyoshi T, Mabuchi M, Nieh TG, Higashi K (1999) Experimental study of energy absorption in a close-celled aluminum foam under dynamic loading. Scripta Mater 40:921–927

Ruan D, Lu G, Wang B, Yu TX (2003) In-plane dynamic crushing of honeycombs – a finite element study. Int J Impact Eng 28:161–182

Tan PJ, Reid SR, Harrigan JJ, Zou Z, Li S (2005a) Dynamic compressive strength properties of aluminium foams. Part I – experimental data and observations. J Mech Phys Solids 53: 2174–2205

Tan PJ, Reid SR, Harrigan JJ, Zou Z, Li S (2005b) Dynamic compressive strength properties of aluminium foams. Part II – 'shock' theory and comparison with experimental data and numerical models. J Mech Phys Solids 53:2206–2230

Wang ZH, Ma HW, Zhao LM, Yang GT (2006) Studies on the dynamic compressive properties of open-cell aluminum alloy foams. Scripta Mater 54:83–87

Zheng ZJ, Yu JL, Li JR (2005) Dynamic crushing of 2D cellular structures: A finite element study. Int J Impact Eng 32:650–664

Shock Enhancement due to Shock Front Propagation in Cellular Materials

S. Pattofatto, I. Nasri, H. Zhao, F. Hild, Y. Girard, and H. Tsitsiris

Abstract In this study, crushing experiments are performed on four kinds of cellular materials using a large diameter (60 mm) nylon Hopkinson bar. The impact velocities are chosen around the critical velocity corresponding to the occurrence of a shock front predicted by the classical RPPL model (Reid and Peng, 1997). The experimental setup allows to measure the stress enhancement due to the shock front propagation. In particular, for one type of material, a high speed camera is used to capture about ten images at 20,000 fps and then the strain field during testing is obtained by a special image correlation program ($\text{Correli}^{\text{LMT}}$). This strain field allows to measure directly the shock front velocity. Moreover, an improved model, including the hardening curve, is proposed to predict this shock enhancement. Finally, numerical analyses using Ls-Dyna explicit code show that for all experiments a macroscopic homogeneous phenomenological material law can reproduce essential features of stress enhancement due to shock front propagation.

Keywords Cellular material · Hopkinson bar · Image correlation

1 Introduction

The concept of shock enhancement effect under high speed impact ($>100\,\text{m/s}$) was originally proposed by (Reid and Peng, 1997) to explain testing results on woods. Afterwards, a number of authors also reported this effect for various cellular materials at high impact speeds (Lopatnikov et al., 2003, 2004; Tan et al., 2002, 2005; Radford et al., 2005). For relatively low impact speeds, there is the so-called critical velocity under which shock enhancement is not significant ($\sim 50\,\text{m/s}$). Experimental

---

S. Pattofatto (✉), I. Nasri, H. Zhao, F. Hild, and H. Tsitsiris
LMT-Cachan (ENS Cachan/CNRS/Université Paris 6/PRES UniverSud Paris), 61 av. du Président Wilson, F-94230 Cachan, France

Y. Girard
EADS-CCR Suresnes, 12 bis rue Pasteur, F-92152 Suresnes Cedex, France

H. Zhao, N.A. Fleck (eds.), *Mechanical Properties of Cellular Materials,*
IUTAM Bookseries 12,

data in previous works prove the existence of the shock effect (Tan et al., 2002, 2005; El Nasri et al., 2007; Zhao and Abdennadher, 2004; Zhao et al., 2005). However, there is no convincing experimental proof because the only available experimental observation is the force measurement behind the supposed shock front. As a consequence, a more direct experimental proof of the shock front propagation is given here. With a single bar, tests with two configurations using a large diameter soft Hopkinson bar behind/ahead of the shock front allow for the estimation of the stress jump across the shock front. Moreover, the shock front is directly observed and analyzed by using a high speed camera and image correlation that allow for the measurement of strain jump during the tests. It also gives indirectly the speed of the shock front.

A simple prediction of the shock front properties is also needed. For example, the Rigid Perfectly Plastic Locking (RPPL) model proposed by (Reid and Peng, 1997) gives a fast estimation. However, the shock stress jump and shock front speed predicted by the RPPL model are too sensitive to the parameters (e.g., the rigid locking strain). It leads us to propose another model that assumes a power law densification and gives a good prediction. Finally, numerical analyses for the two testing configurations using LS-Dyna explicit finite element code (Hallquist, 1998) with a macroscopic constitutive law (crushable foam) are presented. They show that such a simple rate insensitive constitutive model is able to reproduce the shock enhancement.

2 Materials and Experimental Set-up

Four kinds of cellular materials are investigated: aluminium Alporas (ductile) and Cymat (brittle) foam, 5,052 aluminium honeycomb, nickel Ateca hollow spheres. The average densities are the following:

Alporas foam	Hollow spheres	Cymat foam	Honeycomb
$245\,\mathrm{kg/m^3}$	$219\,\mathrm{kg/m^3}$	$235\,\mathrm{kg/m^3}$	$38\,\mathrm{kg/m^3}$

Honeycomb is anisotropic and only its properties in the principal direction are of interest here (i.e., that of hexagonal cell column axis), the others are more or less isotropic. The crushing mode of these materials is different. The Cymat foam is brittle and the crushing mechanism is cracking of the cell wall, whereas Alporas foam, hollow spheres, and honeycombs are much more ductile and exhibit a mode of successive folding of the cell walls. Typical nominal stress-strain curves of these materials under quasi-static loading are shown in Fig. 1. The specimens are cylinders with a diameter of 60 mm and a height of 40 mm.

A 62 mm diameter and 6 m long Nylon Hopkinson bar is used as measuring device and a gas gun with a 70 mm inner diameter barrel is used to launch a projectile. The key measurement feature of these two testing configurations is the use of a

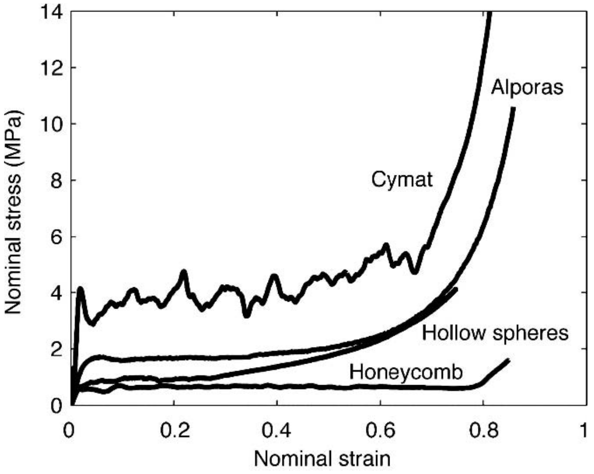

Fig. 1 Nominal compression curve

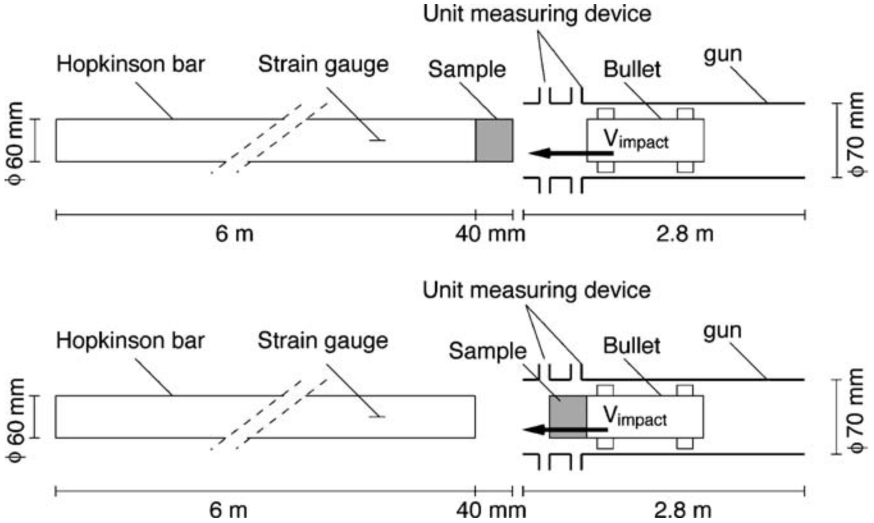

Fig. 2 Two experimental configurations (**a**) configuration 1: direct impact Hopkinson bar test (**b**) configuration 2: Hopkinson bar-Taylor test

large diameter Nylon Hopkinson bar necessary to study large specimens relative to the size of the microstructure. The soft material of the bars is necessary to obtain low signal/noise ratio when testing low strength cellular materials.

The originality of the experimental technique presented here is that two testing configurations are considered to build one result. Thus, configuration 1 consists to put the sample on the Hopkinson bar and to launch the flat ended Nylon bullet to strike the sample (Fig. 2a). Configuration 2 consists to put the sample on the bullet fired at about 60 m/s to strike the Hopkinson bar (Fig. 2b).

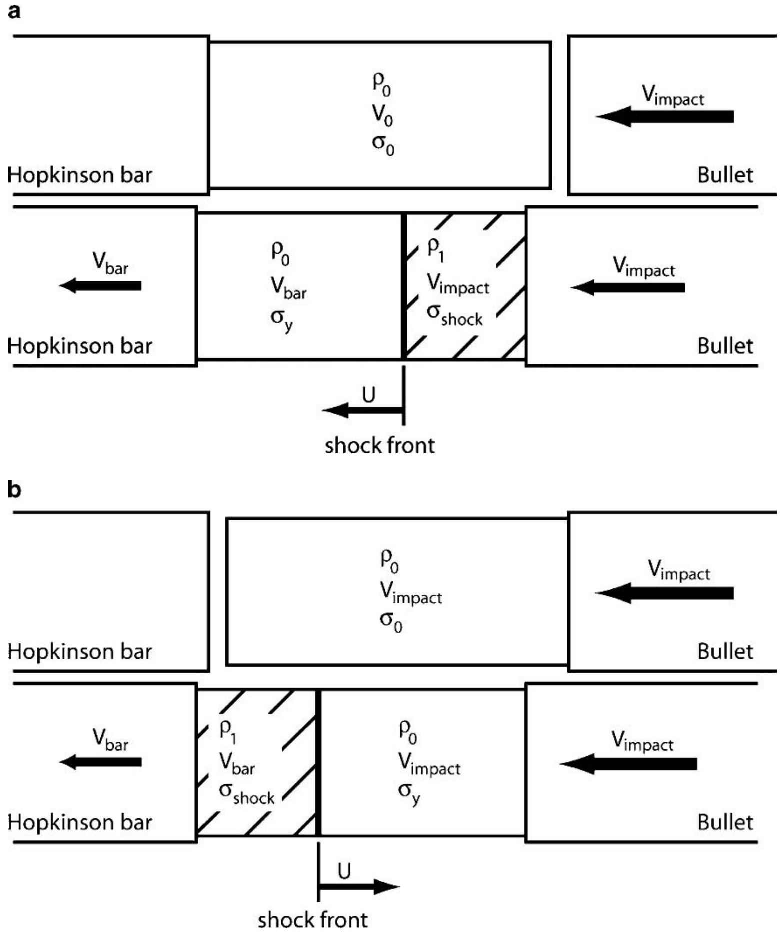

Fig. 3 Depiction of the shock front in the two different testing configurations (**a**) configuration 1 (**b**) configuration 2

As regards the shock front theory related to the experiments, for configuration 1 the shock front will propagate from the bullet side so that the Hopkinson pressure bar will measure the stress ahead of the shock front (Fig. 3a). For configuration 2, the shock front will propagate from the pressure bar side so that the Hopkinson pressure bar will measure the stress behind the shock front (Fig. 3b). The stress jump is the difference between the two stress profiles.

In addition, a high speed Photron camera is used to take images during one test performed in configuration 1. The record rate of the camera is chosen to be 20,000 frames per second (fps) to obtain a sufficient resolution (256 × 384 pixels), necessary for the following digital image correlation analysis. The shutter speed is chosen at 1/60,000 s so that the image is not blurred whereas the powerful lights ensure a correct contrast of the pictures. By considering an image sequence, the displacement fields between images are calculated by a “finite element” correlation algorithm (Correli$^{\mathrm{LMT}}$) developed in our laboratory.

3 Measurement of Shock Enhancement

Correction of raw testing results is performed to reduce the influence of the initial density of the tested samples. For Alporas foam, yield stress ahead of the shock front (configuration 1) is significantly different from stress behind the shock front (configuration 2).

4 Measurement of Shock Front Velocity with Image Correlation Program

The presented test is conducted on Alporas foam only, ten images were processed up to a nominal strain of about 40%. The main difficulty for the use of image correlation on foam-like specimens is the collapse of cells during compaction, which induces an important distortion of the texture. On the basis of the calculated strain field, a quantitative estimation of the shock front velocity is obtained as follows. The mean value of the strain is calculated for each longitudinal position. With this processing, the strain field is converted into a uniaxial mean strain variation. The time history of the mean strain is given in Fig. 4. It shows that, at 56 m/s, the strain field is not homogeneous at the first image. The strain field shows that the specimen can be

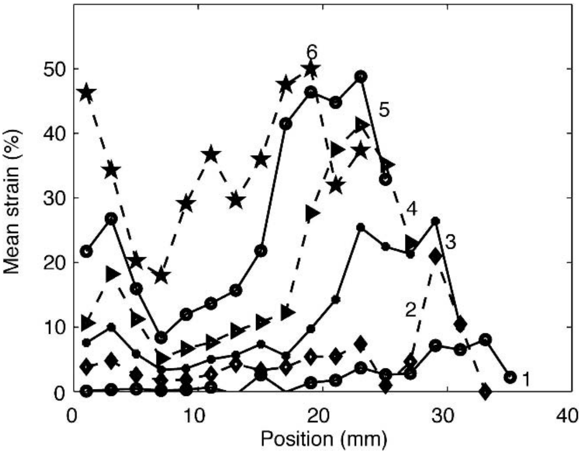

Fig. 4 Strain field in the specimen (56 m/s)

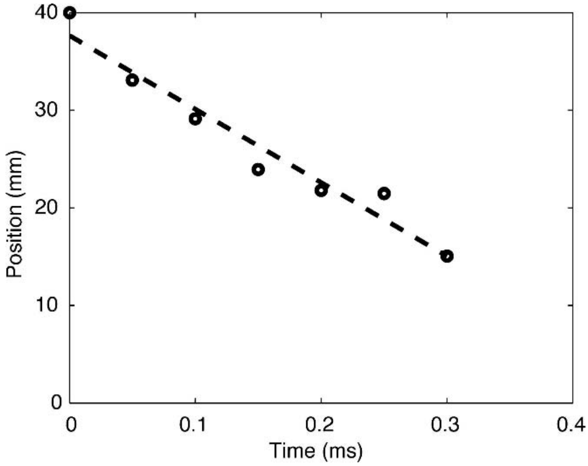

Fig. 5 Estimated position of the shock front

divided into two parts. One part on the right hand side in contact with the striker, which is immediately compacted at 20% and increases finally up to 40%. The other part on the left hand side, in contact with the bar, remains compacted at less than 10%. Same conclusions for the 47 m/s impact. The position of the shock front in the specimen height is calculated by taking the bar face as the reference. The position of the discontinuity is determined arbitrarily by the beginning of the sharp increase of the strain in Fig. 4. Since the capture time of each image is known, the shock front speed is determined (Fig. 5). It appears that the position is quasi-linear, which means a constant shock velocity. For the 56 m/s impact velocity, the value is estimated at 87 m/s (it is estimated at 94 m/s with the Hokpinson bars measurement). For the 47 m/s impact velocity, the value is 70 m/s.

5 Numerical Analysis

The LS-Dyna explicit finite element code is used to perform numerical simulations. The specimen whose diameter is 60 mm and thickness 40 mm is meshed with 32,000 cubic eight-node elements (with 20 elements in the length). The constitutive law of the foam is given by the so-called "crushable foam model" available in the LS-Dyna code (Hallquist, 1998). The comparison between experimental and numerical results is carried out by computing the force measured by the Hopkinson bar in the two configurations. The good agreement between simulated and measured force/time histories validates the FE model and also the experimental procedure based on the two configurations (see El Nasri et al., 2007). The simulated strain map at different instants is also compared with the strain field obtained by image correlation. The simulated average strain is compared to the experimental data. A good agreement is obtained, as depicted in Fig. 6.

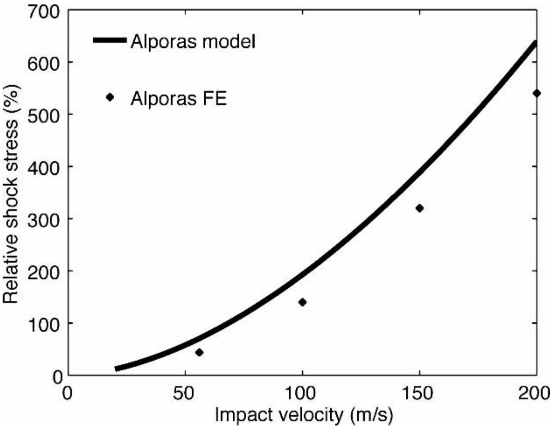

Fig. 6 Comparison of simulated (FE) and measured (CP) strain discontinuity profiles

6 An Improved Predictive Shock Model

A simple shock model should be used to provide an acceptable prediction of the shock enhancement. Let us consider the RPPL model (Reid and Peng, 1997), based on two parameters: the locking strain ε_{lock} and the plastic flow stress σ_y. With the simplifications of the RPPL model, the shock front velocity and stress behind the shock front are calculated as:

$$\mathrm{U} = \frac{\mathrm{V}_{\mathrm{impact}}}{\varepsilon_{\mathrm{lock}}} \qquad \sigma_{shock} - \sigma_y = \frac{\rho_0 V_{impact}^2}{\varepsilon_{lock}} \tag{1}$$

However, the identification of the parameters of the model is not easy. The plastic flow stress σ_y is more or less easy to identify and the value of the locking strain is arbitrary due to the non-linear shape of the densification curve. Therefore, we propose to account for the progressive densification feature. The same impact case as discussed in Eq. (1) is considered. The fact that the densification is progressive implies that the strain reached behind the shock front ε_{shock} is not explicitly known as the locking strain in the RPPL model. The basic continuity equations (Eq. (1)) are replaced by:

$$U = \frac{V_{impact}}{\varepsilon_{shock}} \qquad \sigma_{shock} - \sigma_y = \frac{\rho_0 V_{impact}^2}{\varepsilon_{shock}} \tag{2}$$

and the solution is defined by using the supposed power law model of the material:

$$\sigma_{shock} = f(\varepsilon_{shock}) = \sigma_y + k\varepsilon_{shock}^m \tag{3}$$

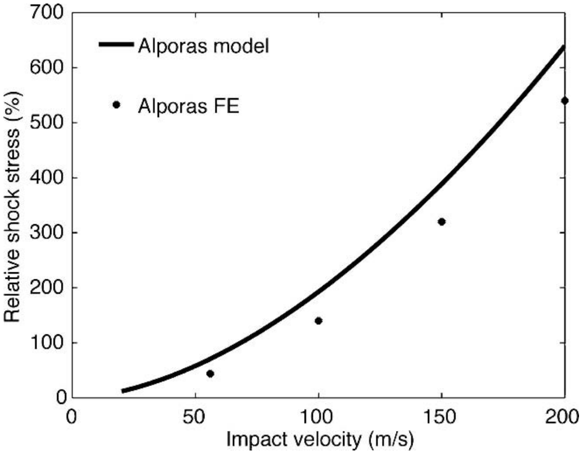

Fig. 7 Shock enhancement effect: power law model and FEM numerical results

The derivation of the shock strain ε_{shock} is straight forward using Eqs. (2) and (3):

$$\varepsilon_{shock} = \left(\frac{\rho_0 V_{impact}^2}{k}\right)^{\frac{1}{m+1}} \tag{4}$$

From experimental stress-strain data, the identification gives: $\sigma_y = 1.70\,\mathrm{MPa}$, $k = 21.2\,\mathrm{MPa}$ and $m = 6.4$. From this power law model the relative shock stress jump $(\sigma_{\mathrm{shock}} - \sigma_{\mathrm{y}})/\sigma_{\mathrm{y}}$ is obtained. The shock enhancement effect is plotted in Fig. 7, so as the comparison between the present model and the FEM simulation results. A reasonable agreement is found. The model allows also to calculate the shock front velocity with a good agreement with experiments (Pattofatto et al., 2007). As a conclusion, the results show that the explicit solution of a power law model gives a satisfactory prediction with a single identification.

7 Conclusion

In this paper, four types of cellular materials are studied. First, experiments based on Hopkinson bar tests performed in two different configurations are presented. They allow to measure the shock enhancement effect. In the case of experiments on Alporas foam, a new measurement technique based on digital images and a correlation program is used to have a direct measurement of the velocity of the shock front. Then, numerical simulations of tests in two different configurations are presented. The results show that shock enhancement of foams is reproduced by numerical simulations using a simple macroscopic, homogenous and rate-insensitive constitutive law based on a nominal stress-strain relationship obtained in a quasi-static compression test. It means that such shock enhancement effect should not be taken into account at the level of the constitutive law itself. Finally, an improved modelling of the shock front effect in cellular materials is proposed. In fact the classical RPRL model is said to be a good first-approximation but it can be improved by considering the non-linear shape of the densification curve of the foam. An improved model based on a power law densification assumption allows for an easy determination of its parameters from experimental data, and gives results in good agreement with experimental data.

References

El Nasri I, Pattofatto S, Zhao H, Tsitsiris H, Hild F and Girard Y (2007) Shock enhancement of cellular structures under impact loading: Part I Experiments, J. Mech. Phys. Solids, 55:2652–2671

Hallquist JO (1998) Ls-Dyna theoretical manual. Livermore Software Technology Corporation, Livermore, CA

Lopatnikov SL, Gama BA, Haque Mdj, Krauthauser C, Gillespie JW, Guden M, Hall IW (2003) Dynamics of metal foam deformation during Taylor cylinder-Hopkinson impact experiment, Compos. Struct., 61:61–71

Lopatnikov SL, Gama BA, Haque Mdj, Krauthauser C, Gillespie JW, Guden M (2004) High-velocity plate impact of metal foams, Int. J. Impact Eng., 30:421–445

Pattofatto S, El Nasri I, Zhao H, Tsitsiris H, Hild F and Girard Y (2007) Shock enhancement of cellular structures under impact loading: Part II analysis, J. Mech. Phys. Solids, 55:2672–2686

Radford DD, Deshpande VS, Fleck NA (2005) The use of metal foam projectile to simulate shock loading on a structure, Int. J. Impact Eng., 31:1152–1171.

Reid SR, Peng C (1997) Dynamic uniaxial crushing of wood, Int. J. Impact Eng., 19:531–570

Tan PJ, Harrigan JJ, Reid SR (2002) Inertia effects in uniaxial dynamic compression of a closed cell aluminium alloy foam, Mater. Sci. Technol., 18:480–488

Tan PJ, Reid SR, Harrigan JJ, Zou Z, Li S (2005) Dynamic compressive strength properties of aluminium foams. Part I—experimental data and observations, J. Mech. Phys. Solids, 53:2174–2205

Zhao H, Abdennadher S (2004) On the strength enhancement of rate insensitive square tubes under impact loading, Int. J. Solids Structs., 4:6677–6697

Zhao H, Nasri I, Abdennadher S (2005) An experimental study on the behaviour under impact loading of metallic cellular materials, Int. J. Mech. Sci., 47:757–774

Close-Range Blast Loading of Aluminium Foam Panels: A Numerical Study

A.G. Hanssen, L. Olovsson, T. Børvik, and M. Langseth

Abstract Hanssen et al. [1] carried out full-scale close-range blast loading tests of aluminium foam panels. In this paper we simulate the experimental tests in [1] by doing coupled finite element analyses which include the charge and blast wave from the explosion using the non-linear finite element code LS-DYNA [2]. The interaction between the detonation gases and the Lagrangian structure ensures a fully coupled analysis between the loading and response of the structure.

Keywords Blast loading · Aluminium foam · Pendulum · Field test · LS-DYNA

1 Introduction

Hanssen et al. [1] completed a test program where aluminium foam panels were subjected to close-range blast loading. The impulse and energy transfer was measured by use of a ballistic pendulum. By varying the foam density and charge mass the effect on the energy and impulse transfer could easily be determined. Hanssen et al. [1] reported that for the majority of the tests, the impulse and energy transfer increased by adding an aluminium foam panel to the base plate of the pendulum. Also, putting a cover plate in front of the foam panel further increased the impulse and energy transfer. From analytical considerations based on shock wave theory, the authors [1] argued that the addition of a foam panel with or without a cover plate should not influence the impulse or energy transfer. It was therefore reasoned that a

---

A.G. Hanssen, T. Børvik, and M. Langseth (✉)
CRI-SIMLab, Centre for Research-based Innovation, Department of Structural Engineering, NTNU, N-7491 Trondheim, Norway

A.G. Hanssen and L. Olovsson
IMPETUS Afea AS, Strandgaten 32, 4400 Flekkefjord, Norway

T. Børvik
Norwegian Defence Estates Agency, Research & Development Department, PB 405, Sentrum, No-0103 Oslo, Norway

H. Zhao, N.A. Fleck (eds.), *Mechanical Properties of Cellular Materials,*
IUTAM Bookseries 12,

possible interaction effect between the flow or pressure build-up of the detonation gases and the deforming aluminium foam panels would somehow increase the load transferred to the pendulum. However, the authors [1] did not discuss the influence of springback of the aluminium foam and cover plate, which could influence the momentum transfer to the pendulum. If the cover plate and foam panel gained considerable momentum in the opposite direction of the pendulum's swing, then—from conservation of momentum, the pendulum's momentum would have to be increased correspondingly. Unfortunately, the positions of the remains of the cover plate and foam panel after the field test by Hanssen et al. [1] were not documented, which could have indicated the significance of the springback.

The results by Hanssen et al. [1] has been utilised by other investigators, e.g. [4–6] and some authors have used the experimental results for validation of numerical codes [6].

This paper establishes a numerical model of the close-range blast tests and compares the numerical results with the experimental ones. A sensitivity study is carried out on changes in material properties and alternative detonation events.

2 Experimental Test Set-up

Figure 1 shows the ballistic pendulum used to study the energy and impulse transfer from close-range blast loading of aluminium-foam panels [1]. In [1], a 2^3 factorial

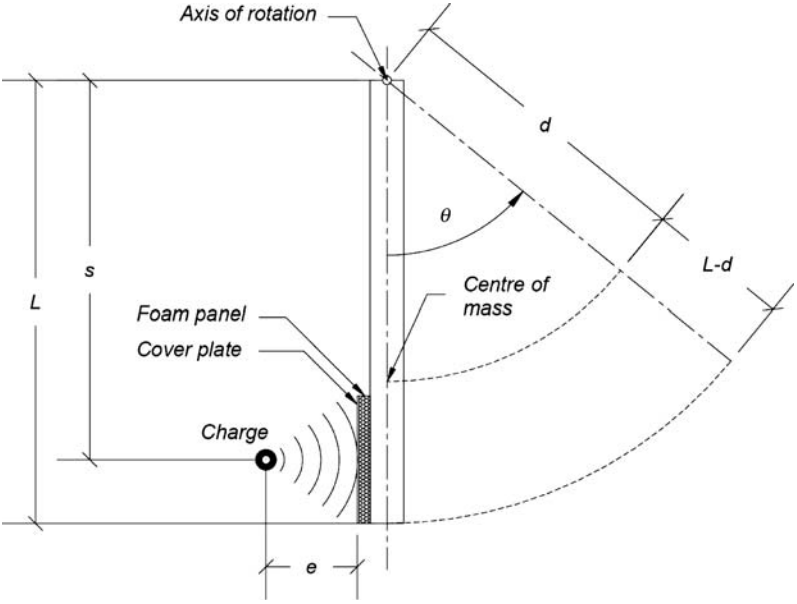

Fig. 1 Experimental test set-up

	Model parameters		
Event/Run	Cover plate	Charge mass (kg)	Foam density (kg/m^3)
A	No	1.0	150
B	Yes	1.0	150
C	No	2.5	150
D	Yes	2.5	150
E	No	1.0	350
F	Yes	1.0	350
G	No	2.5	350
H	Yes	2.5	350
I	Reference test	1.0	No foam panels
J	Reference test	2.5	No foam panels

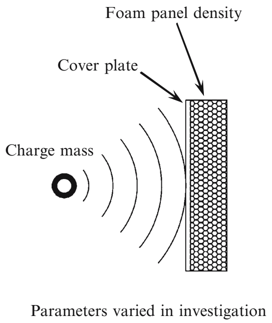

Fig. 2 Experimental program and model parameters

design study was used where the three main parameters were varied according to Fig. 2. The aluminium cover plate was 10 mm thick.

The impulse transfer was calculated from the maximum swing of the ballistic pendulum, see [1] for details. The impulse transfers from all configurations tested were compared to the baseline value, which was the impulse transfer to the bare pendulum. The pendulum's base plate had the same cross sectional dimension as the test panels.

The relative horizontal stand-off distance *e* was 500 mm from the centre of the charge to the front panels (test specimens), Fig. 1, and was kept constant for all tests.

Hanssen et al. [1] showed that the explosive loading was short in duration compared to the eigenperiod of the ballistic pendulum (impulsive loading). This means that the loading and also deformation of the foam panels were completed before the pendulum gained any significant response. Hence, to ease the simulations in this report, we add a rigid, stationary body to the back of the test specimens and record the impulse transferred to this body during loading.

3 Finite Element Model

The LS-DYNA [2] finite element model consisted of three Lagrangian parts. These are the 10 mm aluminium cover plate, the foam panel and the rigid backing plate. The rigid backing plate was fixed during simulation. The thickness of the foam panels was 70 mm when not using a cover plate and 60 mm when using a cover plate, exactly as for the experiments in [1]. The foam panels and cover plate were represented by brick elements (selectively reduced integrated elements).

The model contained two additional parts represented in an Eulerian reference frame, Fig. 3. These are the air and the explosive charge. The ambient pressure of the air was set to 1 bar.

Owing to symmetry, only $1/4$ of the foam panels was represented in the model.

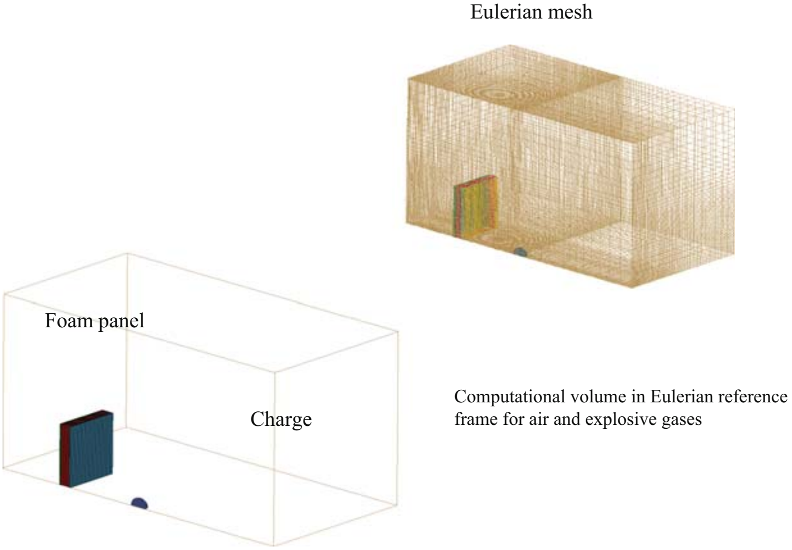

Fig. 3 Finite element mesh

Contact between the explosive gases and the foam panels was defined using a fluid-structure-interface (FSI) of the type *ALE_FSI_PROJECTION. This contact was only applied between the cover plate and the explosive gases. For the simulations without a cover plate, the FSI was applied between the explosive gases and the foam panel.

The detonation of the explosive loading was represented by the card *INITIAL_DETONATION. A programmed burn was adopted. This means that the detonation time of an element is equal to the distance from the detonation point divided by the pre-defined detonation velocity (experimentally determined value defined in *MAT_HIGH_EXPLOSIVE_BURN). The initiation point was located at the centre of the charge for the majority of simulations. However, a sensitivity study on the location of the detonation point is presented later.

To represent the aluminium AA5xxx material of the cover plates we used LS-DYNA material model 107 (*MAT_MODIFIED_JOHNSON_COOK). The model was calibrated using material data from Clausen et al. [7]. Material model 63 of LS-DYNA was used to represent the foam material (*MAT_CRUSHABLE_FOAM). The compressive material curves for both foam densities investigated are given in Fig. 4 and was motivated by material data by Hanssen et al. [8]. The charge mass was represented by LS-DYNA material *MAT_HIGH_EXPLOSIVE_BURN and equation-of-state *EOS_JWL. The ambient air was represented by *MAT_NULL and *EOS_LINEAR_POLYNOMIAL. We did not have the exact properties of the explosive PE4 used in the experiments. However, we approximated the PE4 properties by those of high-explosive C4 from data given in [9].

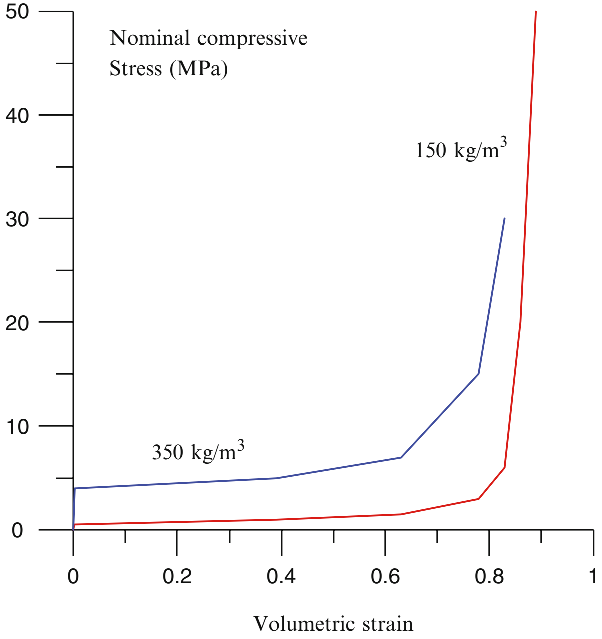

Fig. 4 Compressive input curve data to material model 63 of LS-DYNA

4 Numerical Results

Figure 5 shows the numerical blast loading sequence of Run D, which included a cover plate in front of a low-density foam panel. The high charge mass is used, see Fig. 2. It is evident that the numerical model handles the fluid structure interaction well and that the foam panel is heavily compressed.

Figure 6 shows the foam panels subjected to blast loading. We use the following numbering:

A: Impulse transfer in fluid-structure interface
B: Impulse transferred to rigid backing plate
C: Momentum of foam
D: Momentum of cover plate

Figure 7 gives the corresponding momentum vs. time curves for A–D based on Run B, see Fig. 2. We see from the graph that the impulse transferred to the backing plate (B) reaches a maximum when the foam and cover plate reverses their momentum. The values in the graph represent the $^1/_4$ model. We use momentum measure B when comparing with experimental results later on.

Figure 8 shows the following:

A: Total force from blast loading on front cover plate
B: Total force on backing plate

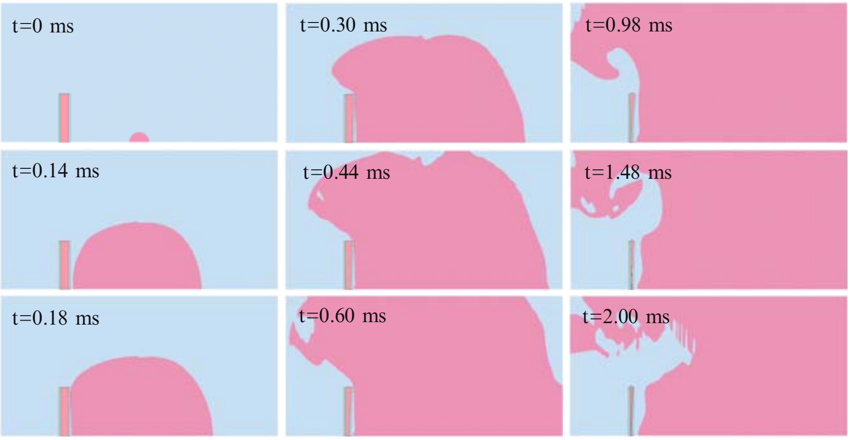

Fig. 5 Sequence from blast loading, Run D

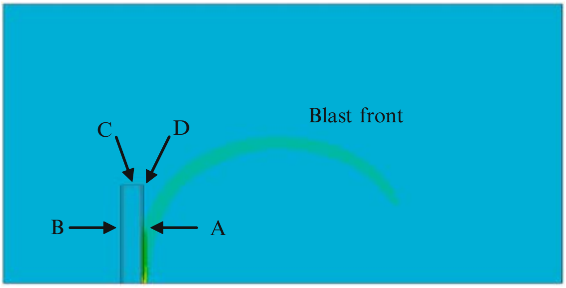

Fig. 6 Test specimen subjected to blast loading

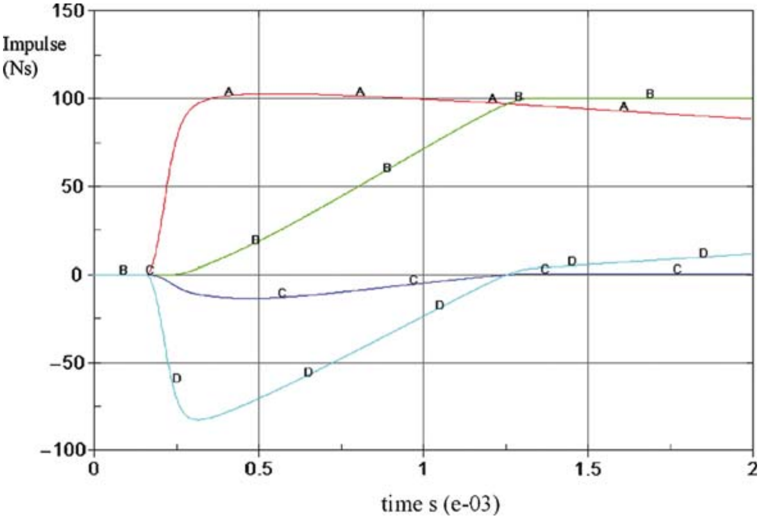

Fig. 7 Momentum-time curves for $^1/_4$ model curves following the definition of Fig. 6

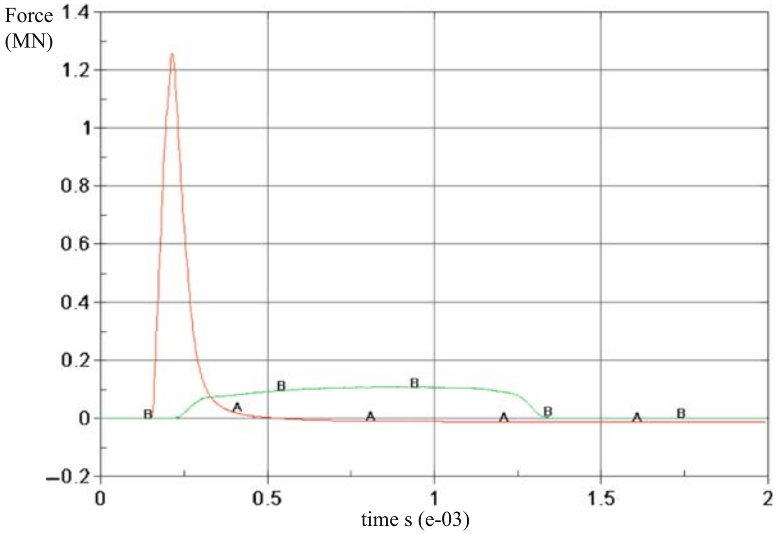

Fig. 8 Force vs. time for front panel (A) and backing plate (B)

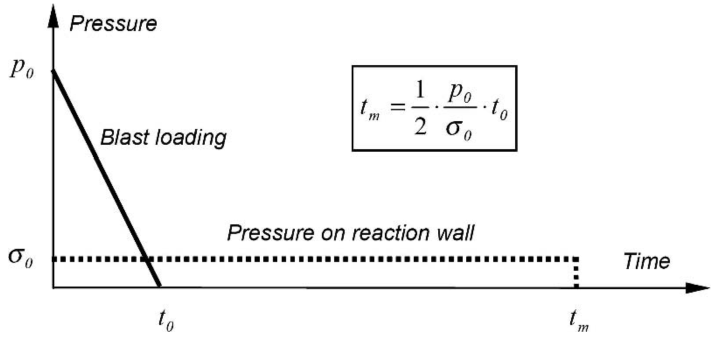

Fig. 9 Pressure on front panel versus reaction wall, from Hanssen et al. [1]

The graph is based on Run B from the simulations and represents the $1/4$ model. We see that the simulations capture the beneficial effect of foam panels used for blast mitigation purposes. The compressive, constant crushing strength of the foam panels controls the loads transferred to the rear structure. As a result of this the loading on the rear part is prolonged in time compared to the frontal blast loading (this is a direct result of conservation of momentum). This corresponds to analytical consideration of Hanssen et al. [1], which derived the duration of loading on the rear parts t_m as function of the blast loading peak pressure p_0, the compressive foam strength σ_0 and the blast loading duration t_0, see Fig. 9.

5 Numerical Sensitivity Study

We investigate two aspects of the test set up numerically. The first is the sensitivity to the position of detonation point. The second is the effect of reducing the Young's modulus of the foam.

The first sensitivity study was done on Run B changing the location of the detonation point, see (Fig. 10).

Figure 11 gives the corresponding momentum transfer to the rigid backing plate for the $^1/_4$ model. As seen, the effect of detonating the charge at the front end increases the momentum transfer by 8% compared to a central detonation point.

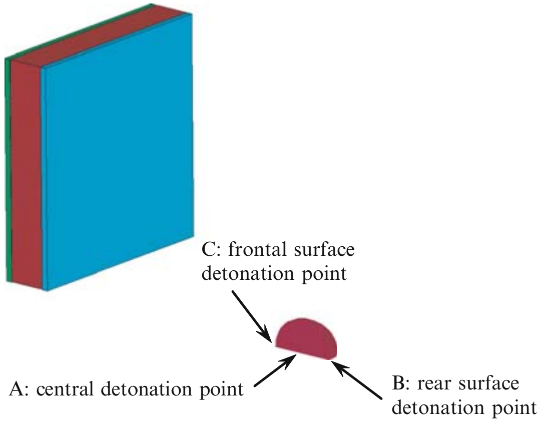

Fig. 10 Sensitivity study on position of detonation point

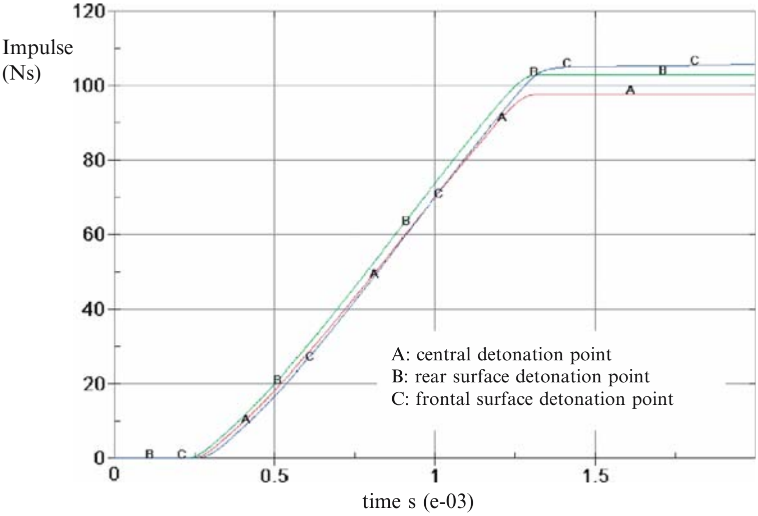

Fig. 11 Momentum transfer to backing plate for detonation positions A–C (Fig. 10)

In the second sensitivity study on Run B, the foam stiffness was reduced by a factor of 3. Figure 12 compares the original Run B with the modified model using the lower foam stiffness for the 1/4 model. It is evident that the foam stiffness influences the springback and then the momentum transfer to the backing plate. Lower foam stiffness produces higher momentum transfer.

6 Comparison: Experimental Versus Numerical Results

Table 1 shows the numerical vs. experimental momentum transfer to the backing panel for all tests. The same data is plotted in Fig. 13. For all events, the simulations consistently underpredict the impulse transfer compared to the experiments. The

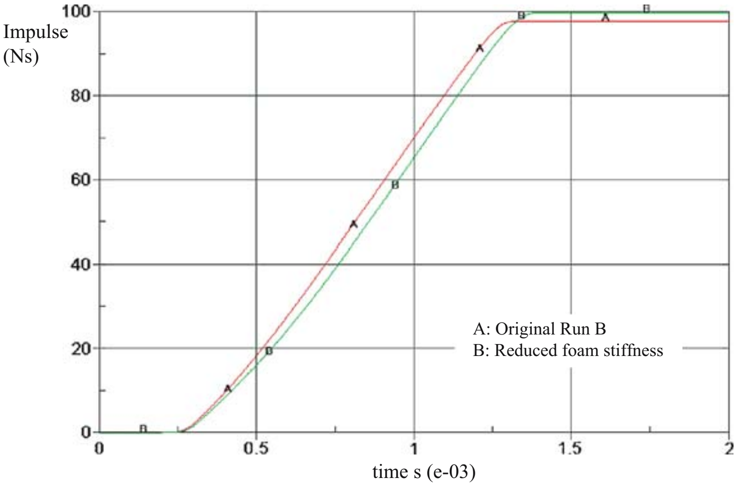

Fig. 12 Effect of reduced foam stiffness on momentum transfer to backing plate

Table 1 Numerical versus experimental results, momentum transfer to backing plate

Series	Cover plate	Charge	Foam density	Impulse transfer (Ns)		Sim	Deviation
				Rep 1	Rep 2		(%)
A	No	Low	Low	607.3	509.3	383.2	−31
B	Yes	Low	Low	630.1	588.4	401.6	−34
C	No	High	Low	978.4	1,088.4	880	−15
D	Yes	High	Low	1,305.3	1,201	891.6	−29
E	No	Low	High	539.7	537.6	422.8	−22
F	Yes	Low	High	547	662.5	458.8	−24
G	No	High	High	1,097.5	1155	869.2	−23
H	Yes	High	High		1,171.6	922	−21
I	Reference	Low	No foam	526.2	558.9	362.4	−33
J	Reference	High	No foam	936.6	947.1	862	−8

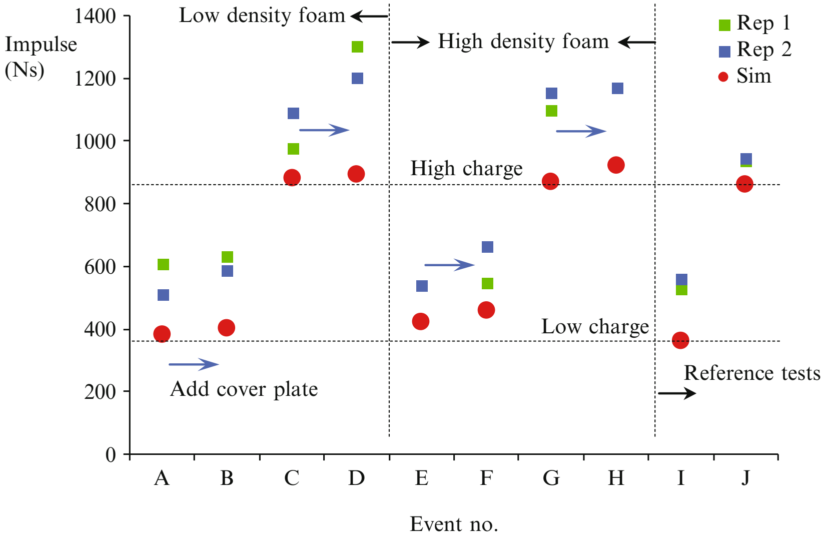

Fig. 13 Momentum transfer to backing plate, numerical versus experimental results

increase in impulse transfer when adding a cover plate is also captured by the model, but the effect is less pronounced than in experiments. The simulations indicate a small increase in the momentum transfer when adding a foam panel compared to the reference tests on the bare pendulum.

7 Discussion

It was observed that the numerical model consistently underpredicts the momentum transfer, also for the case of blast loading against a bare pendulum.

The main reasons for this might be:

1. The simulations do not account for the lower part of the pendulum’s arms, which also are subjected to blast loading and momentum transfer, see Fig. 14.
2. The properties of the PE4 explosive are approximated as those of C4.
3. The detonation point within the explosive is not centered, but lies nearer the surface. The amplification effect of a non-central detonation point was clearly demonstrated in the numerical sensitivity study.
4. The Young’s modulus of the foam used in the tests could have been lower than what was use for the numerical model. As shown in the sensitivity study, a lower stiffness of the foam will increase the springback/rebound effect and therefore increase the momentum transferred to the pendulum.
5. The results may be very sensitive to deviations from a perfectly spherical charge in the same way as the results are sensitive to the position of the detonation point. It is unclear how carefully the charges in the experiments were shaped.

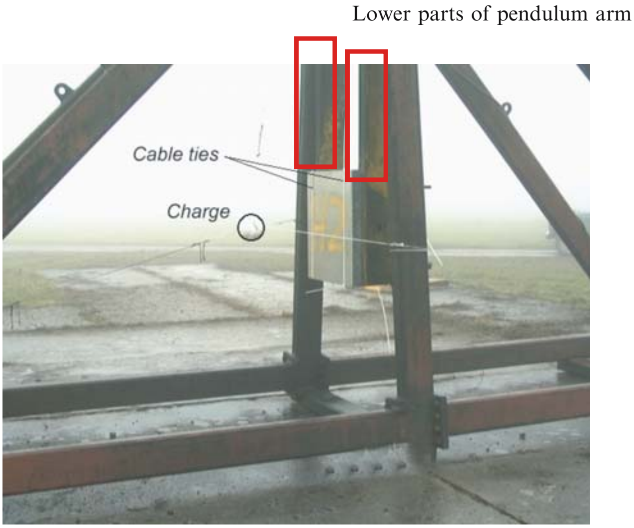

Fig. 14 Ballistic pendulum used in tests

8 Conclusions

It has been demonstrated that the current simulations predict the trend of the full-scale blast loading experiments. However, the simplified model of the pendulum (neglecting the pendulum arms in the fluid structure interaction) quantitatively underpredicts the experimentally measured impulse transfer by 20–30%.

The simulations have revealed that significant scatter in experimental result may be due to variation of the detonation point within the charge.

The importance of controlling the Young's modulus of the foam in a numerical model must be underlined, since this has influence on the extent of the spring-back/rebound effect and therefore also the transfer of momentum to the rear structure. It must be concluded that this effect is a likely reason for the increased impulse and energy transfer observed in the experiments [1].

References

1. A.G. Hanssen, L. Enstock and M. Langseth: *Close-range blast loading of aluminium foam panels*. International Journal of Impact Engineering, Volume 27, pp. 593–618 (2002)
2. J. Hallquist: *LS-DYNA keyword user's manual*. Livermore Software Technology Corporation, Livermore, CA. Version 971, September (2006)
3. G.W. Ma and Z.Q. Ye: *Energy absorption of double-layer foam cladding for blast alleviation*. International Journal of Impact Engineering, Volume 34/2, pp. 329–347 (2007)
4. G.W. Ma and Z.Q. Ye: *Analysis of foam claddings for blast alleviation*. International Journal of Impact Engineering, Volume 34/1, pp. 60–70 (2007)

5. M.J. Mullin and B.J. O'Toole: *Simulation of energy absorbing materials inn blast loaded structures*. 8th international LS-DYNA user's conference
6. A. Clausen, T. Børvik, O.S. Hopperstad and A. Benallal: *Flow and fracture of aluminium alloy AA5083-H116 as function of strain rate, temperature and triaxiality*. Materials Science and Engineering, A364, pp. 260–272 (2004)
7. A.G. Hanssen, O.S. Hopperstad, M. Langseth and H. Ilstad: *Validation of constitutive models applicable to aluminium foams*. International Journal of Mechanical Sciences, Volume 44/2, pp. 359–406 (2002)
8. B.M. Dobratz and P.C. Crawford: *LLNL explosives handbook, Tech. Report UCRL-52997*, Lawrence Livermore National Laboratory, Livermore, CA (1985)

Description of the Behaviour of Cellular Composite with Weak Filling Material

E. Postek and T. Sadowski

Abstract The aim of this presentation is to show the behaviour of a cellular composite material. The material is two-phase consisting of metallic, relatively rigid interfaces and weak filling material. Such type of a generic composite is used as core filler between external layers of sandwich composite material applied in aerospace engineering. We investigate the limit load of a sample varying the initial void ratio in the filling. We are using the Tvergaard-Gurson in order to describe porosity existence in the material and elasto-plastic models with the assumption of presence of the finite deformations. The geometrical model is three-dimensional.

1 Introduction

A generic model of a two-phase composite is presented. This model can be used for an analysis of a cellular composite with weak filling material. The initial porosities can be as high as 60%. The problem is highly non-linear because of initial stress stiffness, plasticity and possibly voids nucleation. In our case we follow the analysis up to appearance of plastic strain which develops close to junctions of the stiff skeleton and close to surfaces where the pressure is applied.

E. Postek (✉)
School of Earth and Environment, Institute of Geophysics and Tectonics, University of Leeds, Woodhouse Lane, Leeds, LS2 9JT, UK
e.w.postek@leeds.ac.uk

T. Sadowski
Faculty of Civil and Sanitary Engineering, Department of Solid Mechanics, Lublin University of Technology, ul. Nadbystrzycka 40, 20-618 Lublin, Poland
tsadow@akropolis.pol.lublin.pl

H. Zhao, N.A. Fleck (eds.), *Mechanical Properties of Cellular Materials,*
IUTAM Bookseries 12,

2 Formulation

2.1 Incremental Equation of Equilibrium

The problem is elasto-plastic with the assumption of large displacements [1–3]. We consider nonlinear terms of the strain tensor. The virtual work equation is of the form

$$\delta\Pi = \int\limits_{\Omega^o}^{t+\Delta t} {}_{\mathrm{o}}\mathbf{S}\cdot\delta^{t+\Delta t}{}_{\mathrm{o}}\mathbf{E}\,d\Omega^{\mathrm{o}} - \int\limits_{\Omega^o} {}^{t+\Delta t}\mathbf{f}\delta^{t+\Delta t}\mathbf{u}\,d\Omega^{\mathrm{o}} - \int\limits_{\partial\Omega^o_\sigma} {}^{t+\Delta t}\mathbf{t}\delta^{t+\Delta t}\mathbf{u}\,d\left(\partial\Omega^{\mathrm{o}}_\sigma\right), \quad (1)$$

where **S** and **E** are the second Piola-Kirchhof stress tensor and Green Lagrange strains, **f, t** and $\mathbf{u} = \{\mathrm{u}, \mathrm{v}, \mathrm{w}\}$ are body forces, boundary tractions and displacements. All of the quantities are determined at time $\mathrm{t} + \Delta\mathrm{t}$ in the initial configuration. To obtain the above equation at time $t + \Delta t$ in the configuration at time t the relations [4, 5], are used

$$^{t+\Delta t}{}_o\mathbf{S} = \frac{\rho}{\rho_o}{}^{t+\Delta t}{}_t\mathbf{S}, \quad ^{t+\Delta t}{}_o\mathbf{E} = \frac{\rho}{\rho_o}{}^{t+\Delta t}{}_t\mathbf{E}, \quad \rho d\Omega^t = \rho_o\, d\Omega^o \quad (2)$$

$$\int\limits_{\Omega^t} {}^{t+\Delta t}{}_t\mathbf{S}\cdot\delta^{t+\Delta t}{}_t\mathbf{E}\,d\Omega^t = \int\limits_{\Omega^t} {}^{t+\Delta t}\mathbf{t}\delta^{t+\Delta t}\mathbf{u}\,d\Omega^t + \int\limits_{\partial\Omega^t_\sigma} {}^{t+\Delta t}\mathbf{t}\delta^{t+\Delta t}\mathbf{u}\,d\left(\partial\Omega^t_\sigma\right). \quad (3)$$

Now, we apply incremental decomposition to the quantities in the equation above: strains, stresses, displacements and forces

$$^{t+\Delta t}{}_t\mathbf{E} = {}^t_t\mathbf{E} + \Delta\mathbf{E},\ {}^{t+\Delta t}{}_t\mathbf{S} = {}^t_t\mathbf{S} + \Delta\mathbf{S},{}^{t+\Delta t}\mathbf{u} = {}^t\mathbf{u} + \Delta\mathbf{u},\ {}^{t+\Delta t}\mathbf{f} = {}^t\mathbf{f} + \Delta\mathbf{S}. \quad (4)$$

Since the second Piola-Kirchhoff tensor at time t in the configuration t is equal to the Cauchy stress tensor the stress decomposition is of the form

${}^t_t\mathbf{S} ={}^t_t \tau$ and ${}^{t+\Delta t}{}_t\mathbf{S} ={}^t_t \tau + \Delta\mathbf{S}$. Then, we employ the following strain increment decomposition into its linear and nonlinear parts in the following form $\Delta\mathbf{E} = \Delta\mathbf{e} + \Delta\eta$, $\Delta\mathbf{e} = \bar{\mathbf{A}}\Delta\mathbf{u}$ and $\Delta\eta = \bar{\bar{\mathbf{A}}}(\Delta\mathbf{u}')\Delta\mathbf{u}'/2$ where $\Delta\mathbf{u}'$ is the vector of the displacement increment derivatives w.r.t. Cartesian coordinates and $\bar{\mathbf{A}}$, $\bar{\bar{\mathbf{A}}}$ are the linear and nonlinear operators [2]. The operators act on linear and nonlinear parts of the strain tensor.

Substituting the described relations, into the virtual work equation, Eq. (3), and assuming that the equation is precisely fulfilled at the end of the step we obtain the following incremental form of the virtual work equation.

$$\int\limits_{\Omega^t} \left({}^t_t\tau\cdot\delta\eta + \Delta\mathbf{S}\cdot\delta\Delta\mathbf{e}\right)\,d\Omega^t = \int\limits_{\Omega^t} \Delta\mathbf{f}\;\delta\Delta\mathbf{u}d\Omega^t + \int\limits_{\partial\Omega^t_\sigma} \Delta\mathbf{t}\;\delta\Delta\mathbf{u}\,d\left(\partial\Omega^t_\sigma\right). \quad (5)$$

Employing the finite element approximation $\Delta\mathbf{u} = \mathbf{N}\Delta\mathbf{q}$ and $\Delta\mathbf{u}' = \mathbf{B}'\Delta\mathbf{q}$ where $\mathbf{N}$ is the set of shape functions and $\Delta\mathbf{q}$ is the increment of nodal displacements and considering the following set of equalities

$$ {}^{t}_{t}\tau^{\mathrm{T}}\delta\eta = {}^{t}_{t}\tau\delta\left(\bar{\bar{\mathbf{A}}}\right)\,\Delta\mathbf{u}' = \delta\left(\Delta\mathbf{u}'\right)^{\mathrm{T}}\,{}^{t}_{t}\bar{\tau}\,\Delta\mathbf{u}' = \delta\left(\Delta\mathbf{q}\right)^{\mathrm{T}}\,{}^{t}_{t}\bar{\tau}\,\mathbf{B}'_{L}, \tag{6} $$

where ${}^{t}_{t}\bar{\tau}$ is the Cauchy stress matrix

$$ {}^{t}_{t}\bar{\tau} = \begin{bmatrix} {}^{t}_{t}\underline{\tau} & & \\ & {}^{t}_{t}\underline{\tau} & \\ & & {}^{t}_{t}\underline{\tau} \end{bmatrix} \qquad {}^{t}_{t}\underline{\tau} = \begin{bmatrix} {}^{t}_{t}\sigma_{xx} & {}^{t}_{t}\tau_{xy} & {}^{t}_{t}\tau_{xz} \\ & {}^{t}_{t}\sigma_{yy} & \tau_{yz} \\ & & {}^{t}_{t}\sigma_{zz} \end{bmatrix}, \tag{7} $$

we obtain the following discretized form of the virtual work equation

$$ \left(\int\limits_{\Omega^t} \mathbf{B}'_{\mathrm{L}}{}^{\mathrm{T}}\,{}^{t}_{t}\bar{\tau} B'_{\mathrm{L}}\, d\Omega^t\right)\Delta\mathbf{q} + \int\limits_{\Omega^t} \mathbf{B}_{\mathrm{L}}^{\mathrm{T}}\Delta\mathbf{S}\, d\Omega^t = \int\limits_{\Omega^t} \mathbf{N}^{\mathrm{T}}\Delta\mathbf{f}\, d\Omega^t + \int\limits_{\partial\Omega^t_\sigma} \mathbf{N}^{\mathrm{T}}\Delta\mathbf{t}\, d\left(\partial\Omega^t_\sigma\right). \tag{8} $$

Now, we will deal with the constitutive model and employ the linearized constitutive equation, in fact with the stress increment, $\Delta\mathbf{S}$.

2.2 *Finite Strains*

When considering the finite strains effect [6, 7], the gradient $\mathbf{F} = \partial\left(\mathbf{X}+\mathbf{u}\right)/\partial\mathbf{x}$ is decomposed into its elastic and plastic parts, $\mathbf{F} = \mathbf{F}^e\mathbf{F}^p$. To integrate the constitutive relations the deformation increment $\Delta\mathbf{D}$ is rotated to the un-rotated configuration by means of rotation matrix obtained from polar decomposition $\mathbf{F} = \mathbf{V}\mathbf{R} = \mathbf{R}\mathbf{U}$, $\Delta\mathbf{d} = \mathbf{R}^T_{n+1}\Delta\mathbf{D}\mathbf{R}_{n+1}$, then the radial return is performed and stresses are transformed to the Cauchy stresses at $n+1$, $\sigma_{n+1} = \mathbf{R}_{n+1}\sigma^u_{n+1}\mathbf{R}^T_{n+1}$. The stresses are integrated using the consistent tangent matrix [8] and the integration is done in the un-rotated configuration as for small strains.

3 Constitutive Model

The constitutive model is the Gurson Tvergaard model [9–11] with the yield function as follows

$$ F = \left(\frac{\sigma^M}{\bar{\sigma}}\right)^2 + 2q_1 f\cosh\left(\frac{3q_2\sigma_m}{2\bar{\sigma}}\right) - \left(1+q_3 f^2\right), \tag{9} $$

where σ^M is the Mises stress, σ_m is the mean stress, $\bar{\sigma}$ is the Mises stress in the matrix, f is the void ratio and $q_1, q_2\ q_3$ are the Tvergaard coefficients.

The stress integration algorithm comprises the elastic trial stress (predictor) and the corrector. It conforms the radial return algorithm. The algorithm can be derived basing on [12]. The elastic trial stress are of the form

$$\sigma^{\mathrm{E}}_{m+1} = \sigma_m + \mathbf{D}\ \Delta\varepsilon^{pl}. \tag{10}$$

The deviatioric and the volumetric stress are of the form

$$q_{m+1} = \sqrt{\left(\frac{3}{2}S_{ij}S_{ij}\right)_{m+1}} \quad p_{m+1} = -\frac{1}{3}(\sigma_{11} + \sigma_{22} + \sigma_{33})_{m+1}. \tag{11}$$

The increment of the plastic strains can be obtained from the normality condition.

$$d\varepsilon^{pl} = d\lambda \frac{\partial F}{\partial \sigma} \tag{12}$$

Further, the plastic strains increment and the unit normal vector are of the form

$$\Delta\varepsilon^{pl} = \Delta\lambda \left(-\frac{1}{3}\frac{\partial F}{\partial p}\mathbf{I} + \frac{\partial F}{\partial q}\mathbf{n}\right)_{m+1} \quad \mathbf{n}_{m+1} = \frac{3}{2q_{m+1}}\mathbf{S}_{m+1}. \tag{13}$$

The stress at the end of the $(\mathrm{m}+1)$ takes the form

$$\sigma_{m+1} = \sigma^{\mathrm{E}} - \mathbf{D}\Delta\varepsilon^{pl}. \tag{14}$$

Since the increment of plastic strains is

$$\Delta\varepsilon^{pl} = \frac{1}{3}\Delta\varepsilon_p\mathbf{I} + \Delta\varepsilon_q\mathbf{n}_{m+1}, \tag{15}$$

the stress at the end of the step may be expressed as follows

$$\sigma_{m+1} = \sigma^{\mathrm{E}}_{m+1} - K\Delta\varepsilon_p\mathbf{I} - 2G\Delta\varepsilon_q\mathbf{n}_{m+1}. \tag{16}$$

The updated stresses are of the form

$$\sigma_{m+1} = \sigma^{\mathrm{E}}_{m+1} - K\Delta\varepsilon_p\mathbf{I} - \frac{3G\Delta\varepsilon_q}{q^{\mathrm{T}}_{m+1}}\mathbf{S}^{\mathrm{E}}_{m+1}, \tag{17}$$

where the quantities designated with the index (E) are the elastic trial stresses.

4 Numerical Example

We consider two cases of the material of the different Young's moduli of the filling material. The Young's moduli are $0.2\mathrm{E}+11\,\mathrm{N/m}^2$ and much lower $0.005\mathrm{E}+11\,\mathrm{N/m}^2$. Both moduli significantly lower the Young's modulus of the skeleton which is $2.1\mathrm{E}+11\,\mathrm{N/m}^2$. The yield limits are $15.0\mathrm{E}+6$ and $297.0\mathrm{E}+6\,\mathrm{N/m}^2$. The initial porosity of the filler is 0.3. We observe the most characteristic features of the behaviour of the material. Our interest is focused on the vertical displacements, equivalent total strains, plastic strains and Mises stress.

Observing all figures (Figs. 1–4) we may notice qualitatively different performance of both materials. The vertical z-displacements (Fig. 1) is more equally distributed and is lower, 0.725E-5 mm, in the case A than in the case B, 0.358E-3 m. This z-displacements distribution gives a picture of roughness of the material during loading. The weaker sample becomes thinner close to the loaded edge. When concerning the total equivalent strain (Fig. 2) we may notice higher contrasts in the case of stronger material. The strain is distinctly lower in all interfaces than in the cells. The maximum strain, 0.691E-3 is lower than in the case of the weaker material, 0.418E-1.

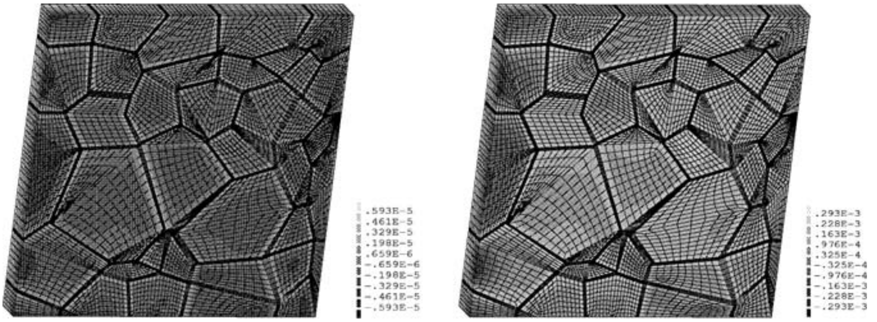

Fig. 1 Veritical displacements distributions (cases A and B)

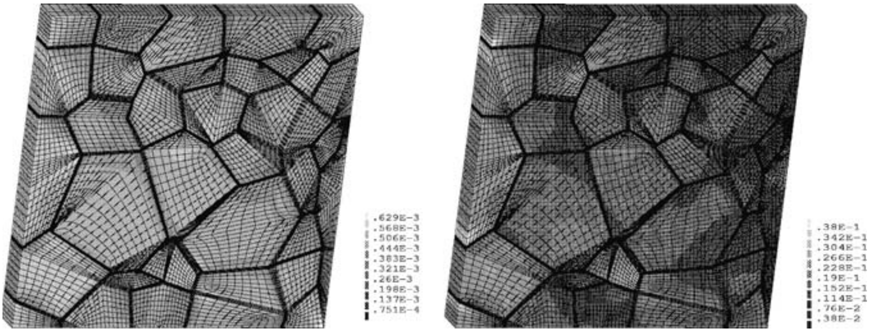

Fig. 2 Equivalent strain distribution (cases A and B)

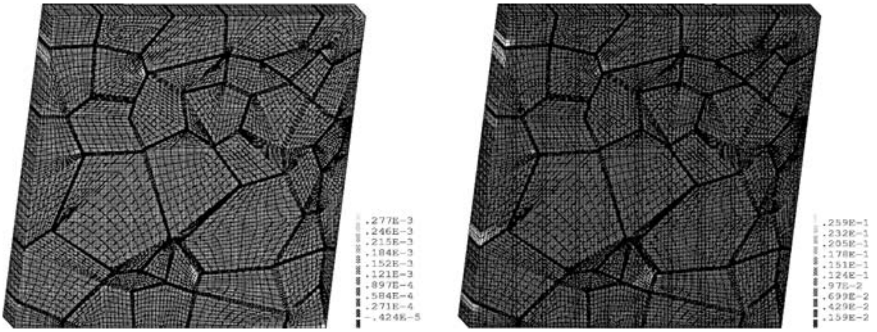

Fig. 3 Equivalent plastic strain distribution (cases A and B)

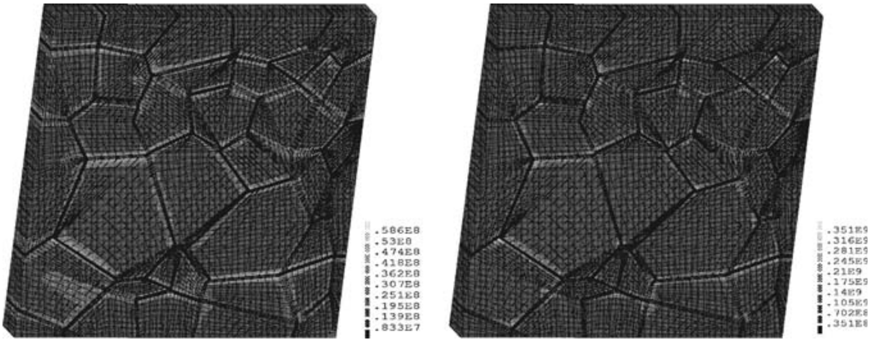

Fig. 4 Mises stress distribution (cases A and B)

The equivalent plastic strain distribution (Fig. 3) is different in both cases. In the case of stronger material there are more equivalent plastic spots within the sample than in the case of weaker material. The plastic strain are more localized in the weaker sample. The equivalent plastic strain reads 0.309E-3 and 0.286E-1, respectively.

The Mises stress distributions are presented in Fig. 4. The Mises stress is the highest in the junctions of the skeleton and in the edges of the skeleton. The maximum stress is higher in the sample with weaker filling material $(0.386\text{E}+9\,\text{Pa})$ than in the case of stiffer sample $(0.642\text{E}+8\,\text{Pa})$. The stress contrasts are higher in the case of weaker sample.

The calculations were performed for the same load level, $80.4\text{E}+6\,\text{Pa}$.

5 Final Remark

A generic numerical model of a material with weak filling material is presented. The weak material is modelled using Tvergaard Gurson material. This approach is convenient and allows to model material with high initial volume of voids.

References

1. Owen, D.R.J., Hinton, E. (1980) Finite Elements in Plasticity: Theory and Practice, Pineridge, Swansea, UK.
2. Bathe, K.J. (1996) Finite Element Procedures, Prentice Hall, Englewood Cliffs, NJ/London.
3. Kleiber, M. (1989) Incremental Finite Element Modelling in Non-linear Solid Mechanics, Polish Scientific, Warsaw, Ellis Horwood, Chichester.
4. Malvern, L.E. (1969) Introduction to the Mechanics of Continuous Medium, Prentice Hall, Englewood Cliffs, NJ/London.
5. Crisfield, M.A. (1991) Non-linear Finite Element Analysis of Solids and Structures, Wiley, New York.
6. Pinsky, P.M., Ortiz, M., Pister, K.S. (1983) Numerical integration of rate constitutive equations in finite deformations analysis, Computer Methods in Applied Mechanics and Engineering, 40, 137–158.
7. Peric, D., Owen D.R.J., Honnor, M.E. (1985) A model for finite strain elasto-plasticity based on logarithmic strains: Computational issues, Computer Methods in Applied Mechanics and Engineering, 94, 101–118.
8. Simo, J.C., Taylor, R.L. (1985) Consistent tangent operators for rate independent elastoplasticity, Computer Methods in Applied Mechanics and Engineering, 48, 101–118.
9. Gurson, L. (1977) Continuum theory of ductile rupture by void nucleation and growth: Part I – yield criteria and flow rules for porous ductile media, Journal of Engineering Materials and Technology, Transactions of ASME, 99, 2–15.
10. Tvergaard, V. (1982) On localization in ductile materials containing spherical voids, International Journal of Fracture, 18, 237–252.
11. Tvergaard, V. (1981) Influence of voids on shear-band instabilities under plane strain conditions, International Journal of Fracture, 17, 389–407.
12. Simo, J.C., Hughes, T.J.R. (1998) Computational Inelasticity, Springer, New York/London.

Studies on the Dynamic Behavior of Aluminum Alloy Foams

H.-W. Ma, Z.-H. Wang, L.-M. Zhao, and G.-T. Yang

Abstract The compressive deformation behavior of open-cell aluminum foams with different densities and morphologies was assessed under quasi-static and dynamic loading conditions. High strain rate experiments were conducted using a split Hopkinson pressure bar technique at strain rates ranging from 500 to $2,000\,\mathrm{s}^{-1}$.The inverse analysis is used to correct the errors that transverse inertial effect and the disperse effect because of the large diameter. The experimental results show that the density is the primary variable characterizing the modulus and yield strength of foams and the cell size appears to have a negligible effect on the strength of foams. It is found that the yield strength is almost insensitive to strain rate, over a wide range of strain rates and deformation is spatially uniform for the open-celled aluminum foams.

1 Introduction

Metal foams, as a new class of engineering materials, have a great potential for absorbing energy because they have an extended stress plateau in the compressive stress–strain curve. Recent development of production methods for metallic foams have offered a variety of application in fields such as the automobile, railway and aerospace industries. In these applications, the foam is subject to high-velocity deformations. Designing for these applications therefore demands a

---

H.-W. Ma (✉)
College of Science & Engineering, Jinan University, Guangzhou 510632, China

Z.-H. Wang, L.-M. Zhao, and G.-T. Yang
Institute of Applied Mechanics, Taiyuan University of Technology, Taiyuan, 030024, China

Z.-H. Wang
State Key Laboratory of Explosion Science and Technology, Beijing Institute of Technology, Beijing 100081, China

H. Zhao, N.A. Fleck (eds.), *Mechanical Properties of Cellular Materials,*
IUTAM Bookseries 12,

full characterization of their mechanical properties under a wide range of strain rates. The quasi-static mechanical properties of aluminum alloy foams, such as compressive strength and the elastic modulus, have been extensively studied and reviewed [1]. However, related studies under dynamic conditions have been relatively limited due to the difficulty of characterizing the high strain rate behavior of aluminum alloy foams. Kenny [2] reported that the specific energy absorption of Alcan foam (open-cell) was independent of applied strain rate in the range 10^{-3}–$10^{3}\,s^{-1}$. No measurements were made however, of the stress-strain curve under dynamic and quasi-static loadings. In line with the findings of Kenny, Deshpande and Fleck [3] found that the strain rate dependence of mechanical strength was negligible for the Doucel (open-cell) and Alulight (closed-cell) foams. Lankford and Dannemann [4] also showed that open-cell alluminum foam did not exhibit the strain rate dependence of plateau stress. On the other hand, Mukai et al. reported that open-cell SG91A AL [5], closed-cell foam Alporas [6], and open-cell AZ91Mg [7], all found a high strain rate sensitivity of the plateau stress. Dannemann and Lankford [8] also demonstrated the strain rate dependence of plateau stress for Alporas (closed-cell) for high strain rates ranging from 4×10^{2} to $2.5 \times 10^{3}\,s^{-1}$. Thus, it is noted that, despite the fact that metallic foams are attractive materials for energy absorption, only limited data are available for dynamic strain rates.

Dynamic behavior at high strain rates is often determined by using the SHPB (Split Hopkinson Pressure Bar) experimental technique. In order to get more accurate experimental data, the cell number should exceed ten in the specimen diameter normally. The cell size of the metallic porous materials relatively is great in practice engineering, sometimes beyond 20 mm, thus the diameter of the pressure bars in the SHPB equipment needs been extended. With extending diameter of the pressure bars, the bar transverse inertial effect and the disperse effect make errors increasingly prominent. In order to overcome this difficulty, the inverse analysis is used to dynamically calibrate the SHPB experimental set-up. The transfer function $h(t)$ of the pressure bar is given using the deconvolution in inverse analysis. The data processing system is performed and an efficient method to investigate the dynamic behavior of metallic porous materials is afforded.

Some studies have also been carried out to evaluate the effect of cell morphology on the mechanical properties of metallic foams. Nieh et al. [9] observed the effect of cell size and shape on the compressive behavior of open-cell AA6101-T6 aluminum foams with different relative density and showed that the former, in contrast to the latter, appeared to have a negligible effect on the strength of foam. It is noted that these studies were all carried out at static strain rates. The effect of cell morphology on the deformation behavior of metallic foams at dynamic strain rates has not been investigated. In the present paper, open-cell aluminum alloy foams with different cell sizes and relative densities were examined under quasi-static and dynamic conditions in order to estimate the effect of cell size on the compressive mechanical property and the energy absorption capability.

2 Experimental

The open-cell aluminum alloy foams produced by the infiltrating process were used in the present study. The composition of the cell wall material is AL-3wt.%Mg–8wt.%Si–1.2wt.%Fe. The relative density (defined as the density of the foam divided by the density of the cell wall material) of the foam ranges from 0.25 to 0.30 and the average cell sizes are 0.9 and 1.6 mm, respectively.

Dynamic compression test at strain rates in the range 10^2–$10^4\,\mathrm{s}^{-1}$ was performed using the split Hopkinson pressure bar (SHPB) technique. The selected specimens are circular cylinders of diameter 35 mm and length 10 mm. With this choice of specimen dimensions, the specimens have at least 6–10 cells in all directions. A brief description of the experiment set-up was given below. The striker, incident pressure and transmitter bars consist of 37 mm diameter aluminum bars and their length are 800, 2,000 and 2,000 mm, respectively. The end surfaces were lubricated to reduce the frictional restraint. The compressive pulse generates by axial impact of the incident pressure bar by the striker bar. When the compressive pulse reaches the specimen, a portion of the pulse is reflected from the interface, while the remainder is transmitted through to the transmitter bar. The incident pulse and reflect wave in the incident bar are recorded by the resistance strain gauge attached at the incident bar. The transmitted wave is also recorded by the semiconductor strain gauge attached at the transmitter bar. Typical incident, reflected and transmitted waves are shown in Fig. 1.

As the three waves are not measured at bar-specimen interfaces in order to avoid their superposition, they have to be shifted from the position of the strain gages to the specimen faces, in time and distance. This shifting leads to two main perturbations. First, waves change in their shapes on propagating along the bar, especially for the large diameter bars. Second, it is very difficult to find an exact delay in the time shifting to ensure that the beginnings of the three waves correspond to the same instant. Those perturbations, if not controlled, can introduce errors in the final result.

In this experiment, the inverse analysis method is used to correct wave disperses due to waves shift from the position of the strain gages to the specimen faces. Firstly, conduct a calibration such as impact with an elastic bar, and measure both the impact

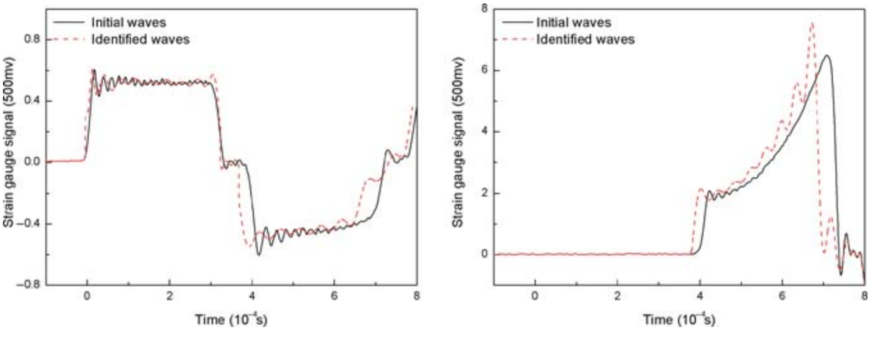

Fig. 1 Initial and identified waves records from the incident and transmitter bars

load $f(t)$ and the response $e(t)$, and then, estimate the transfer function according to Eq. (1),

$$\begin{cases} e(t) = f(t)^{*}h(t) = \int_{0}^{t} h(t-\tau)f(\tau)d\tau \\ f(t) = h(t) = e(t) = 0, t < 0 \end{cases} \tag{1}$$

where $h(t)$ is the impulse response function of the linear system. The problem of estimating the time history can be reduced to the process of deconvolution. A basic scheme for deconvolution is to transform the convolution in the time domain into a multiplication in the frequency domain using Fourier transforms resulting in and then estimate the transfer function $H(\omega)$ according to Eq. (2)

$$E(\omega) = H(\omega)F(\omega) \tag{2}$$

where the symbols in uppercase denote the Fourier transforms of the corresponding ones in lowercase. And then, measure the strain response $e(t)$ induced by any impact load $f(t)$, and estimate the impact load according to Eq. (2) by utilizing the transfer function obtained in the first step. Identified incident, reflected and transmitted waves are shown in Fig. 1.

Compressive test was also performed at a quasi-static strain rate of $10^{-3}\,\mathrm{s}^{-1}$ using a servo-hydraulic test machine and specimens are 35 mm in diameter and 30 mm in height. The detailed experimental results were given in the following.

3 Results and Discussion

Figure 2 shows the stress-strain curves for different cell sizes with the same relative densities under quasi-static and dynamic compression, respectively. The quasi-static deformation of open-cell aluminum alloy foams is uniform, which is different from the closed-cell foams with band formation. At overall macroscopic strains greater than about 30% the whole specimen has crushed and uniform additional strain

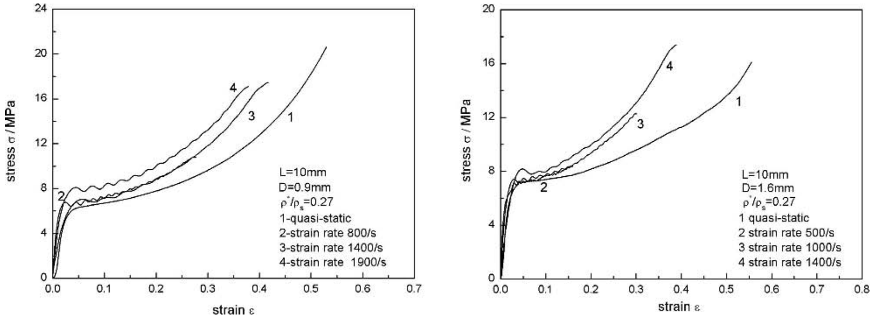

Fig. 2 Stress–strain curves of aluminum alloy foams at different strain rates

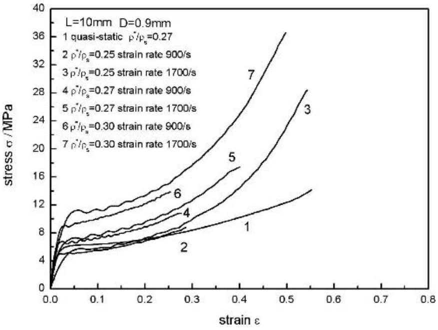

Fig. 3 Quasi-static and dynamic compression stress–strain curves of aluminum alloy foams different in density and strain rate

occurring as observed by Deshpande [3]. The compressive stress–strain curve of aluminum alloy foams, either quasi-static or dynamic compression, exhibits universal three deformation characteristics: an initial linear-elastic region; an extended plateau region where the stress increases slowly as the cells deform plastically; and a final densification as collapsed cells are compacted together. These deformation characteristics of the aluminum alloy foams are similar to those of other metal foams [3, 4]. The only significant difference between the dynamic and static stress versus strain curves is that, while the static curves are smooth, oscillations can be seen in the dynamic curves and the reason can be uninterrupted destabilization of aluminum alloy foams with the plastic collapse in cell walls.

It can be seen from Fig. 2 that linear elasticity can only appear at very low strain (smaller than about 0.05) and seems to be independent of the strain rate. It also can be readily observed in this figure that the cell size appears to have insignificant effect on plastic collapse, even at the dynamic strain rates. This is very similar to the observations of Nieh et al. [9], reported a cell size effect at quasi-static strain rates in Doucel foams.

Figure 3 shows quasi-static and dynamic stress-strain curves for various densities of foams. The higher the foams' relative densities are, the shorter the plateau region is, but higher densities also imply higher yield stresses. Gibson and Ashby analyzed the relationship between the relative stress $\sigma^*_{pl}/\sigma_{ys}$, and the relative density ρ^*/ρ, assuming that plastic collapse occurs when the moment exerted by the compressive force exceeds the fully plastic moment of the cell edges, where σ^*_{pl}, ρ^* are the plastic-collapse stress and the density of the cellular material, σ_{ys}, ρ are the yield stress and the density of the cell wall material, respectively. The relationship between the relative stress and the relative density for open-celled material is given by [1],

$$\frac{\sigma^*_{pl}}{\sigma_{ys}} = C\ (\rho^*/\rho)^{3/2}, \tag{3}$$

Using this equation, the relationship between the relative stress and relative density for the presently studied aluminum alloy foams is plotted in Fig. 4. Also included in the figure are the data from other aluminum foams [6]. The experimental data of the open-celled aluminum alloy foams, in the present investigation are shown

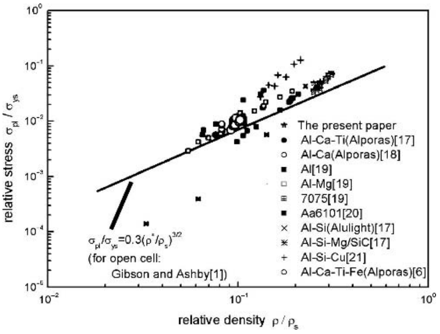

Fig. 4 Relation between the relative stress and relative density for different aluminum foams

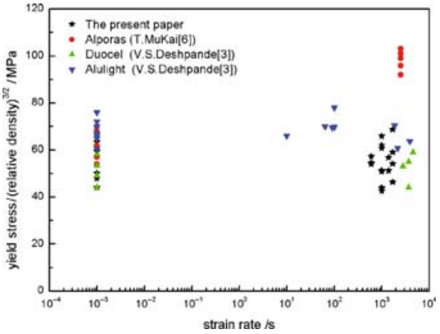

Fig. 5 Strain rate dependence of yield stress per (relative density)$^{3/2}$ for different aluminum Foams

in a reasonable agreement with the values predicted for the case of C = 0.3. This indicates further that relative density is the most important variable determining the mechanical properties of metallic foams. It is of interest to note in Fig. 2 that, despite of six orders of magnitude difference in strain rate, the curves at both the dynamic and quasi-static strain rates are practically the same. It appears that there is no strain rate effect on stress for the open-celled in the present study. Note that we adopt the criterion of a 20% elevation in strength to define the strain rate sensitivity. It is consistent with the fact that metallic foams are highly heterogeneous imperfect materials with dispersion strength of the order of 20%.

The specific yield stress (yield stress per (relative density)$^{3/2}$) of the open-cell foams as a function of strain rate is plotted in Fig. 5. As can be seen in this figure, the strength for the presented foams at the dynamic strain rates are consistent, and essentially the same as that observed at the quasi-static strain rate. This result indicates that the yield stress exhibits the slight strain rate dependence. In contrast, the Alporas foam shows the remarkable dependence. Its yield strength nearly doubles with a six orders of magnitude increase in strain rate. Two reasons may contribute to strain rate sensitivity of a cellular material: cell morphology and strain rate sensitivity of the cell wall material. To characterize the stress dependence on strain rate of the cell materials, Lindholm et al. [7] have performed dynamic tests on 6000-series aluminum alloys, with compositions close to those of the present foams. They found that the strength increases by less than 15% when the strain rate is increased from

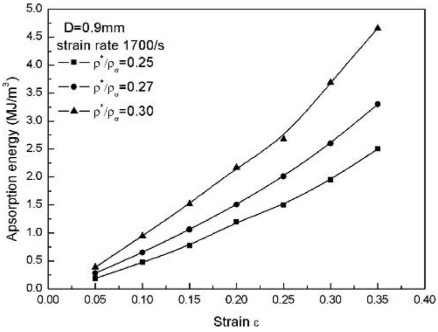

Fig. 6 Energy absorbed of aluminum alloy foams for different densities

10^{-4} to 10^3. This suggests the absence of strain rate effect in the studied aluminum alloy foams is associated with the cellular structure not the microstructure of the cell edge material. Apparently, the intrinsic properties of the cell wall material are overwhelmed by the extrinsic properties of the cell structure during compression. The energy absorbed of aluminum alloy foams increase with the densities of the foam in the experiment (Fig. 6).

4 Conclusions

The quasi-static and dynamic compressive stress–strain curves of aluminum alloy foams for various relative densities and different cell sizes have been studied. Over the range of strain rates employed, the present aluminum alloy foams exhibits slight strain rate dependence in both yield strength and absorption energy. The relation between the relative stress and relative density is a reasonable agreement with the Gibson's equation. It was concluded that the relative density is by far the most important variable and mechanical properties of the present foams appear to be independent of the cell size. Therefore, intensive efforts to modify the cell morphology are probably not an effective way to improve the impact absorption energy capacity.

References

1. L.J. Gibson, M.F. Ashby. Cellular solids: structures and properties, Cambridge University Press, Cambridge. 1997
2. L.D. Kenny. Mechanical properties of particle stabilized aluminum foam. Material Science Forum. 1996, 217–222, 1883.
3. Deshpande V.S., Fleck N.A. High strain rate compressive behavior of aluminum alloy foams. International Journal Impact Engineering. 2000, 24, 277–298.
4. J.J. Lankford, K.A. Dannemann. Strain rate effects in porous materials. Materials Research Society Symposium Proceedings, Materials Research Society, Warrendale, PA, 1998, 521, 103–108.

5. H. kanahashi et al. Dynamic compression of an ultra-low density aluminium foam. Material Science and Engineering Letter. 2000, A280, 349–353.
6. Y. Yamada et al. Compressive properties of open-cellular SG91A Al and AZ91 Mg. Material Science and Engineering Letter. 1999, A272, 455–458.
7. T. Mukai et al. Experimental study of energy absorption in a close-celled aluminum foam under dynamic loading. Scripta Materialia. 1999, 40, 921–927.
8. K.A. Dannemann, J.J. Lankford. High strain rate compression of closed-cell aluminium foams. Material Science Engineering. 2000, A293, 157–164.
9. T.G. Nieh et al. Effect of cell morphology on the compressive properties of open-cell aluminum foams. Material Science and Engineering. 2000, A283, 105–110.

Computational Modelling of Closed- and Open-Cell Cellular Structures with Fillers

M. Vesenjak, A. Öchsner, and Z. Ren

Abstract The research focuses on computational modelling of closed- and open-cell cellular structures subjected to impact loading conditions. The prime aim of computational modelling is to determine and evaluate the influence of different parameters on macroscopic behaviour of cellular structures subjected to impact loading. The explicit finite element code LS-DYNA is used for all computational simulations, also for solving a coupled dynamic problem of interaction between the cellular structure and the filler under large deformations. The influence of gas filler inside the closed-cell cellular structure is analysed with the representative volume element and use of the airbag model. The analysis of the pore fluid filler inside the open-cell cellular structures is done with the combination of the finite element method and the Smoothed particle hydrodynamics meshless method. Computational simulations prove that the increase of relative density and strain rate results in increase of the cellular structure stiffness. Parametric computational simulations have also confirmed that the filler influences macroscopic behaviour of the cellular structures, which depends on the loading type and the size of the cellular structure. In open-cell cellular structures with higher filler viscosity and higher relative density, increased impact energy absorption is observed.

1 Introduction

Cellular structures have an attractive combination of physical and mechanical properties and are being increasingly used in modern engineering applications. The most important parameters of the cellular structures are the base material, morphology,

---

M. Vesenjak (✉) and Z. Ren
University of Maribor, Faculty of Mechanical Engineering, Smetanova 17, SI-2000 Maribor, Slovenia

A. Öchsner
Technical University of Malaysia, Faculty of Mechanical Engineering, 81310 UTM Skudai, Johor, Malaysia

H. Zhao, N.A. Fleck (eds.), *Mechanical Properties of Cellular Materials,*
IUTAM Bookseries 12,

topology, relative density. To achieve adequate properties of the cellular material, the base material has to be carefully chosen in regard to its mechanical (strength, stiffness) and thermal properties (thermal conductivity). The advantages of cellular materials are low density (light-weight structures), high acoustic isolation and damping, hydrophobic (low water absorption), relatively high grade of deformation, and energy absorption, durability at dynamic loadings and fatigue, recyclability [1]. Their micro- and macroscopic properties make them very attractive for use in automotive, rail, naval and aerospace industry as heat exchangers, filters, bearings, acoustic dampers, bio-medical implants and elements for energy absorption. One of the most important areas for the future application of cellular materials is in the automotive industry, where their excellent impact energy absorption through deformation is of crucial importance for increasing passive safety of vehicles [1, 2].

This paper investigates the influence of different parameters on the behaviour of open- and closed-cell cellular structures accounting for pore fillers under impact loading by means of computational simulations using the explicit finite element code LS-DYNA [3, 4].

2 Cellular Material and Pore Fillers

Cellular materials have a characteristic stress-strain relationship in compression, which can be divided into four main areas. After initial quasi-linear elastic response, the cellular materials first experience buckling, plastic deformation and collapse of intercellular walls in the transition zone. Under further loading the mechanism of buckling, and collapse becomes even more pronounced, which is manifested in large strains at almost constant stress (stress plateau) until the cells completely collapse (densification). At this point, the cellular material stiffness increases and consequently converges towards the stiffness of the base material. During this process the cellular material is able to accumulate the mechanical energy through its deformation.

During the manufacturing procedure of closed-cell cellular metals with gas injection (air, CO_2, O_2, Ar) the gas in pores can reach up to 1,200 K and 100 MPa according to Elzey et al. [5] and Öchsner et al. [6]. After solidification and cooling down it can be assumed that the gas is trapped in the base material for a certain time. During impact loading of such materials the gas inside the pores might significantly influence the macroscopic cellular material behaviour. High gas compression under impact loading causes significant gas temperature increase, which influences the overall response of the cellular material that might result in inadvertent collapse of intercellular walls and increase of the material structure porosity [7, 8]. Investigations to incorporate the gas influence on macroscopic mechanical behaviour were done by Kitazono et al. [9], where the authors have in their analytical approach assumed a constant gas pressure in closed pore structure. However, this approach did not consider the change of the gas pressure during the deformation and the concept of large plastic deformation. Therefore, the application of their model is limited to time-independent, small deformations problems.

In open-cell cellular materials the gas can not be trapped in the cellular structure without sealing of the material boundary. A logical solution to increase the energy absorption in open-cell cellular materials is by filling the cellular structure with viscous fluid. Such fluid offers certain level of flow resistance during collapse of cellular structure due to its viscosity, which in turn increases the structure stiffness during the deformation process. Preliminary investigations have shown that in combination with high strain-rate loading this result in substantial increase of energy absorption [8, 10]. Experimental testing and computational simulations carried out have already shown that the filler significantly influences the macroscopic behaviour of materials with open-cell cellular structure [10].

However, a successful computational simulation of the cellular material behaviour under influence of external loading necessitates use of suitable numerical and constitutive models. Some of these models have been developed in the past, but they are limited regarding the loading velocity and do not account for possible cell filler influence on the macroscopic properties of the cellular material. Therefore, it is reasonable to investigate the combination of cellular structures with filler by determining its influence on the macroscopic behaviour of cellular metals by means of computational simulations.

3 Modelling of Closed-Cell Cellular Structures

Detailed modelling of cellular material structure is usually not possible due to insufficient computer capabilities. The cellular materials are therefore usually modelled by considering a "representative volume element", which serves for detailed studies of their mechanical behaviour. A regular closed-cell cellular structure was used in this study (Fig. 1) in order to avoid long computational times. The used representative volume element was cube-shaped with the edge length of 1.8 mm and

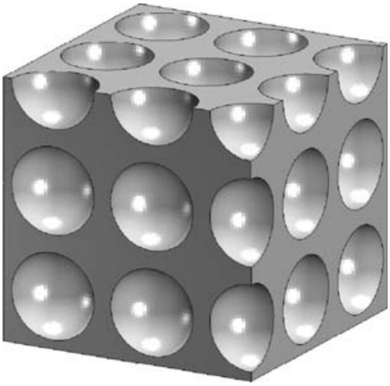

Fig. 1 Regular cellular structure

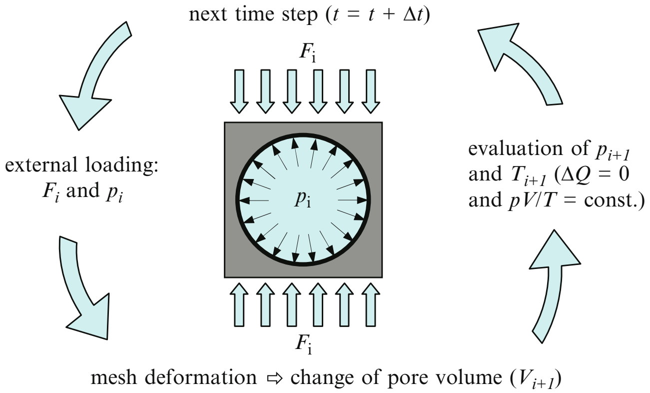

Fig. 2 Interaction between the base material and the pore gas

a spherical pore with radius of 0.75 mm. This corresponds to a relative density of 0.7. Aluminium alloy AlCuMg1 was used as the base material [10]. The strain rate effects were considered by implementing the Cowper-Symonds constitutive relation [3, 4, 11–13]. The base material was meshed with fully integrated eight-noded brick elements [4].

The change of pressure, volume and temperature of the gas inside the pore was computed using a special airbag definition subroutine in the LS-DYNA [4, 11, 14]. It was presumed that the gas inside the cell has ideal properties (pV/T = constant).

The structure deformation (change of the pore volume) results in change of gas temperature and internal pore pressure which acts on the structure. The initial pore (gas) pressure was defined with a load curve pressure vs. time. Different initial pressures (0.5, 5, 50 and 100 MPa) were used. The interaction between the base material and the pore gas is shown in Fig. 2.

The uniaxial load was displacement controlled and applied to the upper surface of the cell to reach a strain rate of $100\,\mathrm{s}^{-1}$ (common for impacts). Two cases were studied: compressive and tensile loading. In the first millisecond of the analysis only the pressure was build up in the pores and only then the structure was exposed to displacement controlled mechanical load. The lower surface was fixed in the vertical direction. Periodic boundary conditions were prescribed at model side surfaces [10]. The pore surface elements were defined as one contact group, thus effectively accounting for multiple self-contacting regimes at large deformations during computational analyses.

3.1 Computational Results

The computational results shows that the pore compresses more in case of lower initial pore pressure than in case of higher pore pressure. High pore pressure also results in higher base material deformation.

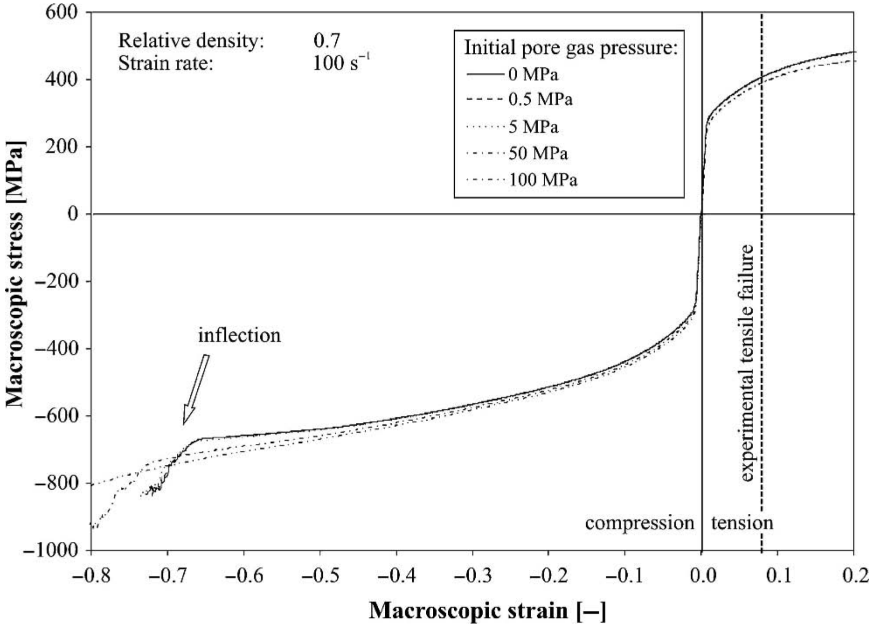

Fig. 3 Influence of the pore pressure at compressive and tensile loading

Figure 3 illustrates the simulated behaviour of the closed-cell cellular structure under compressive and tensile impact loading with different initial pore gas pressures at a strain rate of $100\,\mathrm{s}^{-1}$. Under compressive loading the pore volume decreases and consequently the internal pore gas pressure increases. This mechanism leads to increase of the macroscopic yield stress, since the gas pressure inside the pore acts in the opposite direction than the external loading. With higher pore gas pressure the cellular structure exhibits higher stress levels during the plastic deformation and thus absorbs more impact energy. Furthermore, higher pore gas pressure contributes to delayed and slower densification of the cellular structure, which occurs at a higher strain. During tensile loading the higher pore gas pressure lowers the macroscopic yield. With higher pore gas pressure the cellular structure exhibits lower stress levels during the plastic deformation and thus absorbs less impact energy. Additional computational simulations have shown that the pore gas pressure has higher influence on cellular structures with lower relative density.

The gas pressure change in regard to the initial pore gas pressure is shown in Fig. 4. It is evident that the gas pressure change is higher in case of a lower initial pressure [10].

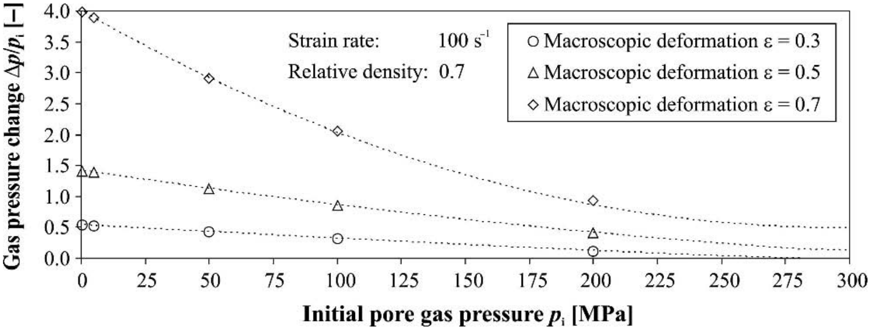

Fig. 4 Gas pressure change regarding the initial pore gas pressure

4 Modelling of Open-Cell Cellular Structures

The influence of viscous pore fillers on behaviour of regular open-cell cellular structures subjected to impact loading was also studied with dynamic computational simulations. The compressive behaviour open-cell cellular structure (Fig. 5) has been studied using three relative densities $\rho/\rho_0 = 0.42$, 0.27 and 0.14. This corresponds to the basic geometry dimensions of $d = 2.5$, 3 and 3.5 mm and $a = 4$ mm. The FullCure 720 polymer was used as the base material with the following mechanical properties: $E = 2{,}323$ MPa, $\nu = 0.3$, $R_e = 48.9$ MPa (tension), $R_e = 91$ MPa (compression), $C = 1{,}050\,\mathrm{s}^{-1}$ and $p = 3.5$ (strain rate constants).

The viscous pore filler ($\rho = 1{,}000\,\mathrm{kg/m}^3$ and $\eta = 10^{-3}$ Pa s at 293 K) was modelled and discretised with the meshless Smoothed particle hydrodynamics method (SPH) [3, 10, 14]. The relationship between the change of volume and pressure has been represented with the Mie-Grüneisen equation of state [3, 10]. The cellular structure was loaded with a displacement controlled compressive load on the upper surface achieving the strain rate of $1{,}000\,\mathrm{s}^{-1}$. Due to regular geometry of cellular structure, the symmetry boundary conditions have been applied. The cellular structure surface elements were defined as one contact group to account for possible self-contact at very large deformations.

4.1 Computational Results

Figure 6 shows the outflow of the filler as a consequence of the cellular structure deformation under dynamic compressive loading for two cases: (i) without pore filler (left) and (ii) with pore filler (right).

The computational simulations have confirmed that the size of the model and the number of the cells influence the macroscopic behaviour of cellular structure. Higher number of cells increases the stiffness of the cellular structure and consequently results in higher ability of energy absorption, since the filler is subjected to higher flow resistance and needs more time during its outflow, as shown in Fig. 7.

Fig. 5 Geometry of the open-cell cellular structure

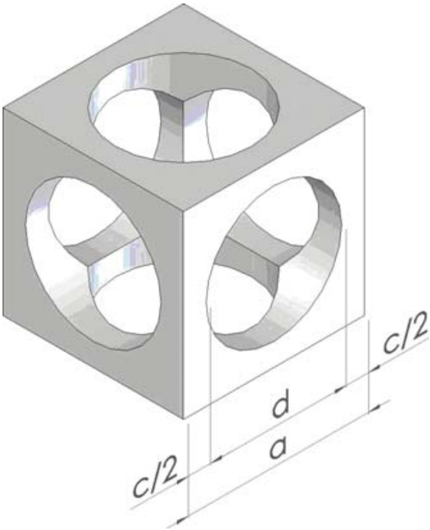

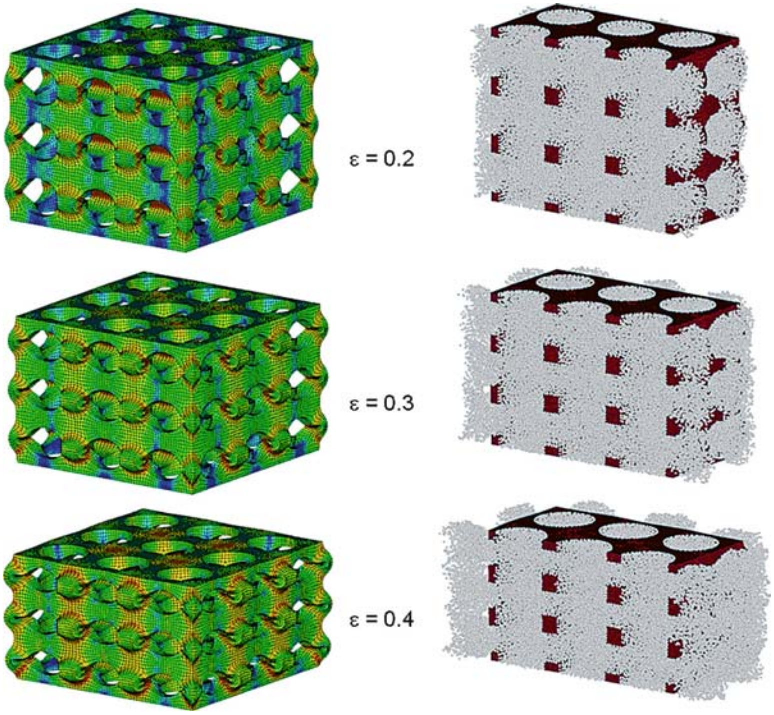

Fig. 6 Deformation of the cellular structure and the fluid filler outflow

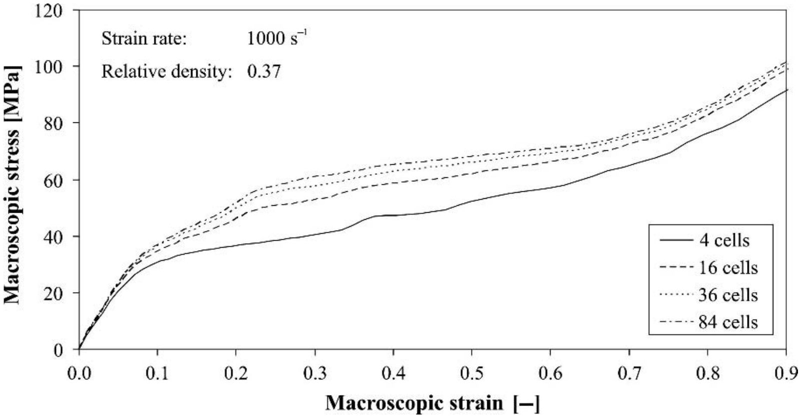

Fig. 7 The influence of the cell number on cellular structure behaviour

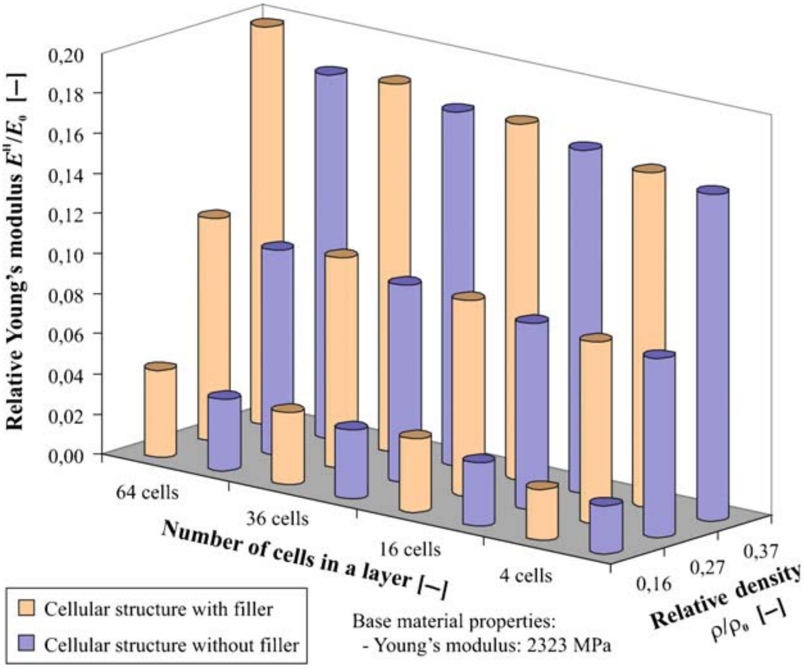

Fig. 8 The influence of relative density and cellular structure size

From the computational results it can also be observed that the filler influences more the behaviour of a cellular structure with a higher relative density than a cellular structure with a lower relative density. The reason for this effect can be found in the pore sizes of the cellular structures.

Figure 8 illustrates the influence of relative density and cellular structure size on relative Young's modulus. From the figure it can be observed that the Young's modulus increases with increase of cellular structure size and relative density.

5 Conclusions

The paper presents computational simulations of closed- and open-cell cellular structures behaviour subjected to impact loading and very large deformations, accounting for the influence of fluid filler inside the cellular structure's pores and connects three very important fields of engineering computational simulations: (i) modelling of cellular structures, (ii) fluid-structure interaction, and (iii) impact loading conditions.

The results of the closed-cell cellular structure simulations show that the gas inside the pores influences the macroscopic behaviour of the cellular structure. The gas influence is more pronounced at lower relative densities of the cellular structure and changes regarding the loading type. Computational results of the open-cell cellular structure have shown that the deformational energy absorption increases with increasing the relative density, the size of the cellular structure and the number of cells, due to a higher resistance and energy dissipation during the viscous filler outflow.

Future research work will be focused on experimental testing and also detailed study of cellular structure subjected to multi-axial impact loading conditions and irregular cellular structures.

References

1. Banhart, J., Manufacture, characterisation and application of cellular metals and metallic foams. Prog. Mater. Sci. 46 (6), 2001.
2. Gibson, L.J., Ashby, M.F., Cellular solids: Structure and properties. Cambridge University Press, Cambridge, 1997.
3. Hallquist, J., LS-DYNA theoretical manual. Livermore Software Technology Corporation, Livermore, CA, 1998.
4. Hallquist, J., LS-DYNA keyword manual. Livermore Software Technology Corporation, Livermore, CA, 2003.
5. Elzey, D.M., Wadley, H.N.G., The limits of solid state foaming. Acta mater. 49: 849–859, 2001.
6. Öchsner, A., Mishuris, G., Gracio, J., Modelling of the multiaxial elasto-plastic behaviour of porous metals with internal gas pressure. Elsevier Science, Amsterdam, 2004.
7. Ohrndorf, A., Schmidt, P., Krupp, U., Christ, H.J., Mechanische Untersuchung eines geschlossenporigen Aluminiumschaums. Bad Nauheim: Deutscher Verband für Materialforschung und –prüfung, 2000.
8. Lankford, J., Dannemann, K.A., Strain rate effects in porous materials, Mat. Res. Soc. Symp. Proc. 521, 1998.
9. Kitazono, K., Sato, E., Kuribayashi, K., Application of mean field approximation to elastic-plastic behaviour for closed-cell foams. Acta mater. 51: 4823–4836, 2003.
10. Vesenjak, M., Computational modelling of cellular structures under impact conditions (in Slovene), Ph.D. thesis, Faculty of Mechanical Engineering, Maribor, Slovenia, 2006.
11. Bodener, S.R., Symonds, P.S., Experimental and theoretical investigation of the plastic deformation of cantilever beam subjected to impulse loading. J. Appl. Mech. 29, 1962.
12. Altenhof, A., Ames, W., Strain rate effects for aluminum and magnesium alloys in finite element simulations of steering wheel impact test. Fatigue Fract. Eng. Mater. Struct. 25, 2002.

13. Vesenjak, M., Öchsner, A., Hribersek, M., Ren, Z., Behaviour of cellular structures with fluid fillers under impact loading. Int. J. Multiphys. 1, 2007.
14. Liu, G.R., Liu, M.B., Smoothed particle hydrodynamics – a meshfree particle method. World Scientific, Singapore, 2003.

Study of Cellular Materials Sandwich Under Dynamic Loading for Bird Strike Application

Y. Girard, I. Elnasri, and H. Zhao

Abstract This paper reports an original inverse perforation tests on foam core sandwich panels under impact loading. The key point is the use of an instrumented Hopkinson pressure bar as a perforator and at the same time a measuring device. It aims at a high quality piercing force record during the whole perforation process, which is not available in common free-flying projectile—target testing schemes. This new testing arrangement allows for the measurement of piercing force-displacement curves under quasi-static and impact loadings of sandwich samples, which is made of 40 mm AlSi7Mg0.5 Cymat foam cores and 0.8 mm thick 2024 T3 aluminium sheet as top and bottom skins. Compared with quasi-static top skin peak loads (the maximal load before the perforation of top skins) obtained under same geometric and clamping conditions and even in the case that the used foam core (Cymat) and aluminium skin sheet are known and have been confirmed to be rate insensitive, a significant enhancement under impact loading (20%) of the top skin peak load is found.

Keywords Perforation · Sandwich panel · Foam · Impact · Hopkinson bars

1 Introduction

Sandwich panels with cellular core materials offer a high specific strength and an interest energy absorbing ability. Such properties make them a good solution for the protection of aeronautic structures from impacting foreign objects. For example,

---

Y. Girard (✉)
EADS IW Suresnes, 12 bis rue Pasteur, 92152 Suresnes cedex, France

I. Elnasri and H. Zhao
Laboratoire de Mécanique et Technologie, ENS-Cachan/CNRS-UMR8535/Université Paris 6, 61, avenue du président Wilson, 94235 Cachan cedex, France
yannick.girard@eads.net

H. Zhao, N.A. Fleck (eds.), *Mechanical Properties of Cellular Materials,*
IUTAM Bookseries 12,

such panels are often used in front of aircrafts to prevent accidental bird strikes [1], which can cause significant damages to equipments and therefore affect their safety. Penetration/perforation resistances at high impact velocity of sandwich panels are then required to qualify different panels made of different skin materials (aluminium, fibre-renforced polymer) and cellular cores (honeycomb, foam, hollow sphere, etc.). Common penetration tests for lower velocity $(<15\,\mathrm{m/s})$ could be performed using a drop hammer with a perforator [2, 3]. The basic measurement in this case is the deceleration of the impact mass, estimated by an accelerometer. The force-displacement curves can be derived even though they are sometimes not accurate enough. However, the common testing technique at higher velocity consists in launching with a gas gun a free flying projectile against an immobile target [4, 5, 6]. Such a technique is also used in the case of sandwich panels [7, 8]. The main records were velocities before and after perforation of the panel and there was a lack of whole perforating force-displacement history. One can only have a global energy absorbed during perforation [8, 9] and this makes it very difficult the understanding of what was happened during high speed perforation processes. This paper presents an inversed perforation test where panels samples were launched at high velocity against an 6 m long pressure bar at rest, which plays the role of perforator and at the same time force cell providing force and displacement recordings during the whole perforation process.

2 Experimental Arrangement

The main deficiency of classical free flying projectile–target perforation tests reported in the open literature is the lack of the force recording during the perforation process. An evident solution is to use an instrumented long rod as the projectile, and the piercing force is then measurable from recorded wave profiles as in the case of a Hopkinson pressure bar [10, 11]. However, it was very difficult to launch a long rod at a uniform speed without frictions during the test. In general, a length of several meters is necessary because the measuring duration is determined by the length over the wave speed in the rod [12]. An alternative is to launch the target sandwich panel to strike the perforating long rod. Therefore, the proposed inversed perforation testing setup used a gas gun with a 70 mm inner diameter barrel and a 16 mm diameter and 6 m-long rod with a semi-spherical nose at its perforating end. The rod is instrumented by strain gauges aimed at accurate force measurements during the whole perforation process. Figure 1 shows an outline of the experimental set-up.

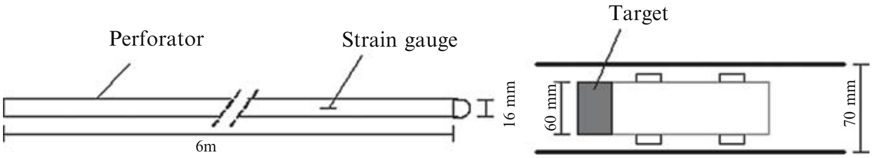

Fig. 1 Experimental set-up

Fig. 2 Photo of projectile

The cylindrical target sandwich sample is launched with the aid of a hollow tube-like projectile, which is made from an aluminium tube with a welded bottom plate at one end. Two Teflon rings are screwed on the tube which allow for a small friction between projectile and the barrel of the gas gun. The cylindrical sandwich samples are mounted between the open end of the aluminium tube and an aluminium clamping ring. The fixture is realised by six uniformly distributed bolts slightly tightened. Figure 2 provides a photograph of this projectile. The tube like projectile together with fixture system has a weight of 720 g. The gas gun can launch such a mass to a speed up to 60 m/s.

3 Measuring Technique with Pressure Hopkinson Bars

With aforementioned inversed perforation testing setup, the piercing strain impulse can be recorded by the strain gauges cemented on the pressure bars. Indeed, Hopkinson pressure bar analysis is based on the following basic assumption: the waves propagating in the bars can be described by the one-dimensional wave propagation theory. According to this wave propagation theory, the stress and the particle velocity associated with a single wave can be calculated from the associated strain measured by the strain gages. Therefore, the piercing force and velocity time history are calculated by Eq. (1)

$$\begin{aligned} \mathrm{F}(\mathrm{t}) &= \mathrm{S_b}.\mathrm{E_b}.\varepsilon(\mathrm{t}) \\ \mathrm{v}(\mathrm{t}) &= \mathrm{C_b}\varepsilon(\mathrm{t}) \end{aligned} . \tag{1}$$

where S_b, E_b, C_b are respectively the cross sectional area, the elastic modulus and elastic wave speed of the pressure bar.

However, such a theory cannot describe the eventual wave dispersion effect which can introduce some error in the necessary virtual shift from the measuring point to the perforating end in time and space because the measuring point is not located at the piercing end. Therefore, the correction of this dispersion effect on the basis of the Pochhammer's wave propagation theory is systematically performed in the data processing of this wave shift [13]. The velocity of launched sandwich plate before strikes is also available, measured with two optical barriers. With this initial impact velocity, it is possible to estimate the piercing displacement. Indeed, the sandwich plated mounted on the projectile is decelerated by the piercing force measured by pressure bar. Thus, the velocity history of the sandwich sample and the relative displacement time history can be evaluated by the Eq. (2).

$$\begin{aligned} \mathrm{v}_{\mathrm{sandwich}}(\mathrm{t}) &= \mathrm{V}_0 - \int_0^{\mathrm{t}} \frac{\mathrm{F}(\tau)}{\mathrm{M}} \mathrm{d}\tau \\ \mathrm{U}(\mathrm{t}) &= \int_0^{\mathrm{t}} (\mathrm{v}_{\mathrm{sandwich}}(\tau) - \mathrm{v}(\tau))\mathrm{d}\tau. \end{aligned} \tag{2}$$

where M is the sum of the mass of the sandwich sample and that of the projectile. In this way, a corresponding force-displacement curve was found, which make possible a quantitative comparison between quasi-static and impact piercing behaviour.

4 Quasi-Static and Impact Perforations of Foam Core Sandwich Panels

The studied sandwich panels is made of 40 mm thick $AlSi_7Mg_{0.5}$ foam cores with an average relative density around 0.085 and two 0.8 mm thick 2024 T3 aluminium skins. It is a potential solution in the Airbus aircrafts. The cylindrical samples of 60 mm diameter were made, which have a range of weight (41–47 g) due to the heterogeneity of foam cores. The behaviour of foam cores has been investigated under quasi-static and impact loadings. Samples used in these material characterisation tests are 60 mm diameter and 40 mm length cylinder. Quasi-static tests are performed with universal testing machines and dynamic tests are performed with a special large diameter Nylon Split Hopkinson pressure bar in [14]. The results provide a general impression that this foam was not sensitive to the loading rate. Indeed, a large number of tests at various loading rate shows that there is a significant scatter but rate sensitivity is quite small (Fig. 3). The behaviour of aluminium skin is also performed under shear quasi-static and dynamic loading. It proofs that the aluminium is rate insensitive.

In order to obtain the same supporting condition for quasi-static and dynamic loadings, the quasi-static test is performed using the tube projectile as the supporting and fixing system. The sandwich sample mounted on the projectile is put into a universal testing machine, and a 16 mm rod with spherical nose is used for perforation. The size effect is neglected because the average pore size is quite small [15]. Perforation tests are conducted at controlled speeds (0.1 mm/s). Piercing forces were

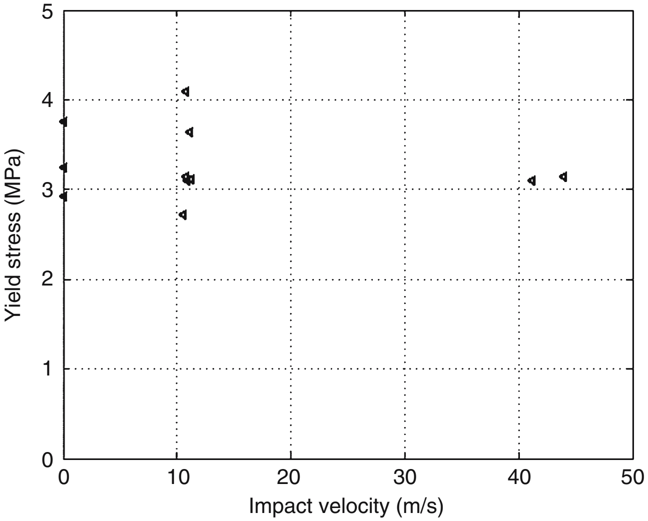

Fig. 3 Rate sensitivity of foam cores

Fig. 4 Bottom skin

recorded with a force cell and displacement is obtained from testing machine measurements. Figures 4 and 5 show post-mortem photographs of the bottom skin and the top skin respectively. One can note in particular the circular marks in these skins, which illustrate a good clumping condition. Figure 6 shows two quasi-static perforating curves, which contain the two peak loads corresponding to the piercing of top and bottom skins. Such curves are the characteristic results for cellular core sandwich panels, reported in many previous works on various panels. In particular, the present results is compared with perforation tests with same perforator but on a 100 × 500 mm clumping system, the peak loads are very close to each other [**?**]. Such a comparison provides another proof that clumping condition is well respected.

Fig. 5 Top skin

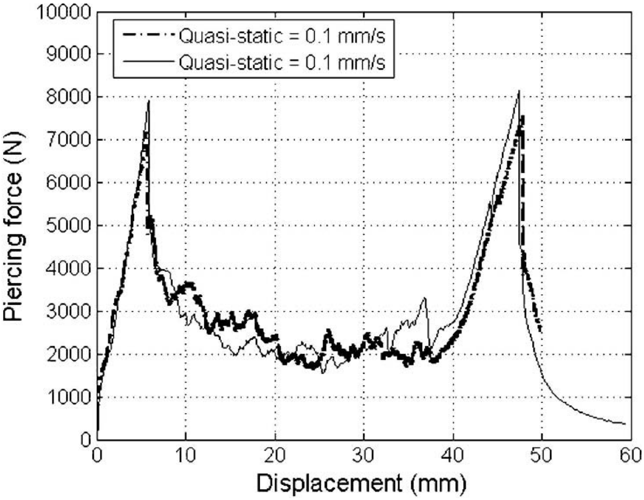

Fig. 6 Two typical perforation tests

5 Dynamic Perforation

Perforation tests under impact speed up to 46 m/s have been performed with presented inversed perforation testing setup. Detailed post mortem images of sandwich samples under impact loading are given in Fig. 7. One of the evident differences is that the foam core has undergone a compression. Therefore, only the observation of the bottom skin failure is not affected by the stopping system (aluminium bumper used to stop the residual velocity of the projectile after complete perforation of the sample). It can be seen that, petaling can occurs under impact loading, which is different from the disking failure mode for bottom skin under quasi-static loading. The force and displacement curve under impact loading can be obtained using Eqs. (1, 2). Figure 8 illustrates a comparison between quasi-static and impact perforations around 45 m/s.

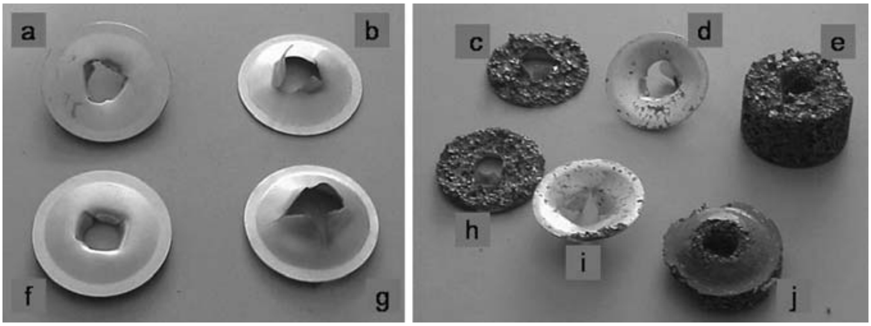

Fig. 7 Post mortem images of perforated sandwich samples. Incident top skins side (**a, f**), distal skins side (**b, g**), opposed incident top skins side (**c, h**), opposed distal bottoms skins side (**d, i**), foam cores (**e, j**). Samples tested at 27 m/s (**a–e**) and 46 m/s (**f–j**)

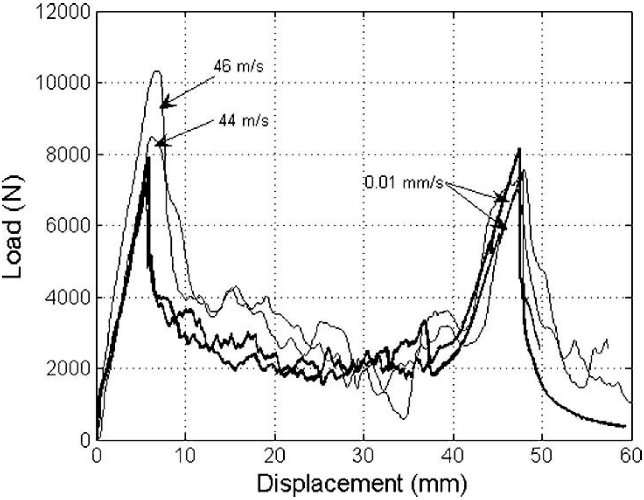

Fig. 8 Quasi-static and impact piercing force versus displacement curves

Such comparisons of static and impact perforation tests show a significant enhancement of the top skin peak load under impact loading. However, what is the scatter of such results? Due to small number of supplied samples, only two impact tests around 20 m/s and two tests around 45 m/s are performed. The scatter found in impact test is quite high. However, the samples have not the same mass and the density of foam core is then different. It is well-known that the foam core strength depends much on its density [16]. On see that in these tests, the rule that denser sample has a higher resistance is respected. In order to weaken such a mass density effect, an affine correction with respect to the mass density is applied. Top skins peak loads after correction are plotted with a logarithmic value of piercing speed in Fig. 9. The enhancement under impact loading is then evident and the average enhancement under impact loading is about 20%.

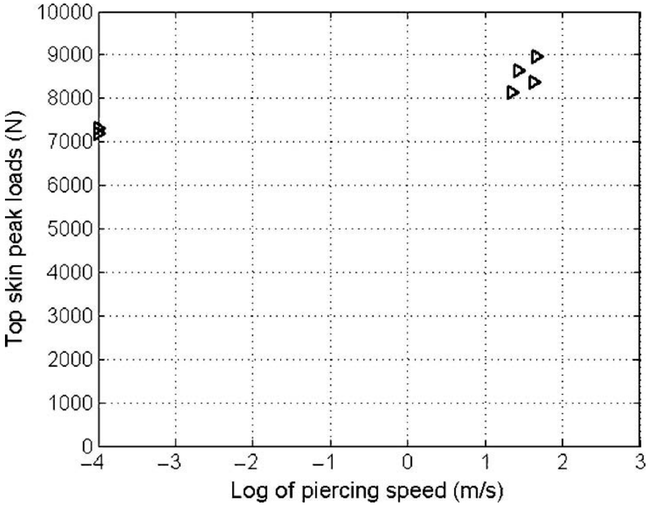

Fig. 9 Density weighted of top skin peak loads

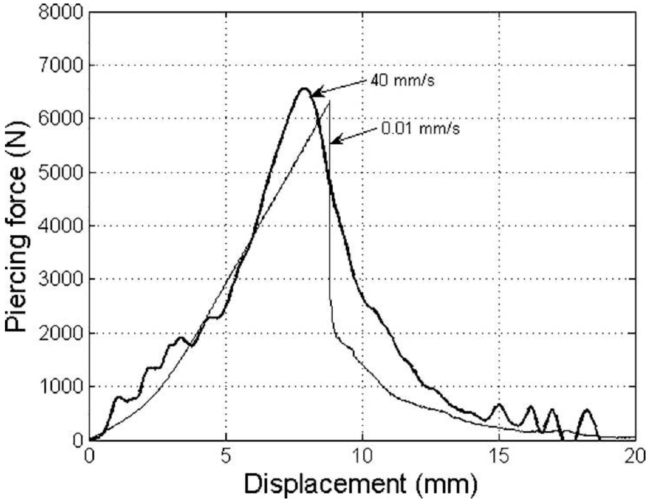

Fig. 10 Piercing force-displacement curve of 0.8 mm 2024 T3 sheet

The enhancement found for the top skin peak loads is quite puzzling. It should not be due to the rate sensitivity of the aluminium sheet because the bottom skin peak loads are nearly rate insensitive. In order to check this argument, the piercing test on the 2024 T3 aluminium sheets mounted on the same tube-like projectile under static and impact loading are performed. It shows, in Fig. 10, that there is nearly no rate sensitivity of skin sheet. It is also noted that the foam core itself is not rate sensitive [14]. This enhancement should be due to the different interaction mechanism under static and impact loadings. Indeed, the piercing force of the top skin depends on the foam core strength. Under quasi-static loading, there exists a simple analytical model [17] which simplify the problem as a membrane sheet supported by rigid plastic media. Under this membrane-rigid plastic support assumption, the penetrating force depends on the tensile strength of the sheet and the equivalent supporting strength of foam cores. As the foam core have a strain hardening [14], the top skin peak load should depend on compressive strain of the foam core reached before the failure of skin sheets, and this strain before the skin failure could be different under static and impact loading, because of the inertia effect for example.

6 Conclusion

The presented inverse perforation testing technique using a long thin instrumented Hopkinson bar allows for the measurement of piercing forces during the whole perforation process. Such measurement is missing in a classical free flying penetrator- immobile target scheme under impact loading. The present method makes it possible to compare directly impact piercing force-displacement curves with the static ones. Such test is applied to sandwich panels made of an $AlSi_7Mg_{0.5}$ aluminium foam core and 0.8 mm thick 2024 T3 aluminium top and bottom skins. Quasi-static, impact tests (around 2 m/s and around 45 m/s) are performed. A significant enhancement of the top skin peak loads under impact loading is found. The origin of such enhancement is puzzling because the skin sheet as well as foam cores are nearly rate insensitive. A possible reason is the difference of strain hardening reached under static and impact loading due to inertia effect. Such localised foam core strength enhancement leads to the increase of the top skin peak loads.

References

1. Hanssen A.G., Girard Y., Olovsson L., Berstad T., Langseth M., “A numerical model for bird strike of aluminium foam-based sandwich panels,” Int. J. Impact Eng., vol. 32, 2006, pp. 1127–1144
2. Mines R.A.W., Worrall C.M., Gibson A.G., “Low velocity perforation behaviour of polymer composite sandwich panels,” Int. J. Impact Eng., vol. 21, 1998, pp. 855–879.
3. Shyr T.W., Pan Y.H., “Low velocity impact responses of hollow core sandwich laminate and interply hybrid laminate,” Compos. Struct., vol. 64, 2004, pp. 189–198.
4. Backman M.E., Goldsmith W., “The mechanics of penetration of projectiles into targets,” Int. J. Eng. Sci, vol. 16, 1978, pp. 1–99.
5. Corbett G.C., Reid S.R., Johnson W., “Impact loading of plates and shells by free flying projectiles. A review,” Int. J. Impact Eng., vol. 18, 1996, pp. 141–230.
6. Borvik T., Clausen A.H., Hopperstad O.S., Langseth M., “Perforation of AA5083-H116 aluminium plates with conical-nose steel projectiles—experimental study,” Int. J. Impact. Eng., vol. 30, 2004, pp. 367–384.
7. Goldsmith W., Wang G.T., Li K., Crane D., “Perforation of cellular sandwich plates,” Int. J. Impact. Eng., vol. 19, 1997, pp. 361–379.

8. Roach A.M., Evans K.E., Jones N., "The penetration energy of sandwich panel elements under static and dynamic loading," Part I, Compos. Struct., vol. 42, 1998, pp. 119–134.
9. Li Y., Li J.B., Zhang R.Q., "Energy-absorption performance of porous materials in sandwich composites under hypervelocity impact loading," Compos. Struct., vol. 64, 2004, pp. 71–78.
10. Hopkinson B., "A method of measuring the pressure produced in the detonation of high explosives or by the impact of bullets," Philos. Trans. R. Soc. London, vol. A 213, 1914, pp. 437–456.
11. Kolsky H., "An investigation of the properties of materials at very high rates, of loading," Proc. Phys. Soc. London, vol. B62, 1949, pp. 676–700.
12. Zhao H., Gary G., "A new method for the separation of waves. Application to the SHPB technique for an unlimited measuring duration," J. Mech. Phys. Solids, vol. 45, 1997, pp. 1185–1202.
13. Zhao H., Gary G., "On the use of SHPB technique to determine the dynamic behavior of the materials in the range of small strains," Int. J. Solid Struct., vol. 33, 1996, pp. 3363–3375.
14. Zhao H., Elnasri I., Abdennadher S., "An experimental study on the behaviour under impact loading of metallic cellular materials," Int. J. Mech. Sci, vol. 47, 2005, pp. 757–774.
15. Olurin O.B, Fleck N.A, Ashby M.F., "Indentation resistance of aluminium foam," Scr. Mater., vol. 43, 2000, pp. 983–989.
16. Gibson L.J., Ashby M.F., Cellular solids, structure and properties, Cambridge University Press, Cambridge, 1987.
17. Wierzbicki T., de Lacruz-Alvarez A., Hoo Fatt M.S., "Impact energy absorption of sandwich plates with crushable core," Proceedings of the ASME/AMD Symposium, Impact Waves, and Fracture, Los Angeles, CA, vol. 205, June 1995, pp. 391–411.